Felix Christian Mehlan

Digital Twins for Fault Prognosis in Offshore Wind Turbine Drivetrains

Doctoral thesis

Felix Christian Mehlan

NTNU
Norwegian University of
Science and Technology

NTNU
Norwegian University of
Science and Technology

NTNU

Felix Christian Mehlan

Digital Twins for Fault Prognosis in Offshore Wind Turbine Drivetrains

Thesis for the degree of Philosophiae Doctor

Trondheim, May 2024

Norwegian University of Science and Technology

NTNU
Norwegian University of
Science and Technology

PRINTED IN
NORWAY
NO - 1598

NORDIC SWAN ECOLABEL

Printed matter
2041 0731

Abstract

This thesis investigates the relatively novel concept of Digital Twin (DT) in the context of offshore wind turbine drivetrains. DT can be described as a virtual representation of a system or asset that calculates system states and makes system information available, through integrated models and data, with the purpose of providing decision support over its life cycle. Applying these ideas to the use case of drivetrains, there remain many research questions on the specifics of drivetrain DTs such as its model architecture, its capability and value to the user, its limitations and remaining development obstacles, and the errors and uncertainty in its output, which are addressed in this thesis. The scope is narrowed to the fault diagnosis and prognosis, i.e. the remaining useful life (RUL) estimation of mechanical drivetrain components such as bearings and gears. Through this capability, DTs can provide wind farm operators with a form of decision support and thereby contribute to a higher reliability and availability.

The investigation is divided into three sections that cover each of the main elements of DT: the data, the models and the decision support. Real-time data streams from physical sensors are crucial to inform the DT on the current state of the drivetrain. The methodology of data acquisition, processing and analysis from different sources such as SCADA and CM systems is presented.

DT models differ from conventional, standalone simulation models, in that they are connected to the physical drivetrain and must be updated continuously to reflect its behaviour. Reduced-order models are investigated, which are computationally efficient to allow real-time simulation while maintaining a sufficient model fidelity to accurately capture the complex drivetrain dynamics. In addition, state estimation and system identification methods are presented to synchronize the DT and the physical drivetrain in the kinematic states and model parameters.

Decision support are services provided by the DT that assist stakeholders in making key decisions. The focus of this thesis is the RUL estimation based on fatigue assessment, which is facilitated through online load monitoring techniques, referred to as virtual sensing. The methodology for virtual load sensing at the main bearings and at the gearbox components is developed and evaluated in numerical and experimental case studies.

This thesis contributes to a better understanding of the DT concept by developing and showcasing concrete applications for offshore wind turbine drivetrains and elaborating their capabilities, as well as the arising challenges and limitations.

Preface

This thesis is submitted to the Norwegian University of Science and Technology (NTNU) for partial fulfilment of the requirements for the degree of philosophiae doctor.

This doctoral work has been performed at the Department of Marine Technology, NTNU, Trondheim, with Professor Amir R. Nejad as main supervisor and with co-supervisor Professor Zhen Gao.

Acknowledgement

I would like to express my gratitude to everybody who has contributed to this thesis. First and foremost, I would like thank my supervisors Professor Amir R. Nejad and Professor Zhen Gao, who were supportive and always had an open door throughout every stage of my PhD project. Their professional guidance helped me find my path and realize my ambitions.

I also greatly appreciate all contributions by the co-authors of my papers. Professor Eilif Pederson's expertise in modelling theory was instrumental during the development of reduced order models for paper 1. Dr. Jonathon Keller's provision of field measurements and collaboration for paper 4 greatly advanced the progress of my work.

I would also like to thank Dr. Andrea Sánchez for the inspiring discussions on rotor imbalance that initiated paper 5 and Dr. Shuaishuai Wang for providing the DTU 10 MW drivetrain model that facilitated the numerical experiments in paper 5 and 6.

My gratitude also extends to my fellow PhD candidates Diederik van Binsbergen, Ali Dibaj, Etienne Purcell, Kelly Tartt, Muhammad Omer Siddiqui, Ashkan Rezai, Jakob Vincent Gebel, Veronica Liverud Krathe, Irene Arreba Rivera and Serag-Eldin Abdelmoteleb, who provided valuable feedback and constructive discussions on my work.

And last, but certainly not least, I am incredibly thankful for my dear friend Gunnbjörg Gunnarsdóttir who helped me through the toughest times.

List of Appended Papers

This thesis consists of an introductory part and six papers, which are appended.

Paper description

Paper 1 [1]:
Modelling of wind turbine gear stages for Digital Twin and real-time virtual sensing using bond graphs.
Authors: Felix C. Mehlan, Eilif Pedersen, Amir R. Nejad
Published in *Jounal of Physics: Conference Series*, 2022, DOI: 10.1088/1742-6596/2265/3/032065.

Paper 2 [2]:
Estimation of wind turbine gearbox loads for online fatigue monitoring using inverse methods.
Authors: Felix C. Mehlan, Zhen Gao, Amir R. Nejad
Published in *Proceedings of the ASME 2021 40th International Conference on Ocean, Offshore and Arctic Engineering*, 2021, DOI: V009T09A021-1.

Paper 3 [3]:
Digital Twin Based Virtual Sensor for Online Fatigue Damage Monitoring in Offshore Wind Turbine Drivetrains.
Authors: Felix C. Mehlan, Zhen Gao, Amir R. Nejad
Published in *Journal of Offshore Mechanics and Arctic Engineering*, 2021, No: 10.1115/1.4055551.

Paper 4 [4]:
Virtual sensing of wind turbine hub loads and drivetrain fatigue damage.
Authors: Felix C. Mehlan, Jonathan Keller, Amir R. Nejad
Published in *Forschung im Ingernieurwesen*, 2023, DOI: 10.1007/s10010-023-00627-0.

Paper 5 [5]:
Rotor imbalance detection and diagnosis in floating wind turbines by means of drivetrain condition monitoring.
Authors: Felix C. Mehlan, Amir R. Nejad
Published in *Renewable Energy*, 2023, DOI: 0.1016/j.renene.2023.04.102.

Paper 6 [6]:
On the uncertainty of digital twin models for load monitoring and fatigue assessment in wind turbine drivetrains
Authors: Felix C. Mehlan, Amir R. Nejad
Submitted to *Wind Energy Science*, 2024

Declaration of Authorship

All six papers that serve as the core content of this thesis are co-authored. In all these papers, I am the first author and responsible for initiating ideas, performing the analysis and calculations, providing the results and writing the papers. Professor Amir R. Nejad and Professor Zhen Gao have contributed to the support, corrections and constructive comments to increase the scientific quality of the publications.

Dr. Jonathan Keller provided field measurements of the DOE 1.5 MW research wind turbine for paper 4 and also contributed with constructive comments and discussions.

Professor Eilif Pedersen taught the Bond Graph theory in the course MR8405 and provided constructive comments during the development of the gear stage reduced order model for paper 1.

The NREL 5 MW drivetrain model used for papers 1, 2, 3 and 6 was provided by Professor Amir R. Nejad and the DTU 10 MW drivetrain model used for papers 5 and 6 was provided by Dr. Shuaishuai Wang.

Abbreviations

AD	Anomaly detection
AI	Artificial intelligence
AKF	Augmented Kalman filter
ANN	Artificial neural networks
CAD	Computer aided sesign
CFD	Computational fluid dynamic
CM	Condition monitoring
DLC	Design load case
DNV	Det Norske Veritas
DOE	U.S. Department of Energy
DOF	Degree of freedom
DT	Digital Twin
DTU	Technical University of Denmark
EMA	Experimental modal analysis
FE	Finite element
FFT	Fast Fourier Transform
FOM	Full-order model
HSS	High-speed shaft
IEC	International Electrotechnical Commission

IMS	Intermediate-speed shaft
IoT	Internet of Things
LCOE	Levelized costs of energy
LDD	Load duration distribution
LSS	Low-speed shaft
MBS	Multi-body simulation
ML	Machine learning
NREL	National Renewable Energy Laboratory
O&M	Operation and maintenance
OEM	Original equipment manufacturer
OMA	Operational modal analysis
PCA	Principal component analysis
PSD	Power spectral density
R&D	Research and development
ROM	Reduced-order model
RUL	Remaining useful life
SCADA	Supervisory control analysis and data acquisition

Contents

List of Tables

List of Figures

Chapter 1

Introduction

1.1 Motivation

Digital Twin (DT) has in recent years attracted tremendous attention among researchers and businesses alike. What was once a fringe idea in the 2000s, has developed to a major technological trend, reportedly one of the top ten strategic technology trends according to the Gartner's report of the years 2017 to 2019 [7]. The DT concept has been adopted in a diverse range of industries ranging from the aerospace to health care and recently making grounds in the offshore wind energy sector.

The exponential growth of research and business activities is fueled on the supply side by technological advancements and on the demand side by market forces (Fig. 1.1). Advancements in sensor technologies and Internet of Things (IoT) platforms enable the acquisition of ever increasing amounts of data that are instantly and remotely accessible via cloud services. In offshore wind turbines the industry standard are supervisory control analysis and data acquisition (SCADA) and condition monitoring (CM) systems that feature a wide range of sensors for the observation of the operational status and the health condition. Artificial Intelligence (AI) and Big Data algorithms are invaluable to transform the large amounts of data into serviceable information, in particular, machine learning (ML) models have proven to be highly effective to analyze SCADA and CMS data. Physics-based models of wind turbine drivetrains have also advanced in recent years. Multi-body simulation (MBS) models have matured to high levels of fidelity and are capable of simulating drivetrain dynamics to great detail and accuracy, while demanding fewer computational resources than finite element (FE) models. These technologies are critical to construct DTs for wind turbine drivetrains.
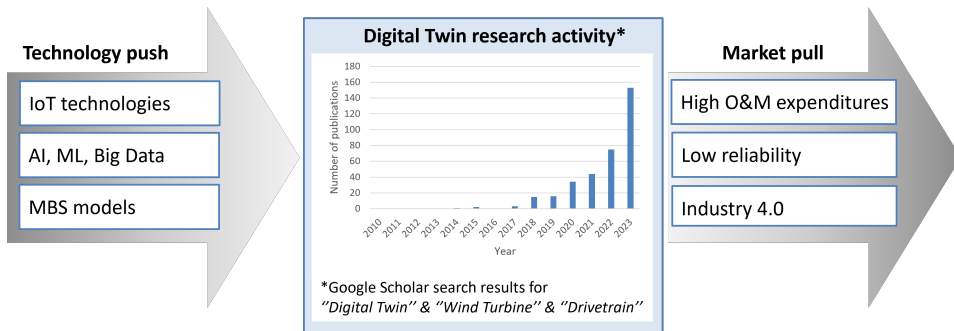
Figure 1.1: Push- and pull-factors for the research into DTs of offshore wind turbine drivetrains.

At the same time, the demand for increased digitization and automation is voiced in the offshore wind energy sector, a trend commonly referred to as Industry 4.0. The major market force that drives this trend are the high operation and maintenance (O&M) expenditures of offshore wind turbines that amount to about 30 % of the levelized cost of energy (LCOE) [8]. The O&M expenditures are elevated due to the harsh environmental conditions at sea and the poor reliability of electrical and mechanical drivetrain components that lead to frequent and premature failures [9]. The repair of such failures is labour intensive, requires specialized maintenance vessels and causes long downtimes. For this reason, there is growing interest in advanced O&M strategies using intelligent controllers or predictive maintenance methods that have the potential of improving the reliability of offshore wind turbines.

While there exists abundant interest in DT, most of the previous publications are of theoretical nature and applied research on this topic is sparse. Hence, there remain numerous research questions on the specifics of drivetrain DTs: Which methods of data acquisition, processing and fusion are needed? Which modelling approach is best suited for drivetrain DTs? How do these methods and models perform in realistic conditions and what is the associated uncertainty? This thesis addresses these research questions by applying the DT concept to the use case of offshore wind turbine drivetrains.

1.2   Aim and scope

This thesis is written as a summary of papers on the topic of DT for offshore wind turbine drivetrains, including two published conference papers, three

published journal articles and one journal article currently under peer review. The overall objective is to develop, evaluate and assess novel methods and models that can provide operators of offshore wind farms with a form of decision support and ultimately improve the reliability and availability of wind turbine drivetrains. Since DT is an extensive subject, it becomes necessary to narrow the scope in the following ways.

- **Drivetrain configuration:** Wind turbine drivetrains serve the purpose of converting mechanical to electrical energy and transmitting rotor loads into the bedplate and tower [10]. While many different drivetrain designs exist, the investigation is limited to geared drivetrains with a medium-speed or high-speed gearbox transmission and excludes direct drive systems. In general, the term drivetrain refers to the entire energy conversion system ranging from the main bearings to the electrical generator and inverter. In this thesis, the focus lies on the mechanical section of the drivetrain, i.e. the main shaft suspension and the gearbox, and excludes all electrical components.

- **Site location:** The tools and methods developed in this thesis are exemplified on offshore wind turbines, however, they are generic in nature and also apply to onshore wind turbines.

- **Data acquisition:** The data input is limited to sensor measurements that are already available in modern offshore wind turbines such as SCADA and CMS data to mitigate the costs of additional sensor installation.

- **Lifecycle phase:** DTs are envisioned to accompany the physical wind turbine during its entire lifecycle, however, only DTs for the operation and maintenance are investigated in this thesis.

- **Decision support capability:** The research focuses on decision support with descriptive, diagnostic and predictive capability such as load monitoring, fault diagnosis and remaining useful life prediction methods. Prescriptive methods that recommend maintenance actions are part of the long-term vision of DT and are not investigated in this thesis.

1.3 Thesis outline

This thesis is structured according to the internal composition of DT with the three main elements of DT Data, DT Models and DT Decision support
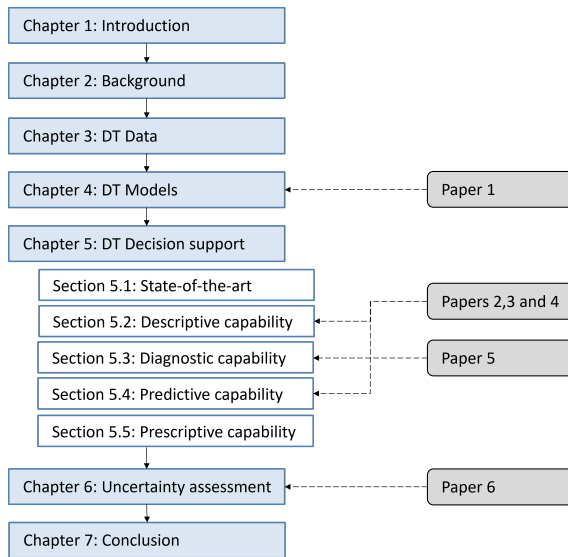
Figure 1.2: Thesis structure

(Fig. 1.2). Following the introductory and the background chapter, one chapter is assigned to each of the three DT elements. These chapters describe the state-of-the-art, as well as the original contributions reported in the appended papers 1 to 5. One additional chapter discusses the overall uncertainty of DT based on the findings of paper 6. A brief description of each chapter is provided as follows.

Chapter 1:
This introductory chapter presents the motivation, the aim and scope, and the thesis outline.

Chapter 2:
This chapter lays out the background of DT. The defining characteristics of DT are formulated, different DT frameworks are presented and potential applications and challenges in the offshore wind energy sector are discussed.

Chapter 3:
This chapter addresses the role of data in DT and presents the methodology of data acquisition, processing and fusion that is used in the appended papers.

Chapter 4:
This chapter covers the utilization of models in DT. The unique challenges and differences to conventional, standalone models are discussed. The modelling approach for the appended papers is described, which is based on physics-based multi-body simulation models and model updating algorithms such as state estimation and system identification methods. In addition, the use of reduced order models for efficient real-time simulation is discussed based on the findings of paper 1.

Chapter 5:
This chapter discusses decision support methods of various capability levels ranging from descriptive to prescriptive. Section 5.2 covers descriptive decision support such as load monitoring and is based on the virtual sensing methods presented in papers 2, 3 and 4. Section 5.3 describes diagnostic methods used for DT and refers to paper 5, which presents a rotor imbalance diagnosis method. Section 5.4. addresses predictive methods, specifically remaining useful life estimation methods for predictive maintenance strategies, and discusses the approach used in papers 2, 3 and 4.

Chapter 6:
This chapter discusses different sources of uncertainty in DT and their impact on the accuracy of remaining useful life estimates. The discussion is based on the results of paper 6.

Chapter 7:
Concluding remarks and an outlook with recommendations for future works are provided.

Chapter 2

Background

2.1 Defining characteristics

The origin of the term *Digital Twin* can be traced back to Michael Grieves, who in 2003 introduced DT in a lecture on product life cycle management and in 2014 published a white paper to formalize the DT concept [11]. Grieves' understanding of DT is "*a set of virtual information constructs that fully describes a potential or actual physical manufactured product from the micro atomic level to the macro geometrical level*" [12]. The DT concept model contains three main parts: the physical product, the virtual product and the connection of data and information between the two. In the following years research and business activities related to DT increased rapidly, as the DT concept was adopted in different fields starting with aerospace and manufacturing industries. With this influx of new ideas, many new, diverging and sometimes contradicting definitions have been put forward that only fed the ambiguity of the DT concept. Several review papers have been published that summarize the recent research with an attempt to define and formalize the DT concept [13, 14, 15, 16, 17]. In 2020 the first formal description by a certifying body was presented by Det Norske Veritas (DNV) in the recommended practice DNVGL-RP-A204 on the "Qualification and assurance of digital twins" [18]. DNVGL-RP-A204 provides a definition, which nicely captures the current understanding of DT and is used for this thesis.

"A digital twin is a virtual representation of a system or asset that calculates system states and makes system information available, through integrated models and data, with the purpose of providing decision support over its life cycle." [18]

This definition summarizes several defining characteristics of DT that may

benefit from further elaboration.

Virtual representation: DTs are first and foremost virtual representations that mirror the behaviour of a physical asset through calculation of system states. The system states range widely depending on the use case and may refer, for instance, to operational states or the health condition. The system states in the physical and virtual realm are synchronized at regular time intervals resulting in a real-time virtual replica of the physical asset.

Integration of models and data: DT is not a singular model, but rather an integrated framework of models, data and algorithms. The individual DT components are defined in DNVGL-RP-A204 as functional elements, *"a part or module of a digital twin with the purpose of supporting the user in making a key decision"*[18]. The fusion of models with real-time data streams collected by physical sensors is a central principle in DTs, since it facilitates updating and synchronizing the DT with its physical counterpart.

Providing decision support: DTs are developed with the clear purpose of providing value for stakeholders and to *"improve business outcomes"* [18]. DTs offer value-adding services by means of *decision support*; they collect, analyze and present information to assist stakeholders in making key decisions.

Life cycle perspective: DTs accompany the physical asset through every stage of its life cycle and continuously evolve to reflect physical changes to the asset. DTs are established during design and manufacturing as a DT prototype, refined during installation with additional asset information and updated during operation with operational and maintenance data [18].

2.2   Digital Twin frameworks

DT frameworks have been developed to further concretize the DT concept and to reduce the level of abstraction without loss of generality. DT frameworks define the DT architecture and characterize the functionality and the relationships between each of the DT components, the so called *functional elements* [18]. The earliest DT framework proposed by Grieves [11] comprised three elements: the physical asset, the virtual model and the connections that transfer data and information between the two. Grieves' framework was further specified in later works by Kritzinger et al. [19], who postulate the *bidirectionality and automation* of the connection. The virtual model receives information from the physical asset in the form of sensor measurements and returns information in the form of decision support (Fig.
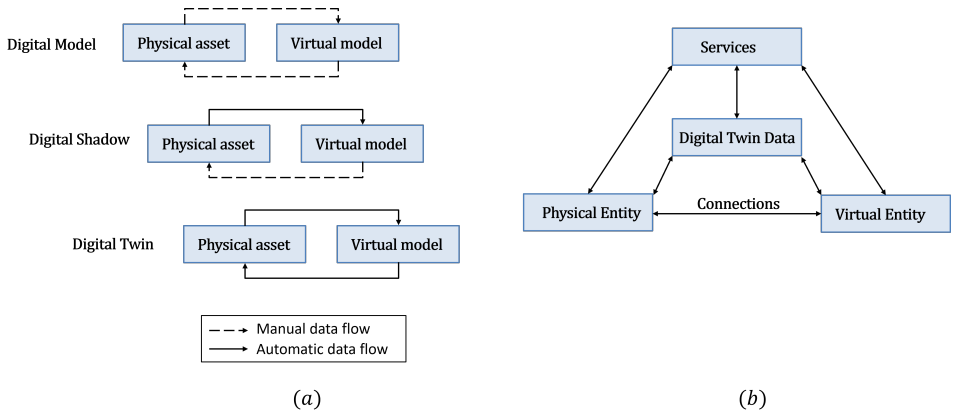
Figure 2.1: DT frameworks: (a) Grieves/Kritzinger et al.[11, 19], (b) Tao et al. [20]

2.1). The bidirectional information exchange must also be automated, which is the case when a change of state in the physical asset automatically leads to a change of state in the digital counterpart and vice versa. Kritzinger et al. introduced the alternative terms *Digital Model* and *Digital Shadow* to describe technologies that do not fulfill the requirements of bidirectionality and automation [19].

Tao et al. expanded this framework to incorporate the elements *Digital Twin Data* and *Services* and thereby recognize the DT characteristics of the data fusion and the provision of decision support [20]. The five-dimensional framework consists of the *Physical Entity*, *Virtual Entity*, *Digital Twin Data* and *Services* interconnected by *Connections* (Fig. 2.1). Each functional element contains a hierarchical substructure to further differentiate subcomponents, for instance, the virtual entity comprises geometric models, physics models, behaviour models and rule models. Tao's DT framework is widely popular and has been adopted for a variety of use cases in the wind energy sector including reliability analysis [21], condition monitoring [22] and prognostics [23].

DNVGL-RP-A204 presents a DT framework that shares Tao's classification into data, models and services, however, the information flow through the DT is considered sequential [18]. The information flows through the functional elements *Input*, *Analysis*, *Output* culminating in the decision support (Fig 2.2). The Input contains different data types collected on the physical asset such as data streams, master data, meta data and historical data. The data are fed into the Analysis comprising different models and algorithms and then further processed in the Output into usable and value-adding in-
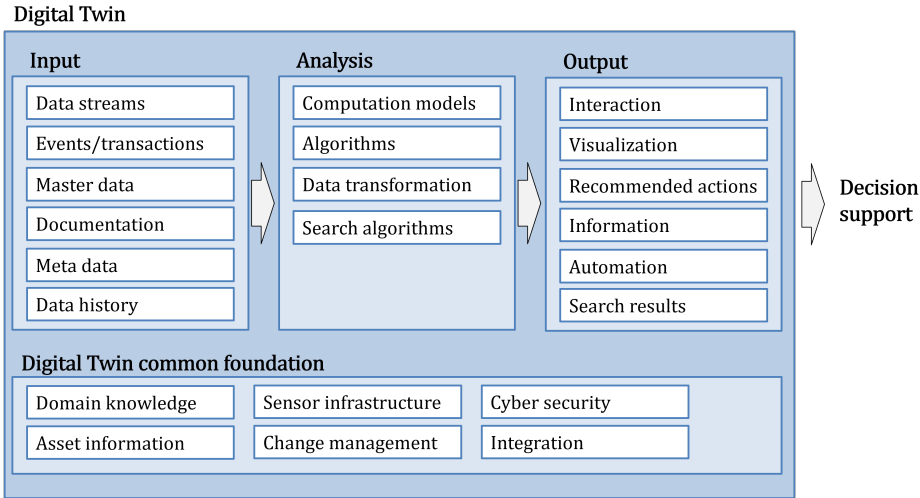
Figure 2.2: DT framework according to DNV [18].

formation.

Mehlan et al. present a DT framework loosely based on earlier works by Tao and DNVGL and tailored to the use case of load monitoring and remaining useful life estimation in wind turbine drivetrains (Fig. 2.3). The DT framework, first conceptualized in paper 2 [3] and further developed in papers 4 and 6 [4, 6], comprises the three functional elements *DT Data*, *DT Model* and *DT Decision support*. The DT Data refers to data streams, historical data, asset information and domain knowledge. The data streams are real-time measurements by SCADA and CMS sensors and are utilized for continuous model updating and synchronization. The historical data refers to the load history of drivetrain components and is used in calculating the accumulated fatigue damage. The asset information includes the gearbox topology and specifications, which are needed along with domain knowledge for model construction.

The second functional element, the DT Model, comprises a drivetrain model along with model updating algorithms. The drivetrain model is a reduced-order model with two torsional degrees of freedom and serves the purposes of simulating the load dynamics in local gear and bearing contacts. The model updating algorithms include a state estimator and a system identification method and are implemented to ensure the convergence of the drivetrain model with its physical counterpart. A Kalman filter is employed to estimate the dynamic states and the unknown rotor torque based on real-time data streams, while a least squares system identification method is used to
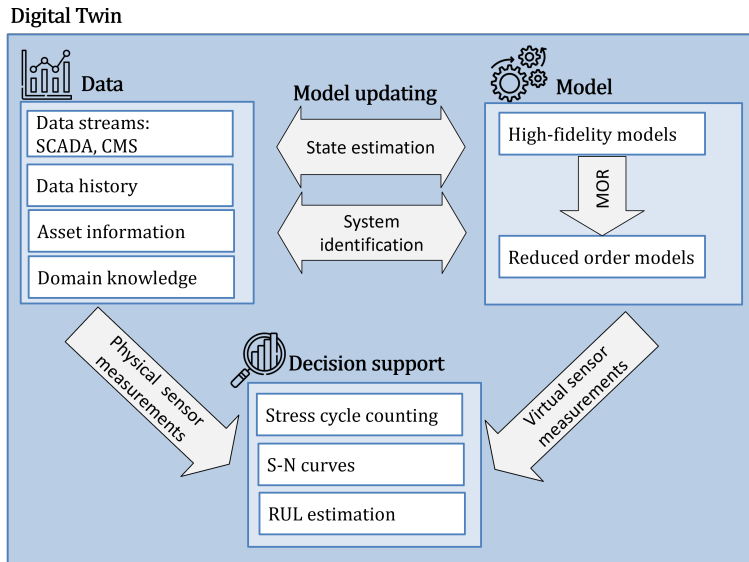
Figure 2.3: DT framework to enable load monitoring and remaining useful life assessment in wind turbine drivetrains according to Mehlan et al. [6].

estimate unknown and time-variant model parameters such as inertia, stiffness and damping values.

The third functional element, the DT Decision support, serves as the human-machine interface and converts measurements and model predictions into interpretable information, specifically the remaining useful life of drivetrain components that can serve for predictive maintenance strategies. The DT Decision support contains a fatigue damage model based on Miner's rule of damage accumulation, material models specified by S-N curves and stress cycle counting algorithms.

2.3 Potential applications in offshore wind

Numerous benefits have been ascribed to DT by researchers and industry, including higher efficiency, reliability, availability and safety of the asset, however, one should be careful to distinguish between validated, tangible benefits and unsubstantiated claims arisen from the hype around DT. In light of the extensive development costs of DT, investors are interested in assessing the economic benefits that yield a return on investment. Unfortunately, relatively little work has been conducted to verify and validate the benefits of potential DT applications, as the technology remains in early

development stages. The following potential applications for the operation and maintenance of offshore wind turbine drivetrains are commonly suggested in the literature [13, 14, 15, 24, 25]:

Optimized control: DT could assist in the development of advanced control algorithms that optimize the energy yield while minimizing operational loads. Model predictive controllers, in particular, could benefit from more accurate DT models to forecast fatigue loads.

Analysis and visualization of data: DT could serve as the human-machine interface that collects, analyzes and visualizes data from the physical wind turbine in a manner that is interpretable for technicians and can assist in decision making.

Virtual inspection: DT could facilitate fully remote inspections using the virtual replica of the wind turbine and thus saving on labour and logistical costs.

Improved fault detection and diagnosis: DT could improve the detection and diagnosis of drivetrain faults through virtual inspection, advanced physical modelling or novel data analysis techniques.

Risk and scenario assessment: DT could be used to simulate a variety of scenarios for risk assessment, for instance, to predict the consequences of future adverse operational conditions.

Predictive maintenance: DTs could advance fault progression forecasts and remaining useful life estimations through advanced condition monitoring techniques and predictive models. The remaining useful life predictions are essential for predictive maintenance strategies, which increase the reliability and availability while utilizing maintenance resources more efficiently.

2.4   Development challenges

While the prospects of DT in the offshore wind energy sector are promising, there remain multiple challenges that must be overcome to realize the adoption of DT. The challenges of DT are discussed in several review papers in the context of condition monitoring [14, 24], risk assessment [25] and from a modelling perspective [13, 26]. A non-exhaustive summary of the challenges specific to the operation and maintenance of offshore wind turbine drivetrains is presented here. Additional challenges related to the data, models and decision support are discussed in their respective chapters.

Connectivity and processing power: Cloud-based solutions are envisioned for many DT applications, however, the low bandwidth of the data connection from remote offshore wind farms to onshore server centers rep-

resents a limiting factor. In particular DT applications that rely on large amounts of data such as data-driven machine learning models would face challenges. Edge computing solutions, on the other hand, are limited by the available processing power onboard of the offshore wind turbine, which is likely insufficient to run high-fidelity simulations in real-time [14, 24, 26].

Intellectual property ownership of models: The ideal that the DT accompanies the physical wind turbine throughout its life cycle stages is difficult to do justice to, when the wind turbine changes ownership from OEMs to wind farm operators. CAD drawings, simulation models and design specifications, which could build the basis for a DT in the operational phase, are proprietary to the OEMs and likely contain confidential information. For wind farm operators this represents a major obstacle in developing DT models and it may become necessary to reverse engineer unknown system properties [27].

Data quality: The performance of DTs hinges on the availability of high-quality data. However, the available sensor data of SCADA and CM systems that are commonly leveraged for DTs have several limiting factors. The low temporal resolution of 10 min is insufficient to observe the dynamics in wind turbine drivetrains [28]. Sensor malfunctions are a common occurrence and lead to data gaps, bias or sensor drift in the measurements. Additionally, data on faulty conditions are very sparse, which makes it challenging to train data-driven models for fault diagnosis [14].

Cyber security: Concerns on the cyber security of offshore wind turbines are raised, as their operation becomes increasingly digitalized and automated, and thus more vulnerable to malicious attacks. Wind turbines are a critical part of the energy infrastructure and their failure can lead to severe consequences, not only economical but also societal in case of a grid loss. The cyber security must therefore be an integral part in the development process of DTs [13, 24].

Chapter 3

Digital Twin Data

3.1 Data categories

Data is one of the fundamental pillars of DT according to the frameworks by Mehlan et al. [3], Tao et al. [20] and DNV [18]. With the rise of inexpensive sensor technologies and IoT-platforms more and more data are collected in modern offshore wind turbines. The large volume of data that is available today offers immense potential for developing DTs, while at the same time introducing challenges related to data analysis, transfer and storage. Intelligent data analysis tools are necessary to convert raw data into serviceable data that can aid in decision making. In addition to the data collected in the physical space through sensor measurements, DT data also includes data acquired in the virtual space by the DT models and algorithms. This distinction is reflected in Tao's classification into the five categories of physical entity data, virtual entity data, service data, domain data and fusion data (Fig. 3.1 [20]). Physical entity data represent data collected at the physical wind turbine such as sensor measurements, maintenance reports or error alerts. Virtual entity data is produced by the virtual model and may refer to simulation results, model parameters or boundary conditions. Service data are the output of the decision support services such as fault diagnosis and prognosis or recommended maintenance actions. Domain data are auxiliary data for the execution of the virtual model and the decision support algorithms such as expert knowledge, industry standards, guidelines and asset information. Lastly, fusion data refers to the integration of data from the physical and the virtual space with the objective of gaining new knowledge or information that can assist in decision making.
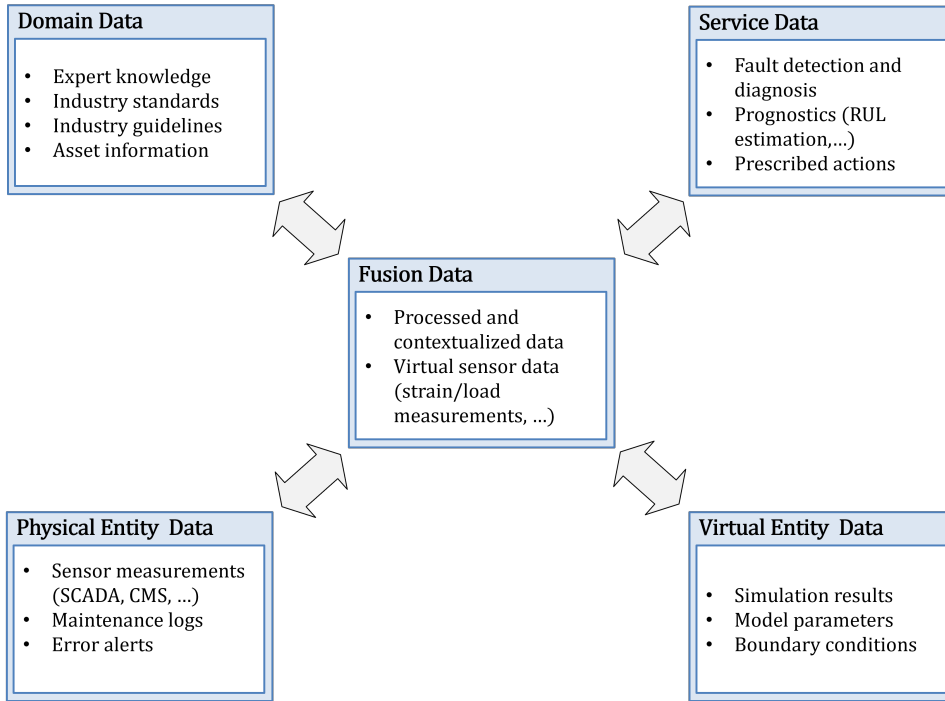
Figure 3.1: Categories of DT data according to Tao et al. [20].

3.2   Data acquisition

The most commonly investigated and cost-effective approach to the acquisition of *physical entity data* is utilizing the existing sensor infrastructure of SCADA and CM systems. SCADA and CM systems include a wide range of sensors for monitoring and control purposes, as standardized by IEC 64100-25-2 [29] and ISO 10816-21 [30]. The most common SCADA and CMS signals are enlisted in Tab. 3.1, where it should be noted that the composition of sensors may vary from turbine to turbine, since not all systems are designed strictly to code. The environmental conditions are monitored in SCADA systems using nacelle mounted anemometers and wind vanes. The operational conditions are controlled with electrical sensors to measure the active and reactive power, shaft encoders to measure the rotor and generator speed, and encoders to measure the yaw and pitch angles. Furthermore, a variety of temperature sensors are installed at different locations such as the main bearings, the gearbox bearings, the generator bearings, the oil in- and outlet, and the nacelle, which may be utilized for health monitoring. Drivetrain CM systems rely primarily on vibration measurements for condition

monitoring and thus include a range of accelerometers mounted on drivetrain. ISO 10816-21 [30] recommends the placement of piezo-resistive or capacitive accelerometers on the housing of the main bearings, the gearbox and the generator, in both radial and axial direction and with a bandwidth of 10 Hz to 5 kHz. Additional accelerometers for structural health monitoring are mounted on the nacelle housing in side-side and fore-aft direction. Some drivetrain CMS also comprise oil particle sensors that measure the quantity, type, shape or size of particles for monitoring the lubricant quality.

The second important source of DT data is *virtual entity data* simulated by the DT model. Under the prerequisite that the DT model reflects the physical wind turbine's behaviour to a satisfactory accuracy, simulated data may complement or in part replace physical measurements. High-fidelity dynamic drivetrain models, as described in Sec. 4.2.2, are used in many academic studies to synthesize SCADA and CMS data, where the access to field measurements is restricted. Simulated data has proven to be crucial for the development and assessment of novel DT technologies, however, the modelling errors should be kept in mind. In particular, CMS vibrations are subject to simulation errors due to simplified modelling approaches to the flexible gearbox housing.

3.3 Data pre-processing

Raw SCADA and CMS sensor data exhibit quality issues such as data gaps, anomalies and scatter, which are addressed with data pre-processing methods. The first step, referred to as data cleaning, involves the treatment of missing data and the detection and removal of anomalies. Data anomalies can be attributed to either sensor malfunctions or abnormal operational conditions such as idling or transient events (shut-down or start-up). In many use cases such as in developing data-driven normal behaviour models, such anomalies are detrimental to the model accuracy and must be filtered out. The filtering of explicit and obvious anomalies may be conducted through discrete thresholds in several operational variables such as wind speeds below cut-in or above cut-out, blade pitch angles of 80° to 90°, low rotor speeds or near zero active power, as practiced by Mehlan et al. [4] and others [28]. Since this simplistic filter does not catch all anomalies, it may be followed up by anomaly detection (AD) algorithms based on machine learning. Morrison et al. [31] investigate different AD algorithms for data cleaning of wind turbine power curves including Gaussian Mixture Modelling (GMM), Isolation Forest (iForest), Local Outlier Factor (LOF)

Table 3.1: Typical sensor signals in SCADA and CM systems.

Sensor system	Signal	Sensor type	Sensor location
SCADA	Wind speed	Anemometer	Nacelle top
	Wind direction	Wind vane	Nacelle top
	Active power	Voltage/current	Generator
	Reactive power	Voltage/current	Generator
	Rotor speed	Encoder	Main shaft
	Generator speed	Encoder	High-speed shaft
	Pitch angle	Encoder	Blade 1, 2, 3
	Yaw position	Encoder	Yaw actuator
	Temperature	Thermometer	Nacelle (ambient)
	”	”	Main bearings
	”	”	Gearbox bearings
	”	”	Generator bearing
	”	”	Generator winding
	”	”	Oil in-/outlet
CMS	Drivetrain vibration	Accelerometer	Main bearings
	”	”	Torque arms
	”	”	Gearbox housing front/back
	”	”	Generator front/back
	Tower top acceleration	Accelerometer	Nacelle side-side/fore-aft
	Oil particle count	Digital imaging	Oil filter

and k-nearest neighbours (kNN), which only represent a small subset of available AD algorithms. Alternative AD approaches use normal behaviour modelling [28] or image-based detection.

The large volume of SCADA and CMS data also necessitates a data compression step with the objective of reducing the data dimensionality while retaining most of the information content. Principal component analysis (PCA) is a powerful data compression tool that finds widespread application in the analysis of SCADA and CMS data. PCA is a linear transformation of measurement vectors into the orthonormal space spanned by principal components that are the eigenvectors of the data's covariance matrix. Only the first few principal components are retained that correspond to the majority of the data's covariance. Further data compression that is typical in CMS is the feature extraction that reduces the raw time series of a sensor measurement to a scalar value. Typical features are statistical characteristics such as the mean, standard deviation or root-mean-square or time-frequency based characteristics calculated by Fourier transform, wavelet transform or Cepstrum analysis [32].

3.4   Data fusion

Data fusion, the combination of data from different sources with the objective of gaining new knowledge or information, is one of the key principles of DT and offers an important avenue of providing value to stakeholders. In DTs, data fusion may take place in both the physical and the virtual domain and in through a variety of fusion methods.

Physical domain data fusion: Data fusion in the physical domain refers to the combination of different sensor signals, predominantly for the purpose of noise reduction and higher robustness against sensor failure. In drivetrain CMS a certain level of redundancy is given by the multitude of vibration sensors across the gearbox housing, which favours the fusion of different sensor signals. A commonly investigated approach is the superposition of sensor signals at the feature level using PCA [33, 34], neural networks [35] or similar machine learning methods. In this procedure the background noise is reduced by averaging over multiple signals, which expedites the detection of weak fault signals, while the robustness is increased through filtering of faulty sensors.

Other use cases of sensor data fusion are found in the combination of SCADA and CMS data for improved fault diagnosis [5]. While fault diagnosis exclusively based on CMS vibration analysis or solely based on SCADA data is extensively researched, comparatively little work has been published on the intelligent fusion of SCADA and CMS data. One scenario, where the fusion of SCADA and CMS can be beneficial, is the diagnosis of rotor imbalance faults such as pitch misalignment, yaw misalignment and mass imbalance. Numerical studies by Mehlan et al. [5] suggest that SCADA data alone is insufficient to reliably classify these faults and that CMS vibration data is crucial for identifying pitch misalignment faults. The results of this study are discussed further in Sec. 5.3

Virtual domain data fusion: Similar to physical sensor signals, data from different virtual models can be combined for greater accuracy and robustness. Ensemble modelling is an approach in machine learning theory, where multiple instances of the same model class are combined to make more accurate predictions. Examples of ensemble models are random forests that are constructed by combining decision trees with bootstrap aggregation and boosting methods.

Physical/virtual domain data fusion: Arguably the greatest innovation and benefit of DT arises from the fusion of data from the physical and the virtual domain. The integration of real-time, physical sensor measurements facilitates the construction of "live", virtual models that are continuously

updated to reflect the behaviour of its physical counterpart at all times. The continuous model updating is realized with various state estimation and system identification methods, as presented in Sec. 4.3. Such virtual models provide the operator with a much more detailed and informative description of the asset's current state, as they can calculate and visualize additional states such as local loads or stresses that are not measured physically. The so called "virtual measurements" of local drivetrain loads have a great potential for condition monitoring and fault prognosis, as discussed in Sec. 5.2 and Sec. 5.4.

Chapter 4

Digital Twin Models

4.1 Modelling challenges and objectives

Conventional models of wind turbine drivetrains were developed for early life cycle stages such as design, manufacturing or research and development (R&D), whereas DT models are intended to be used for the operation and maintenance and face unique challenges. Current guidelines and best practices on drivetrain modelling, presented by Guo et al. [36], are thus not applicable to DT models. DT applications that require real-time simulation such as load monitoring place higher demands on the computational efficiency of DT models. At the same time, the available processing power in remote offshore wind turbines, as well as the bandwidth of data connections to onshore facilities is limited. This causes constrains on the model complexity and favours leaner solutions. The second difference to conventional models lies in the longevity and adaptability of DT models. The DT model must accompany its physical counterpart over its entire lifespan and reflect all physical changes such as faults or part replacements, which requires continuous model maintenance and the ability to update model properties.

Moyne et al. [37] summarize the requirements of DT with the terms reusability, interoperability, interchangeability, maintainability, extensibility, and autonomy across the entire DT life cycle in a requirements-driven framework. The requirements specific to wind turbine drivetrain DTs are elaborated further by Mehlan et al. [1]

Fidelity: The DT model must possess an appropriate modelling depth to capture the wind turbine's behaviour. The DT model fidelity is neither restricted to ultra-realistic levels, as stated in several review papers [38], nor to the low levels of reduced order models; it is instead necessary to tailor the fidelity to the application. For tasks in the design phase, a CAD model

may suffice as DT model, while for use cases in load monitoring, the physics of aerodynamics and elastomechanics may need to be considered.

Computational efficiency: The DT model must be computationally efficient to allow real-time simulation.

Re-usability: The DT model must be re-usable and portable. This is of importance when transferring a developed DT model between individual turbines of a wind farm and necessitates a high model generalizability, i.e. the model is universally applicable.

Interoperability: The communication of the DT model with other DT functional elements or non-DT entities must be facilitated. DT models, data and data analysis tools must be integrated in a DT architecture with well defined interfaces and connections to enable intercommunication.

Maintainability: The DT model must be able to be tuned, rebuilt and replaced. The physical wind turbine undergoes short-term and long-term changes over its life cycle due to faults, material degradation, part replacement or repairs, which must also be reflected in the DT model. Model updating functionalities must be implemented to continuously adapt the model properties and to ensure the convergence of the physical asset and the virtual model.

4.2 Modelling techniques

4.2.1 Physics-based, data-driven and hybrid approaches

The first consideration in model development is whether to employ a physics-based, a data-driven, or a hybrid approach. Physics-based models are developed by understanding the phenomenon of interest and then formulating the governing, physical equations. The physics-based approach is prevalent in classical engineering fields, but with recent advances in AI and the increased availability of data enabled by IoT technologies, data-driven methods find application in more areas. Data-driven models are developed by acquiring large amounts of data and deriving relationships between input and output variables to predict future outcomes. It is often further distinguished between statistical and machine learning models. The general advantages and disadvantages of physics-based and data-driven models for DT applications is discussed by Rasheed et al. [13] and Mehlan et al. [1] and briefly summarized in Tab. 4.1.

The primary advantage of physics-based models lies in the solid foundation of the governing physical equations, which allows for comprehension and

interpretation of the solution by skilled technicians. The high transparency and traceability has a positive impact on the confidence of stakeholders into physics-based models, whereas data-driven models are developed as black-box models, which has the adverse effect. The governing physical equations are also universally applicable and not specific to the domain or the asset, which allows for cross-domain knowledge transfer and re-use of developed models. In fact, the earliest models of geared wind turbine drivetrains were developed with expertise from the automotive industry. Data-driven models on the other hand suffer from low generalizibility and only perform well within the boundaries of the training data set and struggle with prediction tasks in unfamiliar situations. A further advantage of physics-based models are the low costs of model development aided by software with physics engines such as FE, MBS or CFD programs. The model development, or "training" of data-driven models on the other hand requires the acquisition of large amounts of training data, which can become prohibitively expensive. In particular data of faulty conditions is challenging to acquire due to its rare occurrence in natural environments. The development costs of physics-based models is instead shifted to the verification and validation tasks. These tasks are typically conducted experimentally with full-scale test benches and become increasingly more expensive with growing turbine sizes. The validation of data-driven models is performed with cross-validation on the training data-set and does not require any additional resources. Data-driven models also exceed in terms of computational efficiency for predictive tasks. While the training and validation of machine learning models can be quite demanding on processing power, the simulation of the trained model requires minimal numerical operations and is in most use cases capable of real-time simulation. Physics-based models, specifically those with low temporal and spacial resolution such as FE and CFD models, are too resource intensive to be used for DT applications with real-time simulation. Furthermore, the numerical stability of physics-based model is not guaranteed and must be checked for the desired initial conditions, boundary conditions and parametrization.

It is clear that both physics-based and data-driven modelling approaches have their strengths and limitations and that neither can be deemed as the optimal solution for DT models. A promising strategy to achieve the best of both worlds are hybrid approaches that combine physics-based and data-driven modelling techniques. Different modelling approaches may be employed for different system components or for different physical domains. The guiding principle here is to develop models for the physics that are well understood such as classical mechanics, aerodynamics or electromagnetism

Table 4.1: Advantages and disadvantages of physics-based and data-driven modelling approaches for DT [13].

	Physics-based	Data-driven
Transparency, traceability	+	-
Generalizibility	+	-
Development and training costs	+	-
Verification and validation costs	-	+
Computational speed	-	+
Numerical stability	-	+

and to resort to data-driven methods for the physics that are poorly understood such as failure mechanisms. The hybrid approach is, for instance, employed by Guo et al. [39] for the prognosis of white etching cracks in high-speed bearings.

4.2.2   Multi-body simulation models

The best practice for dynamic drivetrain modelling is a physics-based approach, namely multi-body simulation (MBS). MBS models employ a lumped parameter approach, where the system is divided into multiple point masses, referred to as bodies, interconnected by elastic spring-damper connections or rigid joints (Fig. 4.1). This approach is well suited to model the drivetrain dynamics governed by complex multi-body interactions of shafts, gears and bearings. MBS models were pioneered by Schlecht [40] in the early 2000s and further developed with contributions from Peeters [41], Helsen [42], Guo [43] and others. Extensive model fidelity studies were conducted with the objective of determining the optimal modelling depth of drivetrain components and have culminated in the fidelity guidelines presented in [36]. A brief overview of recommended modelling practices is given here.

The system boundaries are typically set around the mechanical drivetrain with interfaces at the rotor hub, the generator shaft and the yaw bearing. The aerodynamic rotor loads and the tower top motions are calculated with external, aeroelastic models and imposed as boundary condition in the drivetrain model. This approach is referred to as the decoupled simulation approach, as it decouples the "global", structural dynamics of the tower and the blades from the internal drivetrain dynamics [44]. The decoupling is motivated by the fact that aerodynamic excitations and the dominant structural modes occur at low frequencies (< 10 Hz), while internal drivetrain dynamics are governed by high-frequency gear and bearing excitations of up to 500 Hz at the HSS. Drivetrain MBS models typically comprise a number of submodels for the shafts, planet carriers, gears, bearings, gearbox
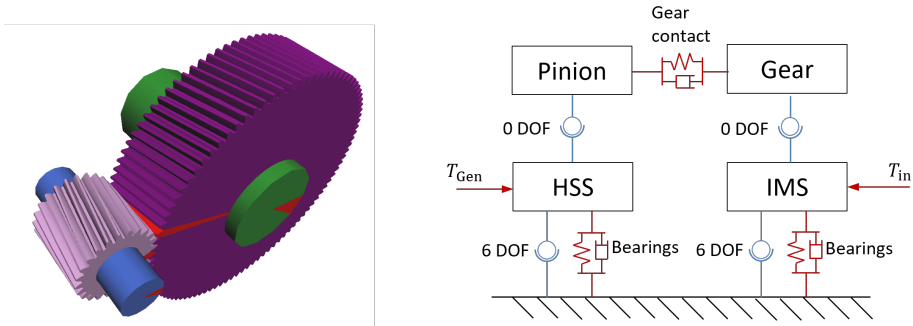
Figure 4.1: MBS modelling principle on the example of a helical gear stage [1]

housing, bedplate and gearbox support.

Shafts: The main shaft is modelled as a flexible body based on Euler-Bernoulli or Timoshenko beam theory or as a condensed FE model derived by modal order reduction. The remaining shafts of the downwind gear stages are generally modelled as rigid bodies with six DOF.

Bedplate, gearbox housing, planet carrier: The bedplate, gearbox housing and the planet carriers are modelled as flexible bodies using condensed FE models.

Gearbox support: The gearbox support including the torque arm and generator bushings are modelled as linear spring-damper connections with six DOFs and diagonal stiffness and damping matrices.

Bearings: The main bearings and the gearbox bearings are modelled as linear spring-damper connections that allow one rotational DOF. Any internal bearing dynamics such as cage or roller slip, characteristic excitations at the ball pass frequency, or the load distribution are not considered at this fidelity level.

Gears: The gears are modelled as rigid bodies by lumping the flexibility into a gear contact function, which describes the gear body, tooth bending and Hertzian contact stiffness. The gear contact stiffness is spatially discretized over the gear flanks, which allows for representing inhomogeneous load distributions and non-torque loads. The gear contact stiffness is furthermore time-invariant, as it varies cyclically for each meshing period depending on the amount and location of tooth contacts in order to represent characteristic gear meshing excitations.
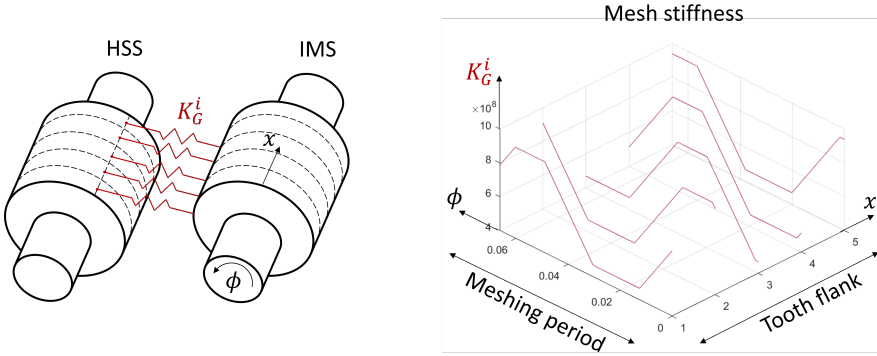
Figure 4.2: ROM of a wind turbine high-speed gear stage with simplified, explicit gear contact force model for DT real-time simulation[1]

4.2.3   Reduced order modelling

Current high-fidelity MBS models are ill-suited for certain DT applications such as load and fatigue damage monitoring due to limitations in the computational costs and the observability of dynamic states. While MBS models are significantly faster than other modelling approaches such as FE or CFD, the simulation of wind turbine drivetrains remains demanding, since higher order drivetrain modes and high-frequency gear meshing excitations drive the necessary numerical step size to 200 Hz and above. The computational speed of current MBS models with conventional desktop computers remains below real-time speed by a factor of up to 10 depending on the load case [1]. Further restrictions on the model complexity are imposed by the observability requirement of the state estimation methods that are used to synchronize the dynamic states of the DT model with the physical wind turbine. The SCADA measurements of the main and generator shaft speeds allow the observation of torsional drivetrain modes, whereas the observability of bending and lateral drivetrain modes is not guaranteed. CMS accelerometers mounted on the gearbox housing may detect non-torsional dynamics, however the sensitivity is relatively low due to measurement noise and the observation function is complex due to the transfer path of the vibration through the housing. Reduced order models (ROMs) are for this reason preferable as DT models.

The simulation of gear meshing dynamics is particularly demanding due to high-frequency discrete state changes in the teeth contacts. The classical approach in MBS software uses an implicit formulation of gear contact

forces. Iterative algorithms are used to determine the contact points and teeth deflections based on the shaft positions and gear geometry, and assign a gear contact force orthonormal to the contact surface. Recent advances in more efficient reduced order modelling of gear meshing dynamics are presented by Mehlan et al. [1]. A simplified, explicit gear contact formulation is proposed that is numerically stable with explicit numerical solvers such as Runge-Kutta variants and increases the computational speed by about 27%. The mesh stiffness is modelled as a piece-wise linear function depending on the shaft angle and the axial position, and the direction of the gear forces are fixed along the line of action (Fig. 4.2). The ROM shows a good agreement with state-of-the-art MBS models with respect to temporal load variations due to gear meshing and with respect to the spatial load distribution over the gear flank (Fig. 4.3). Despite the improvements in computational efficiency, the ROM falls short of real-time capability by a factor of three [1]. The simulation of gear meshing dynamics remains resource intensive due to the small step sizes, which renders it impractical to consider gear meshing in DT.

Further model reduction techniques are commonly employed for the development of DT models such as lumped parameter methods or data-driven surrogate models. Lumped parameter reduction methods refer to decreasing the model complexity by further condensing different model elements into a single element. A common assumption is to replace the elements of a planetary gear stage, the planet carrier, the planets, the ring and the sun with an equivalent inertia, stiffness and damping element. This often coincides with other measures such as limiting the of the body DOFs to only torsional motion and linearizing the gear contact stiffness. The lowest model fidelity is reached with two DOF torsional drivetrain models comprising an equivalent rotor inertia and generator inertia connected by a torsional spring-damper. This fidelity level is best practice in aeroelastic simulation and is used as drivetrain DT for load monitoring by Branlard et al. [45] and Mehlan et al. [6], however, this fidelity level only allows the representation of torsional drivetrain modes and does not consider any complex internal drivetrain dynamics such as gear meshing.

Data-driven surrogate models are regression models that are trained on simulated data to mimic the behaviour of the full-order model (FOM). A large number of load cases is simulated first with the FOM to create a data set of input forces and output variables such as velocities, strains or other variables of interest. Machine learning regression models are then trained to map the input variables onto the output variables. Artificial neural networks are commonly employed for this purpose as they are effective in mapping
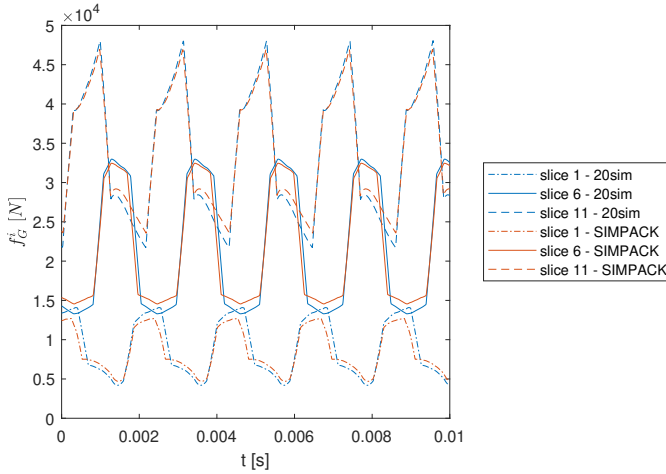
Figure 4.3: Gear contact forces of a 5 MW helical high-speed gear stage calculated with a full-order MBS model (SIMPACK) and a ROM (20sim)[1]

complex, non-linear relationships. The potential of data-driven surrogate for modelling main shaft and main bearing dynamics is demonstrated by Azzam et al. [46], Loriemi et al. [47] and Mehlan et al. [4].

4.3 Model updating techniques

The DT paradigm states that the DT is a virtual copy of the physical asset and mirrors its behaviour at all times. Thus, the states and the model properties of the DT must be updated at regular time intervals to ensure the convergence of DT and physical asset. This is facilitated through state estimation and system identification methods, presented by Mehlan et al. [4] and elaborated in the following sections on the example of a two DOF torsional drivetrain ROM. This fidelity level is commonly used for DT models, since the available SCADA shaft encoder measurements allow the observation of torsional drivetrain dynamics.

4.3.1 State estimation

Consider a drivetrain model expressed by the following linear, stochastic, time-variant system with the state variable $\mathbf{x(t)}$, the input variable $\mathbf{u(t)}$, the output variable $\mathbf{y(t)}$, the process noise $\mathbf{v(t)}$, the measurement noise $\mathbf{w(t)}$
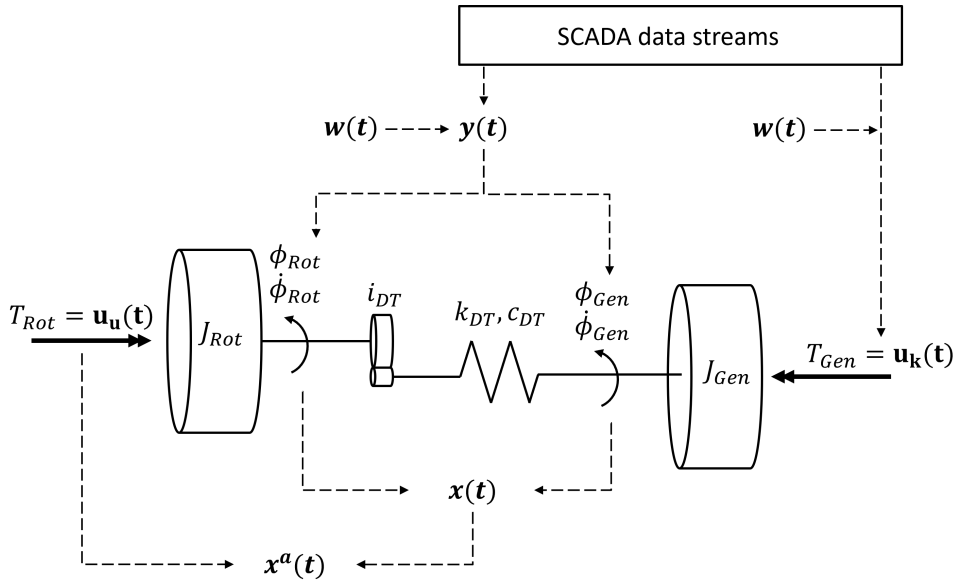
Figure 4.4: The joint input and state estimation problem in drivetrain DTs with a two DOF torsional model and SCADA data input.

and the system matrices $\mathbf{A(t)}, \mathbf{B(t)}, \mathbf{C(t)}$,

$$
\begin{aligned}
\dot{\mathbf{x}} &= \mathbf{A(t)}\mathbf{x(t)} + \mathbf{B(t)}\mathbf{u(t)} + \mathbf{v(t)}, \\
\mathbf{y} &= \mathbf{C(t)}\mathbf{x(t)} + \mathbf{w(t)}.
\end{aligned}
\tag{4.1}
$$

Classical, disconnected models for design or R&D are used for *forward simulation*, where the input variables are known and numerical time integration solvers are used to calculate the unknown states and output variables. A common objective is to simulate the dynamic system response to a set of defined environmental conditions or design load cases (DLCs [48]). In DT models, on the other hand, the objective is the convergence with the physical asset. Here the output variables are known, while the state and input variables are the unknowns, which is considered an *inverse problem* or more specifically a joint input and state estimation problem.

For the use case of a two DOF torsional drivetrain model, the state variables $\mathbf{x(t)}$ comprise angular displacements and velocities of the main and generator shaft and are considered unknown (Fig. 4.4). The input variables are external forces at the system boundaries and are split into known and unknown variables. The generator torque at the high-speed shaft is measured by SCADA systems and considered a known variable $\mathbf{u_k(t)}$, while the rotor torque at the main shaft is considered an unknown input variable $\mathbf{u_u(t)}$.

The output variables $\mathbf{y}$ are measurements of the main and generator shaft speeds obtained from encoders of the SCADA system. The system matrices $\mathbf{A}(\mathbf{t}), \mathbf{B}(\mathbf{t}), \mathbf{C}(\mathbf{t})$ contain the drivetrain inertia J_{Rot}, J_{Gen}, stiffness k_{DT} and damping c_{DT} parameters, and are time-variant due to long-term physical changes to the drivetrain such as material fatigue.

Kalman filters are typically employed to solve joint input and state estimation problems. The linear Kalman filter is a two step algorithms that yields state estimates on the basis of uncertain model predictions and noisy measurements. It is applicable for stochastic, linear, time-invariant systems with white Gaussian process and measurement noise. While the system matrices of drivetrain DT models are considered time-variant, they can be assumed constant for short time sections, since their rate of change is significantly smaller than the gradients of the state variables. Furthermore, numerical studies show that the modelling errors of ROMs that predominantly contribute to the process noise can be described well by Gaussian distributions. For this use case in drivetrain DT, a Kalman filter variation, the augmented Kalman filter (AKF) is employed, where the state vector is augmented with unknown input variables to facilitate simultaneous state and input estimation. The augmented state vector then becomes $\mathbf{x^a} = [\mathbf{x} \ \mathbf{u_u}]^{\mathbf{T}}$. The AKF was first investigated for drivetrain DT by Perisic et al. [49] and later adopted by Branlard et al. [45] and Mehlan et al. [6].

Various non-linear variations are found in literature such as the extended Kalman filter (EKF) or the unscented Kalman filter (UKF) that accept non-linear time-invariant systems and thus reduce model linearization errors. Non-linearities in drivetrain models occur for example in the gear contact model, as presented in [1]. Non-linear Kalman filters would be necessary to mirror gear meshing and similar non-linear dynamics in the DT, however, approach has not yet been investigated. Linearized models are typically used for drivetrain DTs.

4.3.2 System identification

A further complication lies in obtaining the system matrices $\mathbf{A}(\mathbf{t}), \mathbf{B}(\mathbf{t}), \mathbf{C}(\mathbf{t})$. The initial system properties at the time of the wind turbine commissioning may not be available to wind farm operators due to the confidentiality of drivetrain designs. In addition, many model parameters are time-variant across the wind turbine's lifespan due to physical changes in the system properties. The rotor inertia may increase due to accretion of ice, dirt or moisture, as well as decrease as a result of abrasive fault mechanisms such as leading edge erosion [5]. Stiffness and damping parameters of drivetrain components may be affected by material fatigue or local faults such as tooth

root cracks or spalling [50]. Thus, it is necessary to continuously estimate the system properties and update the model parameters accordingly.

Operational modal analysis (OMA) techniques are proposed by various authors for this objective. OMA refers to the estimation of a system's modal properties through analysis of data collected under normal operational conditions. Contrary to experimental modal analysis (EMA), the system is not subjected to artificial excitations as in "hammer tests", but rather only subjected to natural excitations such as stochastic wind loads. Due to limitations in the available SCADA and CMS signals, the presented OMA techniques are restricted to the parameter estimation of two DOF torsional drivetrain models. This problem falls into the category of grey box model identification, since the overall model structure is fixed and auxiliary parameters such as the gearbox ratio i_{DT} are known. The unknown parameters include the rotor inertia J_{Rot}, generator inertia J_{Gen}, drivetrain torsional stiffness and damping value k_{DT}, c_{DT} and the known measurement signals are the main shaft speed $\dot{\phi}_{Rot}$, generator shaft speed $\dot{\phi}_{Gen}$ and the generator torque T_{Gen}. Through integration of the shaft speeds it is furthermore possible to obtain the angular positions ϕ_{Rot}, ϕ_{Gen}, where the sensor drift due to the integration of measurement noise must be mitigated through regularization methods. With this information the generator side equations of motion are fully determined and the model parameters $\theta = [J_{Gen}, c_{DT}, k_{DT}, \alpha_0]$ with exception of the rotor inertia may be estimated with parameter optimization methods.

$$
\hat{\theta} = \arg\min_{\theta} ||J_{Gen}\ddot{\phi}_{Gen} - c_{DT}/i_{DT}(\dot{\phi}_{Rot} - \dot{\phi}_{Gen}/i_{DT})
$$
$$
- k_{DT}/i_{DT}((\phi_{Rot} - \phi_{Gen}/i_{DT}) - \alpha_0) + T_{Gen}||_2^2
$$
(4.2)

Unfortunately, the same approach cannot be employed to obtain the remaining parameter, the rotor inertia J_{Rot}, since the rotor torque is typically not measured by SCADA systems, which leaves the rotor side equations of motion undetermined. Instead, frequency domain OMA techniques may be applied that leverage the relationship of the rotor inertia and the first torsional natural frequency. The first torsional natural frequency $\hat{f}_N$ is estimated through peak finding algorithms in the frequency spectrum of the shaft speed signals. One may then solve for the unknown rotor inertia as follows

$$
\hat{J}_{eq} = \frac{\hat{k}_{DT}}{(2\pi\hat{f}_N)^2},
$$
$$
\hat{J}_{Rot} = (1/\hat{J}_{eq} - 1/\hat{J}_{Gen}/i_{DT})^{-1}.
$$
(4.3)

This approach may also be extended to higher-order torsional drivetrain models, as demonstrated by Moghadam et al. [51], where additional torsional DOFs in the intermediate speed gear shafts and the planets are considered. The caveat is that this fidelity level requires additional angular velocity measurements of the intermediate speed shafts, which are non-customary in SCADA systems. It also remains questionable whether a higher fidelity level necessary yield a more accurate representation of the drivetrain dynamics, since the introduction of more DOF also increases the amount of unknown parameters, each with associated estimation uncertainty. The uncertainty of system identification methods for drivetrain DTs is further discussed in Sec. 6.

4.4 Case studies

DT models are investigated in a variety of case studies, most notably the U.S. Department of Energy (DOE) 1.5 MW research turbine [52], the National Renewable Energy Laboratory (NREL) 5 MW reference turbine [53] and the Technical University of Denmark (DTU) 10 MW reference turbine [54]. The former case study is a commercial General Electric onshore wind turbine of type GE 1.5 SLE located at the NREL campus in Arvada, Colorado that has been customized for research activities. In addition to industrial SCADA and CM systems, the DOE 1.5 MW turbine is equipped with a custom load sensor system comprising strain gauges at the tower base, tower top, blade roots, main shaft and high-speed shaft, which facilitate the measurement of multi-axial loads. Several long-term measurement campaigns were conducted that provide a unique opportunity to validate DT models. Mehlan et al. [4] used a data set recorded in the time frame of Oct. 31 to Dec. 05, 2018 totalling to 138.3 h at a sampling frequency of 50 Hz to validate the load calculation of DT models at the main and high-speed bearings. Limitations of this case study are present in the development of dynamic drivetrain models due to the confidentiality of certain gearbox specifications. The installed gearbox is a commercial Winergy PEAB 4410.4 high-speed gearbox, for which validated high-fidelity dynamic models are not available. Instead, an "analytical" drivetrain model that assumes rigid torque transmission [55][56] is employed by Mehlan et al. [4].

The latter two case studies, the NREL 5 MW and DTU 10 MW turbine, are reference turbines that have been developed to provide researchers with a standardized baseline to conduct research. The reference turbines are fully designed according to the IEC 61400 series [59], however, they have not
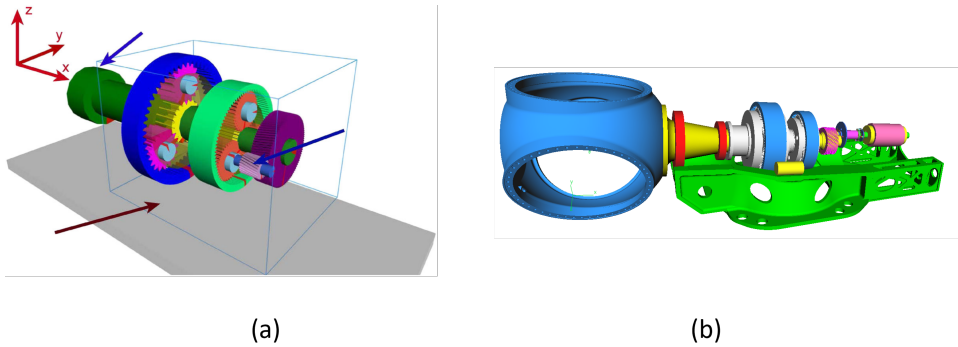
Figure 4.5: High-fidelity MBS models used for numerical case studies: (a) the NREL 5 MW model [57], (b) the DTU 10 MW model [58].

been manufactured and exist only as a concept. Simulation models of the reference turbines have been used in numerous numerical experiments and are invaluable to researchers despite not being validated against a physical wind turbine. Numerical experiments are drastically less expensive than testbench or field experiments and are favourable for testing novel technologies in early development stages, often to demonstrate the proof-of-concept. Global models of the reference turbines have been developed in aeroelastic simulation tools OpenFAST and HAWC2 at NREL and DTU and are kindly provided as open source models. Dynamic drivetrain models have been developed at the Department of Marine Technology (IMT) at the Norwegian University of Science and Technology (NTNU) by Shuaishuai Wang [58] and Amir R. Nejad [57] (Fig. 4.5). The drivetrain models are developed as high-fidelity MBS models in the software SIMPACK according to best practice and model fidelity guidelines, presented in Sec. 4.2.2, and are capable of simulating high-frequency internal drivetrain dynamics, calculating local gear and bearing loads and synthesizing CMS vibration data. Different modelling approaches are employed for the bedplate, which is considered flexible in the DTU 10 MW model and rigid in the NREL 5 MW model. According to a numerical study by Wang et al. [60] the bedplate flexibility has a considerable impact on fatigue loads of gearbox bearings and should be modelled with at least 15 nodes.

All three case studies share similarities in the drivetrain design comprising a three stage gearbox with two planetary and one parallel, helical gear stage. Notable differences, enlisted in Tab. 4.2, are first and foremost the power rating and size, but also other design characteristics. The DOE 1.5 MW turbine is located at an onshore site, while the NREL 5 MW and the

DTU 10 MW turbines are designed as offshore wind turbines. The DOE 1.5 MW turbine's main shaft support also differs; it is designed as a three-point suspension rather than a four-point suspension, which subjects the gearbox to higher non-torque loads. In a four-point suspension, the pair of main bearings are designed to support all non-torque loads. Furthermore, while the turbines share the same gearbox topology, the DTU 10 MW turbine's drivetrain is classified as medium-speed with a transmission ratio of only 1:50.039, while the other turbines fall into the category of high-speed wind turbines. This design choice promises higher reliability, since many premature gearbox faults occur at the high-speed gear stage.

The NREL 5 MW model is used in studies by Mehlan et al. to evaluate DTs for load monitoring at the high-speed gear stage [2, 3] and to develop ROMs for efficient simulation of gear meshing [1]. The DTU 10 MW model is used to evaluate a novel diagnostic method for rotor imbalance [5]. All three case studies are considered by Mehlan et al. in a study on the uncertainty assessment of DT models [6].

Table 4.2: Case studies for the evaluation of DT models and methods.

	DOE 1.5 MW [52]	NREL 5 MW [53]	DTU 10 MW [54]
Used in references	[4, 6]	[1, 2, 3, 6]	[5, 6]
Design specifications			
Site	Onshore	Offshore	Offshore
Rotor configuration	Upwind, three blade	Upwind, three blade	Upwind, three blade
Control strategy	Variable speed, pitch controlled	Variable speed, pitch controlled	Variable speed, pitch controlled
Main shaft support	Three-point suspension	Four-point suspension	Four-point suspension
Gearbox topology	Two planetary, one parallel	Two planetary, one parallel	Two planetary, one parallel
Rated power [MW]	1.5	5	10
Hub height [m]	80	90	119
Rotor diameter [m]	77	126	178.3
Rated wind speed [m/s]	14	11.4	11.4
Cut-in/cut-out wind speed [m/s]	3.5-25	3-25	4-25
Rated rotor speed [rpm]	18.3	12.1	9.6
Rotor speed range [rpm]	10-25	6.9-12.1	6-9.6
Rated generator speed [rpm]	1436	1165	480
Gearbox ratio [-]	1:78.472	1:96.354	1:50.039
Rotor mass [t]	87 (rotor+nacelle)	110	229
Nacelle mass [t]	N.A.	240	446
Tower mass [t]	N.A.	347.46	605
Modelling approaches			
Global model	Aeroelastic (OpenFAST)	Aeroelastic (OpenFAST)	Aeroelastic (OpenFAST)
Drivetrain model	Rigid [55][56]	Flexible MBS (SIMPACK)[57]	Flexible MBS (SIMPACK)[58]

Chapter 5

Digital Twin Decision Support

One of the key principles of DT according to DNV [18] is to provide value-adding services with the purpose of improving the business outcome, a capability referred to as decision support. The decision support is the delineating criteria to standalone models and Digital Shadows, since it represents the information flow back to the physical asset [19]. The importance of the decision support is reflected in the conceptualized DT architectures of different authors. The DT framework by Tao et al. foresees this capability with the functional element called "Services (Ss)" [20], while in Johansen et al. [24] it is referenced as "RUL and Fault prediction". Lastly, in Mehlan et al. [3] a decision support component is proposed for the purpose of fatigue damage monitoring and RUL prediction.

The type of services ultimately define the DT's usefulness and autonomy, referred to as the capability level in DNVGL-RP-A204 [18], ranging from level 0 to level 5 (Fig. 5.1). Level 0 refers to disconnected standalone models such as CAD drawings that are by definition not considered DTs. At level 1 the DT is able to describe the current state of the asset, which may refer to the operational state, the health condition, the environmental conditions or the kinematic state of the asset. Classical descriptive capabilities include condition monitoring, fault detection and operational control. The capability level 2 is reached when the DT is able to perform diagnostic tasks such as the classification and localization of faults. Level 3 refers to predictive capabilities such as the forecast of fault progression and RUL estimation. At the prescriptive capability, level 4, the DT is able to recommend actions to mitigate future adverse conditions, for instance, order maintenance tasks to prevent severe failures. The highest capability level describes fully au-
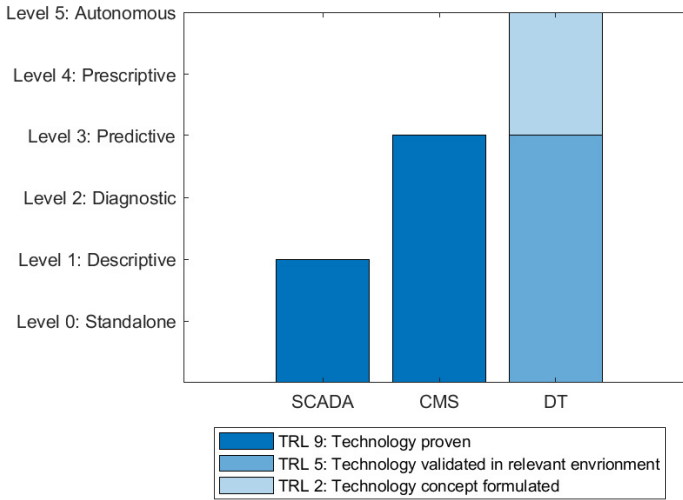
Figure 5.1: The DNV capability level of DT decision support services in comparison to SCADA and CM systems [18].

tonomous DTs. At this level, all operational and maintenance tasks are conducted autonomously without any human interference.

Commercial applications of decision support services are found in SCADA and CM systems. SCADA systems are utilized for supervisory and control tasks, which falls into the descriptive capability (level 1). CM systems may be classified as level 3, as they are used for descriptive, diagnostic and predictive tasks including health monitoring, fault detection, fault diagnosis and RUL estimation. Recent research into DT is not only motivated by the potential of extending the capability level towards fully autonomous systems, but also by the objective of improving the services at lower levels. The DT presented by Mehlan et al. [3] reaches the capability level 3 and provides advanced health monitoring and RUL estimation through the use of virtual load measurements.

A brief overview of the state-of-the-art and recent developments into decision support services is given. The referenced DTs in this chapter are summarized in Tab. 5.1 according to their capability level.
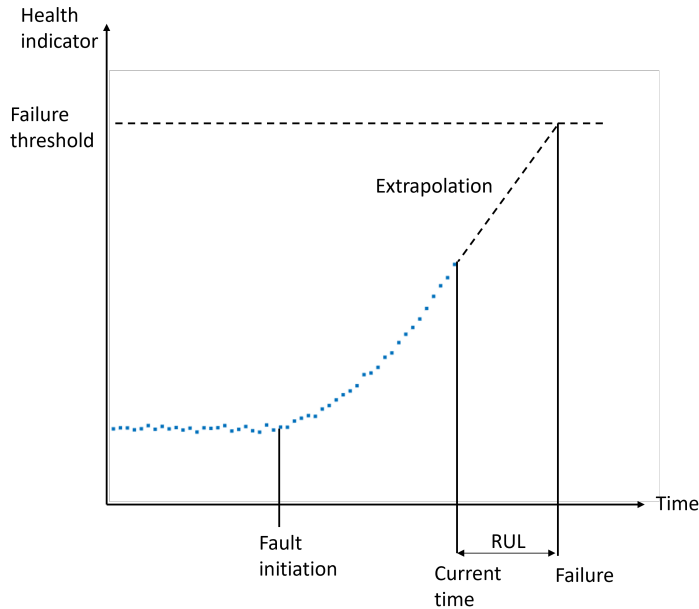
Figure 5.2: Remaining useful life estimation through trend analysis of vibration features.

5.1 State-of-the-art: SCADA and CM systems

SCADA systems are essential equipment for the remote operation of wind turbines and are utilized for tasks such as control, performance monitoring, error alerts and logging maintenance reports. This is realized through the acquisition and analysis of meteorological data, operational data, and maintenance data on component faults, repair and replacements. The capability of commercial SCADA systems can be classified as level 1 (descriptive), however many research activities are devoted to developing higher level decision support services (Sec. 5.4.1). Data mining of large SCADA databases and machine learning models are commonly investigated tools for fault diagnosis and prognosis.

CM systems are installed in most offshore wind turbines and have proven to be crucial to maintain high levels of availability and reliability and to reduce the O&M expenditures. CMS provide services including health monitoring, early fault detection and RUL prediction, and can thus be classified as a level 3 decision support. Vibration analysis emerged as the most effective approach to drivetrain condition monitoring, however, other solutions using oil particle, acoustic, electric or temperature sensors are commercially avail-

able. The primary advantage of vibration measurements lies in early fault detection. Increased vibrations are often the first indicator of drivetrain faults and are typically observable several months before the fault develops into a failure, while oil particles, temperatures and acoustic emissions tend to be affected at later stages. The second advantage lies in the fault-specific vibration responses that allow the distinction of different fault types. For instance, gear faults such as tooth root cracks or surface spalls have characteristic fault signatures at the gear meshing frequency, which are identifiable through frequency-domain methods.

The installation of vibration sensors for CMS is described in ISO 10816-2 [30]. The standard recommends the placement of piezo-resistive or capacitive accelerometers on the housing of the main bearings, the gearbox and the generator, in both radial and axial direction. The vibration signals shall be analysed in the frequency band of 10 Hz to 5 kHz and characterized through the root-mean-square. Four evaluation zones (A-D) are defined that allow the qualitative evaluation of the drivetrain condition and the recommendation of any actions that need to be taken. Zone A describes the lowest vibration levels that occur in newly commissioned wind turbines, while zone D indicate vibrations that are potentially damaging to the drivetrain. However, normative evaluation boundaries are not defined at this point in time, since the available data are not sufficiently representative.

Industrial practice involves more advanced tools such as trend analysis to facilitate fault prognosis, as reviewed by Randall [32]. Trend analysis is based on the premise that vibration amplitudes increase progressively with the fault development, and that the drivetrain's health condition may be correlated with vibration features (Fig. 5.2). The first step lies in the identification of suitable features, referred to as health indicators, that possess a high trendability and sensitivity to drivetrain faults. Commonly used health indicators are time-domain statistical features such as the RMS, mean, standard deviation, skewness and kurtosis. Additional features may be obtained through Fast Fourier transform, Wavelet transforms or Cepstrum analysis. The second step is the definition of thresholds at which the fault develops into a failure. In absence of normative values by ISO 10816-2 [30], the definition of appropriate failure thresholds is very challenging and relies on the operator's expertise and domain knowledge. In the third step, the time until failure or the RUL is estimated through extrapolation of the current trajectory to the failure threshold. The extrapolation is commonly conducted through linear or polynomial regression, while more complex regression models such as artificial neural networks or other machine learning models are the subject of recent research (Sec. 5.4.1).

5.2   Descriptive capability

Potential applications of DT at the descriptive capability level are envisioned in the virtual asset inspection. With improved digital models and sensor technologies, the asset inspection may be performed fully remotely, saving on labour and logistical costs [24]. DT may also be used to extend the monitoring capabilities of current SCADA and CMS systems, specifically the observation of the dynamic state characterised by the environmental loads, the dynamic system response and local component forces or stresses. This information may be utilized for value-adding services such as load-based condition monitoring methods, predictive maintenance strategies based on the consumed fatigue life or advanced control algorithms for load minimization. However, direct load or strain measurements in wind turbine drivetrains are impractical due to geometrical restrictions on sensor placements inside the gearbox, the poor reliability and lifespan of load sensors and prohibitive costs of sensor installation and calibration. Indirect measurement techniques, also referred to as virtual sensor, soft sensor or modelled data techniques, are pursued by different authors for load monitoring purposes. These techniques apply the DT paradigm of fusing data and models, as they take advantage of physics-based or data-driven models to expand the set of physical sensors with a set of virtual sensors to measure the desired quantities. For example, the physical sensor signal of the SCADA generator torque T_{Gen} may be combined with a drivetrain model in the form of $F_t = T_{Gen}/r_b$ to obtain the virtual measurement of the gear force F_t.

The research into virtual sensing of drivetrain loads may be categorized into the distinct challenges of main bearing (Sec. 5.2.1) and internal drivetrain load estimation (Sec. 5.2.2).

5.2.1   Main bearing load estimation

The main bearings are designed to support the rotor weight and transfer aerodynamic loads into the bedplate, which are highly stochastic and non-stationary due to the volatility of the environmental conditions. The aerodynamics are most energetic at lower frequencies (< 1 Hz) with characteristic excitations at the rotor and the blade pass frequency due to imbalance, tower shadow and other effects. The loading at the main bearings is determined by the six rotor load components, torque, thrust, yaw moment, pitch moment, shear force and vertical force, where the non-torque loads are particularly challenging to estimate with current methods. Various studies address this challenge with methodologies that differ in the type of models
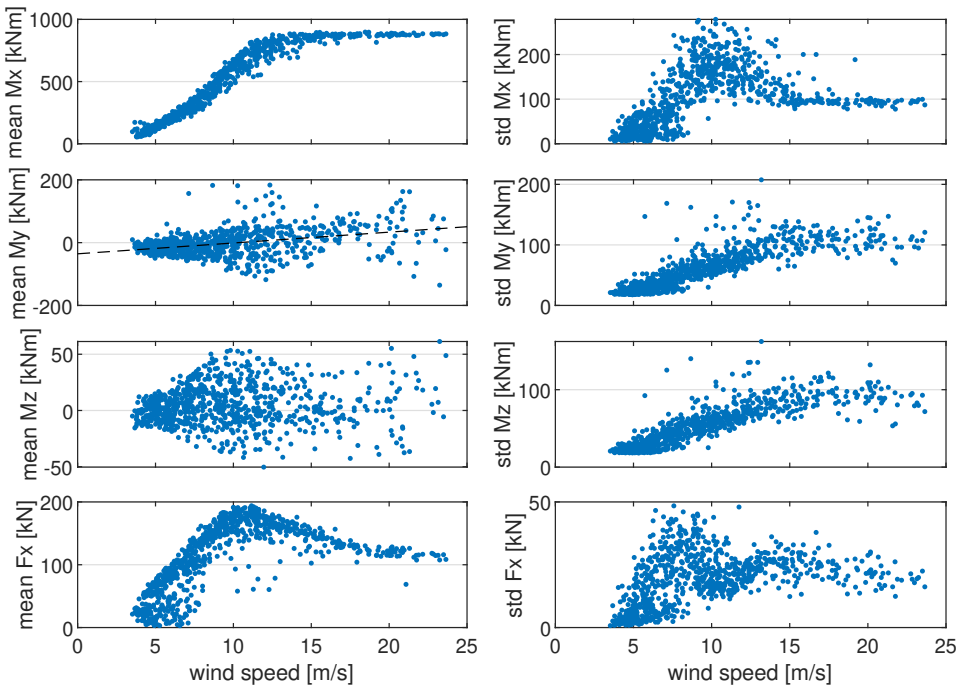
Figure 5.3: 10 min mean and standard deviation of rotor loads measured at the DOE 1.5 MW turbine [4].

(data-driven or physics-based) and the physical sensor input (SCADA, CMS or custom displacement/strain sensors).

One of the first studies on virtual sensing of main shaft loads was conducted by Perisic et al. [49], where a physics-based approach was employed to estimate the rotor torque. The premise is that with knowledge of the torsional response measured with shaft encoders and knowledge of the generator side torque measured with electrical sensors, one can "solve" for the unknown rotor torque. A two DOF torsional drivetrain model is constructed and parameterized through system identification methods. The rotor torque is then estimated using the augmented Kalman filter and SCADA data of the generator torque and rotor and generator shaft speeds.

Branlard et al. [61, 45] build on previous works by Perisic et al. and extend the capability to estimating both rotor torque and thrust. The physical model is derived from linearization of an aeroelastic OpenFAST model and considers also the first tower fore-aft bending mode in addition to the first drivetrain mode. A further novelty is the inclusion of tower top acceleration measurements to better estimate the thrust loads.

Similar studies with a physics-based approach are presented by Bosmans et al. [62], who investigate a virtual torque sensor on the basis of strain gauges mounted on the gearbox housing. The relationship between torque and strain measurements is derived from a FE housing model and validated on a testbench.

The aforementioned studies report a good agreement in the estimated torque and thrust, but are faced with limitations when it comes to physical modelling of the remaining load responses. While the dynamic responses to torque and thrust loads can be approximated reasonably well with the first drivetrain torsional mode and the first tower fore-aft mode, the dynamics of yaw and pitch bending moments are much more complex. These involve various edge- and flap-wise blade bending modes, main shaft bending modes and local drivetrain bending modes, which are more difficult to model and incorporate in a ROM.

To overcome the limitations of physical modelling and to extend the capability to non-torque load estimation, a data-driven approach is pursued, among others, by Azzam et al. [46], Loriemi et al. [47], and Mehlan et al. [4]. Azzam et al. [46] conducted a numerical case study via simulation of a Vestas V52 MBS model, where feedforward neural networks were trained to predict the six DOF main shaft loads based on SCADA signals and the six lateral and angular torque arm displacements. Loriemi et al. present a similar numerical study with a MBS model of a 2.3 MW low speed wind turbine, however, the predictor variables were limited to exclusively displacement signals. Feedforward and LSTM neural networks were selected as regression models. Both studies report coefficients of determination R^2 of higher than 0.95 for all main shaft and main bearing loads, which suggests that the ANNs are suitable regression models to capture the non-linear relationship between displacements and loads. However, these numerical studies fail to address the limitations of displacement measurements. These sources of uncertainty were investigated in a field study of the DOE 1.5 MW turbine located at NREL by Mehlan et al. [4]. A similar data-driven approach using linear regression models, support vector machines and tree ensembles was applied to predict the main shaft loads. Field measurements of SCADA and CMS sensors were postprocessed to extract 10 min statistical features and used as predictor variables. Contrary to the aforementioned numerical studies, only torque arm acceleration measurements in radial and axial direction were used, which are the customary sensors in drivetrain CMS. Compared to displacement measurements, acceleration measurements are particularly vulnerable to measurement noise at the main shaft due to the low signal frequency and signal power. The regression models produced
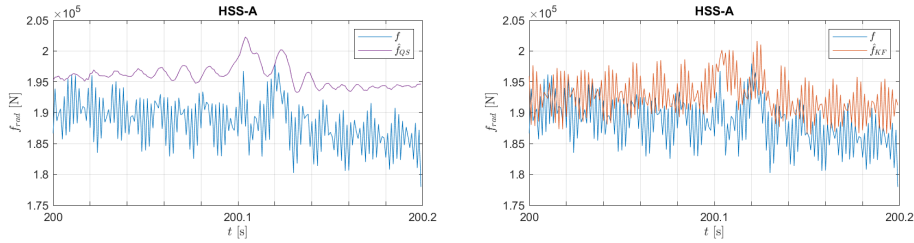
(a) SCADA   (b) SCADA and CMS

Figure 5.4: Virtual load sensing at the high-speed bearing using only SCADA data (a) and combined SCADA and CMS vibration data (b) [3]

estimates of reasonable accuracy, but are ultimately limited by the quality and the resolution of the measurement input. The estimation of the mean and standard deviation of the rotor torque is accurate, since it exhibits a high correlation ($R > 0.99$) with the measured generator torque. Similarly, the thrust estimates are accurate due to clear, albeit non-linear trends with respect to SCADA signals, for example the thrust-wind speed curve shown in Fig. 5.3, which may be captured by regression models. The estimation of the mean yaw and pitch bending moments, on the other hand, remains challenging due to the low sensitivity of SCADA and CMS signals, which was statistically insignificant ($R < 0.5$) for the investigated sensor signals.

5.2.2   Internal drivetrain load estimation

Virtual sensing of the downwind bearing and gear loads poses a different challenge, since in addition to the aerodynamics and structural dynamics the complex internal drivetrain dynamics are of importance. The internal drivetrain dynamics are characterized by non-linear and discontinuous multi-body interaction of different drivetrain components including shafts, gears and bearings. The contacts in the gear teeth and the roller bearings induce mechanical excitations at the gear meshing and ball passing frequencies, which are typically at a much higher frequency range ($10 - 1000$ Hz) than aerodynamic excitations. The inclusion of high-frequency internal drivetrain dynamics into a virtual load sensor would require a much lower step size, which places higher demands on the resolution of the physical sensor

measurements and increases the computational burden of the DT model.
For this reason, the earliest publications on this topic employed a simplified
approach, where the drivetrain dynamics are reduced to a small number of
torsional modes. Moghadam et al. [51] present a methodology for virtual
sensing of drivetrain gear loads using a torsional ROM and angular velocity
measurements. Additional shaft encoders at the intermediate speed shafts,
which are not typically part of SCADA systems, are proposed for improved
measurement of the torsional dynamics. The ROM considers 14 torsional
DOF and reduces the gear and bearing contacts to one-dimensional, linear
elastic contacts.

Later works by Mehlan et al. [3] were motivated by the objective of im-
proving the drivetrain load estimates in the higher frequency range. The
proposed strategy to capture high-frequency internal dynamics is to lever-
age CMS vibration data, which by design have a sufficient resolution and
sensitivity to observe gear meshing and bearing excitations. A numerical
case study with the NREL 5 MW reference turbine is conducted to evalu-
ate different virtual sensing approaches using only SCADA data or SCADA
and CMS data as input. The former approach (QS-method) assumes quasi-
static, rigid transmission of torque throughout the drivetrain, in which case
the radial bearing loads are proportional and only a function of the SCADA
generator torque. The latter approach (KF-method) employs a Kalman fil-
ter to fuse generator torque and CMS vibration data with a linear elastic
drivetrain model. The results show significant improvements in the high-
frequency range of HSS bearing load estimates using CMS data, although
some frequency peaks related to excitations of the intermediate gear stage
were not captured (Fig 5.4). Nonetheless, questions on the feasibility of this
approach remain, as this numerical study represents an idealized scenario.
Measurement noise and the damping due to the transfer of the vibration
signal through the gearbox housing are not considered here. Furthermore
it should be evaluated for each application if the consideration of high-
frequency internal dynamics is necessary. For the use case of bearing fatigue
damage monitoring the gained benefit appears to be small. The numerical
results suggest that the bearing fatigue damage is driven by low-frequency
aerodynamics and only marginally impacted by high-frequency drivetrain
dynamics.

5.3   Diagnostic capability

DT opens up new areas of research in drivetrain fault diagnosis with the
potential to improve upon existing methods. The potential of DT is envi-
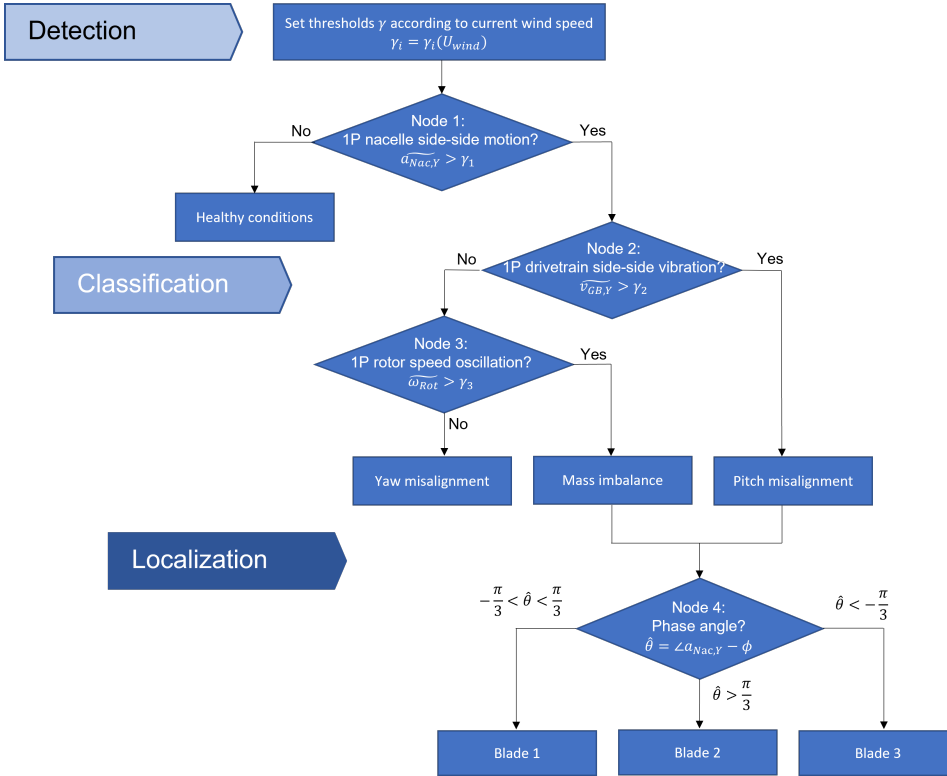
Figure 5.5: Diagnostic method for rotor imbalance faults enabled by the integration of CMS and SCADA data [5].

sioned in the virtual inspection and increased accuracy of the diagnosis and the fault progression forecast [14]. The complete, virtual representation of the physical wind turbine in all its aspects that is pursued in DTs would facilitate virtual inspections and fault diagnosis in the virtual model. While the technology for virtual inspections is currently still at its infancy, there is ongoing research into the use of virtual measurements in the areas of model-based fault diagnosis and fault-tolerant control [63]. Virtual measurements represent a new source of information that can provide a deeper insight and a more accurate observation of developing faults.

Further advances can also be achieved through more efficient utilization of existing SCADA and CMS data. Many publications address fault diagnosis exclusively based on SCADA data using machine learning approaches, or fault diagnosis solely based on CMS data using vibration analysis techniques. The intelligent integration of SCADA and CMS data is proposed by Mehlan et al. [5] to advance fault diagnosis methods. This study inves-

tigates the question whether the information in CMS vibration data may be leveraged for tasks outside its original purpose of drivetrain condition monitoring. A use case is identified in the diagnosis of faults that lead to an aerodynamic or inertial imbalance of the rotor such as pitch misalignment, yaw misalignment and mass imbalance. Rotor imbalance faults are relatively common and contribute to higher loads and fatigue damage in the blades and tower, but may also be damaging to drivetrain components. Recent field studies report that 38% of wind turbines operate with pitch misalignment of $> 0.3°$ that are considered unacceptable according to GL standards [64]. Yaw misalignment is present in most operating turbines due to the inaccuracy of wind direction measurements using nacelle-mounted wind vanes and mass imbalance can occur as a result of manufacturing errors or uneven accumulation of ice, moisture or dirt.

The conventional approach to imbalance detection is based on monitoring the amplitudes at the rotor frequency 1P in tower-top acceleration signals, since rotor imbalance faults are known to excite tower side-side bending modes at this frequency. The classification of different imbalance fault types is more challenging, since each rotor imbalance fault induces similar dynamic wind turbine responses that make it difficult to define effective diagnostic criteria. Kusnick et al. [65] propose the reduction of the electrical power output as a criterion to distinguish pitch misalignment from mass imbalance, however, this signal is very sensitive to changes in wind speed. Other methods rely on physical modelling of the wind turbine structure, which may not be feasible for wind farm operators [66].

An effective alternative is identified in CMS vibration amplitudes. Numerical studies with the DTU 10 MW reference turbine reveal that pitch misalignment induces characteristic yaw and pitch moments that excite local drivetrain bending modes and are observable in the vibration response throughout the drivetrain [5]. Yaw misalignment and mass imbalance, on the other hand, primarily result in higher torque loads and shear forces that do not induce such drivetrain vibration responses.

These findings are used to develop a diagnostic method formulated by three binary decision rules to classify healthy conditions, yaw misalignment, pitch misalignment and mass imbalance (Fig. 5.5). In the first step, a fault is declared if an increase in the nacelle side-side acceleration amplitudes is detected. In the second step, pitch misalignment is isolated from the remaining fault types in case of increased vibration amplitudes on the gearbox housing. Lastly, mass imbalance is distinguished from yaw misalignment by observing the rotor speed amplitudes.

The evaluation of the proposed method under different environmental and

fault conditions yields promising results. While the detection and identification of mass imbalance remains challenging, all pitch misalignment cases ranging from 1° to 3° are correctly detected and classified using CMS vibration data. This illustrates one occasion where DTs may provide more accurate and more robust diagnostic services through intelligent integration and utilization of SCADA and CMS data.

5.4   Predictive capability

The predictive capability refers to the DT's ability to forecast various wind turbine's states ranging from meteorological variables such as incoming wave heights, performance variables such as the power production to the health condition of turbine components. The majority of research activities is focused on predicting the health condition, specifically the RUL, as a step towards predictive maintenance strategies [15]. Predictive maintenance is one of the most investigated research topics related to Industry 4.0. Predictive maintenance is based on the principle of predicting failures and scheduling timely repairs to mitigate more severe damages to the system and to utilize maintenance resources such as labour and material more cost effectively. DT is seen by many authors as the key enabling technology to advance predictive maintenance strategies. The approaches to RUL estimation for predictive maintenance can be categorized into data-driven (Sec. 5.4.1) and physics-based methods (Sec. 5.4.2).

5.4.1   Data-driven trend analysis for RUL estimation

The research into data-driven methods for RUL estimation in wind turbine drivetrains follows an approach similar to the vibration trend analysis in conventional CM systems (Sec. 5.1). Various areas are investigated such as alternative sensor signals, data processing algorithms and machine learning models in hopes of improving the RUL prediction accuracy.
Machine learning models are explored by several authors as a tool to regress and predict failure trends [67, 68, 69]. The strengths of machine learning models lie in their ability to capture complex, non-linear relationships and in their multiple input multiple output (MIMO) capability. Artificial neural networks (ANNs) are a popular choice and reportedly yield higher accuracy than comparable machine learning models. In a study by Carrol et al. [67], feedforward ANNs outperformed support vector machines and logistic regression models in predicting gear and bearing failures. Similarly, Elasha et al. [68] compare feedforward ANNs to polynomial and exponential regres-
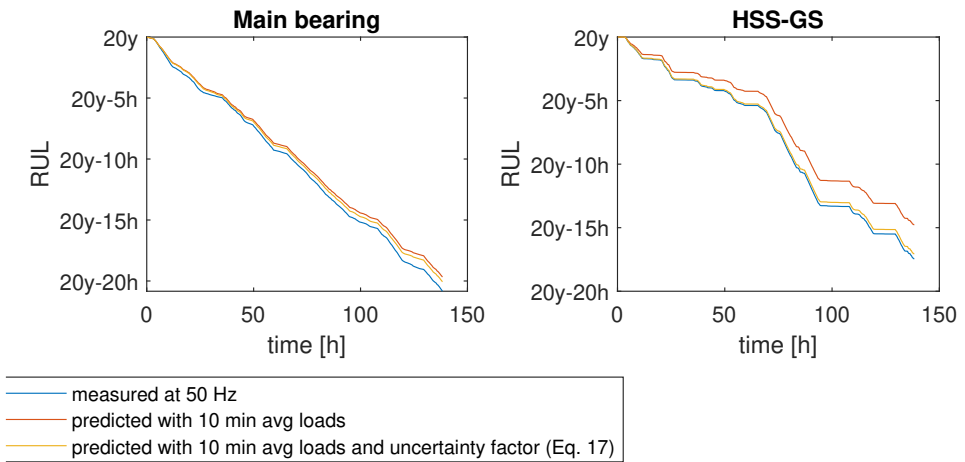
Figure 5.6: RUL estimates of main and high-speed bearing based on direct strain gauge measurements and indirect virtual sensor techniques[4].

sion in a study on bearing RUL estimation and report significantly lower errors for the ANNs. ANNs are also employed by Yucesan et al. [69] to predict the lubricant condition in wind turbine main bearings.

Many authors investigate SCADA signals as additional or alternative signals to CMS vibrations. In different studies it is demonstrated that the prognosis of drivetrain faults several weeks in advance solely based on SCADA data is feasible [70]. Bearing temperature signals are deemed particularly beneficial for fault prognosis, since for many gear and bearing failure modes the temperature tends to rise as result of added friction. In practice, however, temperature signals are less suited for trend analysis due to the large influence of environmental and operational conditions. In a case study on two gear and bearing faults by Carrol et al. [67] none of the SCADA temperature signals exhibited any identifiable trends. Carrol et al. conclude that direct trend analysis of temperature signals is not fruitful and suggest conditioning the temperature on the electrical power or wind speed, or using machine learning models to capture these relationships.

5.4.2 Physics-based virtual sensing for RUL estimation

While data-driven methods for RUL estimation receive much attention in recent scientific publications, physics-based methods remain an underexplored topic. Physical modelling of drivetrain failures by first principles is inherently challenging, since the failure mechanics are often not sufficiently understood, and empirical models perform poorly outside of controlled lab-

oratory environments. This has led the scientific community to gravitate towards purely data-driven solutions, however, there are still many use cases in fault prognosis, where physical modelling can provide tangible benefits. Hybrid approaches that combine data-driven with physics-based models are a promising strategy to achieve the best of both worlds. Hereby, the physics that are well understood such as the drivetrain mechanics are represented by physics-based models, while the poorly understood physics of fault initiation and development are captured with data-driven methods.

The hybrid approach is pursued by Desai et al. [71] and Guo et al. [39] for the prognosis of axial bearing crack failures. Axial bearing cracks commonly occur at the high-speed bearings and can cause premature failures within the first six years of operation. The best physical understanding of the root causes is excessive friction, which occurs in transient events such as emergency stops and induces rapid plastic deformation of the raceway. For this reason, the frictional energy in the roller-raceway contacts is proposed as a metric to predict axial bearing crack failures. Desai et al. and Guo et al. use a physics-based bearing model, presented in [72], to calculate the frictional energy in real-time as a function of SCADA signals. While the authors refer to the frictional energy as "modelled data", it can also be considered a virtual sensor measurement in the context of DT. Guo et al. [39] employ reliability methods to calculate the probability of failure at any given time as a function of the accumulated frictional energy and failure thresholds determined from wind turbine failure records. Desai et al. [71] train various machine learning models including logistic regression, tree ensembles and artificial neural networks on both SCADA and virtual sensor data. The results show significantly improved accuracy in the RUL estimation using virtual sensor data and underline the benefit of physical modelling for fault prognosis.

A second use case for physics-based models is the prognosis of fatigue failures, presented by Mehlan et al. [3, 4]. CM systems typically focus on the detection of premature faults that occur early in the wind turbine's lifecycle rather than material fatigue that marks the end of the 20 year nominal life. Nonetheless, there are clear benefits in monitoring the accumulated fatigue damage and estimating the RUL based on the remaining fatigue damage reserves. Material fatigue driven failures may occur earlier in the lifecycle due to uncertainty in the design procedure. For instance, the actual environmental conditions may be more severe than the assumed design load cases (DLCs [48]). In this case, the operator may benefit from early failure alerts to schedule timely part replacements. RUL estimates are also of great importance in lifetime extension decisions, where they can provide a time

estimate for the continued safe operation beyond the service life [73].

Fatigue assessment of drivetrain gears and bearings is standardized by the codes ISO 6336 [74] and ISO 281 [75], respectively. The fatigue lifetime is expressed as a number of permissible stress cycles and related to the loading conditions through S-N curves. The raw load time signal must be converted to a stress cycle histogram using stress cycle counting algorithms. For rotating machine equipment such as gears and bearings that experience cyclical loading each shaft rotation by entering and exiting the load zone, the load duration distribution (LDD) method is applicable [44].

While fatigue assessment is standard procedure in the design of wind turbine drivetrains, continuous monitoring of fatigue damage in operating systems is not practiced. The limiting factor is the measurement of local gear and bearing loads, which are not available in commercial wind turbines due to economical, geometrical and reliability constrains of load sensors. DT can bridge this gap through virtual sensing techniques (Sec. 5.2) and thus facilitate continuous monitoring of fatigue damage and RUL estimation. This approach is demonstrated by Mehlan et al. in a field study with the 1.5 MW DOE research turbine that is equipped with SCADA and CMS sensors, as well as a custom strain gauge setup that allows the validation of virtual load measurements [4]. The RUL estimates of the main and high-speed bearing based on virtual sensing techniques shows a good agreement with direct strain gauge measurements (Fig. 5.6). Larger errors are observed at the main bearing due to the uncertainty in the yaw and pitch bending moment estimates (Sec. 5.2.1), whereas the high-speed bearing fatigue is predominantly torque driven. The results showcase the potential of physics-based models for RUL estimation, however, they also highlight the limitations of such models. Physics-based models are unable to capture all physics due to unknown process parameters, unknown input variables, or because computational constrains dictate the usage of reduced order models. In this case study, it was necessary to resort to a rigid reduced order drivetrain model due to limited knowledge of drivetrain specifications and thus neglecting the influence of all internal drivetrain dynamics on bearing fatigue damage. The modelling uncertainty of physics-based models should be carefully considered in RUL applications. Further discussion on the uncertainty assessment of this approach is presented in Sec. 6.

5.5 Prescriptive capability

The prescriptive capability refers to the DT's ability to not only predict failures but also recommend mitigating actions such as maintenance tasks

or control strategies. Prescriptive maintenance strategies have been conceptualized for a long time, but the technology readiness level of such strategies in wind turbine drivetrains remains low and publications on this topic are sparse. However, one may refer to studies in relatable fields such as Momber et al. who present a methodology for prescriptive maintenance of protective coating of wind turbine structures [76]. The prescriptive capability is realized through a "maintenance model" that recommends maintenance actions ranging from "No measures required", "Inspection required", "Repair planning" to "Repair required" as a function of the deterioration degree and the component criticality. Strack et al. [77] present a similar maintenance model for a GE onshore wind turbine. The maintenance tasks are determined based on interviews with domain experts and collected in a structured measure catalog. Each component specific failure mode is linked to a maintenance task through a so called function tree. The development of maintenance models for wind turbine drivetrains, however, is more challenging due to the multitude of drivetrain components, unique failure modes and their effects. More research into this this area is needed to develop prescriptive DTs.

Table 5.1: *Digital Twins in offshore wind turbine drivetrains and related fields.*

Reference	Application	Capability	Model	Data	Decision support
Perišić et al. (2013) [49]	Main bearing	Descriptive	Physics-based	SCADA	Torque virtual sensor
Branlard et al. (2020) [61, 45]	Wind turbine tower	Descriptive	Physics-based	SCADA	Torque & thrust virtual sensor
Remigius et al. (2021) [78]	Main bearing	Descriptive	Physics-based	SCADA	Torque virtual sensor
Azzam et al. (2021) [46]	Main bearing	Descriptive	Data-driven	SCADA/Displacements	Torque & non-torque virtual sensor
Loriemi et al. (2022) [47]	Main bearing	Descriptive	Data-driven	Displacements	Torque & non-torque virtual sensor
Mehlan et al. (2022) [4]	Main & HSS bearing	Descriptive	Hybrid	SCADA/CMS	Torque & non-torque virtual sensor
Bosmans et al. (2023) [62]	Main bearing	Descriptive	Physics-based	Strain	Torque virtual sensor
Moghadam et al. (2021) [49]	Drivetrain	Descriptive	Physics-based	SCADA	Gear force virtual sensor
Mehlan et al. (2023)[5]	Rotor	Diagnostic	Hybrid	SCADA/CMS	Rotor imbalance diagnosis
Carrol et al. (2018) [67]	Drivetrain	Predictive	Data-driven	SCADA/CMS	RUL prediction
Sivalingam et al. (2018) [79]	Power converter	Predictive	Hybrid	SCADA	RUL prediction
Elasha et al. (2019) [68]	HSS bearing	Predictive	Data-driven	CMS	RUL prediction
Yucesan et al. (2019) [69]	Main bearing	Predictive	Hybrid	SCADA	RUL prediction
Desai et al. (2020) [71]	HSS bearing	Predictive	Hybrid	SCADA	RUL prediction
Guo et al. (2020) [39]	HSS bearing	Predictive	Hybrid	SCADA	RUL prediction
Mehlan et al. (2022)[3][1]	Main and HSS bearing	Predictive	Hybrid	SCADA/CMS	RUL prediction
Momber et al. (2021) [76]	Protective coating	Prescriptive	Data-driven	Photographic	Prescriptive maintenance
Strack et al. (2021) [77]	Wind turbine	Prescriptive	Data-driven	SCADA/CMS	Prescriptive maintenance

Chapter 6

Uncertainty assessment

The continued digitization and automation of wind turbines through DTs poses significant risks, since wind turbines are high-value assets and an important part of the energy infrastructure. Malfunctions or erroneous decisions made by DTs could potentially have severe consequences. False negatives such as missed fault detections could develop to a system level failure, long down times and expensive repairs, while false positives could lead to frequent and unnecessary maintenance activities. Therefore, it becomes imperative to assess the uncertainty in the decision process of DTs and conduct a risk analysis before implementing higher levels of autonomy. The uncertainty in DT can be divided to two categories [80]:

- *Aleatory uncertainty* refers to the natural uncertainty in physical phenomena that is inevitable and irreducible with additional information. Typical sources of aleatory uncertainty in wind turbines are the stochastic wind and wave loads or the variability of material parameters.

- *Epistemic uncertainty* is caused by the lack of knowledge or model limitations and may be reduced by collecting more information. The predominant source of epistemic uncertainty in wind turbines are assumptions or simplifications in modelling physical phenomena.

Recent studies on the uncertainty assessment of wind turbine models are focused on the aleatory uncertainty of the environmental conditions. In the design of wind turbine drivetrains the uncertainty of environmental parameters such as the wind distribution, turbulence intensity and wave spectra are significant factors due to limitations of the site assessment. Reliability-based design methods are investigated to explicitly address the aleatory
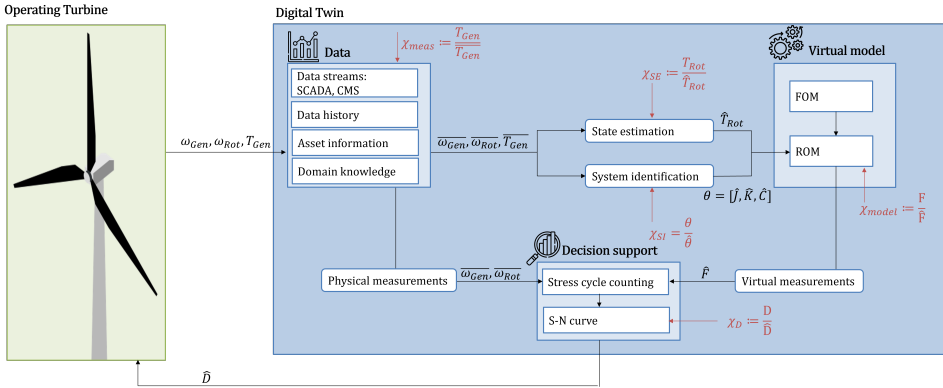
Figure 6.1: Sources of uncertainty (red) in the proposed DT framework for RUL estimation [6].

uncertainty in the design process. Li et al. present a study on reliability-based design optimization of gear profiles and consider the uncertainty of the wind conditions with a joint probability density function of the wind speed and turbulence intensity [81]. In DTs, however, the challenge shifts from aleatory to epistemic uncertainty, since the unknown environmental conditions are continuously measured using state estimation techniques. These state estimation techniques, along with other DT models and algorithms, introduce additional epistemic uncertainty. A systematic assessment of the uncertainty in DTs for fatigue damage monitoring in wind turbine drivetrain is presented by Mehlan et al. [6]. Numerical case studies with the NREL 5 MW and DTU 10 MW reference turbine, as well as field case studies with the DOE 1.5 MW research turbine are investigated. The uncertainty is defined as the ratio of the true and estimated signal and is assessed for each of the DT components: the measurement input, the state estimation methods, the system identification methods, the drivetrain ROM and the fatigue damage model, as illustrated in Fig 6.1. For the uncertainty quantification, log-normal distributions are used, defined as $X = \exp(\mu + \sigma Z)$, where Z is a standard normal variable. Note that the parameters μ and σ differ from the distribution's mean and standard deviation. The findings of this study are summarized in table 6 and discussed in the following sections.

6.1   Measurement uncertainty

Measurement uncertainty is present in the DT's data input due to measurement noise, sensor malfunctions or the limited sensor resolution of SCADA

Table 6.1: Summary of the uncertainty quantification in DTs.

Uncertainty	distribution	μ-parameter	σ-parameter
Measurement χ_{meas}	log-normal	0	0.02...0.75
State estimation χ_{SE}	log-normal	0	0.03...0.07
System identification χ_{SI}	log-normal	$-0.86..0.38$	0.01...0.55
Model χ_{model}	log-normal	$-0.45...0.28$	0.01...0.17

systems that typically store data as 10 min averages. Studies by Gonzalez [28] suggest that a 10 min resolution is ill-suited for load monitoring applications. The generator torque signal, which is foundational for monitoring drivetrain loads, reportedly has the fastest decaying autocorrelation out of all SCADA signals, thus the loss of information is significant when using time averaged signals. Further evidence is reported by Mehlan et al. [4], where the load dynamics and consequently the accumulated fatigue damage in the main and high-speed bearings are underestimated with 10 min SCADA data (Fig. 5.6). 10 min averages are insufficient to observe load dynamics due to the volatile wind speed or characteristic excitations at the rotor or blade passing frequency (1P, 3P,...). For this reason, higher frequency SCADA systems that operate with a sampling frequency of 1 Hz are increasingly adopted by the industry, however, even at this resolution a relevant loss of information is to be expected. The first torsional natural frequency and internal excitation frequencies such as gear meshing frequencies lie well above the Nyquist frequency of 0.5 Hz and thus cannot be observed with 1 Hz signals. The effects of 1 Hz and 10 min averaging of the SCADA generator torque is illustrated in Fig. 6.2. The measurement uncertainty of 10 min data is particularly high in the operational regime below rated wind speed, where the drivetrain torque is highly volatile. With a 1 Hz resolution the measurement uncertainty is significantly reduced and it is apparent that torsional dynamics are captured to a higher degree.

6.2   State estimation uncertainty

The second source of epistemic uncertainty is the lack of knowledge on the aerodynamic loads and the resultant main shaft loads. These are typically not measured directly in commercial wind turbines, but are necessary to define the DT model's boundary conditions. Indirect measurement techniques such as the augmented Kalman filter (AKF) presented in Sec. 4.3.1 can be employed. The AKF fuses uncertain information from model predictions and noisy measurements to produce state estimates of the unknown rotor
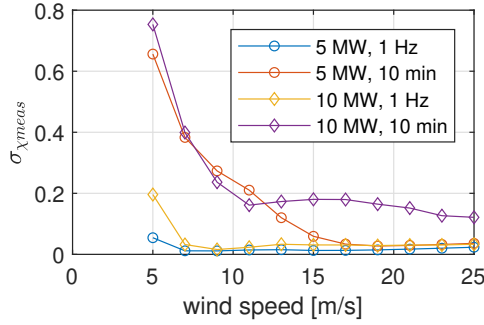
Figure 6.2: σ-parameter of fitted log-normal distributions for measurement uncertainty as a function of wind speed [6]

torque. The uncertainty in the estimated rotor torque is illustrated in Fig. 6.3. The low-frequency (< 1 Hz) torsional dynamics induced by aerodynamic excitations are captured well, whereas higher errors are observed at the high-frequency internal drivetrain dynamics. In the 5 MW numerical case study it is apparent that the first torsional mode at ~ 2 Hz is underpredicted. This has the effect that the load amplitudes and the fatigue damage in drivetrain gears and bearings is underestimated.

6.3 System identification uncertainty

Aleatory uncertainty is present in the system properties including inertia, stiffness and damping values that are required to parameterize the DT model. Not only do the system properties deviate from its design specifications due to the stochastic nature of material properties and manufacturing tolerances, but they also vary across the drivetrain's life cycle as a result of material degradation, component faults, repairs and replacements or environmental factors such as ice accretion. System identification methods, as described in Sec. 4.3.2, are utilized in DTs to continuously estimate the system properties and update the DT model accordingly. The limitations of such system identification methods represent an additional source of epistemic uncertainty in drivetrain DTs. The uncertainty in the parameters generator inertia, rotor inertia, drivetrain stiffness and drivetrain damping is shown in Fig. 6.4. Local maxima in the bias and variance are observed near cut-in (5 m/s) and near rated wind speeds (11-13 m/s), while the minimum is located at cut-out wind speed (25 m/s). It appears that the quasi-stationary conditions in the operational regime above rated wind speeds are conducive to accurate parameter estimation, while the transient dynamics
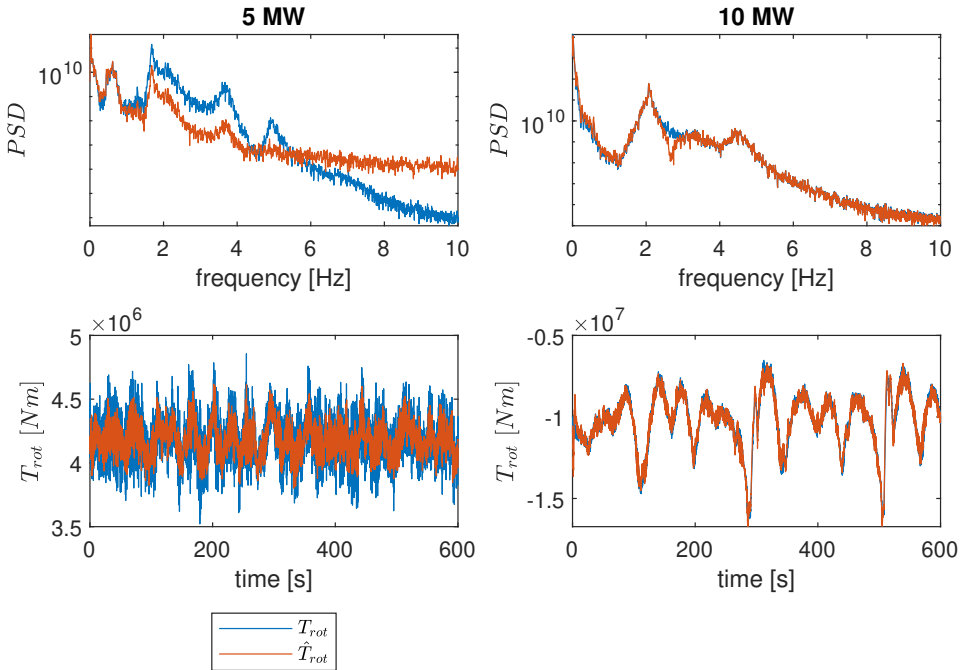
Figure 6.3: True and estimated rotor torque $T_{rot}, \hat{T}_{rot}$ using joint state-input estimation methods [6].

at rated wind speeds due to activation and deactivation of the pitch controller introduce higher estimation errors. The second finding is that the damping parameter estimates have a significantly higher uncertainty than the inertia or stiffness estimates. The damping parameter has under the considered operational conditions, outside of resonance areas, a small influence on the dynamic response. Hence, system identification methods that are based on the measured torsional drivetrain response are more inaccurate in the damping parameter estimation.

6.4 Model uncertainty

The model uncertainty χ_{model} characterizes the uncertainty in the calculated bearing and gear loads due to modelling errors and the complexity reduction of ROMs. ROMs are favourable as DT models due to constrains on the computational costs and on the observability of the model's dynamic states, as discussed in Sec. 4.2.3. Torsional ROMs with one and two DOFs, respectively, are considered in the study by Mehlan et al. [6] and compared
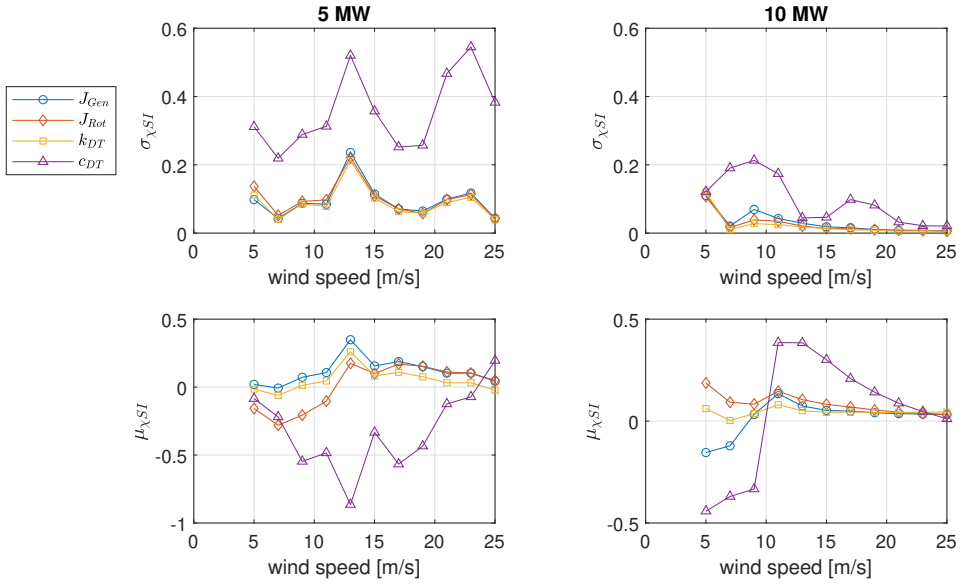
Figure 6.4: μ- and σ-parameter of fitted log-normal distributions for system identification uncertainty as a function of wind speed [6].

to high-fidelity MBS drivetrain models. The discussion of the model uncertainty is divided into a frequency domain analysis (Sec. 6.4.1), the analysis of the model bias (Sec. 6.4.2) and the analysis of the dynamic model error (Sec. 6.4.3).

6.4.1 Characterization of drivetrain dynamics

To identify the sources of model uncertainty one must first understand the complex dynamics of wind turbine drivetrains. The drivetrain dynamics can be generally characterized as dynamic responses to a variety of both internal and external excitations. These excitations can be further differentiated into torque and non-torque loads, i.e lateral forces and bending moments (Tab. 6.2).

External excitations are mainly the result of aerodynamics and are prevalent at low frequencies. Aerodynamic imbalance is present in healthy conditions due to turbulence, wind shear, the vertical wind profile and the rotor axis tilt, or caused by faulty yaw and pitch misalignment. This results in periodic load variations in the rotor torque, thrust and bending moments at the rotor frequency 1P [5]. The tower shadow is also known to induce similar torque and non-torque excitations at the blade passing frequency 3P.

Table 6.2: Type of excitations and characteristic frequencies in wind turbine drivetrains.

	Torque	Non-Torque
External	Aerodynamic imbalance (f_{1P})	Aerodynamic imbalance (f_{1P})
	Tower shadow (f_{3P})	Tower shadow (f_{3P})
	Blade edgewise modes (f_N)	-
	-	Blade flapwise modes (f_N)
	-	Tower bending modes (f_N)
Internal	Planet carriers (f_{plc})	Planet carriers (f_{plc})
	Gear meshing (f_{gm})	Gear meshing (f_{gm})
	-	Bearings (f_{bpf})

The system boundaries of the drivetrain models cut through the rotor hub and the yaw bearing, hence, all structural dynamics of the blades and the tower are considered as external excitations. These are simulated with the global aeroelastic models and the resulting main shaft loads and tower motions are applied as boundary conditions in the drivetrain models. The deformation of the blades with edgewise bending modes translates to torque excitations at the main shaft, while flapwise bending modes cause primarily non-torque excitations. Similarly, fore-aft and side-side tower bending introduces excitations in the thrust and bending moments.

Internal excitations are caused by periodic changes of component stiffnesses and occur generally at much higher frequencies. Gear mesh excitations are a result of the changing number of tooth contacts during one meshing cycle. Gear meshing primarily results in periodic variation of the transmitted torque, but may also have non-torque components in helical gear stages. Bearing excitations are caused by roller elements passing the load zone and result in non-torque excitations at the ball passing frequencies. Further internal excitations are observed at the planet carrier rotational frequencies. Shaft misalignment, mass imbalance or non-torque loading may result in bending of the flexible planet carrier and in skewing of the load distribution between planets, such that each planet bearing experiences periodic load changes during one planet carrier revolution.

  The characteristic excitations are observable in the power spectral densities (PSD) of the bearing loads (Fig 6.5). Shown are the simulated bearing loads at each gear stage for EC8 (17 m/s) using the FOM and the rigid and flexible ROM. The rigid ROM exhibits a good agreement in the lowest frequency range ($< 1~Hz$) governed by wind and wave load excitations, but generally underestimates higher frequency dynamics, as it is only considering rigid body modes. The flexible ROM achieves more accurate load estimates by inclusion of the first torsional drivetrain mode. It is able to
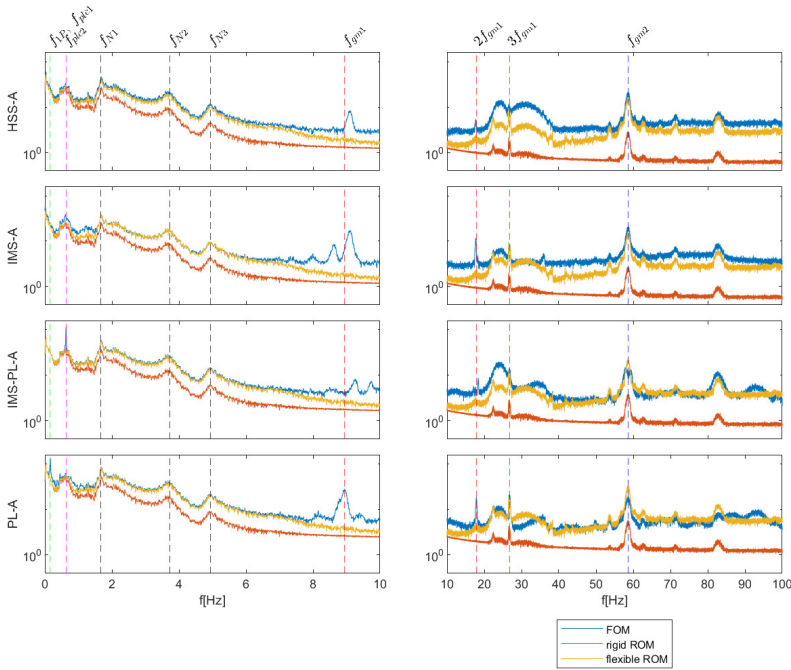
Figure 6.5: Power spectral densities of bearing radial loads simulated with the 5 MW FOM, rigid ROM and flexible ROM [6]

match the peaks of external excitations such as the first collective edgewise blade bending mode (f_{N1}) and higher order modes. The internal dynamics are captured reasonably well with a good agreement in the second stage gear meshing frequency (f_{gm2}). However, some discrepancies remain in the first stage gear meshing frequency peak (f_{gm1}) and in the planet carrier excitations (f_{plc1}, f_{plc2}) visible at the first and second stage planet bearings (PL-A, IMS-PL-A). These suggest the presence of non-torque loads at the planet carriers. The investigated 5 and 10 MW drivetrain models are designed with a four-point main bearing suspension, where it is generally assumed that all non-torque loads of the rotor are fully compensated by the main bearings, but it appears that this is not the case and that non-torque loads partially propagate further downwind into the drivetrain. The results showcase the limitations of torsional ROMs and suggest that a significant source of uncertainty originates from neglecting planetary carrier bending modes.

6.4.2 Model bias

Model biases in drivetrain ROMs can arise due to the model complexity reduction and result in persistent under- or overestimation of the drivetrain loads and fatigue damage that is largely independent of the environmental or operational conditions. The model bias is quantified in a statistical analysis by the μ-parameter of the model uncertainty's fitted log-normal distributions. As shown in Fig. 6.6, the loads at the upwind HSS-A and IMS-A bearings are consistently underestimated, while the loads at the downwind HSS-B and IMS-B bearings are overestimated. One reason for these discrepancies could lie in the physical simplifications of the ROMs, which reduces the gear contact force to a singular vector along the line of action. The load distribution along the gear flank is not considered and thus the bending moments resulting from inhomogeneous load distributions are neglected. Other authors introduce a "twist stiffness" perpendicular to the circumferential gear meshing stiffness to account for the load distribution [82]. However, in this approach the solution requires knowledge of gear and bearing stiffness parameters, which are difficult to determine and validate in practice. Another factor could be the assumption of open-ended shafts that do not allow the transfer of non-torque loads. In the FOMs this is not the case, since the generator coupling at the HSS and the sun-planet gear contact at the IMS allow the transfer of shear forces. These could skew the HSS and IMS bearing loads and further contribute to the model bias.

6.4.3 Dynamic error

The σ-parameter of the of the fitted uncertainty distributions indicates how well the ROMs capture drivetrain dynamics compared the FOM. As depicted in Fig. 6.7, the σ-parameter is positive for all considered cases, which suggests that the ROMs generally underestimate the load dynamics. The uncertainty distributions show similar trends across all bearing and gear types. The highest values are observed near cut-in wind speeds (5 m/s), followed by a steep decline to the global minimum at 9 m/s and a gradual progressive trend towards cut-out wind speeds (25 m/s). Similarly to the high model bias, the high uncertainty at cut-in wind speeds can be attributed to start-up and shut-down effects. The progressive trend can be attributed to aerodynamic non-torque loads transferred from the rotor into the drivetrain. While the torque is controlled to rated conditions above rated wind speed, the non-torque loads, in particular pitch and yaw bending moments, continue to increase with higher wind speeds [4]. These can excite
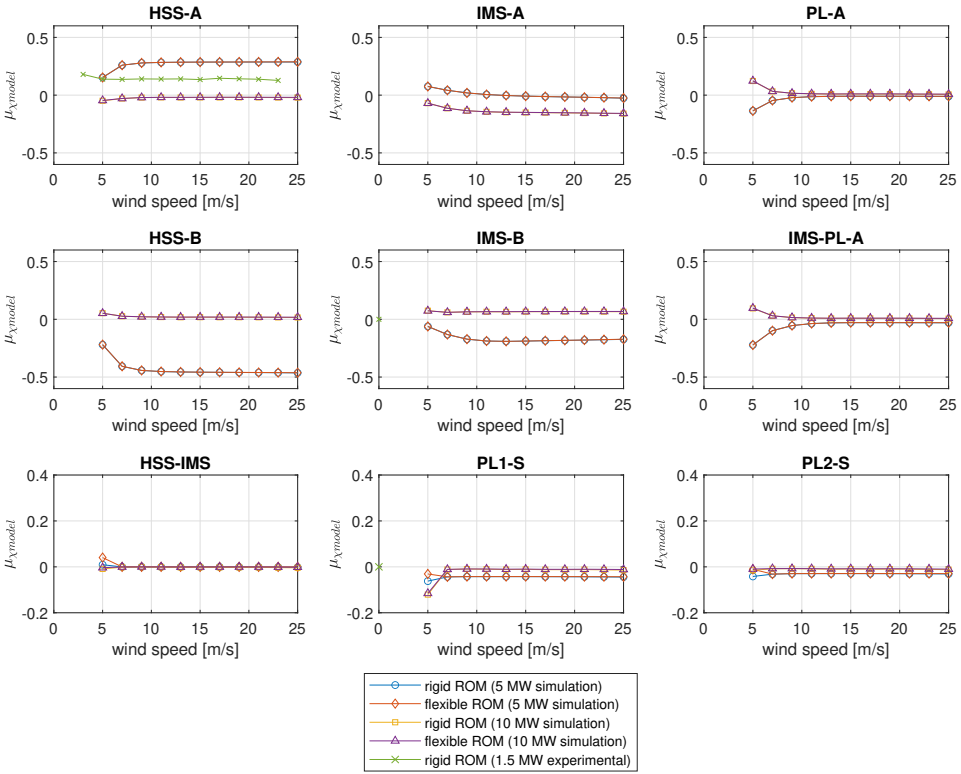
Figure 6.6: μ-parameter of fitted log-normal distributions for model uncertainty as a function of wind speed [6]

non-torsional modes of the drivetrain, in particular planet carrier bending modes (see Sec. 6.4.1), which the purely torsional ROMs do not account for.

The flexible ROM appears to capture the drivetrain dynamics to a much higher degree than the rigid ROM resulting in lower uncertainty values across all bearing and gear locations. The largest differences are observed above rated wind speed, where the excitation of the first drivetrain torsional mode becomes increasingly more energetic. Below rated wind speed the relative improvement is much lower, since in this operational regime the drivetrain dynamics are governed by rigid-body modes.

Figure 6.7: σ-parameter of fitted log-normal distributions for model uncertainty as a function of wind speed [6]

6.5   Fatigue damage uncertainty

The use case of long-term fatigue damage monitoring is considered to assess the impact of the uncertainties in the DT framework. Three scenarios are hereby considered with increasing resolution of SCADA measurements, ranging from 10 min, 1 Hz to 200 Hz. The resolution of 10 min and 1 Hz limits the DT model to the rigid torsional ROM, since the first torsional natural frequency lies above the Nyquist-frequency, while the case of 200 Hz measurements allows the application of the flexible ROM.

The relative error in long-term fatigue damage for each of the scenarios is shown in Fig. 6.8. The long-term fatigue damage is generally underestimated by the DTs due to underestimation of the load amplitudes. It should be noted that the error in the bearing and gear load estimates is amplified by exponentiation with the S-N curve exponent of 10/3 and 6.225, respectively. Hence, the gear fatigue damage error tends to be larger due to the
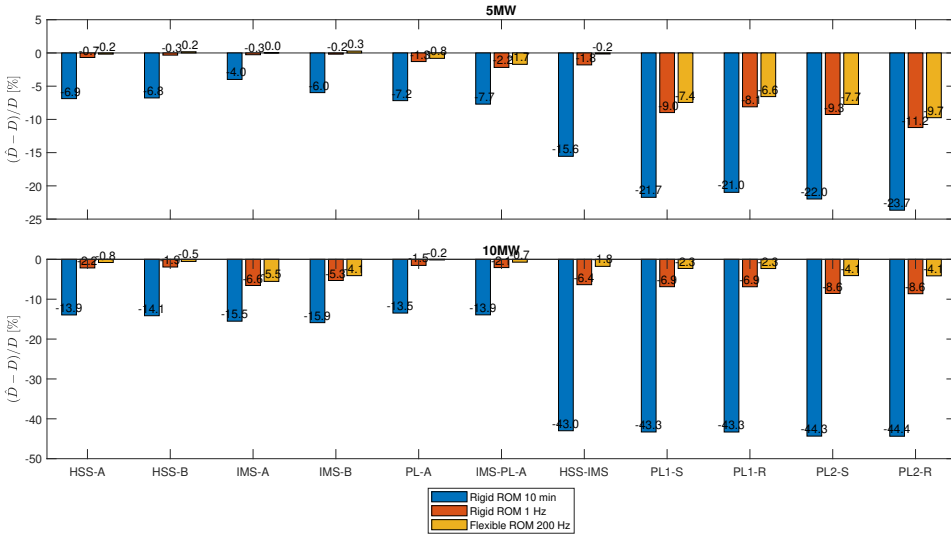
Figure 6.8: Relative error [%] in long-term bearing and gear fatigue damage [6]

larger exponent.

The first scenario with 10 min SCADA data results in relative errors of up to -44.4% in the gear fatigue damage and up to -15.9% in the bearing fatigue damage due to the high measurement uncertainty χ_{meas}. The resolution is insufficient to capture neither the low-frequency aerodynamics nor the high-frequency internal drivetrain dynamics. The second scenario with 1 Hz data yields significantly smaller relative errors limited to -11.2% and -6.6% in the gear and bearing fatigue damage, respectively. In this case, the rigid ROM is able to represent low frequency load variations due to wind and wave excitations, but is limited with respect to higher frequency internal dynamics dynamics. The third scenario with 200 Hz measurements and the two DOF flexible ROM results in only marginally lower fatigue damage errors of -9.7% and -5.5%, which showcase the trade-off of increasing the model fidelity. While the addition of a torsional DOF in the flexible ROM significantly reduces the modelling errors and the model uncertainty χ_{model}, it introduces one unknown variable in the rotor torque and four unknown parameters in the rotor inertia, generator inertia, drivetrain stiffness and damping. The estimation of the rotor torque and the parameters by inverse methods cause additional uncertainty χ_{SE}, χ_{SI}, which partially diminish the benefit of the lower model uncertainty.

Chapter 7

Conclusions

This chapter presents the original contributions of the six appended papers (Sec. 7.1), concluding remarks on each area of the proposed DT framework (Sec. 7.1) and recommendations for future works (Sec. 7.3).

7.1 Original contributions

Each of the six appended papers contribute to different areas of DT through the development of novel methods, numerical and experimental verification and the assessment of errors and uncertainty.

I: **Paper 1**

    (a) A numerically efficient gear contact model was developed for the purpose of real-time load monitoring and evaluated against a state-of-the-art model.

II: **Paper 2 and 3**

    (a) A DT framework was conceptualized and tailored for the application of load monitoring and RUL estimation of offshore wind turbine drivetrains.

    (b) Different state estimation methods for virtual sensing of drivetrain loads including the Kalman filter, a least squares and a quasi-static method were compared in a numerical case study.

    (c) CMS vibration data were found to be beneficial to observe high-frequency internal drivetrain dynamics.

III: **Paper 4**

    (a) The proposed DT framework was applied in a field study of the DOE 1.5 MW research turbine.

    (b) A data-driven approach using machine learning regression models was presented to predict the main shaft loads from SCADA and CMS data.

IV: **Paper 5**

    (a) A novel diagnostic method for rotor imbalance faults, namely pitch misalignment, yaw misalignment and mass imbalance was developed and evaluated in a numerical case study.

    (b) The diagnosis hinges on CMS vibration data that are found to be particularly useful to identify pitch misalignment faults.

V: **Paper 6**

    (a) A systematic uncertainty assessment of the proposed DT framework was conducted with numerical and experimental data.

    (b) The statistical distributions of the epistemic uncertainty in the DT data input, state estimation methods, system identification methods and drivetrain ROMs are analyzed.

    (c) From a uncertainty perspective, the optimal model fidelity for drivetrain DTs is reached with a two DOF torsional ROM.

7.2   Conclusions and discussions

Digital Twin is certainly a divisive topic: by proponents DT is perceived as the key enabling technology that drives the Industry 4.0 and as revolutionary as the advent of AI, by critics DT is seen as a vapid hype, the latest buzzword used by marketing departments. This disparity is rooted in the ambiguity of the DT concept itself, which is not caused by a lack of understanding, but rather left intentionally vague to suit the needs of businesses and researchers, who wish to label their particular approach as DT. In light of the multitude of diverging and sometimes contradicting definitions of DT it is inherently challenging to formulate a concise and objective description of DT. What researchers can agree on is limited to a few characteristics: DT is a virtual representation of a physical asset, it is enabled through the integration of data, simulation models and algorithms, it is developed for the purpose of proving decision support to the user, and it evolves over the

physical asset's entire life cycle. Applying these ideas to the use case of off-shore wind turbine drivetrains there remain many questions on how exactly a drivetrain DT would look like in practice. The first question is concerned with the desired functionality of the DT. A qualitative cost benefit analysis showed that the RUL estimation of drivetrain components is both techno-logically attainable and able to provide tangible economic benefits in terms of reduced O&M expenditures. To facilitate the RUL estimation, a general DT framework was formulated that comprises the three functional elements *DT Data, DT Model* and *DT Decision support*.

7.2.1 Digital Twin Data

The first functional element is *DT Data*, which is a collective term for data that are acquired both in the physical realm through sensor measurements and in the virtual realm through data processing algorithms and simulation models. Real-time data streams from physical sensors are instrumental to inform the DT on the current state of the physical asset. The primary data source for drivetrain DTs are SCADA and CM systems that part of the standard equipment of modern offshore wind turbines. Essential SCADA sensors for drivetrain DTs are the encoders at the main and the generator shaft that measure the respective shaft speeds. The main shaft and gen-erator shaft speed signals contain information on the torsional drivetrain dynamics and through frequency domain methods enable the observation of torsional modes. The SCADA signal of the generator torque is critical for the calculation of local gear and bearing loads, which can be approximated under stationary conditions as torque-proportional. The major limitation of SCADA data is their low temporal resolution, which is typically set to 10 min by industry guidelines and is insufficient to implement dynamic DT models. Studies in paper 4 [4] and paper 6 [6] have shown that the fatigue damage is significantly underestimated using 10 min average SCADA data due to disregarding dynamic load effects.

This motivates the integration of CMS vibration data to inform dynamic drivetrain DTs. CMS accelerometers typically operate with a sampling frequency in the kHz range, which is sufficient to observe high-frequency drivetrain dynamics. Numerical studies in paper 5 [5] also suggest that CMS signals, unlike SCADA signals, can be used to observe non-torsional drivetrain dynamics such as bending modes excited by pitch misalignment faults. However, the integration of CMS data in physics-based DTs remains challenging due the low signal energy at lower frequencies and the complex vibration transfer path through the gearbox housing.

7.2.2   Digital Twin Models

The second functional element is the *DT Model* that contains multiple sub-models to describe the physics at different scales, at the wind turbine level, the drivetrain level, the component level and the material level. For the development of DT models, one can draw from a wealth of experience in different modelling approaches such as aeroelastic, FE and MBS methods, however, the direct transfer of current modelling practices is not fruitful due to the unique development challenges of DT. Current state-of-the-art models are developed for early life cycle stages such as design or R&D and as such are "static" and disconnected models, while DT models for the O&M are "live" models connected to the physical wind turbine. Two additional model requirements arise from these circumstances: the *real-time capability* to simulate states of the operating turbine and the *model maintainability* to ensure the convergence of the simulated and the real behaviour.

The real-time capability requirement sets a limit on the model complexity. The best practice in dynamic drivetrain simulation using high-fidelity MBS models remains below real-time speeds with typical desktop computers, hence, more efficient ROMs are needed for DT. Particularly resource intensive is the simulation of gear meshing dynamics, since the high-frequency state changes in the tooth contacts require a very small numerical step size. The first paper [1] examines this topic and presents a ROM with a simplified gear contact model. In comparison to a state-of-the-art MBS model, the ROM reproduces the spatial load distribution over the gear flank and the temporal load variations to a high accuracy, while increasing the computational speed by about 27%. Despite the improvements in computational efficiency, the simulation of gear meshing dynamics remains below real-time speeds. Therefore, it is likely not feasible to include gear meshing in DT models and thus in the later works it is not considered. In papers 2 and 3 [2, 3] a ROM is developed by linearization of a high-fidelity MBS model, which reduces the complex gear contact function to a linear, elastic connection. In paper 4 [4] a drivetrain ROM is used that assumes rigid transmission of torque and by this assumption neglects all internal drivetrain dynamics. Paper 6 [6] investigates the model uncertainty of the two most likely scenarios: a fully rigid ROM and a flexible ROM with two torsional DOFs. Numerical experiments with a benchmark MBS model demonstrate that the rigid ROM is only able to capture low-frequency rigid body modes that are excited by wind and wave loads. The flexible ROM, on the other hand, is able to represent higher-frequency internal drivetrain dynamics charac-

terised by torsional modes. Remaining modelling errors are identified in the non-torsional drivetrain dynamics such as planet carrier bending modes, however, it appears that these are much less energetic than torsional modes and only contribute marginally to the model uncertainty. The results suggest that two DOF flexible ROMs are a suitable candidate for drivetrain DTs.

The second unique development challenge of DT models, the maintainability requirement, states that the DT must be updated continuously to synchronize its behaviour with the physical wind turbine. The model updating contains two separate tasks, the *state estimation* for synchronizing system states such as kinematic states, forces or stresses and the *system identification* for adjusting model properties such as inertia, stiffness or damping parameters.

Different state estimation methods for drivetrain DTs including a quasi-static method, a least-squares method and the linear Kalman filter are investigated in papers 2 and 3 [2, 3] in a numerical case study. The linear Kalman filter yielded the highest accuracy due to its ability to optimally fuse information from noisy sensor measurements and uncertain model predictions. However, there remained estimation errors by assuming unknown input forces such as the rotor torque as white Gaussian noise. This appears to be an invalid assumption and thus it becomes necessary to employ the augmented Kalman filter variation, as described in paper 6, where the kinematic states and the unknown input forces are estimated simultaneously.

Secondly, it is of importance to continuously update the DT model parameters, since the physical system properties may change over time due to environmental influences, material degradation, faults, part replacements or repairs. Paper 6 presents a system identification approach based on operational modal analysis of SCADA data to estimate the parameters rotor inertia, generator inertia, drivetrain torsional stiffness and damping. The approach could be verified in numerical experiments, however, high levels of uncertainty were observed near cut-in and near rated wind speeds as a result of the transient operational conditions. Hereby, the estimation of the damping parameter was the most inaccurate, as its effect on the drivetrain dynamics outside of resonance areas is minimal.

In addition to computational efficiency considerations, the model maintainability also constrains the fidelity of DT models. With higher model complexity the number of unknown kinematic states and model parameters rises and with it the model uncertainty. In paper 6 an effect of diminishing returns was already observed, when increasing the model fidelity from a rigid one DOF model to a flexible two DOF model. From a perspective of model

uncertainty the optimal model fidelity for drivetrain DTs appears to reached with two DOF torsional models.

7.2.3 Digital Twin Decision Support

DTs are developed for the purpose of improving business outcomes by assisting stakeholders in making key decisions. This functionality is realized with the *DT Decision support*, which provides a range of services and acts as the human-machine interface. According to DNVGL-RP-A204 [18], the decision support can be categorized into five capability levels: descriptive, diagnostic, predictive, prescriptive and autonomous. While SCADA and CM systems already provide such decision support of up to level 3 (predictive), DTs have the potential of elevating the capability level by developing methods with higher autonomy. Fully autonomous DTs are not viable at the current state of technology, nonetheless, DTs can add value by improving upon existing methods at the descriptive, diagnostic and predictive level. The key technology that DTs bring to the table is *virtual sensing*, enabled by the fusion of physical sensor measurements with model predictions. Virtual sensing allows the measurement of local gear and bearing loads, which are difficult to measure directly due geometrical constrains and low lifespans of load sensors. Measuring drivetrain loads is not only useful for condition monitoring purposes, but also for intelligent controllers, improved fault diagnosis or RUL estimation. In this thesis, the RUL estimation based on the measured accumulated fatigue damage and load history is pursued, which corresponds to a capability level of 3 (predictive). Two distinct challenges in virtual load sensing are investigated, the estimation of main bearing loads and the estimation of gearbox loads.

The main bearings are designed to transfer aerodynamic rotor loads into the bedplate and thus it becomes imperative to determine the six load components torque, yaw moment, pitch moment, thrust, shear force and veer force. In paper 4 [4] a data-driven approach is proposed, where SCADA and CMS data features are mapped onto the six rotor load components using machine learning regression models. The results showed a good agreement in the estimated torque and thrust, however, the estimation of the bending moments remains challenging. Unlike torque and thrust, the bending moments do not exhibit a characteristic trend with respect to the wind speed or other SCADA signals, but show a large scatter due to turbulence or yaw misalignment effects. Furthermore, the sensitivity with respect to CMS vibration signals is rather small due to the low signal energy in the frequency range of aerodynamic excitations.

The downwind gears and bearings are governed by the torque and are less affected by non-torque rotor loads, which are mostly compensated by the main bearings. For this reason and due to limitations of the available drivetrain model, the gearbox bearing loads were assumed to be torque-proportional in paper 4 [4]. This approach yields a good first approximation, but disregards many aspects of the drivetrain dynamics such as planet load sharing and excitations from gear meshing and roller bearing contacts. Capturing such high-frequency internal drivetrain dynamics is investigated in papers 2 and 3 [2, 3]. This is realized through the integration of CMS vibration data using Kalman filter or least squares methods and results in a much higher accuracy in the load estimates compared to torque-proportional methods. The main challenge with this approach lies in formulating the physical relationship between vibrations and drivetrain loads, which is difficult based on first principles due to the complex vibration transfer path through the flexible gearbox housing. The assumption of a rigid gearbox housing was taken in these studies, however, the validity of this assumption has not yet been tested in an experimental setting.

Virtual load sensing enables a novel approach to the RUL estimation of drivetrain components. Contrary to current data-driven methods of CM systems that employ a *data-driven* trend analysis on vibration features to predict the RUL, the proposed method is *physics-based* and utilizes established fatigue damage models comprising stress-cycle counting algorithms and S-N curves. Calculating the fatigue damage reserves could prove to be beneficial for predictive maintenance strategies or lifetime extension considerations. It should be noted, however, that many gear and bearing failures are not driven by material fatigue and occur prematurely before the end of the designed fatigue lifetime. Therefore, the physics-based RUL estimation method should be considered as an addition rather than a replacement to existing data-driven methods.

7.3 Recommendations for future works

This thesis is among the first studies exploring the DT concept on the case study of offshore wind turbine drivetrains and there remain several research areas beyond the scope of this thesis. Extensive testing and validation of DT methods in experimental and field settings is recommended to elevate the technology readiness level and work towards commercial adoption. Part of the developed DT methods including the augmented Kalman filter for rotor torque estimation and the system identification methods for model

parameter estimation were only tested and verified in numerical experiments. Limitations in the available dataset of the DOE 1.5 MW research turbine prohibited the experimental validation of such DT methods and thus it remains a research objective for future works.

Further optimization is possible in several areas of the proposed DT framework that could improve the accuracy and robustness of the RUL estimates. Continued research into the integration of CMS vibration data is recommended, which contain valuable information on the high-frequency internal drivetrain dynamics, but are currently underutilized. Accurate models of the relationship between vibration signals and drivetrain loads are needed, either through physics-based modelling of the flexible gearbox housing, or through data-driven approaches.

Reduced order modelling remains a relevant research topic for DT. Research into the efficient modelling of the complex drivetrain dynamics, in particular, non-torsional modes could greatly advance the capability of DT models. Lastly, the RUL estimation could also benefit from more accurate damage models. The presented RUL estimation method was limited to the prediction of fatigue driven failures and could be extended to other failure modes such as slip-induced or overload damages.

References

[1] Felix C. Mehlan, Eilif Pedersen, and Amir R. Nejad. Modelling of wind turbine gear stages for digital twin and real-time virtual sensing using bond graphs. *Journal of Physics: Conference Series*, 2265(032065), 2022.

[2] Felix C. Mehlan, Amir R. Nejad, and Zhen Gao. Estimation of wind turbine gearbox loads for online fatigue monitoring using inverse methods. In *International Conference on Offshore Mechanics and Arctic Engineering*, volume 85192, 2021.

[3] Felix C. Mehlan, Amir R. Nejad, and Zhen Gao. Digital twin based virtual sensor for online fatigue damage monitoring in offshore wind turbine drivetrains. *Journal of Offshore Mechanics and Arctic Engineering*, 144(6), 2022.

[4] Felix C. Mehlan, Jonathan Keller, and Amir R. Nejad. Virtual sensing of wind turbine hub loads and drivetrain fatigue damage. *Forschung im Ingenieurwesen*, 87(1):207–218, 2023.

[5] Felix C. Mehlan and Amir R. Nejad. Rotor imbalance detection and diagnosis in floating wind turbines by means of drivetrain condition monitoring. *Renewable Energy*, 212:70–81, 2023.

[6] Felix C. Mehlan and Amir R. Nejad. On the uncertainty of digital twin models for load monitoring and fatigue assessment in wind turbine drivetrains. *Wind Energy Science*, 2024. [Preprint].

[7] Kasey Panetta. Gartners top 10 technology trends 2017. `https://www.gartner.com/smarterwithgartner/gartners-top-10-technology-trends-2017`, 2016. Accessed 01.02.2024.

[8] Tyler Stehly and Philipp Beiter. 2018 cost of wind energy review. Report NREL/TP-5000-81209, National Renewable Energy Laboratory, 2020.

[9] M. Wilkinson, B. Hendriks, F. Spinato, E. Gomez, H. Bulacio, J. Roca, P. Tavner, Y. Feng, and H. Long. Methodology and results of the reliawind reliability field study. In *European Wind Energy Conference*, Warsaw, Poland, 20-23 April 2010.

[10] A. R. Nejad, J. Keller, Y. Guo, S. Sheng, H. Polinder, S. Watson, J. Dong, Z. Qin, A. Ebrahimi, R. Schelenz, F. Gutiérrez Guzmán, D. Cornel, R. Golafshan, G. Jacobs, B. Blockmans, J. Bosmans, B. Pluymers, J. Carroll, S. Koukoura, E. Hart, A. McDonald, A. Natarajan, J. Torsvik, F. K. Moghadam, P.-J. Daems, T. Verstraeten, C. Peeters, and J. Helsen. Wind turbine drivetrains: state-of-the-art technologies and future development trends. *Wind Energy Science*, 7(1):387–411, 2022.

[11] M. Grieves. Digital twin: manufacturing excellence through virtual factory replication. white paper, 2014.

[12] Michael Grieves and John Vickers. *Digital Twin: Mitigating Unpredictable, Undesirable Emergent Behavior in Complex Systems*, pages 85–113. Springer International Publishing, Cham, 2017.

[13] Adil Rasheed, Omer San, and Trond Kvamsdal. Digital twin: Values, challenges and enablers from a modeling perspective. *IEEE Access*, 8:21980–22012, 2020.

[14] Obafemi O. Olatunji, Paul A. Adedeji, Nkosinathi Madushele, and Tien-Chien Jen. Overview of digital twin technology in wind turbine fault diagnosis and condition monitoring. In *2021 IEEE 12th International Conference on Mechanical and Intelligent Manufacturing Technologies (ICMIMT)*, 2021.

[15] Itxaro Errandonea, Sergio Beltrán, and Saioa Arrizabalaga. Digital twin for maintenance: A literature review. *Computers in Industry*, 123, 2020.

[16] Mengnan Liu, Shuiliang Fang, Huiyue Dong, and Cunzhi Xu. Review of digital twin about concepts, technologies, and industrial applications. *Journal of Manufacturing Systems*, 58:346–361, 2021.

[17] Concetta Semeraro, Mario Lezoche, Hervé Panetto, and Michele Dassisti. Digital twin paradigm: A systematic literature review. *Computers in Industry*, 130, 2021.

[18] Det Norske Veritas. DNVGL-RP-A204: Qualification and assurance of digital twins, 2020.

[19] Werner Kritzinger, Matthias Karner, Georg Traar, Jan Henjes, and Wilfried Sihn. Digital twin in manufacturing: A categorical literature review and classification. *IFAC-PapersOnLine*, 51(11):1016–1022, 2018.

[20] Fei Tao, Meng Zhang, Yushan Liu, and A. Y. C. Nee. Digital twin driven prognostics and health management for complex equipment. *CIRP Annals*, 67:169–172, 2018.

[21] Mengmeng Wang, Chengye Wang, Anna Hnydiuk-Stefan, Shizhe Feng, Incecik Atilla, and Zhixiong Li. Recent progress on reliability analysis of offshore wind turbine support structures considering digital twin solutions. *Ocean Engineering*, 232, 2021.

[22] Minh-Chau Dinh, Manh-Tuan Ngo, Changhyun Kim, Seok Ju Lee, In-Keun Yu, and Minwon Park. Implementation of digital twin-assisted condition monitoring and fault diagnosis for wind turbines. In *2023 12th International Conference on Renewable Energy Research and Applications (ICRERA)*, pages 146–150. IEEE, 2023.

[23] Muhammad Fahim, Vishal Sharma, Tuan-Vu Cao, Berk Canberk, and Trung Q. Duong. Machine learning-based digital twin for predictive modeling in wind turbines. *IEEE Access*, 10:14184–14194, 2022.

[24] Sigrid S. Johansen and Amir R. Nejad. On digital twin condition monitoring approach for drivetrains in marine application. In *Proceedings of the ASME 2019 38th International Conference on Ocean, Offshore and Arctic Engineering*, volume 10, pages 146–150. ASME, 2019.

[25] Michaela Ibrion, Nicola Paltrinieri, and Amir R. Nejad. On risk of digital twin implementation in marine industry: Learning from aviation industry. *Journal of Physics: Conference Series*, 1357(012009), 2019.

[26] Jeroen D. M. De Kooning, Kurt Stockman, Jeroen De Maeyer, Antonio Jarquin-Laguna, and Lieven Vandevelde. Digital twins for wind energy

conversion systems: A literature review of potential modelling techniques focused on model fidelity and computational load. *Processes*, 9(12), 2021.

[27] Amir R. Pedersen Eilif Torsvik, Jone; Nejad. Main bearings in large offshore wind turbines: development trends, design and analysis requirements. *Journal of Physics: Conference Series*, 1037(042020), 2018.

[28] Elena Gonzalez, Bruce Stephen, David Infield, and Julio J. Melero. Using high-frequency SCADA data for wind turbine performance monitoring: A sensitivity study. *Renewable Energy*, 131:841–853, 2019.

[29] International Electrotechnical Commission. IEC 61400-25-2: Wind turbines - Part 25-2: Communications for monitoring and control of wind power plants - Information models, 2015.

[30] International Organization for Standardization. ISO10816-21: Mechanical vibration — Evaluation of machine vibration by measurements on non-rotating parts — Part 21: Horizontal axis wind turbines with gearbox, 2015.

[31] Rory Morrison, Xiaolei Liu, and Zi Lin. Anomaly detection in wind turbine scada data for power curve cleaning. *Renewable Energy*, 184:473–486, 2022.

[32] R. B. Randall. *Vibration based condition monitoring: Industrial, Aerospace and Automotive Applications*. Wiley & Sons Ltd, 2010.

[33] Y. Lu, J. Tang, and H. Luo. Wind turbine gearbox fault detection using multiple sensors with features level data fusion. *Journal of Engineering for Gas Turbines and Power*, 134(4), 2012.

[34] Yubin Pan, Rongjing Hong, Jie Chen, Jaskaran Singh, and Xiaodong Jia. Performance degradation assessment of a wind turbine gearbox based on multi-sensor data fusion. *Mechanism and Machine Theory*, 137:509–526, 2019.

[35] Dong Yang, Hui Li, Yaogang Hu, Jie Zhao, Hongwei Xiao, and Yongsen Lan. Vibration condition monitoring system for wind turbine bearings based on noise suppression with multi-point data fusion. *Renewable Energy*, 92:104–116, 2016.

[36] Yi Guo, J. Keller, W. La Cava, J. Austin, A. R. Nejad, C. Halse, L. Bastard, and J. Helsen. Recommendations on model fidelity for wind

turbine gearbox simulations. In *Conference for Wind Power Drives (CWD)*, number NREL/CP-5000-63444, 2015.

[37] James Moyne, Yassine Qamsane, Efe C. Balta, Ilya Kovalenko, John Faris, Kira Barton, and Dawn M. Tilbury. A requirements driven digital twin framework: Specification and opportunities. *IEEE Access*, 8:107781–107801, 2020.

[38] Elisa Negri, Luca Fumagalli, and Marco Macchi. A review of the roles of digital twin in cps-based production systems. *Procedia Manufacturing*, 11:939–948, 2017.

[39] Yi Guo, Shuangwen Sheng, Caleb Phillips, Jonathan Keller, Paul Veers, and Lindy Williams. A methodology for reliability assessment and prognosis of bearing axial cracking in wind turbine gearboxes. *Renewable and Sustainable Energy Reviews*, 127, 2020.

[40] B. Schlecht, T. Schulze, and J. Demtröder. Simulation of torsional vibrations or multibody simulation - which technique does the wind power industry need for solving the present-day problems? In *Proceedings of the ASME 2003 International Design Engineering Technical Conferences and Computers and Information in Engineering Conference. Volume 4: 9th International Power Transmission and Gearing Conference, Parts A and B*, pages 325–332. ASME, September 2-6 2003.

[41] J. Peeters, D. Vandepitte, and P. Sas. Structural analysis of a wind turbine and its drive train using the flexible multibody simulation technique. In *Proceedings of ISMA*, pages 3665–3680, 2006.

[42] Jan Helsen, Frederik Vanhollebeke, Ben Marrant, Dirk Vandepitte, and Wim Desmet. Multibody modelling of varying complexity for modal behaviour analysis of wind turbine gearboxes. *Renewable Energy*, 36(11):3098–3113, 2011.

[43] Y. Guo, J. Keller, and Y. Moan, T. Xing. Model fidelity study of dynamic transient loads in a wind turbine gearbox. Technical Report NREL/CP-5000-58414, National Renewable Energy Laboratory, 2013.

[44] Amir Rasekhi Nejad, Zhen Gao, and Torgeir Moan. On long-term fatigue damage and reliability analysis of gears under wind loads in offshore wind turbine drivetrains. *International Journal of Fatigue*, 61:116–128, 2014.

[45] Emmanuel Branlard, Dylan Giardina, and Cameron S. D. Brown. Augmented kalman filter with a reduced mechanical model to estimate tower loads on a land-based wind turbine: a step towards digital-twin simulations. *Wind Energy Science*, 5(3):1155–1167, 2020.

[46] Baher Azzam, Ralf Schelenz, Björn Roscher, Abdul Baseer, and Georg Jacobs. Development of a wind turbine gearbox virtual load sensor using multibody simulation and artificial neural networks. *Forschung im Ingenieurwesen*, 85(2):241–250, 2021.

[47] D. Bosse A. Loriemi, G. Jacobs. Estimation of rotor and main bearing loads using artificial neural networks. *Journal of Physics: Conference Series*, 2151(012002), 2022.

[48] International Electrotechnical Commission. IEC 61400-1: Wind energy generation systems - Part 1: Design requirements, 2019.

[49] Nevena Perišić, Poul Henning Kirkegaard, and Bo Juul Pedersen. Cost-effective shaft torque observer for condition monitoring of wind turbines. *Wind Energy*, pages 1–19, 2013.

[50] Mahdi Ghane, Amir Rasekhi Nejad, Mogens Blanke, Zhen Gao, and Torgeir Moan. Condition monitoring of spar-type floating wind turbine drivetrain using statistical fault diagnosis. *Wind Energy*, 21(7):575–589, 2018.

[51] Farid K. Moghadam, Geraldo F. de S. Rebouças, and Amir R. Nejad. Digital twin modeling for predictive maintenance of gearboxes in floating offshore wind turbine drivetrains. *Forschung im Ingenieurwesen*, 85(2):273–286, 2021.

[52] R. Santos and J. van Dam. Mechanical loads test report for the u.s. department of energy 1.5-megawatt wind turbine. Report NREL/TP-5000-63679, National Renewable Energy Laboratory, 2015.

[53] J. Jonkman, S. Butterfield, W. Musial, and G. Scott. Definition of a 5-MW reference wind turbine for offshore system development. Report NREL/TP-500-38060, National Renewable Energy Laboratory (NREL), 2009.

[54] Christian Bak, Frederik Zahle, Robert Bitsche, Taeseong Kim, Anders Yde, Lars Christian Henriksen, Morten Hartvig Hansen, José Pedro Blasques, Albergaria Amaral, Mac Gaunaa, and

Anand Natarajan. The DTU 10-MW reference wind tur-
bine. `https://backend.orbit.dtu.dk/ws/portalfiles/portal/`
`55645274/The_DTU_10MW_Reference_Turbine_Christian_Bak.pdf`,
2013. Accessed: 01.02.2024.

[55] Roger Bergua Archeli, Jon Keller, Olle Bankestrom, Mark Dunn,
Yi Guo, Alicia Key, and Emma Young. Up-tower investigation of main
bearing cage slip and loads. Report NREL/TP-5000-81240, National
Renewable Energy Laboratory, 2021.

[56] Yi Guo, Olle Bankestrom, Roger Bergua, Jonathan Keller, and Mark
Dunn. Investigation of main bearing operating conditions in a three-
point mount wind turbine drivetrain. *Forschung im Ingenieurwesen*,
85(2):405–415, 2021.

[57] Amir Rasekhi Nejad, Yi Guo, Zhen Gao, and Torgeir Moan. Devel-
opment of a 5 mw reference gearbox for offshore wind turbines. *Wind
Energy*, 19(6):1089–1106, 2016.

[58] Shuaishuai Wang, Amir R. Nejad, and Torgeir Moan. On design, mod-
elling, and analysis of a 10-mw medium-speed drivetrain for offshore
wind turbines. *Wind Energy*, 23(4):1099–1117, 2020.

[59] International Electrotechnical Commission. IEC 61400-4: Wind tur-
bines, Part 4: standard for design and specification of gearboxes, 2012.

[60] Shuaishuai Wang, Amir R. Nejad, Erin E. Bachynski, and Torgeir
Moan. Effects of bedplate flexibility on drivetrain dynamics: Case
study of a 10 mw spar type floating wind turbine. *Renewable Energy*,
161:808–824, 2020.

[61] Scott Dana Paula Doubrawa Emmanuel Branlard, Jason Jonkman. A
digital twin based on openfast linearizations for real-time load and fa-
tigue estimation of landbased turbines. *Journal of Physics: Conference
Series*, 1618(022030), 2020.

[62] Jelle Bosmans, Matteo Kirchner, Jan Croes, and Wim Desmet. Vali-
dation of a wind turbine gearbox strain simulation model in service to
virtual sensing. *Forschung im Ingenieurwesen*, 87(1):107–117, 2023.

[63] Hamed Habibi, Ian Howard, and Silvio Simani. Reliability improve-
ment of wind turbine power generation using model-based fault detec-
tion and fault tolerant control: A review. *Renewable Energy*, 135:877–
896, 2019.

[64] Matthias Saathoff, Malo Rosemeier, Thorsten Kleinselbeck, and Bente Rathmann. Effect of individual blade pitch angle misalignment on the remaining useful life of wind turbines. *Wind Energy Science*, 6(5):1079–1087, 2021.

[65] Josh Kusnick, Douglas E. Adams, and D. Todd Griffith. Wind turbine rotor imbalance detection using nacelle and blade measurements. *Wind Energy*, 18(2):267–276, 2015.

[66] Jenny Niebsch and Ramlau. Ronny. Simultaneous estimation of mass and aerodynamic rotor imbalances for wind turbines. *Journal of Mathematics in Industry*, 4(12), 2014.

[67] James Carroll, Sofia Koukoura, Alasdair McDonald, Anastasis Charalambous, Stephan Weiss, and Stephen McArthur. Wind turbine gearbox failure and remaining useful life prediction using machine learning techniques. *Wind Energy*, 22(3):360–375, 2019.

[68] F. Elasha, S. Shanbr, X. Li, and D. Mba. Prognosis of a wind turbine gearbox bearing using supervised machine learning. *Sensors (Basel)*, 19(14), 2019.

[69] Y. A. Yucesan and F. A. C. Viana. Wind turbine main bearing fatigue life estimation with physicsinformed neural networks. In *Annual conference of the PHM society*, volume 11, pages 1–14, 2019.

[70] A. Encalada-Davila, B. Puruncajas, C. Tutiven, and Y. Vidal. Wind turbine main bearing fault prognosis based solely on scada data. *Sensors (Basel)*, 21(6), 2021.

[71] Y.; Sheng S.; Phillips C.; Williams L. Desai, A.; Guo. Prognosis of wind turbine gearbox bearing failures using scada and modeled data. *Annual conference of the prognostics and health management society*, 2020.

[72] Yi Guo and Jonathan Keller. Validation of combined analytical methods to predict slip in cylindrical roller bearings. *Tribology International*, 148, 2020.

[73] Kelly Tartt, Amir R. Nejad, Abbas Kazemi-Amiri, and Alasdair McDonald. On lifetime extension of wind turbine drivetrains. In *Proceedings of the ASME 2021 40th International Conference on Ocean, Offshore and Arctic Engineering*, volume 85192, 2021.

[74] International Organization for Standardization. ISO 6336: Calculation of load capacity of spur and helical gears, 2006.

[75] International Organization for Standardization. ISO 281: Rolling bearings — Dynamic load ratings and rating life, 2007.

[76] Andreas W. Momber, Torben Möller, Daniel Langenkämper, Tim W. Nattkemper, and Daniel Brün. A digital twin concept for the prescriptive maintenance of protective coating systems on wind turbine structures. *Wind Engineering*, 46(3):949–971, 2021.

[77] Bernhard Strack, Jana Frank, Volker Stich, and Florian Pfau. Prescriptive maintenance for onshore wind turbines. In *ESSN*, pages 2701–6277, 2021.

[78] W. Dheelibun Remigius and Anand Natarajan. Identification of wind turbine main-shaft torsional loads from high-frequency SCADA (supervisory control and data acquisition) measurements using an inverse-problem approach. *Wind Energy Science*, 6(6):1401–1412, 2021.

[79] M.; Spepudelva M.; Davies P. Sivalingam, K.; Spring. A review and methodology development for remaining useful life prediction of offshore fixed and floating wind turbine power converter with digital twin technology perspective. In *2018 2nd international conference on green energy and applications (ICGEA)*, pages 197–204. IEEE, 2018.

[80] Adam Thelen, Xiaoge Zhang, Olga Fink, Yan Lu, Sayan Ghosh, Byeng D. Youn, Michael D. Todd, Sankaran Mahadevan, Chao Hu, and Zhen Hu. A comprehensive review of digital twin—part 2: roles of uncertainty quantification and optimization, a battery digital twin, and perspectives. *Structural and Multidisciplinary Optimization*, 66(1), 2022.

[81] Huaxia Li, Hyunkyoo Cho, Hiroyuki Sugiyama, K. K. Choi, and Nicholas J. Gaul. Reliability-based design optimization of wind turbine drivetrain with integrated multibody gear dynamics simulation considering wind load uncertainty. *Structural and Multidisciplinary Optimization*, 56(1):183–201, 2017.

[82] Tugan Eritenel and Robert G. Parker. Three-dimensional nonlinear vibration of gear pairs. *Journal of Sound and Vibration*, 331(15):3628–3648, 2012.

Appendix A

Appended papers

A.1   Paper 1

PAPER • OPEN ACCESS

Modelling of wind turbine gear stages for Digital Twin and real-time virtual sensing using bond graphs

To cite this article: F C Mehlan *et al* 2022 *J. Phys.: Conf. Ser.* **2265** 032065
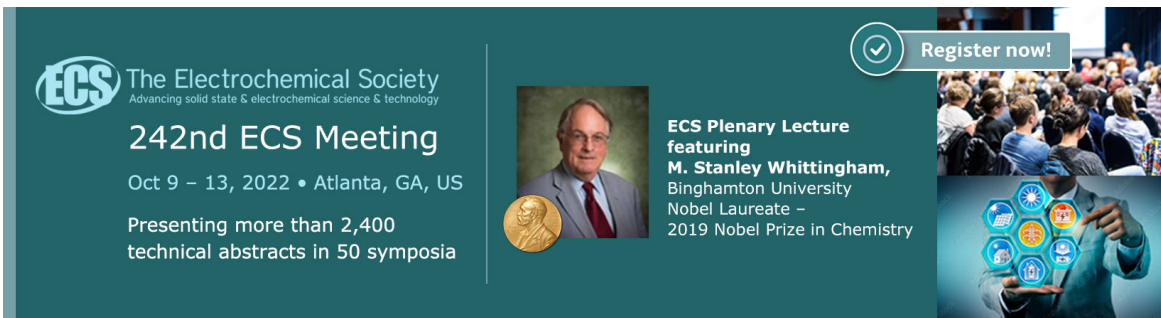
View the article online for updates and enhancements.

Modelling of wind turbine gear stages for Digital Twin and real-time virtual sensing using bond graphs

F C Mehlan, E Pedersen, A R Nejad

Department of Marine Technology (IMT), Norwegian University of Science and Technology (NTNU), Trondheim, Norway

E-mail: `felix.c.mehlan@ntnu.no`

Abstract. In this paper a wind turbine high-speed gear stage model is developed for the purpose of real-time virtual sensing of gear and bearing loads in a Digital Twin framework. The model requirements are: accurate representation of gear meshing and shaft dynamics, high computational efficiency and compatibility with other Digital Twin components, such as physical sensors signals and virtual sensing methods. State equations are derived analytically using the Bond Graph method and implemented in the software 20sim for simulation. As opposed to standard multi-body simulation (MBS) software, 20sim allows for higher flexibility in implementing interfaces to other Digital Twin components. The model fidelity is close to state-of-the-art MBS models considering 6 DOF body motion, however a simplified gear contact formulation is used, which assumes ideal kinematic meshing. Nonetheless, the Bond Graph model is able to accurately reproduce the inhomogeneous load distribution over the tooth flank, as well as the cyclic compression and decompression for each meshing period. The results suggest that the presented model is capable of monitoring fatigue loads in gear contacts and bearings in a Digital Twin framework.

1. Introduction

Digital Twin (DT) is an emerging technology fueled by advances in information and communication technologies with many proposed applications in prognostics and health management (PHM). Especially the offshore wind industry could benefit from DT solutions to increase reliability and availability, and reduce unscheduled, expensive down times [1]. DT can be defined as a 'virtual representation of a physical asset enabled through data and simulators for real-time prediction, optimization, monitoring, controlling, and improved decision making' [2]. We envision a DT framework loosely based on the model of Tao et al. [3] to facilitate predictive maintenance (PdM) strategies in wind turbine drivetrains. The central components of the DT framework are the *Virtual model*, *Data* and *Decision support* (Fig. 1).

Data that can be leveraged in wind turbines include process, operational or organizational data, e.g. sensor measurements of the drivetrain condition monitoring system (CMS) and the Supervisory Control and Data Acquisition (SCADA) system. The *virtual model* is a virtual representation, that experiences the same environment as its physical counterpart and evolves over its life cycle. To ensure that the virtual and physical wind turbines are synchronized at all times, the virtual model is supplied with real-time, physical measurements and updated using system identification [4] and state estimation techniques [5]. *Decision support* is a collective term for services that the DT provides to assist in the operator's maintenance or control decisions.
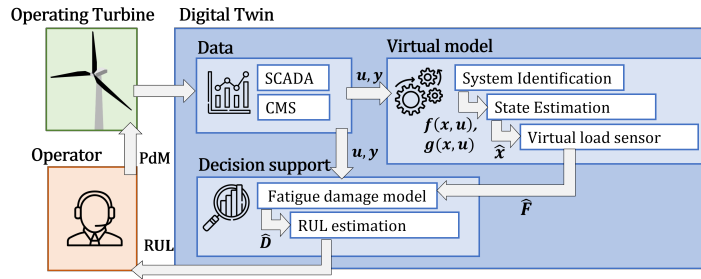
Figure 1. Digital Twin framework for predictive maintenance of wind turbine drivetrains.

Focus of our research is online monitoring of gear and bearing loads through virtual sensors and subsequent estimation of the remaining useful life (RUL) using fatigue damage models.

This study is concerned with developing a dynamic simulation model of a wind turbine high-speed gear stage to fit such a DT framework. The most essential model requirements are formulated based on Moyne et al. [6]:

- *Accuracy* in the representation of gear meshing and shaft dynamics
- *Computational efficiency* to enable real-time simulation
- *Interoperability* to interact with other DT-components, such as physical sensor signals and virtual sensing methods
- *Maintainability* to update model properties and match physical changes, such as material degradation

The task of balancing model accuracy and computational speed involves finding the optimal fidelity. Guidelines on modelling of wind turbine drivetrains are reported by Guo et al. [7], where recommendations on the degrees of freedom (DoF) for each moving drivetrain component, consideration of body flexibility and the fidelity of gear contact and bearing formulations are given, which concludes to a relatively high model fidelity. Hence, state-of-the-art multi-body simulation (MBS) models of wind turbine drivetrains including virtual test benches [8] and academic reference models [9, 10] are generally not capable of real-time simulation. Developing efficient Reduced Order Models (ROM) is identified as one of the major challenges in Predictive Maintenance and Condition Monitoring [11]. ROM are constructed either as data-driven surrogate models [12] or by physical simplification. In this study a simplified gear contact formulation is developed.

Secondly, to satisfy the requirements of interoperability with other DT-components, appropriate interfaces must be implemented. For instance, the virtual load sensor in the decision support component must be supplied with a mathematical description of the virtual model, which is elaborated further in Sec. 2.4. However, commercial MBS software including SIMPACK [13] and ADAMS only support the export of linearized models (state-space representation), which is insufficient to represent the highly non-linear dynamics of drivetrains [5].

Similar shortcomings of MBS software are identified concerning the model's maintainability. The DT paradigm requires the virtual model to evolve along its physical counterpart and be updated to match physical changes, such as material fatigue or component faults. While parametric updating is possible in MBS software, it is challenging to model gear and bearing faults due to restricted access to the respective component subroutines.

In this study a wind turbine gear stage model is developed with respect to the above mentioned
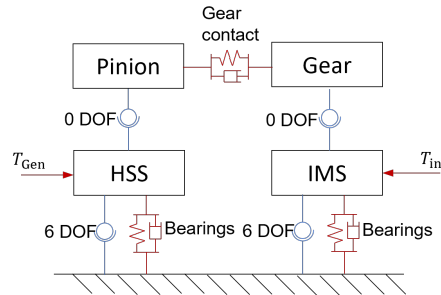
Figure 2. Gear stage model topology

DT requirements. The Bond Graph (BG) method, a graphical, energy-based modelling language [14], is employed to construct the model and derive state equations.

2. Methodology

2.1. Bond graph theory

BG is an energy-based, graphical modelling language that bridges the gap between purely equation-based modelling approaches and diagram techniques such as electrical circuit diagrams[14]. The universal currency of BG are the multi-physical effort $e(t)$ and flow $f(t)$ variables, which multiply to the instantaneous power $P(t)$. In the mechanical domain, for example, the energy variables are force and velocity, but the BG method also extends to other physical domains. The system is divided into components according to their capability of energy storage, dissipation or transmission. Kinetic and potential energy storage is represented by I- an C-elements, energy dissipation by R-elements and lossless energy transformation by TF-elements. The components are interconnected with power bonds representing the energy exchange. Power bonds are denoted with half arrows and define both the sign of the power by the arrow orientation and the causality of effort and flow variables with an orthogonal stroke. Causality determines whether variables are considered as input or output in the respective BG elements. The BG method is selected as modelling approach for the following reasons: First, it provides a systematic approach to deriving state equations for numerical simulation, while maintaining the physical structure of the system. Second, BG is not limited to any physical domain. Hence, other wind turbines components, for instance generator and converter, could be developed and integrated in the same framework. Third, the causality of state variables is visible in the BG structure, which eases the identification and prevention of algebraic loops that are detrimental to computational speed.

2.2. Reference model

The BG model in this study is based on a reference model of the NREL 5MW baseline wind turbine and respective gearbox [9] in terms of parameterization and topology. The reference model implemented in MBS software SIMPACK satisfies general guidelines on model fidelity [7] and is the basis for validation of the BG model's dynamics (Sec. 3). Parameter values of both models are listed in Tabs. 1 and 2, and the overall topology is shown in Fig. 2. The scope is limited to the high-speed stage, a helical gear stage with the bodies of intermediate speed shaft (IMS), high-speed shaft (HSS), gear wheel and pinion. Both gear shafts are considered rigid bodies with six degrees of freedom (DOF). Each shaft is supported by one cylindrical roller bearing (-A) and two tapered roller bearings (-B,-C), which are modelled as spring-damper
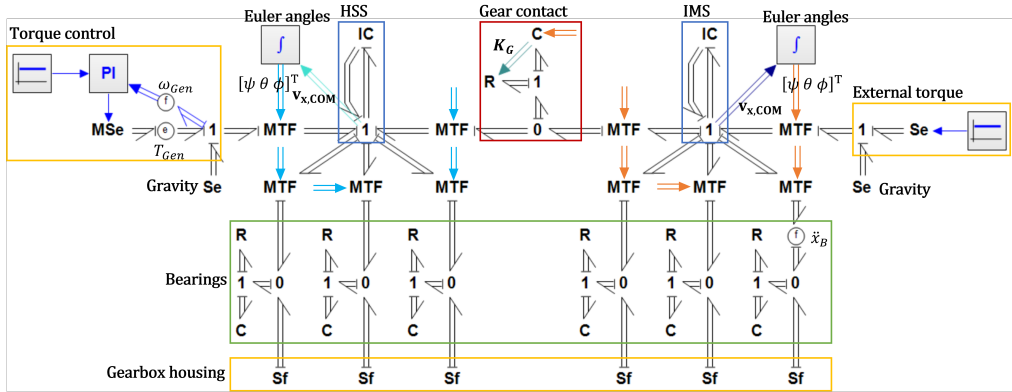
Figure 3. Bond graph structure of high-speed gear stage model

connections to the static gearbox housing. Gear wheel and pinion are rigidly connected to their respective shafts (0 DOF). The elasticity of gear bodies and teeth is lumped into a spring-damper element with time-variant mesh stiffness connecting pinion and gear wheel. External loads T_{in} are applied on the IMS, while a PI-controller sets the desired speed of the HSS with the counter-acting generator torque T_{Gen}.

The key difference between BG and reference model lies in the gear contact formulation, which in SIMPACK is realized with the built-in force subroutine 225. The subroutine incorporates an algorithm to find the 3D contact points and respective surface normal vectors of gear tooth pairings. The contact forces are then determined as a function of relative contact displacement. Hence, the SIMPACK subroutine is able to capture non-linear effects of backlash, micro geometry (profile modifications) and misalignment of shaft axes. Contact stiffness is load-dependent and accounts for gear wheel body deformation stiffnesses, tooth bending and shear stiffnesses, and Hertzian contact stiffness using the 'Weber/ Banaschek' approach. In comparison, the BG model employs a simplified contact formulation, which assumes ideal, kinematic meshing, as presented in Sec. 2.3.4.

2.3. Bond graph model
In the following sections the BG model of a wind turbine high-speed gear stage is presented consisting of submodels of the shafts (Sec. 2.3.2), bearings (Sec. 2.3.3) and helical gear contact (Sec. 2.3.4). The underlying model equations of each submodel given and the graphical representation as BG structure is shown in Fig. 3.

2.3.1. Coordinate systems and transformations
The BG model relies on different coordinate systems in the body fixed and inertial frame. The formulation of shaft inertia is most convenient with body-fixed velocities $\mathbf{v_x} \in \mathbb{R}^{6\times1}$ comprising of lateral and angular velocities (Eq. 1), while the boundary conditions align with the inertial frame

$$\mathbf{v_x} = [\mathbf{v_1}, \mathbf{v_2}]^T = [v_x, v_y, v_z, \omega_x, \omega_y, \omega_z]^T. \tag{1}$$

Transformation from body-fixed $\mathbf{v_x}$ to inertial velocities $\mathbf{v_X}$ is realized by three consecutive rotations around the Euler angles ψ (yaw), θ (pitch), ϕ (roll) [15]

$$\mathbf{v_X} = \mathbf{m}_{\psi\theta\phi} \cdot \mathbf{v_x}, \quad \mathbf{m}_{\psi\theta\phi} = \begin{bmatrix} \mathbf{R}_\psi\mathbf{R}_\theta\mathbf{R}_\phi & \mathbf{0} \\ \mathbf{0} & \mathbf{R}_\psi\mathbf{R}_\theta\mathbf{R}_\phi. \end{bmatrix}, \tag{2}$$

Table 1. Geometric parameters.

Variable	Symbol	Unit	Value	
			IMS	HSS
Mass	m	[kg]	5059.26	350.89
Moments of inertia	$J_{xx}/J_{yy}/J_{zz}$	[kg · m^2]	994.1 / 723.7 / 723.7	4.6 / 11.1 / 11.1
Number of teeth	z	[-]	95	24
Normal modul	m_n	[mm]	14	
Axis distance	a	[mm]	861	
Gear tooth width	b	[mm]	360	
Operating pitch radius	r_w	[mm]	687.4	173.6
Base radius	r_b	[mm]	633.4	160.0
Tip radius	r_a	[mm]	697.7	190.3
Pressure angle	α	[deg]	20	
Helix angle	β	[deg]	10	
Operating pressure angle	α_w	[deg]	22.86	
Transversal operating pressure angle	α_{wt}	[deg]	22.54	
Number of gear tooth slices	N	[-]	11	
Gear contact stiffness	k_G	[N/m]	$4.69 \cdot 10^8$	
Slope of gear contact stiffness function	$\partial K/\partial \phi^i$	[N/m/deg]	116	
Gear damping to stiffness ratio	ξ	[s]	10^{-3}	

with the individual rotational matrices

$$\mathbf{R}_\psi = \begin{bmatrix} \cos\psi & -\sin\psi & 0 \\ \sin\psi & \cos\psi & 0 \\ 0 & 0 & 1 \end{bmatrix}, \quad \mathbf{R}_\theta = \begin{bmatrix} \cos\theta & 0 & \sin\theta \\ 0 & 1 & 0 \\ -\sin\theta & 0 & \cos\theta \end{bmatrix}, \quad \mathbf{R}_\phi = \begin{bmatrix} 1 & 0 & 0 \\ 0 & \cos\phi & -\sin\phi \\ 0 & \sin\phi & \cos\phi \end{bmatrix}. \quad (3)$$

The time-variant Euler angles are found by integration of body-fixed angular velocities

$$\dot{\theta} = \cos(\phi)\omega_y - \sin(\phi)\omega_z,$$
$$\dot{\psi} = \frac{\sin(\phi)}{\cos(\theta)}\omega_y + \frac{\cos(\phi)}{\cos(\theta)}\omega_z, \quad (4)$$
$$\dot{\phi} = \omega_x + \sin(\phi)\tan(\theta)\omega_y + \cos(\phi)\tan(\theta)\omega_z$$

In addition to rotational Euler transformations, lateral transformations are necessary, for instance to relate velocities at bearings with center of mass velocities. The lateral change of coordinate systems from a point A to B is expressed as

$$\mathbf{v_B} = \mathbf{m_{A\to B}} \cdot \mathbf{v_A}, \quad \mathbf{m_{A\to B}} = \begin{bmatrix} \mathbf{I} & -[\delta_{\mathbf{A\to B}}]_\times \\ \mathbf{0} & \mathbf{I} \end{bmatrix}. \quad (5)$$

The notation $[\cdot]_\times$ is used for compact matrix representation of the cross product between two vectors ($[\mathbf{a}]_\times \mathbf{b} = \mathbf{a} \times \mathbf{b}$). The rotational and lateral transformation matrices $\mathbf{m}_{\psi\theta\phi}$, $\mathbf{m_{A\to B}}$ are orthogonal and thus power-conserving, which are represented in bond graph terminology by transformer elements (TF). In the case of Euler transformation, the transformation matrix is time-variant and a function of the continuously changing Euler angles. Hence, a modulated transformer element (MTF) is used here (Fig 3).

Table 2. Bearing parameters.

Variable	Symbol	Unit	Value					
			IMS-A	IMS-B	IMS-C	HSS-A	HSS-B	HSS-C
Bearing stiffness	K_{xx}	$[\mathrm{N \cdot m^{-1}}]$	0	$7.41 \cdot 10^7$	$7.87 \cdot 10^7$	$1.26 \cdot 10^8$	$6.70 \cdot 10^7$	$7.93 \cdot 10^7$
	K_{yy}	$[\mathrm{N \cdot m^{-1}}]$	$6.12 \cdot 10^7$	$5.17 \cdot 10^8$	$7.37 \cdot 10^8$	$8.21 \cdot 10^8$	$8.09 \cdot 10^8$	$1.04 \cdot 10^9$
	K_{zz}	$[\mathrm{N \cdot m^{-1}}]$	$1.16 \cdot 10^9$	$4.84 \cdot 10^8$	$3.26 \cdot 10^8$	$8.21 \cdot 10^8$	$1.33 \cdot 10^8$	$7.29 \cdot 10^7$
Bearing damping	D_{xx}	$[\mathrm{N \cdot m^{-1} \cdot s}]$			$4.53 \cdot 10^4$			
	D_{yy}	$[\mathrm{N \cdot m^{-1} \cdot s}]$			$4.20 \cdot 10^4$			
	D_{yy}	$[\mathrm{N \cdot m^{-1} \cdot s}]$			$3.06 \cdot 10^4$			
Axial position	x_B	[mm]	-230	230	260	-230	230	260

2.3.2. Shaft model Each gear shaft is considered a rigid body in six DOF. The equations of motion (EOM) governing rigid bodies are derived with the Langrange-Hamiltonian method, which yields second order differential equations for each shaft [15]

$$\mathbf{M\dot{v}} + \mathbf{C(v)v} = \tau, \tag{6}$$

where $\mathbf{M} \in \mathbb{R}^{6 \times 6}$ denotes the mass matrix, $\mathbf{C(v)} \in \mathbb{R}^{6 \times 6}$ the coriolis matrix, $\mathbf{v} \in \mathbb{R}^{6 \times 1}$ the velocity vector and $\tau \in \mathbb{R}^{6 \times 1}$ the vector of external forces. It is convenient to align the coordinate system with the body-fixed, principal axes at the center of mass ($\mathbf{v} = \mathbf{v_{x,COM}}$) to eliminate off-diagonal elements in the mass matrix, which then becomes

$$\mathbf{M} = \begin{bmatrix} m\mathbf{I} & \mathbf{0} \\ \mathbf{0} & \mathbf{J} \end{bmatrix}, \quad \mathbf{J} = \begin{bmatrix} J_{xx} & 0 & 0 \\ 0 & J_{yy} & 0 \\ 0 & 0 & J_{zz} \end{bmatrix}, \tag{7}$$

where m represents the body mass, $\mathbf{J}$ the moments of inertia and $\mathbf{I} \in \mathbb{R}^{3 \times 3}$ denotes the identity matrix. The coriolis matrix can then be expressed with Eq. 1 as

$$\mathbf{C} = \begin{bmatrix} \mathbf{0} & -m[\mathbf{v_1}]_\times \\ -m[\mathbf{v_1}]_\times & -[\mathbf{Jv_2}]_\times \end{bmatrix}. \tag{8}$$

The coupled, second order EOM (Eq. 6) can be reformulated as a set of first order differential equations (Lagrange-Hamiltonian form) with the unknowns of generalized displacements $\mathbf{q}$ and momenta $\mathbf{p}$

$$\begin{aligned} \dot{\mathbf{q}} &= \mathbf{M^{-1}p} \\ \dot{\mathbf{p}} &= -\mathbf{C(\dot{q})\dot{q}} + \tau \end{aligned} \tag{9}$$

This relationship is represented with an IC-field in the BG model, highlighted in blue in Fig. 3. Velocities $\dot{\mathbf{q}}$ are determined according to the constitutive laws of a classical I-field (Eq. 9, line 1). Then, gyroscopic forces $\mathbf{e'} = \dot{\mathbf{p}}$ are computed as a function of given velocities in the fashion of a C-field (Eq. 9, line 2) [16].

2.3.3. Bearing model The gear shafts are connected with bearings to the gearbox housing, which is considered static in the inertial frame ($\mathbf{v_0} = \mathbf{0}$). Supporting bearing forces are determined by relative velocities $\Delta\mathbf{v_{X,B}}$ given by local shaft velocities $\mathbf{v_{X,B}}$ at the respective bearing seats

$$\Delta\mathbf{v_{X,B}} = \mathbf{v_{X,B}} - \mathbf{v_0} = \mathbf{v_{X,B}} \tag{10}$$

The local, inertial shaft velocities $\mathbf{v_{X,B}}$ are related to body-fixed velocities $\mathbf{v_{x,COM}}$ at the center of mass through consecutive Euler and lateral transformations

$$\mathbf{v_{X,B}} = \mathbf{m}_{\psi\theta\phi}\mathbf{m_{COM\to B}} \cdot \mathbf{v_{x,COM}}, \quad \delta_{\mathbf{COM\to B}} = \begin{bmatrix} x_B \\ 0 \\ 0 \end{bmatrix}. \tag{11}$$

Bearings are considered parallel spring-dampers with diagonal stiffness matrices $\mathbf{K_B}$ and damping matrices $\mathbf{D_B}$. The elastic force component $\mathbf{f_{B,K}}$ is proportional to the relative displacement, which is obtained by integration of relative velocities

$$\mathbf{f_{B,K}} = \mathbf{K_B} \int \Delta\mathbf{v_{X,B}} \, \mathrm{dt}, \quad \mathbf{K_B} = \begin{bmatrix} K_{xx} & 0 & 0 \\ 0 & K_{yy} & 0 \\ 0 & 0 & K_{zz} \end{bmatrix}. \tag{12}$$

The damping force component $\mathbf{f_{B,D}}$ is expressed as follows

$$\mathbf{f_{B,D}} = \mathbf{D_B} \cdot \Delta\mathbf{v_{X,B}} , \quad \mathbf{D_B} = \begin{bmatrix} D_{xx} & 0 & 0 \\ 0 & D_{yy} & 0 \\ 0 & 0 & D_{zz} \end{bmatrix}. \tag{13}$$

Bearings are represented with a combination of C- and R-elements for their energy storing (elastic) and the dissipative (damping) capabilities, as shown in green in Fig. 3.

2.3.4. Helical gear contact model The helical gear contact is modelled with a parallel spring-damper connection with a time-variant contact stiffness. The tooth flanks are evenly discretized in N slices with superscript i to account for the uneven load distribution. The contact forces are calculated for each slice separately and are a function of relative, normal velocities $\Delta v_{\mathrm{X,CPn}}^{\mathrm{i}}$ in the teeth contact points CP

$$\Delta v_{\mathrm{X,CPn}}^{\mathrm{i}} = (v_{\mathrm{X,CPn}}^{\mathrm{i}})_{\mathrm{HSS}} - (v_{\mathrm{X,CPn}}^{\mathrm{i}})_{\mathrm{IMS}}. \tag{14}$$

To obtain the velocity component normal to the tooth's surface, the assumption of ideal, kinematic meshing is taken. Under kinematic meshing the normal surface vector and thus the contact force vector is aligned with the line of action at all times. The line of action connects the base circles of gear and pinion and can be expressed in terms of the operating pressure angle α_w and the helix angle β. The normal velocity component $v_{\mathrm{X,CPn}}^{\mathrm{i}}$ is then given by

$$\begin{aligned} v_{\mathrm{X,CPn}}^{\mathrm{i}} &= \mathbf{m_{CPn}} \, \mathbf{v_{X,CP}^{i}}, \\ \mathbf{m_{CPn}} &= \begin{bmatrix} -\sin(\beta) & \sin(\alpha_w)\cos(\beta) & \cos(\alpha_w)\cos(\beta) & 0 & 0 & 0 \end{bmatrix}. \end{aligned} \tag{15}$$

The inertial velocities in the contact points $\mathbf{v_{X,CP}^{i}}$ are related to body-fixed, COM velocities $\mathbf{v_{x,COM}}$ through lateral and Euler transformations

$$\mathbf{v_{X,CP}^{i}} = \mathbf{m}_{\psi\theta\phi}\mathbf{m_{COM\to CP}^{i}} \cdot \mathbf{v_{x,COM}}. \tag{16}$$

The contact points are defined in the center of each tooth slice with radial distance of r_w (operating pitch radius) to the COM. The relative distance $\delta_{\mathbf{COM\to CP}}^{\mathbf{i}}$ for the lateral transformation can be expressed as follows

$$\delta_{\mathbf{COM\to CP}}^{\mathbf{i}} = \begin{bmatrix} x_{CP}^{i} \\ y_{CP} \\ z_{CP} \end{bmatrix} = \begin{bmatrix} (i - \frac{N+1}{2})\frac{b}{N} \\ -\cos(\phi)r_w \\ \sin(\phi)r_w \end{bmatrix}. \tag{17}$$
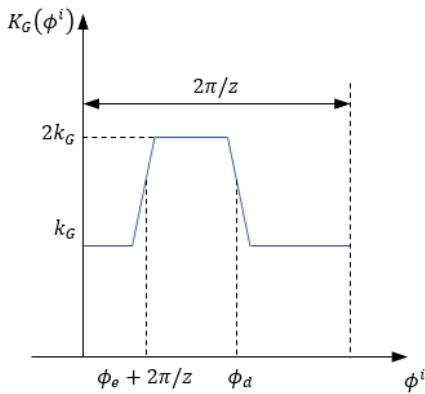
Figure 4. Gear contact stiffness as a function of gear slice angular position ϕ^i and periodical for each meshing period $2\pi/z_1$.
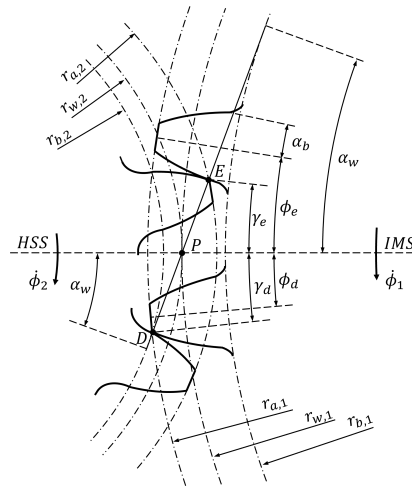
Figure 5. Geometric relations defining the angular position ϕ_e, ϕ_d of the IMS when tooth pairings engage and disengage.

The elastic gear contact forces $f_{\mathrm{G,K}}^{\mathrm{i}}$ are a function of the relative contact displacements obtained by integration and time-variant contact stiffness

$$f_{\mathrm{G,K}}^{\mathrm{i}} = K_G^i(\phi^i) \int \Delta v_{\mathrm{X,CPn}}^{\mathrm{i}} \, \mathrm{dt}. \tag{18}$$

Additionally, stiffness proportional damping is considered in the gear contacts. The damping forces $f_{\mathrm{G,D}}^{\mathrm{i}}$ are a function of relative contact velocities, where the damping coefficient is $D_G^i(\phi^i)$ is assumed proportional to the contact stiffness

$$\begin{aligned} f_{\mathrm{G,D}}^{\mathrm{i}} &= D_G^i(\phi^i)\Delta v_{\mathrm{X,CPn}}^{\mathrm{i}} \\ D_G^i(\phi^i) &= \xi K_G^i(\phi^i). \end{aligned} \tag{19}$$

The formulation of the contact stiffness takes the periodical change in the number of actively engaging teeth into account. For this model with a transverse contact ratio of 1.48 either one or two teeth are in contact simultaneously. As depicted in Fig. 4 the contact stiffness is formulated as a piece-wise linear function of the gear angle ϕ^i switching from a value of k_G, when one tooth is in contact, to $2k_G$, when two teeth are in contact. For improved numerical properties the discrete step in contact stiffness is smoothed with a linear function. The gear angles ϕ^i of each slice are shifted relative to the shaft Euler angle ϕ_1 due to the helical shaping of gear teeth

$$\phi^i = \left(\phi_1 - \frac{x_{CP}^i}{r_w}\tan(\beta)\right) \mathrm{mod} \; \frac{2\pi}{z_1}. \tag{20}$$

The gear angles ϕ_e, ϕ_d, at which the contact stiffness function changes values are defined by the engaging and disengaging contact points E and P, as shown in Fig. 5. Under the assumption of ideal, kinematic meshing, E and P are positioned in the intersections of tip radii and the line of action. Using geometric relations, ϕ_e, ϕ_d can be derived as a function of only time-invariant,

geometric parameters

$$
\begin{aligned}
\phi_{e,d} &= \tan(\gamma_{e,d} + \alpha_w) - \alpha_w - \alpha_b, \\
\alpha_b &= \frac{\pi}{2z_1} + \tan(\alpha_w) - \alpha_w, \\
\sin(\gamma_e) &= -\frac{\cos(\alpha_w)\sqrt{r_{a,1}^2 - r_{b,1}^2} - \sin(\alpha_w)r_{w,1}}{r_{a,1}}, \\
\sin(\gamma_d) &= \frac{\cos(\alpha_w)\sqrt{r_{a,2}^2 - r_{b,2}^2} - \sin(\alpha_w)r_{w,2}}{r_{a,1}}.
\end{aligned}
\tag{21}
$$

where $\gamma_{e,d}$ are auxiliary parameters, α_w denotes the operating pressure angle, α_b the half angle of tooth thickness on the base circle, z_1 the tooth number and r_a, r_b, r_w the tip, base and pitch radii respectively.

Analogously to the bearing model, the gear contact model comprises of an energy storing C-element and dissipative R-element representing stiffness and damping forces, as indicated in red in Fig. 3.

2.3.5. Boundary conditions The gear stage is under load from external sources such as aerodynamic excitations. In this model all external loads are applied at the IMS's center of mass, while a PI-controller provides the counter-acting generator torque to reach the desired HSS speed. External loads and generator torque constitute force boundary condition and are represented by effort source elements (Se) in the bond graph structure (Fig. 3, yellow). Furthermore, the model assumption of a static gearbox housing sets a zero velocity boundary condition, which is represented with flow source elements (Sf).

2.4. Model Integration in Digital Twin Framework

This section provides an outlook on the integration of the presented BG model in the envisioned DT framework, shown in Fig. 1. State estimation methods such as the Extended Kalman Filter (EKF) are employed to synchronize the virtual model with the physical turbine on the basis of physical sensor measurements. These require a mathematical description of the virtual model in the form of state-transition function $\mathbf{f}(\mathbf{x}, \mathbf{u})$, and measurement function $\mathbf{g}(\mathbf{x}, \mathbf{u})$

$$
\begin{aligned}
\dot{\mathbf{x}} &= \mathbf{f}(\mathbf{x}, \mathbf{u}), \\
\mathbf{y} &= \mathbf{g}(\mathbf{x}, \mathbf{u}).
\end{aligned}
\tag{22}
$$

The independent state variables $\mathbf{x}$ can be identified from the BG structure (Fig. 1) as the momenta $\mathbf{p_1}, \mathbf{p_2}$ of each shaft, displacements of bearings $\mathbf{q_B}$ and gear slices $\mathbf{q_G}$ and euler angles $[\psi, \theta, \phi]_{1,2}^T$

$$
\mathbf{x} = [\mathbf{p_1}, \mathbf{p_2}, \mathbf{q_B}, \mathbf{q_G}, \psi_1, \theta_1, \phi_1, \psi_2, \theta_2, \phi_2,]^T.
\tag{23}
$$

The measurement variables $\mathbf{y}$ include the HSS rotational speed ω_{gen} and the generator torque T_{gen} from SCADA data, as well as bearing accelerations $\ddot{x}_B$ from CMS vibration data. In the virtual model the interface to these physical measurements is represented with effort (e) and flow (f) sensors (Fig. 1)

$$
\mathbf{y} = [\omega_{gen}, T_{gen}, \ddot{x}_B]^T.
\tag{24}
$$

The state equations (Eq. 22) can be derived analytically using the systematic procedure of the BG method or automatically generated with the BG software 20sim [17]. 20sim supports the export as executable MATLAB functions, which can be referenced by an EKF implemented in
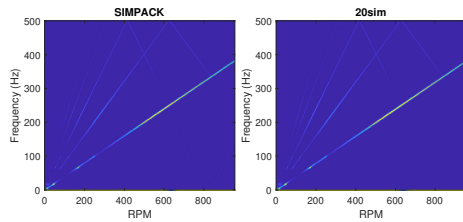
Figure 6. Run-up spectrogram of angular velocity ω_X of IMS. l.: reference model (SIMPACK), r.: bond graph model (20sim)
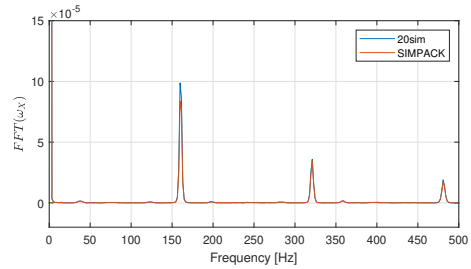
Figure 7. Slice of run-up spectrogram (Fig. 6) at 400 rpm.

MATLAB. The EKF is extended to incorporate virtual sensors for estimation of gear and bearing loads by augmenting the state vector similar to the approach of Branlard et al. [18]. Preliminary studies show compatibility of the BG model with the proposed virtual sensing method, however analysis and verification is part of future work.

3. Results and Discussion

3.1. Model validation

Validation of the BG model is conducted with the reference model implemented in SIMPACK (Sec. 2.2) under two basic load cases: run-up from standstill to rated speed $n_{gen} = 1165.94$ rpm and a stationary load case at rated speed. Under each load case the gear stage is loaded with rated torque of $T_{in} = 162.1$ kNm at the IMS.

The torsional system dynamics are evaluated in the run-up load case using the angular velocity ω_X of the IMS. As evident from the spectogram depicted in Fig. 6, the bond graph model displays dynamic behaviour similar to the reference model. The bright line indicates excitation from gear meshing at the mesh frequency $f_{mesh} = n_{gen}/60 \cdot z_{HSS}$, while the darker lines show higher harmonics ($2 \times f_{mesh}, 3 \times f_{mesh}$). The decreasing line segments can be attributed to aliasing effects, since the higher harmonics exceed the Nyquist frequency of 500 Hz here. Resonance can be observed at particular shaft speeds where the gear meshing frequency coincides with the system's natural frequencies. As shown in Tab. 3 the natural frequencies of both models match with a relative error of less than 2%. A slice through the spectrogram at a shaft speed of 400 rpm also shows a good agreement in the amplitudes of ω_X.

The stationary load case allows a closer look at time series of gear contact forces and bearing forces. Shown in Fig. 8 are gear contact forces at the left edge slice 1, center slice 6 and right edge slice 11. The bond graph model is able to accurately reproduce the inhomogeneous load distribution over the tooth flank, as well as the cyclic compression and decompression for each meshing period. The mean values of gear forces agree well across all slices with a maximum error of 5.6%, while the amplitudes appear to be overestimated by up to 22.0% at the left edge slice.

Axial and radial forces of bearing HSS-A are selected as representatives for bearing behaviour (Fig. 9). Bearing forces have a large stationary component due to supporting a stationary gear stage torque and an oscillatory component induced by gear meshing. The error in mean value of forces is below 2.0% for all gear stage bearings, however force amplitudes differ by up to 37.1%.

Table 3. First five non-trivial eigen frequency pairs of bond graph model (20sim) and reference model (SIMPACK).

f_i [Hz]	$f_{4/5}$	$f_{6/7}$	$f_{8/9}$	$f_{10/11}$	$f_{12/13}$	$f_{14/15}$
SIMPACK	5.98	19.14	27.56	67.05	98.93	105.5
20sim	6.06	19.13	27.66	67.16	98.74	106.5
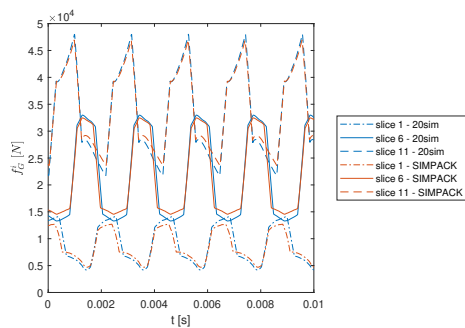
Figure 8. Gear contact forces at rated speed and torque for bond graph model (20sim) and reference model (SIMPACK).
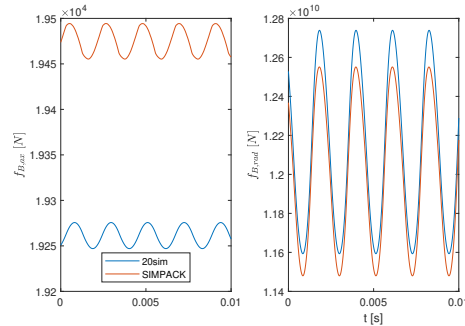
Figure 9. Axial and radial bearing forces at HSS-A at rated speed and torque for bond graph model (20sim) and reference model (SIMPACK).

3.2. Computational speed

Since the BG model is intended for real-time simulation in DT, it is important to consider the computational efficiency. A real-time factor of $t_{CPU}/t_{real} = 3.0$ is measured with the BG model and $t_{CPU}/t_{real} = 4.1$ with the reference model in SIMPACK, when simulating the stationary load case on a desktop computer. The explicit solver Runge-Kutta 4 is used for simulation of the BG model, while for the reference model the default SIMPACK solver SODASRT2, an implicit backward differential solver is used. Admittedly, real-time capability is not reached with the BG model, however an improvement in computational speed can be observed. Further investigations on optimizing the computational performance are planned. One numerically advantageous property of the BG model is the absence of any algebraic loops. Algebraic loops are circular dependencies of state variables and result in constraint equations of the form $\mathbf{0} = \mathbf{h}(\mathbf{x}, \mathbf{u})$, which have to be solved iteratively for each time step adding to the computational cost. In the BG model algebraic loops are avoided by modelling gear contact forces explicitly as a function of body velocities (Eq. 18). The gear contact model in SIMPACK on the other hand is formulated implicitly, as the position of tooth contacts and the resultant force vector orientation are calculated iteratively

4. Conclusion

In this paper a wind turbine high-speed gear stage model for the purpose of for real-time virtual sensing of gear and bearing loads in a DT framework was presented. The model was developed with the energy-based BG method and implemented in the software 20sim for numerical integration. The BG method provides a systematic approach to derive state equations, which are required for the state estimating methods employed in virtual sensors. The model fidelity is close to state-of-the-art MBS models considering 6 DOF rigid body motion,

however a simplified gear contact formulation with the assumption of ideal, kinematic meshing is used. Nonetheless, comparative simulations with a with a reference model implemented in MBS software SIMPACK show good agreement in gear contact and bearing loads in a stationary and a run-up load case. Errors in mean value are below 5.6% and 2.0% for gear and bearing forces respectively. Force amplitudes are overestimated by the BG model with maximum errors of 22.0% and 37.1%. The BG model shows favourable computational performance with a real-time factor of 3.0 as opposed to 4.1. This is likely a result of the explicit gear contact formulation, which avoids computationally expensive iterations to find contact displacements. The results suggest that the developed model is capable and suitable for the proposed virtual load sensing approach. Further investigations are planned on the analysis and verification of this approach.

Acknowledgments

References

[1] Stehly T and Beiter P 2020 2018 cost of wind energy review Report National Renewable Energy Laboratory
[2] Rasheed A, San O and Kvamsdal T 2020 *IEEE Access* **8** 21980–22012 ISSN 2169-3536
[3] Tao F, Zhang M, Liu Y and Nee A Y C 2018 *CIRP Annals* **67** 169–172 ISSN 00078506
[4] Moghadam F K and Nejad A R 2020 *Journal of Physics: Conference Series* **1618**
[5] Mehlan F C, Nejad A R and Gao Z *International Conference on Ocean, Offshore and Arctic Engineering* **9**
[6] Moyne J, Qamsane Y, Balta E C, Kovalenko I, Faris J, Barton K and Tilbury D M 2020 *IEEE Access* **8** 107781–107801 ISSN 2169-3536
[7] Guo Y, Keller J, Cava W L, Austin J, Nejad A R, Halse C, Bastard L and Helsen J 2015 *Conference for Wind Power Drives (CWD)*
[8] Matzke Dand Schelenz R, Reisch S, Roscher B, Jacobs G; Theling J, Schroers M, Loepenhaus C and Brecher C 2018 *Journal of Physics: Conference Series* **1037**
[9] Nejad A R, Guo Y, Gao Z and Moan T 2016 *Wind Energy* **19** 1089–1106 ISSN 10954244
[10] Wang S, Nejad A R and Moan T 2020 *Wind Energy* **23** 1099–1117 ISSN 1095-4244 1099-1824
[11] Nejad A R, Keller J, Guo Y, Sheng S, Polinder H, Watson S, Dong J, Qin Z, Ebrahimi A, Schelenz R, Guzmán F G, Cornel D, Golafshan R, Jacobs G, Blockmans B, Bosmans J, Pluymers B, Carroll J, Koukoura S, Hart E, McDonald A, Natarajan A, Torsvik J, Moghadam F K, Daems P J, Verstraeten T, Peeters C, and Helsen J 2022 *Wind Energ. Sci.* **7**(1)
[12] Li X and Zhang W 2022 *Renewable Energy* **185** 932–944 ISSN 09601481
[13] URL https://www.3ds.com/products-services/simulia/products/multibody-system-simulation/
[14] Karnopp D C, Margolis D L and Rosenberg R C 1990 *Modeling, Simulation, and Control of Mechatronic Systems* System dynamics (John Wiley Sons, Inc)
[15] Pedersen E 2009 *Mathematical and Computer Modelling of Dynamical Systems* **15** 337–352 ISSN 1387-3954 1744-5051
[16] Karnopp D 1992 *Journal of the Franklin Institute* **329** 65–75 ISSN 0016-0032
[17] URL https://www.20sim.com/
[18] Branlard E, Giardina D and Brown C S D 2020 *Wind Energy Science* **5** 1155–1167 ISSN 2366-7451

A.2 Paper 2

OMAE2021-62181

ESTIMATION OF WIND TURBINE GEARBOX LOADS FOR ONLINE FATIGUE MONITORING USING INVERSE METHODS

Felix C. Mehlan,[*] **Amir R. Nejad, Zhen Gao**
Department of Marine Technology (IMT)
Norwegian University of Science and Technology (NTNU)
Trondheim, 7491
Norway
felix.c.mehlan@ntnu.no

ABSTRACT

In this article a novel approach for the estimation of wind turbine gearbox loads with the purpose of online fatigue damage monitoring is presented. The proposed method employs a Digital Twin framework and aims at continuous estimation of the dynamic states based on CMS vibration data and generator torque measurements from SCADA data. With knowledge of the dynamic states local loads at gearbox bearings are easily determined and fatigue models are be applied to track the accumulation of fatigue damage. A case study using simulation measurements from a high-fidelity gearbox model is conducted to evaluate the proposed method. Estimated loads at the considered IMS and HSS bearings show moderate to high correlation ($R = 0.50 - 0.96$) to measurements, as lower frequency internal dynamics are not fully captured. The estimated fatigue damage differs by $5-15$ % from measurements.

INTRODUCTION

Recent trends show an increased shift towards offshore wind turbine installations due to the higher energy yield and fewer issues with land displacement and noise [1]. However, offshore sites face additional reliability challenges. Replacement or repair of components is expensive and time-consuming due to difficulties accessing the site and dependency on good weather conditions. Thus, unscheduled down times as a result of component failure can lead to high operational and maintenance expenditures (O&M). For offshore wind turbines the O&M expenditures can reach 34 % of the levelised cost of energy (LCOE) [2]. A major contributor to the O&M expenditures is the gearbox with a failure rate of 0.1 - 0.15/year and average downtimes of 6 days per failure [3, 4]. Early detection of gearbox faults is realized by fault prognosis methods based on sensor input from Supervisory Control and Data Analysis (SCADA) and Condition Monitoring Systems (CMS). Commercial fault prognosis systems analyse trends of health indicators extracted from sensor data, that correlate with the damage progression [5]. This purely data-driven approach has its strengths in detecting patterns indicating faulty behaviour from large, complex data sets without the need of modelling the system's behaviour. The drawbacks of data-driven methods often lie in the limited availability of historical failure data or expert knowledge for training, low generalizability across assets and lack of insight into of possible failure causes. A hybrid approach tries to circumvent some of these limitations by incorporating physics-based models in the fault prognosis process, see for example [6, 7]. For the hybrid approach knowledge of the load history at critical locations in the gearbox (bearings, gear contacts) is essential as it allows the application of physical damage progression models such as fatigue [8], crack propagation [9] or frictional energy models [6]. In research local gearbox loads are generally calculated with computationally expensive simulations using aero-hydro-servo-elastic code in conjunction with multi-body simulation gearbox models, however this approach is

---

[*]Address all correspondence to this author.

FIGURE 1: PROPOSED ONLINE FATIGUE MONITORING METHOD

FIGURE 2: HIGH-FIDELITY PHYSICAL MODELS FOR VALIDATION OF THE PROPOSED METHOD

estimation method is developed in Sec. 3. Three state estimators with different levels of fidelity and requirements to sensory input are studied: Kalman Filter, Least Squares and a quasi-static approach (Sec. 4). With knowledge of the dynamic states local loads at gearbox bearings are easily determined and fatigue models, outlined in Sec. 5, are applied to track the accumulation of fatigue damage.

1 High-fidelity physical models

A reference gearbox based on the NREL offshore 5 MW baseline wind turbine and mounted on the floating OC3 Hywind spar structure is considered in this study [23, 24]. The reference gearbox was developed by Nejad et al. with reference to minimal weight and following offshore wind turbine design codes [25]. The gearbox comprises of two planetary and one parallel gear stage totalling to a gear ratio of 1:96.354. The main shaft support is a 4-point design with two main bearings to minimize non-torque loads entering the gearbox. A decoupled approach is employed, as shown in Fig. 2. The global response to a set of environmental conditions is determined with the global model, which is implemented in the aero-hydro-servo-elastic code SIMO-Riflex-AeroDyn. The internal dynamics are then simulated with a high-fidelity gearbox model implemented in the multi-body simulation environment SIMPACK. External loads (torque and non-torque) are applied on the main shaft, the nacelle movements are applied on the bed plate and the generator torque is applied on the HSS to control the generator speed.

2 Simulation measurements

Due to the lack of field measurements, simulation measurements from high-fidelity models are used in this study to evaluate the proposed load estimation method. A reference load case at rated wind speed of 12 m/s (load case EC4, spar in [26]) is simulated. The duration of the simulation is 3800 s, where the first 200 s are cut off to avoid simulation start-up effects. The simulation time step is 1 ms. From the simulation results the generator torque, shaft vibration and bearing loads are of interest. The generator torque and the shaft vibration are used to generate

not viable for real-time condition monitoring or fault prognosis. A more direct approach would be the reconstruction of gearbox loads from sensory data using inverse methods. Inverse methods have been developed to find solutions to the Inverse Problem, that is identifying excitation forces for a known dynamic state of a system [10]. A multitude of deterministic and probabilistic solutions are available, which have been reviewed by Sanchez et al. [11]. The most prominent applied methods in literature are Kalman filtering and least sqares estimators. Recent research has focused primarily on the identification of wind or wave loads on structural elements including aircraft [12], bridges [13], tall buildings [14–16] and wind turbine towers [17, 18]. A few studies also worked on machine elements with multi-body dynamics such as railway vehicles [19, 20], mining trucks [21] and diesel engines [22]. These results suggest, that this approach could also be applied to wind turbine drivetrains.

The detailed methodology is described in the following section. The proposed method is evaluated in a case study using a reference gearbox model and a reference load case. Estimated loads and loads from simulation measurements are compared using metrics in the time and frequency domain. Additionally, the relative error in fatigue damage based on estimated loads is analysed. Lastly, some concluding remarks are given.

METHODOLOGY

In this article a novel approach for the estimation of wind turbine gearbox loads with the purpose of online fatigue damage monitoring is presented (Fig. 1). The proposed method employs a Digital Twin framework and aims at continuous estimation of the dynamic states based on CMS vibration data and generator torque measurements from SCADA data. A case study is conducted to evaluate the proposed method using simulation measurements from high-fidelity drivetrain model, outlined in Sec. 2. The underlying linear physical model or Digital Twin for the load

synthetic SCADA and CM data as input for the load estimation method. Vibration signals are measured by virtual acceleration sensors mounted on the intermediate (IMS) and high-speed shaft (HSS) with a sampling frequency of 1 kHz. To capture yaw and pitch movements each shaft is equipped with two virtual sensors measuring axial and radial acceleration. White gaussian measurement noise $\mathbf{v} \sim \mathcal{N}(\mathbf{0}, \mathbf{R})$ is added to all acceleration measurements in postprocessing, where the covariance $\mathbf{R}$ is chosen, so that the signal-to-noise-ratio (SNR) is equal to 10 for all measurement signals. Additionally, the radial and axial loads at the IMS and HSS-bearings are extracted from simulation measurements for comparison with the estimated loads.

3 Linearized physical model

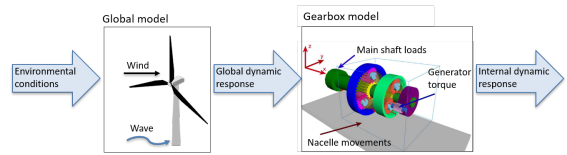In the following section the high-fidelity drivetrain model is linearized and brought into state-space form, which is required for the state estimation algorithm discussed in Sec. 4. This study focuses on the bearing loads at the parallel gear stage. Hence, the system boundaries are set around the gear stage as depicted in Fig. 3. The system contains two moving rigid bodies, namely the shafts IMS and HSS with its rigidly connected gearwheels, and can be characterised as open-ended, meaning it is controlled by forces crossing the system boundaries. These are connection forces at the interfaces to the generator and the upwind planetary gear stage and are only partially known in this study. The forces on the generator side are fully defined with the generator torque, which is available through measurements. The loads on the IMS comprise of the known counteracting torque T_{IMS} and unknown disturbance forces f_{dis} from either internal dynamic excitations of upwind gear components, such as gear meshing of the planetary stages, or from external, non-torque, aerodynamic loads entering the gearbox. The model linearization is conducted with SIMPACKs built in linearization solvers, which compute the system matrices $\mathbf{A}, \mathbf{B}, \mathbf{C}, \mathbf{D}$ of the linear state-space representation. The general formulation of the linear state-space model is given by

$$\dot{\mathbf{x}} = \mathbf{A}\mathbf{x} + \mathbf{B}\mathbf{u} + \mathbf{w}, \qquad (1)$$

$$\mathbf{y} = \mathbf{C}\mathbf{x} + \mathbf{D}\mathbf{u} + \mathbf{v}, \qquad (2)$$

Eq. 1 is the state transition model, also referred to as the physical model in this paper, since it is derived from the equations of motion. Eq. 2 is the observation model and describes the relation of the system output to the states. In this case the state vector $\mathbf{x}$ is a stack of positions and velocities of the IMS and HSS relative to the gearbox housing. The input variable $\mathbf{u}$ is defined as the generator torque. The unknown disturbance forces $\mathbf{f_{dis}}$ are regarded as process noise with covariance $\mathbf{Q}$. The output variables $\mathbf{y}$ are measurements from virtual acceleration sensors on the IMS and HSS. The ouput is corrupted with measurement noise $\mathbf{v}$, which
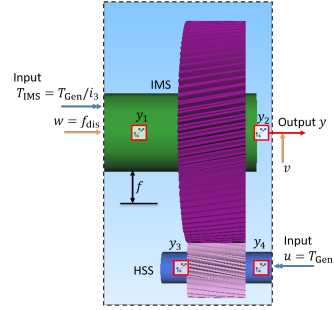
FIGURE 3: SYSTEM BOUNDARIES AND VARIABLE DEFINITION OF LINEARIZED MODEL

is modeled as white gaussian noise with covariance $\mathbf{R}$. In this case study measurement noise is added to the (exact) simulation measurements in postprocessing

$$
\begin{aligned}
\mathbf{x} &:= [\tilde{\mathbf{x}} \; \dot{\tilde{\mathbf{x}}}]^{\mathrm{T}}, \\
\tilde{\mathbf{x}} &:= \tilde{\mathbf{x}}_{\mathrm{IMS,HSS}} - \tilde{\mathbf{x}}_{\mathrm{housing}} = [x \; y \; z \; \alpha \; \beta \; \gamma]^{\mathrm{T}} \\
\mathbf{u} &:= T_{\mathrm{Gen}}, \\
\mathbf{y} &:= [y_{\mathrm{rad}} \; y_{\mathrm{ax}}]_{1-4}^{\mathrm{T}}, \\
\mathbf{w} &:= \mathbf{f}_{\mathrm{dis}} = [F_x \; F_y \; F_z \; M_x \; M_y \; M_z]^{\mathrm{T}} \sim \mathcal{N}(\mathbf{0}, \mathbf{Q}), \\
\mathbf{v} &\sim \mathcal{N}(\mathbf{0}, \mathbf{R}), \\
\mathbf{f} &:= [F_x \; F_y \; F_z \;]_{\mathrm{IMS/HSS-A,B,C}}^{\mathrm{T}}.
\end{aligned}
\qquad (3)
$$

In order to obtain the bearing loads $\mathbf{f}$ the general state-space model is augmented with an algebraic equation, which relates bearing loads to system states with the stiffness and damping matrix $\mathbf{K}$. Since the bearings are considered as spring-damper elements in the drivetrain model, this relationship is linear. The matrix $\mathbf{K}$ reflects the bearing stiffness and damping properties, as well as the transformation from body-fixed shaft coordinates to local bearing coordinates

$$\mathbf{f} = \mathbf{K}\mathbf{x}. \qquad (4)$$

The continuous state-space model is discretized in time, where n indicates the time step

$$\mathbf{x_{n+1}} = \mathbf{A_d}\mathbf{x_n} + \mathbf{B_d}\mathbf{u_n} + \mathbf{w_n}, \qquad (5)$$

$$\mathbf{y_n} = \mathbf{C}\mathbf{x_n} + \mathbf{D}\mathbf{u_n} + \mathbf{v_n}, \qquad (6)$$

$$\mathbf{f_n} = \mathbf{K}\mathbf{x_n}. \qquad (7)$$

The matrices $\mathbf{C}, \mathbf{D}, \mathbf{K}$ of the discrete model remain unchanged, as they only appear in algebraic equations, whereas $\mathbf{A_d}, \mathbf{B_d}$ are expressed as follows

$$\mathbf{A_d} = \exp(\mathbf{A}\Delta t), \tag{8}$$

$$\mathbf{B_d} = \mathbf{A}^{-1}(\mathbf{A_d} - \mathbf{I})\mathbf{B}. \tag{9}$$

4 Bearing load estimation

The load estimation is intended to be used for online monitoring applications and is thus conducted in the time domain for each time step n. Three different state estimators with different levels of fidelity and requirements to measurement inputs are studied, Kalman Filter, Least Squares and Quasi-static. In each case, the system states $\hat{\mathbf{x}}_\mathbf{n}$ are estimated first. Subsequently, the bearing loads are determined, as these are linear dependent on the system states

$$\hat{\mathbf{f}}_\mathbf{n} = \mathbf{K}\hat{\mathbf{x}}_\mathbf{n}. \tag{10}$$

4.1 Kalman Filter

The first load estimation method is based on Kalman filtering, which has been widely studied [13, 15–18, 21]. The Kalman Filter produces state estimates $\hat{\mathbf{x}}$ of a system, that is governed by stochastic, linear state equations as formulated in Eq. 5, 6 [27]. The optimal state estimates are determined by minimizing the estimate covariance, given by $\hat{\mathbf{P}} = \text{cov}(\mathbf{x} - \hat{\mathbf{x}})$, which is a measure of the estimation accuracy. The algorithm involves a two-step process for each time step. In the prediction step the a priori state estimates $\hat{\mathbf{x}}_{\mathbf{n}|\mathbf{n}-\mathbf{1}}$ are predicted with the physical model taking into account state estimates of the previous time step $\hat{\mathbf{x}}_{\mathbf{n}-\mathbf{1}|\mathbf{n}-\mathbf{1}}$ and known input variables $\mathbf{u_n} = \mathbf{T_{Gen}}$. The disturbance forces and moments $\mathbf{f_{dis}}$ on the system are not included in the prediction step, as they are regarded as process noise. The a priori estimated covariance $\hat{\mathbf{P}}_{\mathbf{n}-\mathbf{1}|\mathbf{n}-\mathbf{1}}$ is also predicted based on previous knowledge and the known process noise covariance Q

$$\hat{\mathbf{x}}_{\mathbf{n}|\mathbf{n}-\mathbf{1}} = \mathbf{A_d}\hat{\mathbf{x}}_{\mathbf{n}-\mathbf{1}|\mathbf{n}-\mathbf{1}} + \mathbf{B_d}\mathbf{u}_{\mathbf{n}-\mathbf{1}}, \tag{11}$$

$$\hat{\mathbf{P}}_{\mathbf{n}|\mathbf{n}-\mathbf{1}} = \mathbf{A_d}\hat{\mathbf{x}}_{\mathbf{n}-\mathbf{1}|\mathbf{n}-\mathbf{1}}\mathbf{A_d^T} + \mathbf{Q}. \tag{12}$$

In the second step the a priori state estimates are updated with measurements $\mathbf{y_n}$ resulting in the a posteriori state estimates $\mathbf{x_{n|n}}$

$$\mathbf{M_n} = \hat{\mathbf{P}}_{\mathbf{n}|\mathbf{n}-\mathbf{1}}\mathbf{C^T}(\mathbf{C}\hat{\mathbf{P}}_{\mathbf{n}|\mathbf{n}-\mathbf{1}}\mathbf{C^T} + \mathbf{R})^{-1}, \tag{13}$$

$$\hat{\mathbf{x}}_{\mathbf{n}|\mathbf{n}} = \hat{\mathbf{x}}_{\mathbf{n}|\mathbf{n}-\mathbf{1}} + \mathbf{M_n}(\mathbf{y_n} - \mathbf{C}\hat{\mathbf{x}}_{\mathbf{n}|\mathbf{n}-\mathbf{1}} - \mathbf{Du_n}), \tag{14}$$

$$\hat{\mathbf{P}}_{\mathbf{n}|\mathbf{n}} = (\mathbf{I} - \mathbf{M_n}\mathbf{C})\hat{\mathbf{P}}_{\mathbf{n}|\mathbf{n}-\mathbf{1}}. \tag{15}$$

The measurement update is weighted with the Kalman gain $\mathbf{M_n}$, which relates the confidence in state predictions of the physical model to the confidence in the measurement. With a high confidence in the physical model ($\hat{\mathbf{P}}_{\mathbf{n}|\mathbf{n}-\mathbf{1}} \to \mathbf{0}$) the Kalman gain approaches zero, hence, the measurements update is given a low weight. On the other hand, with a high confidence in the measurements ($\mathbf{R} \to \mathbf{0}$) the Kalman gain approaches $\mathbf{C}^{-\mathbf{1}}$. In this case the measurements have a higher significance compared to state predictions.

4.2 Quasi-static approach

The quasi-static (QS) method employs a low-fidelity approach, where the bearing loads are considered stationary, reactionary forces proportional to the drivetrain torque. This approach is used in a similar fashion for the calculation of gear contact forces in [8]. Contrary to the Kalman Filter, the QS state estimates are solely based on the physical model (Eq. 5) and do not take into account vibration measurements (Eq. 6). Additionally, the assumption is made, that the drivetrain is in quasi-static equilibrium and that internal dynamics are negligible. In the case quasi-static of equilibrium, where $\mathbf{x}_{\mathbf{n}+\mathbf{1}} - \mathbf{x_n} = \mathbf{0}$, the physical model (Eq. 5) reduces to

$$\mathbf{0} = (\mathbf{A_d} - \mathbf{I})\mathbf{x_n} + \mathbf{B_d}\mathbf{u_n} + \mathbf{w_n}. \tag{16}$$

Consequently, the state estimates can directly be determined from the input variable (generator torque) by disregarding the process noise

$$\hat{\mathbf{x}}_{\mathbf{stat},\mathbf{n}} = -(\mathbf{A_d} - \mathbf{I})^{-1}\mathbf{B_d}\mathbf{u_n}. \tag{17}$$

4.3 Least squares approach

A least squares approach to inverse state and load estimation is applied in [14, 19, 20]. This approach can be thought of as an asymptotic version of the Kalman Filter with high confidence in the measurements and low confidence in the physical model. In this case only the observation model (Eq. 6) of the state-space model is considered

$$\mathbf{y_n} = \mathbf{Cx_n} + \mathbf{Du_n} + \mathbf{v_n}. \tag{18}$$

The state estimates are found by minimizing the least squares error function

$$\hat{\mathbf{x}}_{\mathbf{LS},\mathbf{n}} = \arg\min_{\mathbf{x_n}}(\mathbf{y_n} - \mathbf{Cx_n} - \mathbf{Du_n})^{\mathbf{T}}(\mathbf{y_n} - \mathbf{Cx_n} - \mathbf{Du_n}). \tag{19}$$

The solution of the least-squares problem in closed form is given with the the Moore-Penrose pseudoinverse $\mathbf{C}^+$

$$\hat{\mathbf{x}}_{\mathbf{LS},\mathbf{n}} = \mathbf{C}^+(\mathbf{y_n} - \mathbf{Du_n}). \tag{20}$$

5 Fatigue damage

For evaluation of the proposed method the relative fatigue damage error is calculated, where $\hat{D}$ and D are the fatigue damage based on estimated and measured bearing loads respectively

$$e = \frac{\hat{D} - D}{\hat{D}}. \tag{21}$$

The Palmgren-Miner linear damage hypothesis is assumed for calculation of the fatigue damage, where n_i denote the experienced stress cycles, N_i the number of cycles until failure and i indicates the stress range

$$D = \sum_i \frac{n_i}{N_i}. \tag{22}$$

For calculation of N_i the nominal bearing life equation with the basic dynamic load rating C and the equivalent bearing load P is used

$$N_i = \left(\frac{C}{P}\right)^{\frac{10}{3}}. \tag{23}$$

P is a linear combination of the axial and radial load with the factors X and Y, which are bearing specific values taken from manufacturer's data

$$P = X \cdot F_{ax} + Y \cdot F_{rad}. \tag{24}$$

The stress cycles n_i are counted with the load distribution method according to IEC 61400-4 [28]. The LDD method is applicable for rotating machinery components under slowly varying loads, that experience cyclic loading due to entering and exiting the load zone each rotation. One stress cycle is counted for each rotation with a stress range equal to the current load.

DISCUSSION OF RESULTS

The inverse load estimation methods Kalman Filter (KF), Least Square (LS) and Quasi-Static (QS) presented in Sec. 4 are evaluated in a case study. The estimated radial loads at the IMS and HSS bearings are compared to simulation measurements obtained from the high-fidelity drivetrain model outlined in Sec. 2. First, the correlation of estimated and measured loads is analyzed in the time and frequency domain. Secondly, the error in calculated fatigue damage is discussed.
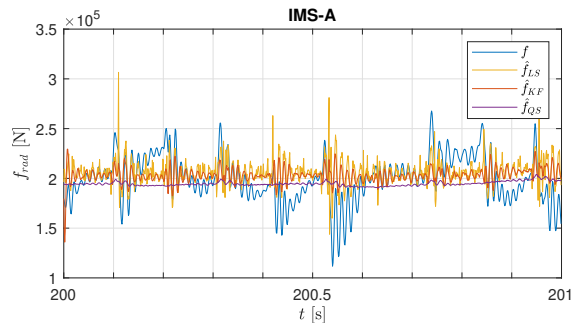
FIGURE 4: REPRESENTATIVE SECTION OF TIME SERIES
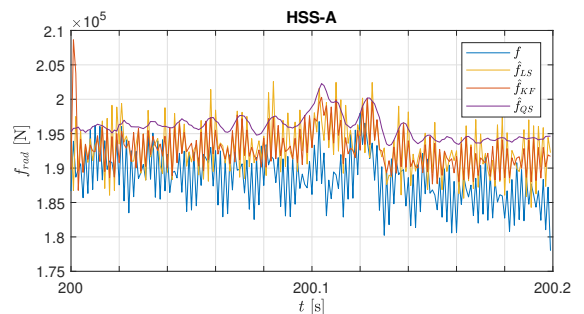
FIGURE 5: REPRESENTATIVE SECTION OF TIME SERIES OF MEASURED AND ESTIMATED LOADS AT HSS-A

6 Estimated loads

For a qualitative assessment a representative section of the time series of measured and estimated radial loads in the IMS-A and HSS-A bearings are shown in Fig. 4, 5. Notice the different time scales of the figures. The measured loads f are highly dynamic with components in both lower ($<$ 10 Hz) and higher frequencies ($>$ 100 Hz) and are offset by a non-zero mean value. The load estimates of the QS method $\hat{f}_{QS}$ are quasi-static with oscillations of small amplitudes and do not reflect the dynamics of measured loads. The mean value of measured loads is matched quite well by the QS method, although at the HSS-A a slight bias is observed. The LS method produces load estimates $\hat{f}_{LS}$ with high frequency oscillations of similar amplitudes to measured loads, however at the IMS-A there appear to be several outliers, which significantly overestimate measured loads. In the low-frequency range the LS method is not able to fully capture the internal gearbox dynamics. This is especially noticeable at the IMS-A, where the measured loads have a high-energy frequency component of about 5 Hz. The KF load estimates $\hat{f}_{KF}$
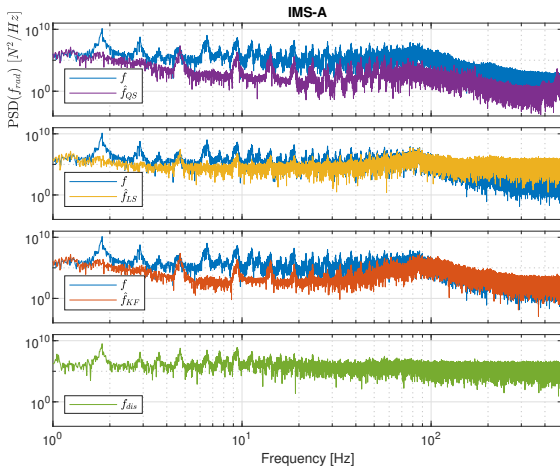
FIGURE 6: PSD OF MEASURED AND ESTIMATED RADIAL AT IMS-A LOADS FOR FULL TIME SERIES (3600 s).

FIGURE 7: PSD OF MEASURED AND ESTIMATED RADIAL LOADS AT HSS-A FOR FULL TIME SERIES (3600 s).

are smoother and do not suffer from extreme outliers. Similar to the LS method high frequency oscillations are captured well, while some lower frequency components are not reflected.

For analysis of the behaviour in the frequency domain the power spectral densities (PSD) of measured and estimated bearing loads are calculated, as shown in Fig. 6, 7. The measured load spectrum shows several lower-frequency peaks (< 10 Hz) and higher-frequency peaks at 80 Hz for IMS-A and at 464.2 Hz for HSS-A. The higher frequency peaks coincide with the gear meshing frequencies of the parallel and second planetary gear stage respectively. The lower frequency peaks are not fully identified as of now.

The QS method matches the measured load spectrum of HSS-A reasonably well with the exception of the high-frequency range with the gear meshing peak, which is underestimated significantly. In the low frequency range the peaks at 4.75 Hz, 9.47 Hz and 14.22 Hz are matched. These likely correspond to pure torsional oscillations of the HSS, which directly translate to oscillations in the generator torque. The dynamics of the IMS are not represented well with the QS method, as the QS load spectrum shows significantly lower energy in all frequencies.

In addition to the torsional oscillation peaks both the LS and KF method are able to match the gear meshing peaks. In the high-frequency range the LS method leads to a significant overestimation due to a high confidence in noisy measurements. The KF load estimates achieve a higher correlation by weighing the measurement update according to the measurement noise covariance R and thus filtering outliers. In the lower frequency range some peaks at 1.83 Hz, 2.91 Hz and 6.58 Hz, which are more

pronounced at the IMS-A, are missed by both the LS and KF method.

The missed lower-frequency peaks likely relate to radial disturbance forces f_{dis} on the IMS, as the spectrum of measured disturbance forces suggests. The measured disturbance forces are extracted from the high-fidelity drive train simulations as connection forces of the second planetary gear stage to the IMS and show several low-frequency components of higher energy. The load estimation methods are unable to take these into account via state predictions, since the disturbance forces are assumed as white gaussian process noise in the underlying physical model. Furthermore, it is challenging to consider low-frequency disturbance force excitations via vibration measurements, because these cause relatively low acceleration responses with a low signal-to-noise-ratio.

For a quantitative assessment of the load correlation the Pearson correlation coefficient is calculated for the complete time series of 3600 s, as shown in Tab. 1. The correlation of IMS loads is quite poor, as the studied methods are unable to reproduce aforementioned low frequency load components. The KF is the best performing method, resulting in correlation values of 0.50 to 0.61. At the HSS the QS method is sufficient to estimate bearing loads with high correlation ($R > 0.8$), as internal dynamics have less significance here. The LS and KF method do not lead to significant improvements at the HSS.

Copyright © 2021 by ASME

TABLE 1: CORRELATION OF ESTIMATED LOADS

	QS	LS	KF
IMS-A	0.36	0.48	0.50
IMS-B	0.43	0.37	0.58
IMS-C	0.42	0.35	0.61
HSS-A	0.96	0.95	0.96
HSS-B	0.82	0.83	0.85
HSS-C	0.84	0.84	0.83

TABLE 2: FATIGUE DAMAGE ERROR

	QS [%]	LS [%]	KF [%]
IMS-A	11.8	11.6	12.3
IMS-B	5.7	0.8	3.8
IMS-C	-9.4	-13.6	-11.1
HSS-A	-5.2	-6.1	-5.9
HSS-B	10.7	8.3	8.5
HSS-C	15.2	11.2	11.4

7 Fatigue damage

Tab. 2 shows the relative fatigue damage error for the IMS and HSS bearings. The QS method results in low errors of 5 - 15 % across all bearings in the considered load case. The results of the higher fidelity methods LS and KF differ only marginally from those of the QS method despite considering internal dynamics and providing load estimates of higher correlation. The error can be slightly reduced at the bearings IMS-B and HSS-B,C, however at the bearings IMS-C and HSS-A a slightly higher error is calculated. These results suggest, that for the considered load case and drive train design the fatigue damage at the IMS and HSS bearings is mainly dependent on the drive train torque and effects of internal gearbox dynamics are negligible. This becomes more clear, when looking at the bearing stress cycles, which are not only a function of the load oscillations depicted in Fig. 4, but also of the rotational speed [8]. A rotating bearing experiences cyclic loading due to entering and exiting the load zone. This is reflected in the use of the stress cycle counting method LDD as opposed to the rainflow counting (RFC) method, which is commonly used for structural elements.

The LDD method counts one stress cycle per revolution with a stress range equal to the current radial load. Thus, the quasi-static reactionary forces to the drive train torque cause major stress ranges and contribute significantly to the bearing fatigue, whereas the load variations from internal dynamics cause comparatively small stress ranges. In the studied load case at rated wind speed under normal operational conditions the QS method would be sufficient to monitor fatigue damage with high accuracy and computational speed. However, it is uncertain how the QS method would perform in load cases with greater internal dynamics, such as an emergency stop or gear faults. Further studies are planned to address this topic.

CONCLUSION

In this article a novel approach for the estimation of wind turbine gearbox loads with the purpose of online fatigue damage monitoring was presented. The proposed method employs a Digital Twin framework and aims at continuous estimation of the dynamic states based on CMS vibration data and generator torque measurements from SCADA data. The proposed method was evaluated in a load case at rated wind speed under normal operational conditions. With a quasi-static approach, which assumes proportionality to the drive train torque, the overall level of bearing loads were estimated with high accuracy, however the dynamic behaviour was not reflected well. The quasi-static method was sufficient to estimate fatigue damage with an error of 5-15 % across all bearings. The Kalman Filter approach produced the highest correlation of bearing loads ranging from 0.5-0.96 and was able to capture high-frequency dynamics accurately, but missed several low-frequency components. These are caused by disturbance forces on the IMS, which are not reflected in the underlying physical model and are not available through measurements. Despite considering internal dynamics, the KF method did not result in significant improvements with reference to fatigue damage. It appears, that in this load case the stress cycles caused by internal dynamics are insignificant relative to torque induced stress cycles. The Least-squares estimator performed worse than the Kalman Filter, as it is more sensitive to measurement noise. However, it has its advantages in computational speed, since it requires only one initial matrix inversion as opposed to the Kalman Filter with one matrix inversion for each time step. Further studies are planned to extend this work to different load cases or fault cases, assess the sensitivity to measurement noise and model uncertainties and quantify computational costs.

ACKNOWLEDGMENT

REFERENCES

[1] Kumar, Y., Ringenberg, J., Depuru, S., Devabhaktuni, V. K., Lee, J., Nikolaidis, E., Andersen, B., and Afjeh, A., 2016. "Wind energy: Trends and enabling technologies". *Renewable and Sustainable Energy Reviews, 53*, pp. 209–224.

[2] Stehly, T., and Beiter, P., 2020. 2018 cost of wind energy review. Report, National Renewable Energy Laboratory.

[3] Faulstich, S., Hahn, B., and Tavner, P. J., 2011. "Wind turbine downtime and its importance for offshore deployment". *Wind Energy, 14*(3), pp. 327–337.

[4] Carroll, J., McDonald, A., and McMillan, D., 2016. "Failure rate, repair time and unscheduled o&m cost analysis of offshore wind turbines". *Wind Energy, 19*(6), pp. 1107–1119.

[5] Randall, R. B., 2010. *Vibration based condition monitoring: Industrial, Aerospace and Automotive Applications.* Wiley & Sons Ltd.

[6] Desai, A., Guo, Y., Sheng, S., Phillips, C., and Williams, L., 2020. "Prognosis of wind turbine gearbox bearing failures using scada and modeled data". *Annual conference of the prognostics and health management society.*

[7] Djeziri, M. A., Benmoussa, S., and Sanchez, R., 2018. "Hybrid method for remaining useful life prediction in wind turbine systems". *Renewable Energy, 116*, pp. 173–187.

[8] Nejad, A. R., Gao, Z., and Moan, T., 2014. "On long-term fatigue damage and reliability analysis of gears under wind loads in offshore wind turbine drivetrains". *International Journal of Fatigue, 61*, pp. 116–128.

[9] Dong, W., Nejad, A. R., Moan, T., and Gao, Z., 2020. "Structural reliability analysis of contact fatigue design of gears in wind turbine drivetrains". *Journal of Loss Prevention in the Process Industries, 65*.

[10] Gladwell, G. M., 2004. *Inverse Problems in Vibration*, Vol. 119 of *Solid mechanics and its applications.* Kluwer academic publishers.

[11] Sanchez, J., and Benaroya, H., 2014. "Review of force reconstruction techniques". *Journal of Sound and Vibration, 333*(14), pp. 2999–3018.

[12] Wang, L., and Liu, Y., 2020. "A novel method of distributed dynamic load identification for aircraft structure considering multi-source uncertainties". *Structural and Multidisciplinary Optimization, 61*(5), pp. 1929–1952.

[13] Petersen, Ø. W., Øiseth, O., and Lourens, E., 2019. "Full-scale identification of the wave forces exerted on a floating bridge using inverse methods and directional wave spectrum estimation". *Mechanical Systems and Signal Processing, 120*, pp. 708–726.

[14] Kazemi Amiri, A., and Bucher, C., 2017. "A procedure for in situ wind load reconstruction from structural response only based on field testing data". *Journal of Wind Engineering and Industrial Aerodynamics, 167*, pp. 75–86.

[15] Hwang, J.-S., Kareem, A., and Kim, H., 2011. "Wind load identification using wind tunnel test data by inverse analysis". *Journal of Wind Engineering and Industrial Aerodynamics, 99*(1), pp. 18–26.

[16] Zhi, L.-h., Fang, M.-x., and Li, Q. S., 2017. "Estimation of wind loads on a tall building by an inverse method". *Structural Control and Health Monitoring, 24*(4).

[17] Maes, K., Weijtjens, W., de Ridder, E. J., and Lombaert, G., 2018. "Inverse estimation of breaking wave loads on monopile wind turbines". *Ocean Engineering, 163*, pp. 544–554.

[18] Branlard, E., Giardina, D., and Brown, C. S. D., 2020. "Augmented kalman filter with a reduced mechanical model to estimate tower loads on a land-based wind turbine: a step towards digital-twin simulations". *Wind Energy Science, 5*(3), pp. 1155–1167.

[19] Zhu, T., Xiao, S., Yang, G., Ma, W., and Zhang, Z., 2013. "An inverse dynamics method for railway vehicle systems". *Transport, 29*(1), pp. 107–114.

[20] Uhl, T., 2006. "The inverse identification problem and its technical application". *Archive of Applied Mechanics, 77*(5), pp. 325–337.

[21] Siegrist, P. M., and McAree, P. R., 2006. "Tyre-force estimation by kalman inverse filtering: applications to off-highway mining trucks". *Vehicle System Dynamics, 44*(12), pp. 921–937.

[22] Leclère, Q., Pezerat, C., Laulagnet, B., and Polac, L., 2005. "Indirect measurement of main bearing loads in an operating diesel engine". *Journal of Sound and Vibration, 286*(1-2), pp. 341–361.

[23] Jonkman, J., Butterfield, S., Musial, W., and Scott, G., 2009. Definition of a 5-mw reference wind turbine for offshore system development. Report, National Renewable Energy Laboratory (NREL).

[24] Jonkman, J., 2010. Definition of the floating system for phase IV of OC3. Report, National Renewable Energy Laboratory (NREL).

[25] Nejad, A. R., Guo, Y., Gao, Z., and Moan, T., 2016. "Development of a 5 mw reference gearbox for offshore wind turbines". *Wind Energy, 19*(6), pp. 1089–1106.

[26] Nejad, A. R., Bachynski, E. E., Kvittem, M. I., Luan, C., Gao, Z., and Moan, T., 2015. "Stochastic dynamic load effect and fatigue damage analysis of drivetrains in land-based and tlp, spar and semi-submersible floating wind turbines". *Marine Structures, 42*, pp. 137–153.

[27] Welch, G.; Bishop, G., 1997. "An introduction to the kalman filter".

[28] IEC 61400-4, 2012. Wind turbines, part 4: standard for design and specification of gearboxes.

A.3   Paper 3

Digital Twin Based Virtual Sensor for Online Fatigue Damage Monitoring in Offshore Wind Turbine Drivetrains

Felix C. Mehlan[1]

Department of Marine Technology (IMT),
Norwegian University of Science and
Technology (NTNU),
Trondheim 7491, Norway
e-mail: felix.c.mehlan@ntnu.no

Amir R. Nejad

Department of Marine Technology (IMT),
Norwegian University of Science and
Technology (NTNU),
Trondheim 7491, Norway
e-mail: amir.nejad@ntnu.no

Zhen Gao

Department of Marine Technology (IMT),
Norwegian University of Science and
Technology (NTNU),
Trondheim 7491, Norway
e-mail: zhen.gao@ntnu.no

In this article a virtual sensor for online load monitoring and subsequent remaining useful life (RUL) assessment of wind turbine gearbox bearings is presented. Utilizing a Digital Twin framework the virtual sensor combines data from readily available sensors of the condition monitoring (CMS) and supervisory control and data acquisition (SCADA) system with a physics-based gearbox model. Different state estimation methods including Kalman filter, Least-square estimator, and a quasi-static approach are employed for load estimation. For RUL assessment the accumulated fatigue damage is calculated with the Palmgren–Miner model. A case study using simulation measurements from a high-fidelity gearbox model is conducted to evaluate the proposed method. Estimated loads at the considered intermediate and high-speed shaft bearings show moderate to high correlation ($R = 0.50 - 0.96$) to measurements, as lower frequency internal dynamics are not fully captured. The estimated fatigue damage differs by 5–15% from measurements.
[DOI: 10.1115/1.4055551]

Keywords: computational mechanics and design, fatigue and fracture reliability and control

1 Introduction

Recent market trends show an increased shift toward offshore wind turbine installations due to the higher energy yield and fewer issues with land displacement and noise [1]. However, offshore sites face additional reliability challenges. Replacement or repair of components is expensive and time consuming due to difficulties accessing the site and dependency on good weather conditions. Thus, unscheduled down times as a result of component failure can lead to high operational and maintenance expenditures (O&M). For offshore wind turbines the O&M expenditures can reach 34% of the levelized cost of energy (LCOE), twice as much as for land-based turbines [2]. A major contributor to the O&M expenditures is the gearbox with a failure rate of 0.1–0.15/year and average downtimes of 6 days per failure [3,4].

Predictive maintenance strategies are proposed in the offshore industry to increase reliability and availability, and decrease O&M expenditures. As a subcategory of condition-based maintenance (CBM) predictive maintenance depends on continuous monitoring of the systems' operational condition for the assessment of the remaining useful life (RUL). Alerts are triggered in the case of severe deviation of RUL to nominal life and the operator may schedule immediate maintenance tasks in addition to regular, time-based maintenance routines. Currently, the predictive capabilities of condition monitoring systems (CMS) are limited. In practice, trends of vibration-based statistical features are extrapolated to a predefined failure threshold to predict the RUL, which suffers from a high level of uncertainty [5].

Digital twin (DT) is identified as an emerging technology that could facilitate predictive maintenance strategies [6]. DT can be described as a virtual representation of a physical asset enabled through real-time measurements and simulators for the purpose of improved decision making [7]. The authors previously proposed a Digital Twin framework, shown in Fig. 1, with the three components *Virtual model, Data*, and *Decision support* to move toward predictive maintenance [8].

Virtual models of wind turbines have matured in the past two decades to a high level of fidelity. Generally a decoupled approach is employed with aeroelastic models for global dynamics, multi-body simulation (MBS) models for drivetrain dynamics, and finite element (FE) models for component dynamics [9]. While many authors associate DT with high-fidelity models, recent publications move toward reduced-order models (ROM) to meet requirements of computational speed for real-time monitoring tasks [8]. The DT model is updated with data such that it virtually experiences the same environment as its physical counterpart.

Data that can be leveraged in wind turbines are sensor measurements of the drivetrain CMS or the supervisory control and data acquisition (SCADA) system. Typical signals include vibration on the gearbox housing, electrical signatures of the generator and shaft speeds.

Decision support is a collective term for services that the DT provides to assist the operators' maintenance or control decisions. Focus of this research are methods for online monitoring of loads in drivetrain components (gears, bearings) and subsequent RUL estimation. Direct measurements of component level loads are difficult and require custom solutions, such as bearings with integrated strain gauges, which are generally not available for commercial wind turbines. Hence, indirect (or inverse) methods of load estimation that combine more accessible sensor measurements and a DT model would provide a cost-effective alternative. This procedure is often referred to as *Virtual sensing*, as it can be interpreted as taking measurements in a fully synchronized virtual model. Synchronization is achieved by continuously estimating the dynamic states of the system. Different state estimation methods are employed for this purpose, most prominently the Kalman filter and its variations, as well as least-square estimators.

The DT and virtual sensing approach are often pursued for estimating damage equivalent loads or stresses for structural health monitoring (SHM), for example in wind turbine towers. Virtual
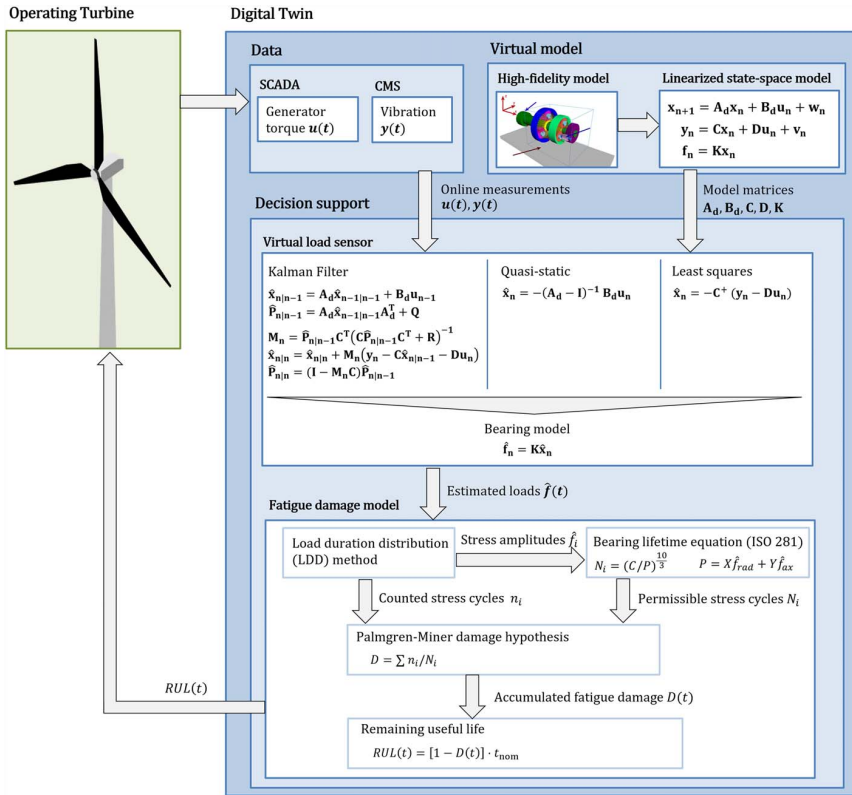
Fig. 1   Digital twin framework with three components of Data, Virtual model, and Decision support used in this study for online fatigue damage monitoring

sensing of tower loads based on a limited number accelerometers and strain gauges has been demonstrated both in numerical and experimental studies [10,11]. However, limited research has been conducted for drivetrains with the exception of a study by Bosmans et al., who present a virtual sensor for wind turbine planetary gear loads based on strain gauge measurements and a FE model [12]. The use case of drivetrains comes with unique challenges: The internal dynamics of drivetrains are much more complex due to multi-body interactions and there are limitations in the existing drivetrain sensors (SCADA, CMS) related to signal resolution, sensor locations, and noise that make it difficult to observe the current dynamic state.

The main contribution of this work is to apply a virtual sensing approach that has proven to be effective in other areas to the use case of wind turbine drivetrains and demonstrate the proof of concept in a numerical case study. In addition, this article discusses the challenges that are unique to drivetrains and provides some recommendations on suitable sensor signals and state estimation methods.

The remainder of this paper is organized as follows. In Sec. 2, the mathematical development of the virtual load sensor and its use case in a wind turbine high-speed gear stage are outlined. Section 3 discusses the performance of the virtual sensor in a numerical case study. Lastly, Sec. 4 provides some concluding remarks.

2   Methodology

The virtual load sensor is developed in a DT framework with the three components of Data, Virtual model, and Decision support (Fig. 1). Section 2.1 presents the high-fidelity model of a reference

wind turbine gearbox, which is linearized for integration with the virtual sensor, as shown in Sec. 2.2. Synthetic CMS and SCADA data are generated by means of simulation with high-fidelity models (Sec. 2.3). Different state estimators including the Kalman filter, Least-squares estimator, and a quasi-static approach are used for virtual sensing of bearing loads (Sec. 2.4). Subsequently, the accumulation of fatigue damage is tracked with the standard Palmgren–Miner model and the bearing lifetime equation according to ISO 281 (Sec. 2.5).

2.1   High-Fidelity Models. A reference gearbox based on the NREL offshore 5 MW baseline wind turbine and mounted on the floating OC3 Hywind spar structure is considered in this study [13,14]. The reference gearbox was developed by Nejad et al. with reference to minimal weight and following offshore wind turbine design codes [15]. The gearbox comprises of two planetary and one parallel gear stage totalling to a gear ratio of 1:96.354. The main shaft support is a 4-point design with two main bearings to minimize non-torque loads entering the gearbox. A decoupled approach is employed, which is best practice for drivetrain simulation [9]. The global response to a set of environmental conditions is determined with the global model, which is implemented in the aero-hydro-servo-elastic code SIMO-Riflex-AeroDyn. The internal dynamics are then simulated with a high-fidelity gearbox model implemented in the multi-body simulation environment SIMPACK. External loads (torque and non-torque) are applied on the main shaft, the nacelle movements are applied on the bed plate and the generator torque is applied on the high-speed shaft to control the generator speed.

2.2 Linearized Model. In the following section the high-fidelity drivetrain model is linearized and brought into state-space form, which is required for the state estimation algorithm discussed in Sec. 2.4. This study focuses on the bearing loads at the high-speed gear stage. Hence, the system boundaries are set around the gear stage as depicted in Fig. 2 containing two moving rigid bodies, namely, the intermediate and the high-speed shaft (IMS, HSS). The shafts are coupled with an elastic gear contact formulation and connected to the gearbox housing with spring–dampers representing roller bearings. The dynamics of such a gear stage system can be expressed with the following equations of motion [16] (Eq. (1)):

$$\mathbf{M}\ddot{\tilde{\mathbf{x}}} + [\mathbf{C_m} + \mathbf{C_b}]\dot{\tilde{\mathbf{x}}} + [\mathbf{K_m} + \mathbf{K_b}]\tilde{\mathbf{x}} = \mathbf{f_{ex}} \tag{1}$$

Six degrees-of-freedom (DOF) are assumed for each gear shaft, hence the state vector $\tilde{\mathbf{x}} \in R^{12\times1}$ contains a total of 12 lateral and angular displacements. $\mathbf{M}$ denotes the diagonal mass matrix comprised of inertia terms. The stiffness and damping matrices contain terms from the elastic couplings of bearings ($\mathbf{C_b}$, $\mathbf{K_b}$) and gear meshing ($\mathbf{C_m}$, $\mathbf{K_m}$). The detailed matrix composition is given in Ref. [16]. External forces and moments crossing the system boundary at the generator and rotor side shaft interfaces are represented by $\mathbf{f_{ex}} \in R^{12\times1}$. The equations of motion are first linearized and then transformed into a set of first-order differential equations, the so-called state-space representation (Eq. (2)). In this step the time-variant mesh stiffness is reduced to a constant value $\overline{\mathbf{C_m}}$, hence the linearized model is unable to reproduce periodic excitation at the gear meshing frequency.

$$\dot{\mathbf{x}} = \mathbf{A}\mathbf{x} + \mathbf{B}\mathbf{u} + \mathbf{w} \tag{2}$$

The new state vector $\mathbf{x}$ of the state-space model is a stack of body-fixed displacements and velocities (Eq. (3)), while the external forces $\mathbf{f_{ex}}$ are split into known input variables $\mathbf{u}$ (Eq. (4)) and unknown disturbance forces regarded as process noise $\mathbf{w}$ (Eq. (5)). Of the 12 external force terms only the generator torque is considered available from SCADA measurements and thus a known input variable, while the remaining non-torque loads are modeled as white gaussian noise with covariance $\mathbf{Q}$. The system matrix $\mathbf{A}$ (Eq. (6)) describes the dynamic state-transition and is

Fig. 2 System boundaries and variable definition of linearized model

obtained by rearranging mass, stiffness, and damping matrices [17]. The control matrix $\mathbf{B}$ (Eq. (7)) represents the influence of input variables on the dynamic states.

$$\mathbf{x} := [\tilde{\mathbf{x}} \ \dot{\tilde{x}}]^T \in R^{24\times1} \tag{3}$$

$$\mathbf{u} = [0 \ 0 \ \cdots \ T_{Gen} \ \cdots \ 0 \ 0]^T \in R^{12\times1} \tag{4}$$

$$\mathbf{w} \sim \mathcal{N}(\mathbf{0}, \mathbf{Q}) \in R^{12\times1} \tag{5}$$

$$\mathbf{A} = \begin{bmatrix} \mathbf{0}^{12\times12} & \mathbf{I}^{12\times12} \\ \mathbf{M}^{-1}[\overline{\mathbf{C_m}} + \mathbf{C_b}] & \mathbf{M}^{-1}[\overline{\mathbf{K_m}} + \mathbf{K_b}] \end{bmatrix} \in R^{24\times24} \tag{6}$$

$$\mathbf{B} = \begin{bmatrix} \mathbf{0}^{12\times12} & \mathbf{M}^{-1} \end{bmatrix}^T \in R^{24\times12} \tag{7}$$

The output variables $\mathbf{y}$ (Eq. (9)) are measurements of virtual accelerometers placed at the shaft bearings in axial and radial direction (Fig. 2) that represent CMS vibration sensors. These are analogously related to the state and input variables through a linear model (Eq. (8)), where $\mathbf{C}$ denotes the observation matrix and $\mathbf{D}$ the feedthrough matrix. The exact matrix composition cannot be shown, as these are generated numerically by SIMPACK's linearization solvers.

$$\mathbf{y} = \mathbf{C}\mathbf{x} + \mathbf{D}\mathbf{u} + \mathbf{v} \tag{8}$$

The output is corrupted with measurement noise $\mathbf{v}$ (Eq. (10)), which is modeled as white gaussian noise with covariance $\mathbf{R}$. In this case study measurement noise is added to the (exact) simulation measurements in postprocessing

$$\mathbf{y} := [\mathbf{y_1} \ \mathbf{y_2} \ \mathbf{y_3} \ \mathbf{y_4}]^T \in R^{8\times1} \tag{9}$$

$$\mathbf{v} \sim \mathcal{N}(\mathbf{0}, \mathbf{R}) \in R^{8\times1} \tag{10}$$

In order to obtain the desired bearing loads $\mathbf{f}$ the general state-space model is augmented with an algebraic equation, which relates bearing loads to system states with the matrix $\mathbf{K}$ (Eq. (11)). Since the bearings are considered as spring–damper elements in the drivetrain model, this relationship is linear. The matrix $\mathbf{K}$ contains terms of bearing stiffness $\mathbf{K_b}$ and damping $\mathbf{C_b}$, and is generated numerically by SIMPACK.

$$\mathbf{f} = \mathbf{K}\mathbf{x} \tag{11}$$

The continuous state-space model is discretized in time, where $\mathbf{n}$ indicates the time-step

$$\mathbf{x_{n+1}} = \mathbf{A_d}\mathbf{x_n} + \mathbf{B_d}\mathbf{u_n} + \mathbf{w_n} \tag{12}$$

$$\mathbf{y_n} = \mathbf{C}\mathbf{x_n} + \mathbf{D}\mathbf{u_n} + \mathbf{v_n} \tag{13}$$

$$\mathbf{f_n} = \mathbf{K}\mathbf{x_n} \tag{14}$$

The matrices $\mathbf{C}$, $\mathbf{D}$, $\mathbf{K}$ of the discrete model remain unchanged, as they only appear in algebraic equations, whereas $\mathbf{A_d}$, $\mathbf{B_d}$ can be derived as follows [17]:

$$\mathbf{A_d} = \exp(\mathbf{A}\Delta t) \tag{15}$$

$$\mathbf{B_d} = \mathbf{A}^{-1}(\mathbf{A_d} - \mathbf{I}^{24\times24})\mathbf{B} \tag{16}$$

The matrices $\mathbf{A}, \mathbf{B}, \mathbf{C}, \mathbf{D}, \mathbf{K}$ are calculated with SIMPACK's built-in linearization solvers and integrated in the virtual load sensor in MATLAB.
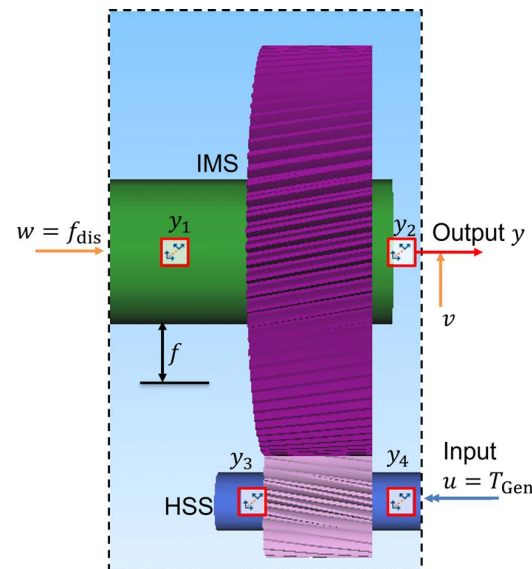
2.3 Sensor Data. In this numerical study simulation measurements from high-fidelity models are used to evaluate the proposed

Table 1 Environmental conditions of numerical case study adopted from Nejad et al. (EC4, spar) [9]

Wave height H_s (m)	5.0
Wave period T_p (s)	12.0
Wind speed U (m/s)	12.0
Turbulence intensity I (—)	0.15
Simulation seeds	6

load estimation method. A reference load case at rated wind speed of 12 m/s (load case EC4, spar in [9]) is selected, since conditions near rated wind speeds are shown to induce the most severe drivetrain loads and have the highest contribution to long-term fatigue damage [18]. Six simulations each with a duration of 3800 s are conducted to comply with IEC 61400 guidelines [19]. The first 200 s are disregarded to avoid simulation start-up effects and the simulation time-step is set to 1 ms to capture high-frequency gear meshing dynamics. From the simulation results the generator torque, shaft vibration, and bearing loads are of interest. The generator torque and the shaft vibration are used to generate synthetic SCADA and CMS data as input for the load estimation method. Vibration signals are measured by virtual acceleration sensors mounted on the intermediate (IMS) and high-speed shaft (HSS) with a sampling frequency of 1 kHz. To capture yaw and pitch movements each shaft is equipped with two virtual sensors measuring axial and radial acceleration. White gaussian measurement noise $\mathbf{v} \sim \mathcal{N}(\mathbf{0}, \mathbf{R})$ is added to all acceleration measurements in postprocessing, where the covariance $\mathbf{R}$ is chosen, so that the signal-to-noise-ratio (SNR) is equal to 10 for all measurement signals. Additionally, the radial and axial loads at the IMS and HSS-bearings are extracted from simulation measurements for comparison with the estimated loads (see Table 1).

2.4 Virtual Load Sensor.
The load estimation is intended to be used for online monitoring applications and is thus conducted in the time domain for each time-step n. Three different state estimators with different levels of fidelity and requirements to measurement inputs are studied, Kalman filter, Least Squares, and Quasi-static. In each case, the system states $\hat{\mathbf{x}}_n$ are estimated first. Subsequently, the bearing loads are determined, as these are linearly dependent on the system states

$$\hat{\mathbf{f}}_n = \mathbf{K}\hat{\mathbf{x}}_n \qquad (17)$$

2.4.1 Kalman Filter. The first load estimation method is based on Kalman filtering, which has been widely studied [10,20–24]. The Kalman filter produces state estimates $\hat{\mathbf{x}}$ of a system, which is governed by stochastic, linear state equations as formulated in Eqs. (12) and (13) [25]. The optimal state estimates are determined by minimizing the estimate covariance, given by $\hat{\mathbf{P}} = \text{cov}(\mathbf{x} - \hat{\mathbf{x}})$, which is a measure of the estimation accuracy. The algorithm involves a two-step process for each time-step. In the prediction step the a prioristate estimates $\hat{\mathbf{x}}_{n|n-1}$ are predicted with the physical model taking into account state estimates of the previous time-step $\hat{\mathbf{x}}_{n-1|n-1}$ and known input variables $\mathbf{u}_n$. The disturbance forces and moments $\mathbf{w}$ on the system are not included in the prediction step, as they are regarded as process noise. The a priori estimated covariance $\hat{\mathbf{P}}_{n-1|n-1}$ is also predicted based on previous knowledge and the known process noise covariance $\mathbf{Q}$

$$\hat{\mathbf{x}}_{n|n-1} = \mathbf{A_d}\hat{\mathbf{x}}_{n-1|n-1} + \mathbf{B_d}\mathbf{u}_{n-1} \qquad (18)$$

$$\hat{\mathbf{P}}_{n|n-1} = \mathbf{A_d}\hat{\mathbf{x}}_{n-1|n-1}\mathbf{A_d^T} + \mathbf{Q} \qquad (19)$$

In the second step the a priori state estimates are updated with measurements $\mathbf{y}_n$ resulting in the a posteriori state estimates $\mathbf{x}_{n|n}$

$$\mathbf{M_n} = \hat{\mathbf{P}}_{n|n-1}\mathbf{C^T}(\mathbf{C}\hat{\mathbf{P}}_{n|n-1}\mathbf{C^T} + \mathbf{R})^{-1} \qquad (20)$$

$$\hat{\mathbf{x}}_{n|n} = \hat{\mathbf{x}}_{n|n-1} + \mathbf{M_n}(\mathbf{y_n} - \mathbf{C}\hat{\mathbf{x}}_{n|n-1-\mathbf{Du}_n}) \qquad (21)$$

$$\hat{\mathbf{P}}_{n|n} = (\mathbf{I} - \mathbf{M_n}\mathbf{C})\hat{\mathbf{P}}_{n|n-1} \qquad (22)$$

The measurement update is weighted with the Kalman gain $\mathbf{M_n}$, which relates the confidence in state predictions of the physical model to the confidence in the measurement. With a high confidence in the physical model ($\hat{\mathbf{P}}_{n|n-1} \rightarrow \mathbf{0}$) the Kalman gain approaches zero; hence, the measurements update is given a low weight. On the other hand, with a high confidence in the measurements ($\mathbf{R} \rightarrow \mathbf{0}$) the Kalman gain approaches $\mathbf{C}^{-1}$. In this case the measurements have a higher significance compared to state predictions.

2.4.2 Quasi-Static Approach. The quasi-static (QS) method employs a low-fidelity approach, where the bearing loads are considered stationary, reactionary forces proportional to the drivetrain torque. This approach is used in a similar fashion for the calculation of gear contact forces in [18]. Contrary to the Kalman filter, the QS state estimates are solely based on the physical model (Eq. (12)) and do not take into account vibration measurements (Eq. (13)). Additionally, the assumption is made that the drivetrain is in quasi-static equilibrium and that internal dynamics are negligible. In the case quasi-static of equilibrium, where $\mathbf{x}_{n+1} - \mathbf{x}_n = \mathbf{0}$, the physical model (Eq. (12)) reduces to

$$\mathbf{0} = (\mathbf{A_d} - \mathbf{I})\mathbf{x}_n + \mathbf{B_d}\mathbf{u}_n + \mathbf{w}_n \qquad (23)$$

Consequently, the state estimates can directly be determined from the input variable (generator torque) by disregarding the process noise

$$\hat{\mathbf{x}}_{\text{QS},n} = -(\mathbf{A_d} - \mathbf{I})^{-1}\mathbf{B_d}\mathbf{u}_n \qquad (24)$$

2.4.3 Least-Squares Approach. A least-squares approach to inverse state and load estimation is applied in [17,26,27]. This approach can be thought of as an asymptotic version of the Kalman filter with high confidence in the measurements and low confidence in the physical model. In this case only the observation model (Eq. (13)) of the state-space model is considered

$$\mathbf{y_n} = \mathbf{Cx_n} + \mathbf{Du_n} + \mathbf{v_n} \qquad (25)$$

The state estimates are found by minimizing the least-squares error function

$$\hat{\mathbf{x}}_{\text{LS},n} = \arg\min_{\mathbf{x_n}} (\mathbf{y_n} - \mathbf{Cx_n} - \mathbf{Du_n})^{\mathbf{T}}(\mathbf{y_n} - \mathbf{Cx_n} - \mathbf{Du_n}) \qquad (26)$$

The solution of the least-squares problem in closed form is given with the Moore–Penrose pseudoinverse $\mathbf{C^+}$

$$\hat{\mathbf{x}}_{\text{LS},n} = \mathbf{C^+}(\mathbf{y_n} - \mathbf{Du_n}) \qquad (27)$$

2.5 Fatigue Damage Model.
The Palmgren–Miner linear damage hypothesis [18] is assumed for the calculation of the fatigue damage, where n_i denotes the experienced stress cycles, N_i the number of cycles until failure, and i indicates the stress range

$$D = \sum_i \frac{n_i}{N_i} \qquad (28)$$

For calculation of N_i the nominal bearing life equation according to ISO 281 [28] with the basic dynamic load rating C and the equivalent bearing load P is used

$$N_i = \left(\frac{C}{P}\right)^{\frac{10}{3}} \qquad (29)$$

P is a linear combination of the axial and radial load with the factors X and Y, which are bearing specific values taken from the

manufacturer's data

$$P = X \cdot F_{ax} + Y \cdot F_{rad} \qquad (30)$$

The stress cycles n_i are counted with the load duration distribution (LDD) method according to IEC 61400-4 [19]. The LDD method is applicable for rotating machinery components under slowly varying loads that experience cyclic loading due to entering and exiting the load zone each rotation. One stress cycle is counted for each rotation with a stress range equal to the current load.

The remaining useful life can be estimated by monitoring the accumulated fatigue damage $D(t)$ over time and observing the damage reserves. By definition, the end of the component's nominal design life t_{nom} is reached at $D = 1$ [18]. Hence, the RUL is retrieved as follows:

$$RUL(t) = [1 - D(t)]t_{nom} \qquad (31)$$

3 Discussion

The virtual load sensor using the state estimators Kalman filter (KF), Least-Square (LS), and Quasi-Static (QS) presented in Sec. 2.4 are evaluated in a case study. Radial loads at the IMS and HSS bearings estimated with the virtual sensor are compared to simulation measurements obtained from the high-fidelity drivetrain model outlined in Sec. 2.3. First, the correlation of estimated and measured loads is analyzed in the time and frequency domain. Secondly, the error in calculated fatigue damage is discussed.

3.1 Estimated Loads. For a qualitative assessment the time series of measured and estimated radial loads in the IMS-A and HSS-A bearings is shown in Figs. 3 and 4. The measured loads f can be characterized as highly dynamic with lower frequency dynamic components (<10 Hz) as a result of slowly changing environmental conditions, as well as higher frequency dynamics (>100 Hz) induced by internal gearbox excitations such as gear

meshing. The load estimates of the QS method $\hat{f}_{QS}$ are sufficient to capture the long-term trend of bearing loads, but unable to reproduce any high-frequency internal dynamics seen at a time scale of 1 s. However, a slight bias at the HSS-A is observed, which could potentially be due to non-torque loads at the high-speed gear stage, which the torque-proportional QS does not take into account. The LS method produces load estimates $\hat{f}_{LS}$ with high-frequency oscillations of similar amplitudes to measured loads, however at the IMS-A there appear to be several outliers, which significantly overestimate measured loads. In the low-frequency range, the LS method is not able to fully capture the internal gearbox dynamics. This is especially noticeable at the IMS-A, where the measured loads have a high-energy frequency component of about 5 Hz. The KF load estimates $\hat{f}_{KF}$ are smoother and do not suffer from extreme outliers. Similar to the LS method high-frequency oscillations are captured well, while some lower frequency components are not reflected.

For the analysis of the behavior in the frequency domain the power spectral densities (PSD) of measured and estimated bearing loads are calculated, as shown in Figs. 5 and 6. The measured load spectrum shows several lower-frequency peaks (<10 Hz) and higher-frequency peaks at 80 Hz for IMS-A and at 464.2 Hz for HSS-A. The higher frequency peaks coincide with the gear meshing frequencies of the parallel and second planetary gear stage, respectively. The lower frequency peaks are not fully identified as of now.

The QS method matches the measured load spectrum of HSS-A reasonably well with the exception of the high-frequency range with the gear meshing peak, which is underestimated significantly. In the low frequency range the peaks at 4.75 Hz, 9.47 Hz, and 14.22 Hz are matched. These likely correspond to pure torsional oscillations of the HSS, which directly translate to oscillations in the generator torque. The dynamics of the IMS are not represented well with the QS method, as the QS load spectrum shows significantly lower energy in all frequencies.

In addition to the torsional oscillation peaks both the LS and KF method are able to match the gear meshing peaks. In the high-

Fig. 3 Long-term and short-term time series of measured loads f and estimated loads $\hat{f}$ at IMS-A bearing
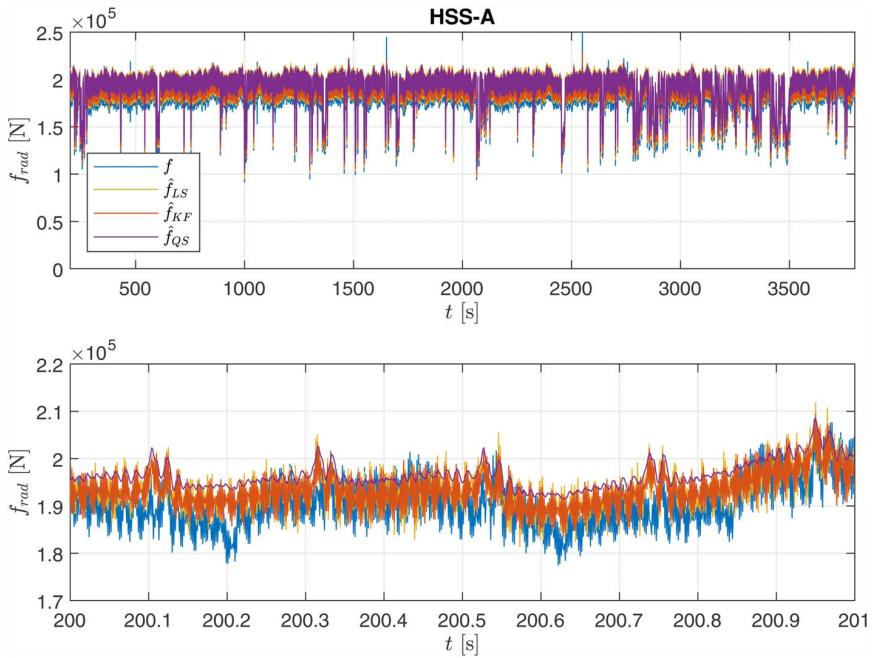
Fig. 4 Long-term and short-term time series of measured loads *f* and estimated loads *f̂* at HSS-A bearing
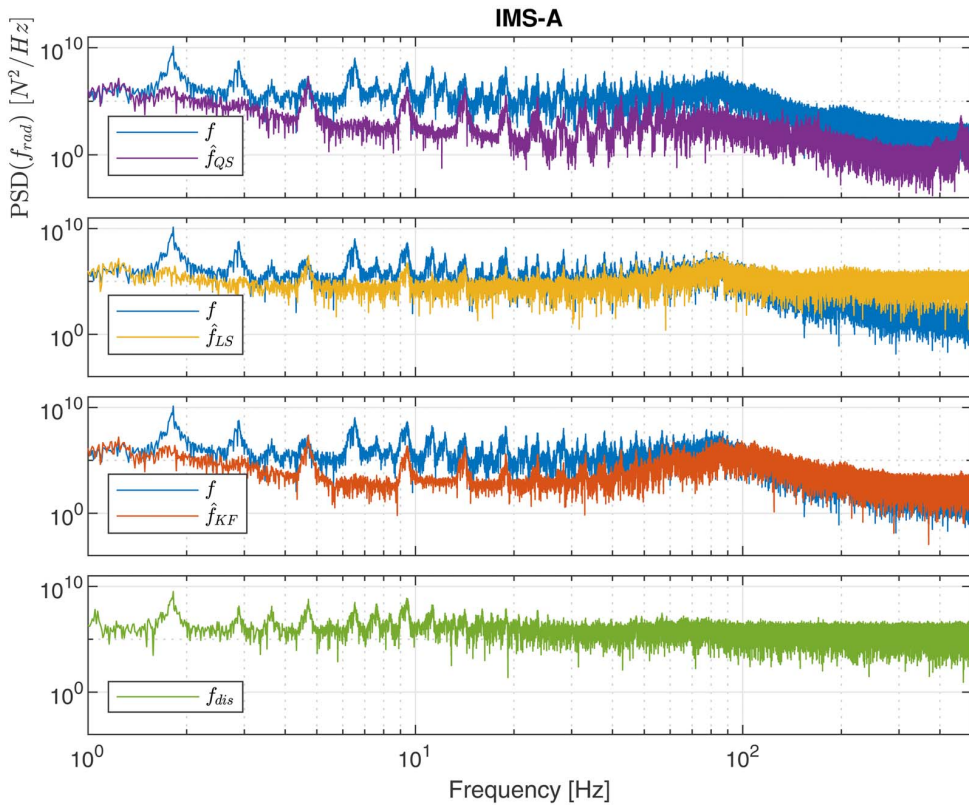
Fig. 5 Frequency spectrum of measured and estimated radial loads at IMS-A bearing for full time series (3600 s)
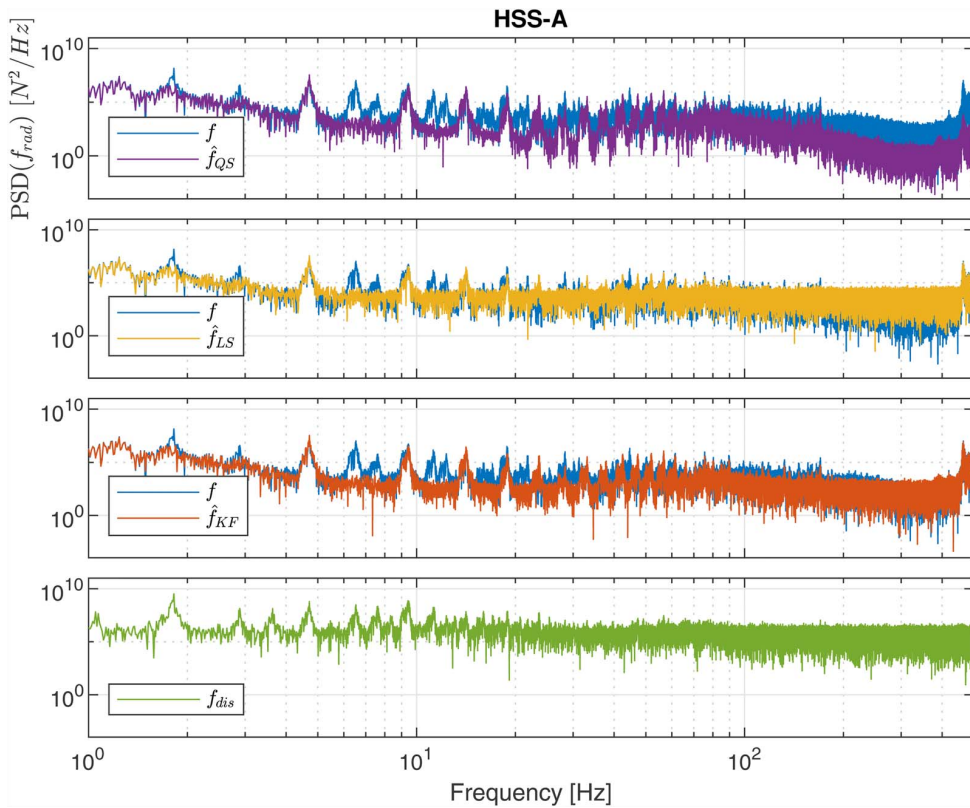
Fig. 6 Frequency spectrum of measured and estimated radial loads at HSS-A bearing for full time series (3600 s)

frequency range the LS method leads to a significant overestimation due to a high confidence in noisy measurements. The KF load estimates achieve a higher correlation by weighing the measurement update according to the measurement noise covariance R and thus filtering outliers. In the lower frequency range some peaks at 1.83 Hz, 2.91 Hz, and 6.58 Hz, which are more pronounced at the IMS-A, are missed by both the LS and KF methods.

The missed lower-frequency peaks likely relate to radial disturbance forces f_{dis} on the IMS, as the spectrum of measured disturbance forces suggests. The measured disturbance forces are extracted from the high-fidelity drive train simulations as connection forces of the second planetary gear stage to the IMS and show several low-frequency components of higher energy. The load estimation methods are unable to take these into account via state predictions since the disturbance forces are assumed as white gaussian process noise in the underlying physical model. Furthermore, it is challenging to consider low-frequency disturbance force excitations via vibration measurements, because these cause

relatively low acceleration responses with a low signal-to-noise ratio.

For a quantitative assessment of the load correlation, the Pearson correlation coefficient is calculated for the complete time series of 3600 s, as shown in Table 2. The correlation of IMS loads is quite poor, as the studied methods are unable to reproduce aforementioned low-frequency load components. The KF is the best performing method, resulting in correlation values of 0.50–0.61. At the HSS, the QS method is sufficient to estimate bearing loads with high correlation ($R > 0.8$), as internal dynamics have less significance here. The LS and KF method do not lead to significant improvements at the HSS.

3.2 Fatigue Damage. Shown in Table 3 are the relative fatigue damage errors $(\hat{D} - D)/\hat{D}$ for the IMS and HSS bearings. The QS method results in low errors of 5–15% across all bearings in the considered load case. The results of the higher fidelity methods

Table 2 Correlation of estimated loads

	QS	LS	KF
IMS-A	0.36	0.48	0.50
IMS-B	0.43	0.37	0.58
IMS-C	0.42	0.35	0.61
HSS-A	0.96	0.95	0.96
HSS-B	0.82	0.83	0.85
HSS-C	0.84	0.84	0.83

Table 3 Fatigue damage error

	QS (%)	LS (%)	KF (%)
IMS-A	11.8	11.6	12.3
IMS-B	5.7	0.8	3.8
IMS-C	−9.4	−13.6	−11.1
HSS-A	−5.2	−6.1	−5.9
HSS-B	10.7	8.3	8.5
HSS-C	15.2	11.2	11.4

LS and KF differ only marginally from those of the QS method despite considering internal dynamics and providing load estimates of higher correlation. The error can be slightly reduced at the bearings IMS-B and HSS-B,C, however at the bearings IMS-C and HSS-A a slightly higher error is calculated. These results suggest that for the considered load case and drive train design, the fatigue damage at the IMS and HSS bearings is mainly dependent on the drive train torque and effects of internal gearbox dynamics are negligible. This becomes more clear when looking at the bearing stress cycles, which are not only a function of the load oscillations depicted in Fig. 3 but also of the rotational speed [18]. A rotating bearing experiences cyclic loading due to entering and exiting its load zone. This is reflected in the use of the stress cycle counting method LDD as opposed to the rainflow counting (RFC) method, which is commonly used for structural elements. The LDD method counts one stress cycle per revolution with a stress range equal to the current radial load. Thus, the quasi-static reactionary forces to the drive train torque cause major stress ranges and contribute significantly to the bearing fatigue, whereas the load variations from internal dynamics cause comparatively small stress ranges. In the studied load case at rated wind speed under normal operational conditions, the QS method would be sufficient to monitor fatigue damage with high accuracy and computational speed. However, it is uncertain how the QS method would perform in load cases with greater internal dynamics, such as an emergency stop or gear faults. Further studies are planned to address this topic.

4 Conclusion

In this article a novel approach for the estimation of wind turbine gearbox loads with the purpose of online fatigue damage monitoring was presented. The proposed method employs a Digital Twin framework and aims at continuous estimation of the dynamic states based on CMS vibration data and generator torque measurements from the SCADA data. The proposed method was evaluated in a load case at rated wind speed under normal operational conditions. With a quasi-static approach, which assumes proportionality to the drive train torque, the overall level of bearing loads was estimated with high accuracy, however the dynamic behavior was not reflected well. The quasi-static method was sufficient to estimate fatigue damage with an error of 5–15% across all bearings. The Kalman filter approach produced the highest correlation of bearing loads ranging from 0.5 to 0.96 and was able to capture high-frequency dynamics accurately, but missed several low-frequency components. These are caused by disturbance forces on the IMS, which are not reflected in the underlying physical model and are not available through measurements. Despite considering internal dynamics, the KF method did not result in significant improvements with reference to fatigue damage. It appears that in this load case the stress cycles caused by internal dynamics are insignificant relative to torque induced stress cycles. The least-squares estimator performed worse than the Kalman filter, as it is more sensitive to measurement noise. Further studies are planned to extend this work to different load cases or fault cases, assess the sensitivity to measurement noise and model uncertainties and quantify computational costs.

Acknowledgment

Conflict of Interest

There are no conflicts of interest.

Data Availability Statement

The datasets generated and supporting the findings of this article are obtainable from the corresponding author upon reasonable request.

References

[1] Kumar, Y., Ringenberg, J., Depuru, S., Devabhaktuni, V. K., Lee, J., Nikolaidis, E., Andersen, B., and Afjeh, A., 2016, "Wind Energy: Trends and Enabling Technologies," Renewable. Sustainable. Energy. Rev., **53**(1), pp. 209–224.

[2] Stehly, T., and Beiter, P., 2020, 2018 Cost Of Wind Energy Review. Report, National Renewable Energy Laboratory.

[3] Faulstich, S., Hahn, B., and Tavner, P. J., 2011, "Wind Turbine Downtime and Its Importance for Offshore Deployment," Wind Energy, **14**(3), pp. 327–337.

[4] Carroll, J., McDonald, A., and McMillan, D., 2016, "Failure Rate, Repair Time and Unscheduled O&M Cost Analysis of Offshore Wind Turbines," Wind Energy, **19**(6), pp. 1107–1119.

[5] Randall, R. B., 2010, Vibration Based Condition Monitoring: Industrial, Aerospace and Automotive Applications, Wiley & Sons Ltd., Hoboken, NJ.

[6] Johansen, S. S. N., and Nejad, A. R., 2019, "On Digital Twin Condition Monitoring Approach for Drivetrains in Marine Application," Proceedings of the ASME 2019 38th International Conference on Ocean, Offshore and Arctic Engineering, Glasgow, Scotland, UK, June 9–14.

[7] Rasheed, A., San, O., and Kvamsdal, T., 2020, "Digital Twin: Values, Challenges and Enablers From a Modeling Perspective," IEEE Access, **8**(1), pp. 21980–22012.

[8] Mehlan, F. C., Pedersen, E., and Nejad, A R, 2022, "Modelling of Wind Turbine Gear Stages for Digital Twin and Real-Time Virtual Sensing Using Bond Graphs," J. Phys.: Conf. Ser. **2265**(032065).

[9] Nejad, A. R., Bachynski, E. E., Kvittem, M. I., Luan, C., Gao, Z., and Moan, T., 2015, "Stochastic Dynamic Load Effect and Fatigue Damage Analysis of Drivetrains in Land-Based and TLP, Spar and Semi-Submersible Floating Wind Turbines," Mar. Struct., **42**(1), pp. 137–153.

[10] Branlard, E., Giardina, D., and Brown, C. S. D., 2020, "Augmented Kalman Filter With a Reduced Mechanical Model to Estimate Tower Loads on a Land-based Wind Turbine: A Step Towards Digital-Twin Simulations," Wind Energy Sci., **5**(3), pp. 1155–1167.

[11] Iliopoulos, A., Weijtjens, W., Van Hemelrijck, D., and Devriendt, C., 2017, "Fatigue Assessment of Offshore Wind Turbines on Monopile Foundations Using Multi-band Modal Expansion," Wind Energy, **20**(8), pp. 1463–1479.

[12] Bosmans, J., Vanommeslaeghe, Y., Geens, J., Fiszer, J., Croes, J., Kirchner, M., Denil, J., De Meulenaere, P., and Desmet, W, 2020, "Development and Embedded Deployment of a Virtual Load Sensor for Wind Turbine Gearboxes," J. Phys.: Conf. Ser. **1618**(022011).

[13] Jonkman, J., Butterfield, S., Musial, W., and Scott, G., 2009, Definition of A 5-MW Reference Wind Turbine for Offshore System Development. Report, National Renewable Energy Laboratory (NREL).

[14] Jonkman, J., 2010, Definition of the Floating System for Phase IV of OC3. Report, National Renewable Energy Laboratory (NREL).

[15] Nejad, A. R., Guo, Y., Gao, Z., and Moan, T., 2016, "Development of a 5 MW Reference Gearbox for Offshore Wind Turbines," Wind Energy, **19**(6), pp. 1089–1106.

[16] Kahraman, A., 1994, "Dynamic Analysis of a Multi-Mesh Helical Gear Train," ASME J. Mech. Des., **116**(3), pp. 706–712.

[17] Zhu, T., Xiao, S., Yang, G., Ma, W., and Zhang, Z., 2013, "An Inverse Dynamics Method for Railway Vehicle Systems," Transport, **29**(1), pp. 107–114.

[18] Nejad, A. R., Gao, Z., and Moan, T., 2014, "On Long-Term Fatigue Damage and Reliability Analysis of Gears Under Wind Loads in Offshore Wind Turbine Drivetrains," Int. J. Fatigue., **61**(1), pp. 116–128.

[19] IEC 61400-4, 2012. Wind Turbines, Part 4: Standard for Design and Specification of Gearboxes.

[20] Petersen, Ø. W., Øiseth, O., and Lourens, E., 2019, "Full-Scale Identification of the Wave Forces Exerted on a Floating Bridge Using Inverse Methods and Directional Wave Spectrum Estimation," Mech. Syst. Signal. Process., **120**(1), pp. 708–726.

[21] Hwang, J.-S., Kareem, A., and Kim, H., 2011, "Wind Load Identification Using Wind Tunnel Test Data by Inverse Analysis," J. Wind Eng. Ind. Aerodyn., **99**(1), pp. 18–26.

[22] Maes, K., Weijtjens, W., de Ridder, E. J., and Lombaert, G., 2018, "Inverse Estimation of Breaking Wave Loads on Monopile Wind Turbines," Ocean. Eng., **163**, pp. 544–554.

[23] Zhi, L.-h., Fang, M.-x., and Li, Q. S., 2017, "Estimation of Wind Loads on a Tall Building by an Inverse Method," Struct. Control Health Monit., **24**(4), p. e1908.

[24] Siegrist, P. M., and McAree, P. R., 2006, "Tyre-force Estimation by Kalman Inverse Filtering: Applications to Off-highway Mining Trucks," Vehicle Syst. Dyn., **44**(12), pp. 921–937.

[25] Welch, G., and Bishop, G., 1997, "An Introduction to the Kalman Filter."

[26] Kazemi Amiri, A., and Bucher, C., 2017, "A Procedure for In Situ Wind Load Reconstruction From Structural Response Only Based on Field Testing Data," J. Wind Eng. Ind. Aerodyn., **167**(1), pp. 75–86.

[27] Uhl, T., 2006, "The Inverse Identification Problem and Its Technical Application," Arch. Appl. Mech., **77**(5), pp. 325–337.

[28] ISO 281, 2007. Rolling Bearings—Dynamic Load Ratings and Rating Life.

A.4   Paper 4

Paper 4:
Virtual sensing of wind turbine hub loads and drivetrain fatigue damage.
Authors: Felix C. Mehlan, Jonathan Keller, Amir R. Nejad
Published in *Forschung im Ingernieurwesen*, 2023, DOI:
10.1007/s10010-023-00627-0.

ORIGINALARBEITEN/ORIGINALS

Virtual sensing of wind turbine hub loads and drivetrain fatigue damage

Felix C. Mehlan[1] [ID] · Jonathan Keller[2] · Amir R. Nejad[1]

Abstract

This paper presents a Digital Twin for virtual sensing of wind turbine aerodynamic hub loads, as well as monitoring the accumulated fatigue damage and remaining useful life in drivetrain bearings based on measurements of the Supervisory Control and Data Acquisition (SCADA) and the drivetrain condition monitoring system (CMS). The aerodynamic load estimation is realized with data-driven regression models, while the estimation of local bearing loads and damage is conducted with physics-based, analytical models. Field measurements of the DOE 1.5 research turbine are used for model training and validation. The results show low errors of 6.4% and 1.1% in the predicted damage at the main and the generator side high-speed bearing respectively.

Virtuelle Sensoren für die Messung von Hauptwellenlasten und Ermüdungsschäden im Antriebstrang von Windenergieanlagen

Zusammenfassung

In diesem Aufsatz wird ein digitaler Zwilling für Windenergieanlagen vorgestellt, welcher die virtuelle Erfassung der Hauptwellenlasten und die Zustandsüberwachung von Ermüdungschäden und der verbleibende Nutzungsdauer der Antriebsstranglager ermöglicht. Der digital Zwilling nutzt Messdaten des Supervisory Control and Data Acquisition (SCADA) Systems und des Zustandsüberwachungssystems des Antriebsstranges (CMS). Die Berechnung der Hauptwellenlasten ist mit datenbasierten Regressionsmodellen umgesetzt, während die Berechnung der Lagerkräfte und der Ermüdungsschaden mit physikbasierten Modelle durchgeführt wird. Für die Modellentwicklung und -validierung werden Feldmessdaten der DOE 1.5 MW Turbine eingesetzt. Die Abweichungen in den Ermüdungsschäden am Hauptwellenlager und am Generatorwellenlager betragen lediglich 6,4 % beziehungsweise 1,1 %.

1 Introduction

Offshore wind turbine installations are projected to accelerate rapidly in the near future driven by better wind resources and higher social acceptance rates compared to onshore sites [24]. However, a major economic limitation of off-

shore wind turbines are high operational and maintenance expenditures (OPEX), which amount to about 34 % of the levelized cost of energy (LCOE) [19]. These are caused by lower reliability due to harsher environmental conditions and time-consuming replacement or repair due to difficulties accessing the site and dependency on good weather conditions. A major contributor to OPEX is the geared drivetrain with frequent failures and long downtimes and is thus the subject of current research [23].

Digital Twin (DT) is an emerging technology with prospects of decreasing operational and maintenance expenditures and improving the market competitiveness of offshore wind farms. The wind turbine drivetrain DT proposed by the authors in [readacted] would enable monitoring of fatigue loads at otherwise inaccessible locations such as bearings and gear contacts using 'virtual sensors'

✉ Felix C. Mehlan
  felix.c.mehlan@ntnu.no

Jonathan Keller
  jonathan.keller@nrel.gov

Amir R. Nejad
  amir.nejad@ntnu.no

1 IMT, NTNU, Jonsvannsveien 82, 7050 Trondheim, Norway

2 NREL, 15013 Denver W Pkwy, Golden, 80401, USA
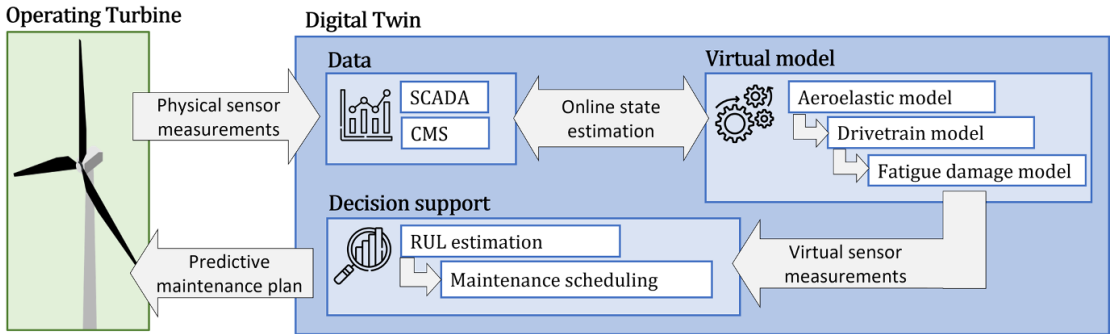
Fig. 1 Digital Twin framework for continuous remaining useful life estimation in wind turbine drivetrain components

and thus support Remaining Useful Life (RUL) assessment based on the true load history. A framework with the three components Data, Virtual model and Decision support is envisioned for this objective (Fig. 1). *Data* is collected continuously by sensors of the Supervisory Control and Data Acquisition system (SCADA), the condition monitoring system (CMS), and from other sources such as metocean forecasts and maintenance logs. The *Virtual model* comprises of decoupled simulation models to represent the physics at different scales. Aerodynamics and structural dynamics of tower and blades are captured with the aeroelastic model. The resulting hub loads and nacelle motions are imposed as boundary conditions on the drivetrain model, which produces local bearing and gear forces. These are used as input for the fatigue damage model consisting of stress cycle counting algorithms and S-N curves. The virtual model and its physical counterpart are synchronized with real-time field measurements using state estimators such as the Kalman Filter. The synchronization, also referred to as data fusion or Digital Twinning, is essential as it facilitates measurements of virtual sensors in the synchronized model. The virtual sensor measurements are converted to value adding information for the turbine operator in the component called *Decision support*. In this study the focus is on RUL assessment of drivetrain components, which is necessary to move from corrective to predictive maintenance strategies.

Preliminary investigations on the feasibility of the proposed DT have been conducted in a numerical case study in [redacted]. In this study the proposed DT is further validated with with field measurements of the DOE 1.5 MW turbine instrumented by NREL [18]. Main bearing loads estimated with the proposed virtual sensing method are compared to field measurements obtained from shaft strain gauges under different operational conditions.

Other studies are found in literature, which are concerned with estimating main shaft loads with a virtual sensing approach. Several works pursue an inverse approach for real-time estimation of the rotor torque based on SCADA measurements. By simplifying the drivetrain dynamics to a two degrees of freedom (DOF) torsional system, the SCADA signals generator torque along with the LSS and HSS speeds contain enough information to predict the unknown rotor torque [3, 12, 15, 17]. The drivetrain model may be constructed without knowledge of manufacturer's specifications using data-driven system identification techniques such as least-squares estimators [15]. Data fusion is realized with state estimators, for example Kalman Filters (KF) [15], or regularization methods [17].

Several works are concerned with virtual sensing of rotor thrust, but with the objective of structural health monitoring of the tower rather than drivetrain components. A common approach involves constructing a dynamic, flexible tower model and use state estimation methods based on tower top acceleration and/or strain gauge measurements [20].

Notable publications that fit the proposed Digital Twin framework (Fig. 1) are presented by Branlard et al. and Azzam et al. [2, 4]. Branlard et al. present a holistic wind turbine DT capable of estimating both thrust and torque based on SCADA measurements and a linearized aeroelastic model [4]. Validation of the DT is conducted with both simulation and field measurements, however the scope is limited to structural dynamics of the tower and blades. Azzam et al. present a DT that also considers drivetrain dynamics [2]. The DT is constructed by regression on aeroelastic and drivetrain multi-body simulations and serves the purpose of estimating all six main shaft load components based on SCADA measurements. Unfortunately, their work is purely numerical and not supported by experimental or field measurements.

The novel contributions of this paper in comparison to existing research are summarized as follows.

- Validating the concept of virtual sensing of drivetrain loads with field measurements rather than numerical simulations

Fig. 2 Overall methodology for virtual sensing of drivetrain loads and remaining useful life estimation
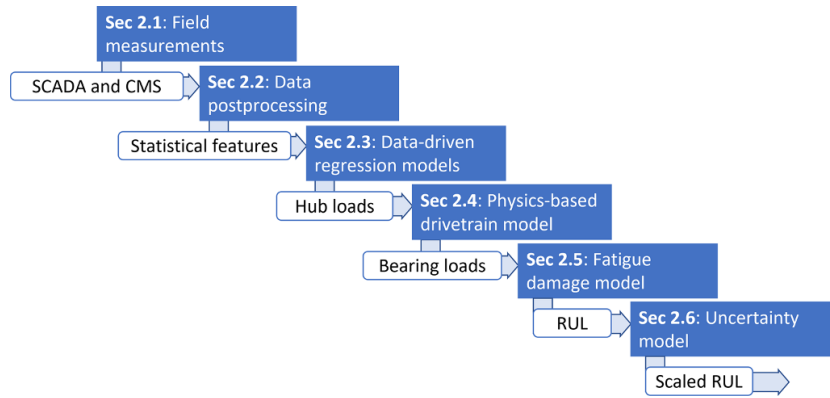
- Monitoring fatigue damage in drivetrain components rather than the tower or blades
- Leveraging high-frequency CMS vibration measurements as opposed to using only SCADA measurements

The remainder of this paper is organized as follows. Sect. 2 presents the proposed methodology for virtual sensing of drivetrain loads and remaining useful life estimation. It follows a discussion of the errors between field measurements and predictions using the virtual sensors in Sect. 3. Concluding remarks are given in Sect. 4.

2 Methodology

The overall methodology is illustrated in Fig. 2. Several SCADA and CMS signals, described in Sect. 2.1, are filtered and postprocessed to extract statistical features (Sect. 2.2). Data-driven regression models are then trained to map the SCADA and CMS features onto measured aerodynamic hub loads (torque, yaw moment, pitch moment, thrust), as detailed in Sect. 2.3. Local forces at the main bearing and the high-speed shaft generator side (HSS-GS) bearing are then calculated with a low-fidelity, physics-based drivetrain model, presented in Sect. 2.4. The remaining useful life (RUL) is estimated based on the fatigue

Table 1 Field measurements of the DOE 1.5 turbine [18] used in this study

Category	Signal	Sensor type	Symbol
SCADA	Active Power	Voltage	P
	LSS speed	Encoder	ω_{LSS}
	HSS speed	Encoder	ω_{HSS}
	Nacelle wind speed	MET tower	u
	Acceleration tower top east-west	Accelerometer	$a_{Nac,EW}$
	Acceleration tower top north-south	Accelerometer	$a_{Nac,NS}$
CMS	Acceleration generator back	Accelerometer	$a_{Gen,B}$
	Acceleration generator front	Accelerometer	$a_{Gen,F}$
	Acceleration HSS generator side	Accelerometer	$a_{HSS,GS}$
	Acceleration HSS rotor side	Accelerometer	$a_{HSS,RS}$
	Acceleration Planetary	Accelerometer	a_{PL}
	Acceleration Torque arm 1 frame	Accelerometer	$a_{TA1,F}$
	Acceleration Torque arm 1 horizontal	Accelerometer	$a_{TA1,H}$
	Acceleration Torque arm 1 vertical	Accelerometer	$a_{TA1,V}$
	Acceleration Torque arm 2 horizontal	Accelerometer	$a_{TA2,H}$
	Acceleration Torque arm 2 vertical	Accelerometer	$a_{TA2,V}$
Hub loads	Torque	Main shaft strain gauges	$M_{a,x}$
	Pitch moment	Main shaft strain gauges	$M_{a,y}$
	Yaw moment	Main shaft strain gauges	$M_{a,z}$
	Thrust	Tower base strain gauges	$F_{a,x}$

damage model of ISO 281 (Sect. 2.5). Lastly, the RUL is scaled with a safety factor to account for uncertainties in the load estimation (Sect. 2.6).

2.1 Description of dataset

The dataset was acquired as part of a field measurement campaign with the U.S. Department of Energy 1.5 MW (DOE 1.5) turbine at the National Renewable Energy Laboratory (NREL) [18]. The DOE 1.5 turbine is based on a commercial GE 1.5 SLE turbine with a custom configuration. In addition to a standard SCADA system and drivetrain CMS the turbine is equipped with strain gauges at the tower base, tower top, blade roots and the main shaft to fully monitor multiaxial aerodynamic loads.

The sensor signals used in this study are listed in Table 1. The following SCADA signals are considered in this study, which are reportedly sensitive to the main shaft loading: Active power, HSS and LSS speed, Nacelle wind speed, as well as tower top acceleration. The CMS sensors are installed in a typical configuration and positioned on the housing of the generator (Gen), the high-speed gear stage (HSS), planetary gear stage (PL) and each of the torque arms (TA). The aerodynamic loads at the rotor hub including the torque, pitch moment, yaw moment and thrust are measured with strain gauges at the main shaft downwind of the main bearing and at the tower base. The calibration of the strain gauges is described in [18].

The dataset used in this study comprises of a total of 830 measurements of 10 min length recorded from 31. Oct 2018 to 05. Dec 2018. The sampling frequency is 50 Hz for all signals.

2.2 Data postprocessing

The dataset is filtered for normal power production, which is identified by three criteria

- Main shaft speed > 10.5 rpm
- Blade 1 pitch angle < 50°
- Active power > 0 kW

In addition, a moving average filter with window size of 1 s is applied on the recorded strain gauge signals.

Best practice in drivetrain condition monitoring is the extraction of statistical features, which are indicative of faults or damage [16]. The recorded SCADA and CMS measurements are partitioned into 10 min segments and the features listed in Table 2 are calculated for each segment. These include a wide range of the most commonly used features in the time domain (x) and frequency domain (S_{xx}). The features that are eventually utilized as input for the regression models are determined by a sensitivity analysis in Sect. 3.2.

2.3 Data-driven regression models

Regression models are used in this study to map the predictors, the SCADA and CMS statistical features, onto the targets, the aerodynamic hub loads. Several linear and nonlinear regression models are investigated for this purpose including Linear Regression (LR), Support Vector Machine (SVM) and Tree ensembles, as described in Table 3. For a detailed description of each regression model type it is referred to [6]. Implementation and training is realized with MATLAB's Statistics and Machine Learning Toolbox [9]. The dataset is partitioned 80/20 into training data and test data, and the models are regressed onto the training data

Table 2 Statistical features calculated for SCADA and CMS signals

Feature	Symbol	Formula
Mean	μ	$E\left[x\right]$
Standard deviation	σ	$\sqrt{E\left[\left(\frac{x-\mu}{\sigma}\right)^2\right]}$
Skewness	skew	$E\left[\left(\frac{x-\mu}{\sigma}\right)^3\right]$
Kurtosis	kurt	$E\left[\left(\frac{x-\mu}{\sigma}\right)^4\right]$
Root mean square	RMS	$\sqrt{\frac{1}{N}\sum_{n=1}^{N}x_n^2}$
Maximum	max	$\max_n x$
Minimum	min	$\min_n x$
Peak amplitude	peak	$\max_n x - \min_n x$
1P-amplitude	A_{1P}	$\parallel S_{xx}(f_{1P}) \parallel$
2P-amplitude	A_{2P}	$\parallel S_{xx}(f_{2P}) \parallel$
3P-amplitude	A_{3P}	$\parallel S_{xx}(f_{3P}) \parallel$

Table 3 Statistical regression models for predicting hub loads based on SCADA and CMS measurements

Regression model	Hyperparameters		Training function
Linear regression (LR)	–		Least squares
Support vector machine	KernelFunction	Linear/quadratic	Least squares
(SVM)	BoxConstraint	Default	
	KernelScale	Default	
	Epsilon	Default	
Tree ensemble	MinLeafSize	8	Least-squares boosting/
(Boosted Trees/Bagged Trees)	NumLearningCycles	30	Bootstrap aggregation
	LearnRate	0.1	

Fig. 3 Definition of forces and moments
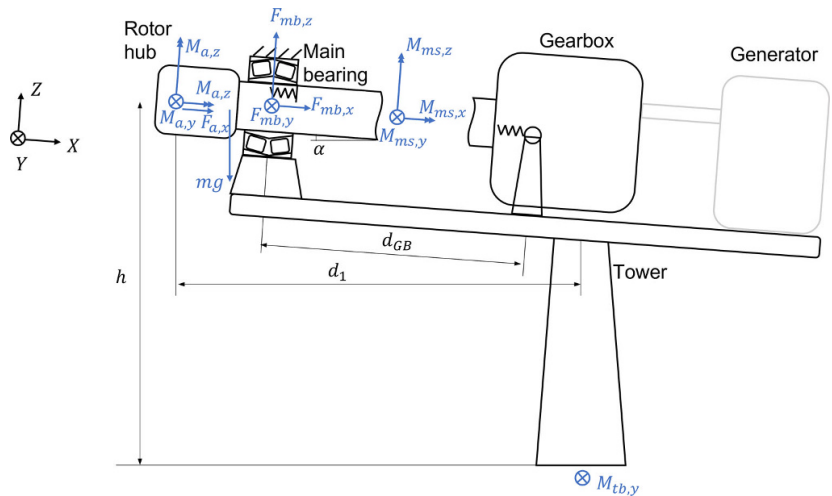
using least squares regression and five-fold cross validation. Hyperparameters are not optimized and are set to the default values provided by MATLAB.

2.4 Physics-based drivetrain model

The DOE 1.5 MW turbine is instrumented with strain gauges at the blade roots, the main shaft and the tower top and base to monitor the multiaxial loading of the turbine. The aerodynamic loads at the rotor hub, as well as loads at the main bearing and HSS-GS bearing are calculated from strain gauge measurements using an analytical model, presented in [1, 5]. The analytical model assumes steady state operation and neglects any torsional or bending dynamics of the main shaft and the tower. With this assumption it is possible to determine bearing loads by moment balances.

First, the aerodynamic moments including torque $M_{a,x}$, pitch moment $M_{a,y}$ and yaw moment $M_{a,z}$ are determined from the measured main shaft moments M_{ms} by moment balance around the main bearing (Fig. 3) and expressed in the fixed coordinate frame at the hub. The thrust $F_{a,x}$ is calculated from the tower base moment $M_{tb,y}$ by moment balance around the tower base (Fig. 3)

$$M_{a,x} = M_{ms,x} \tag{1}$$

$$M_{a,y} = M_{ms,y} - M_{ms,y0} \tag{2}$$

$$M_{a,z} = M_{ms,z} \tag{3}$$

$$F_{a,x} = -\frac{M_{a,y} + M_{tb,y} - M_{tb,y0}}{h\cos(\alpha) - d_1\sin(\alpha)} \tag{4}$$

where $M_{ms,y0}$ and $M_{tb,y0}$ are gravitational moments due to the rotor overhang expressed at the main bearing and tower base respectively, h denotes the tower height, d_1 the

distance from the hub to the tower top and α the main shaft tilt angle (Table 4)

The installed main bearing is a SKF 240/600 BC spherical roller bearing in a 3-point configuration and thus considered to only support radial and axial forces. The torque arms are also considered to only experience radial and axial forces and the stiffness of the generator coupling is neglected. In steady state operation the main bearing forces F_{mb} are then calculated as follows (Eqs. 5–7). The axial force is governed by thrust, while the radial force is governed by the yaw and pitch moments.

$$F_{mb,x} = F_{mb,x0} + F_{a,x} \tag{5}$$

$$F_{mb,y} = -M_{a,z}/d_{GB} \tag{6}$$

$$F_{mb,z} = F_{mb,z0} - M_{a,y}/d_{GB} \tag{7}$$

where $F_{mb,x0}$ and $F_{mb,z0}$ is the rotor, shaft and gearbox weight projected onto the x an z axis respectively and d_{GB} is the distance from the main bearing to the torque arms (Table 4).

The HSS-GS bearing is a SKF NU232 cylindrical roller bearing and thus only supports radial forces. The radial force is governed by the transmitted gear force at the high-speed gear stage, which is calculated from the rotor torque by neglecting all torsional dynamics

$$F_{HSS,rad} = \frac{M_{a,x}}{i_{GB}r_b}\frac{d_{RS}}{d_{GS}} \tag{8}$$

$$F_{HSS,x} = 0 \tag{9}$$

where i_{GB} denotes the gearbox ratio, r_b the base radius of the pinion and d_{RS}, d_{GS} the distance from the generator- and rotor side HSS bearings to the pinion center (Table 4).

Table 4 Parameters of analytical model for bearing load calculation according to [1, 5]

Parameter	Symbol	Unit	Value
Gravity force projected on x-axis	$F_{mb,x0}$	kN	43.0
Gravity force projected on z-axis	$F_{mb,z0}$	kN	618.0
Gravity moment at main bearing	$M_{ms,y0}$	kNm	−198.0
Gravity moment at tower base	$M_{tb,y0}$	kNm	−943.83
Tower height	h	m	80
Distance hub – tower top	d_1	m	3.65
Distance main bearing – torque arms	d_{GB}	m	2.09
Distance HSS-GS bearing – pinion	d_{GS}	mm	327.5
Distance HSS-RS bearing – pinion	d_{RS}	mm	225.5
HSS pinion base radius	r_b	mm	87.4
Main shaft tilt angle	α	deg	5
Gearbox ratio	i_{GB}	–	78.292
Main bearing axial load factor	Y_1	–	2.3
Main bearing axial load factor	Y_2	–	3.4
Main bearing limiting value	e	–	0.3
Main bearing basic dynamic load rating	C	kN	8502
HSS-GS bearing basic dynamic load rating	C	kN	585
Nominal design life	t_{nom}	year	20

2.5 Fatigue damage and remaining useful life

The bearing fatigue damage and remaining useful life is based on ISO 281 [7], which defines the equivalent dynamic load P for cylindrical roller bearings (CRB) and tapered roller bearings (TRB) as

$$\text{for CRB:} \quad P = F_{\text{rad}} \tag{10}$$

$$\text{for TRB:} \quad P = \begin{cases} F_{\text{rad}} + Y_1 F_{ax}, & \text{if } F_{ax}/F_{\text{rad}} \leq e \\ 0.67 F_{\text{rad}} + Y_2 F_{ax}, & \text{otherwise} \end{cases} \tag{11}$$

where Y_1, Y_2, e are bearing specific parameters (Table 4). The equivalent dynamic load is calculated with 10 min average load estimates denoted as $\overline{P}_i$. For each 10 min section indexed by i the permissible stress cycles N_i are then calculated with the bearing lifetime equation

$$N_i = 10^6 \left(\frac{C}{\overline{P}_i} \right)^m \tag{12}$$

where C is the basic dynamic load rating and m equals 10/3 for roller bearings. The experienced stress cycles n_i are determined using the load duration distribution (LDD) method, which counts one stress cycle per shaft revolution due to entering and exiting the bearing load zone [13]. Using 10 min average shaft speeds $\overline{\omega}_i$ the LDD method simplifies to

$$n_i = \overline{\omega}_i \, \Delta t, \tag{13}$$

where Δt equals 10 min. It follows the dimensionless short-term fatigue damage D_i^{ST}, which is defined as the ratio of experienced to permissible stress cycles

$$D_i^{ST} = n_i / N_i \tag{14}$$

The long-term damage $D^{LT}(t)$ is obtained with the Palmgren-Miner linear damage hypothesis by summation of all previous short-term damage and is updated in 10 min intervals for real-time damage monitoring

$$D^{LT}(t) = \sum_{i=0}^{t/\Delta t} D_i^{ST} \tag{15}$$

By definition, the bearing has consumed its damage reserves and reached its end of life at $D^{LT} = 1$. With a nominal life t_{nom} of 20 years the remaining useful life RUL is then calculated as follows

$$\text{RUL}(t) = t_{nom} \left(1 - D^{LT}(t) \right) \tag{16}$$

2.6 Damage uncertainty model

Using 10 min average load estimates for the damage calculation reduces computational costs and enables real-time monitoring, however it introduces uncertainties by neglecting high-frequency load fluctuations, which may originate in the aerodynamics or internal drivetrain dynamics. The damage is generally underestimated with averaged loads, since load peaks are disproportionally more damaging than load minima due to the exponentiation with m (Eq. 12). The

uncertainty χ_{avg} is expressed as the ratio of the true short-term damage $D^{ST}_{50\,Hz}$ measured at 50 Hz and the short term damage based on 10 min average load estimates $D^{ST}_{10\,min\text{-}avg}$. The fluctuations of the equivalent dynamic load within a 10 min period are modelled with a statistical variable $X \sim N(\mu, \sigma)$, which is normally distributed with mean value μ and standard deviation σ. It is further assumed that variations of the shaft speed are negligible, such that Eq. 13 remains valid. It follows for the uncertainty χ_{avg}

$$\chi_{avg} := \frac{D^{ST}_{50\,Hz}}{D^{ST}_{10\,min\text{-}avg}} = \frac{E(X^m)}{[E(X)]^m} \tag{17}$$

where the expected values E are given by the law of the unconscious statistician (LOTUS) [8] using the standard normal statistical variable $Z = \frac{X-\mu}{\sigma}$

$$E(X^m) = \frac{1}{\sqrt{2\pi}} \int_{-\infty}^{\infty} (\mu + \sigma z)^m \exp(-z^2/2)\,dz \tag{18}$$

$$E(X)^m = \mu^m \tag{19}$$

It is evident that the uncertainty χ_{avg} is only a function of the 10 min mean and standard deviation, which are both estimated with data-driven regression models (Sect. 2.3).

3 Results and Discussion

3.1 Measured hub loads and fatigue damage

Shown in Fig. 4 are the distributions of the measured hub loads for verification of the results. The mean torque follows the analytical thrust curve and levels out at rated torque, while the highest torque variance is observed at about 10 m/s slightly below rated wind speed of 14 m/s. This behaviour is similarly reported in other works [13] and is likely due to effects of the pitch controller, which frequently activates and deactivates in this region causing high torque amplitudes. The aerodynamic pitch moment is predominantly a result of thrust differences between the upper and lower rotor disk due to the vertical wind profile. Positive trends of the mean and variance with reference to wind speed is observed. The yaw moment is similarly a result of aerodynamic imbalance, predominantly yaw misalignment. Contrary to the pitch moment, the yaw moment is centered around zero mean and is independent of wind speed. The measured thrust agrees well with simulated thrust curves, as demonstrated in [5]. The highest variance in thrust is measured at around 8 m/s, which is slightly lower than the peak of torque variance.

The calculated bearing damage based on the measured hub loads are presented in Fig. 5. It is emphasized here that rotating machine elements such as bearings and gears experience stress cycles even at stationary environmental loads due to the shaft rotation. For this reason the LDD method [13] is used in this study for stress cycle counting

Fig. 4 10 min mean and standard deviation of measured aerodynamic loads in fixed frame of the rotor hub
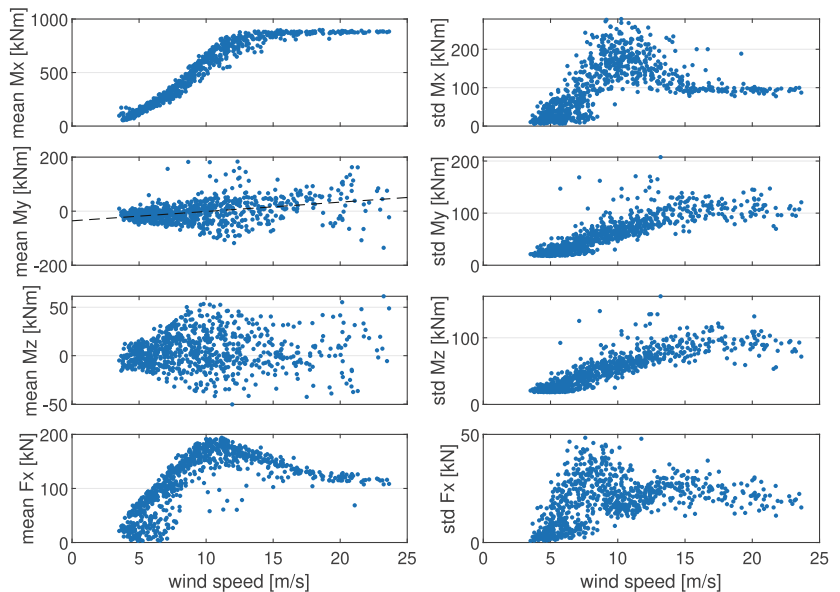
Fig. 5 10min fatigue damage at the main bearing and HSS-GS bearing based on measured hub loads
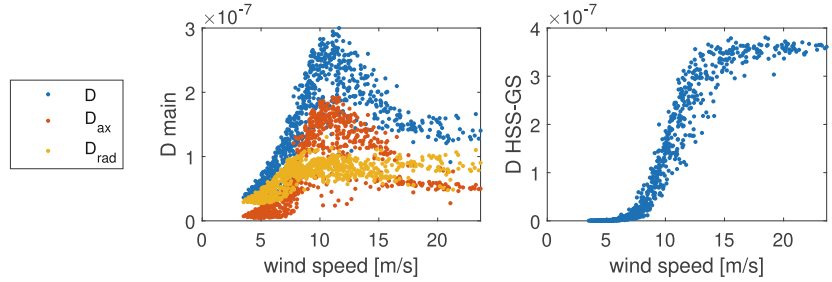
as opposed to the rainflow counting method commonly used for (non-rotating) structural elements. The fatigue damage at the main bearing comprises of two components, an axial component $D_{ax} = X F_{ax}/P \cdot D$ due to thrust and a radial component $D_{rad} = Y F_{rad}/P \cdot D$ due to gravity and pitch moments. The maximum in fatigue damage is observed at 11 m/s and coincides with the thrust peak. In this operational region the axial forces dominate and amount to about 66% of the equivalent dynamic load P. At wind speeds above 16 m/s the contribution of radial forces due to pitch moments becomes dominant and below 8 m/s with relatively low aerodynamic loads the contribution of gravity forces becomes dominant.

The HSS-GS bearing experiences only radial forces, which are considered to be proportional to the rotor torque (Eq. 8). Thus, the fatigue damage is governed by the mean rotor torque and reaches its maximum above rated wind speeds.

3.2 Sensitivity analysis

A sensitivity analysis is conducted with the objective of dimensionality reduction of the predictor variables. The sensor signals (Table 1) and statistical features (Table 2) are selected, which are the best predictors of hub loads according to the metric of the Neyman-Pearson correlation coefficient. Presented in Fig. 6 are the ten best performing signals SCADA signals (in blue) and CMS signals (in red) for each hub load component.

The generator torque is as expected an excellent predictor of both the mean and the standard deviation of rotor torque with $R > 0.99$. Prediction of the absolute values of the bending moments on the other hand is challenging, as neither of the SCADA or CMS signals show statistically significant correlation ($R < 0.5$). However, the moment standard deviations show high correlation ($R = 0.88$) with respect to the wind speed, as well as other SCADA signals. The torque correlates well with all SCADA signals, as well
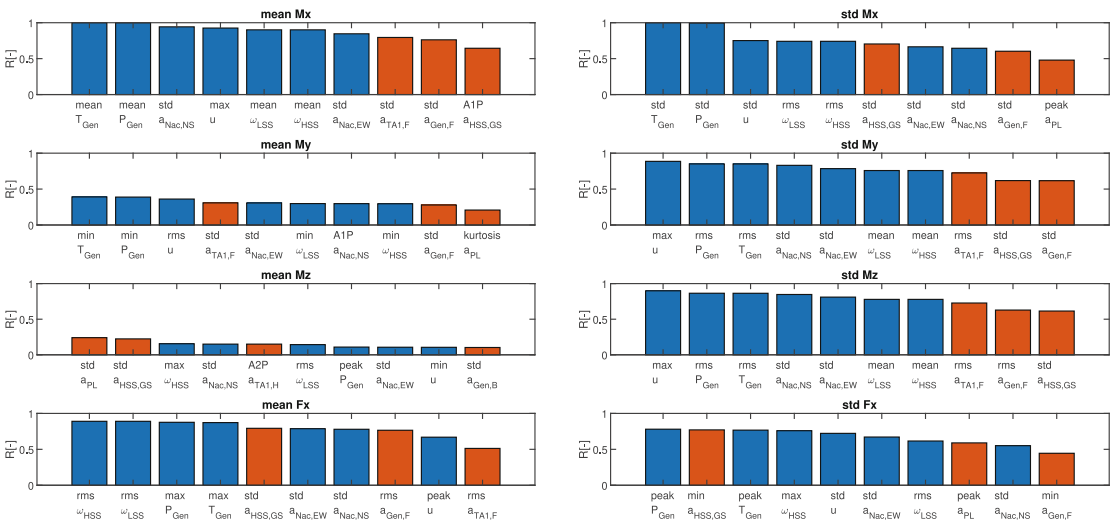
Fig. 6 SCADA (*blue*) and CMS signals (*red*) ranked according to their correlation with mean and standard deviation of hub loads

Fig. 7 Normalized RMSE between measured and predicted hub loads with different regression models and different SCADA/CMS input
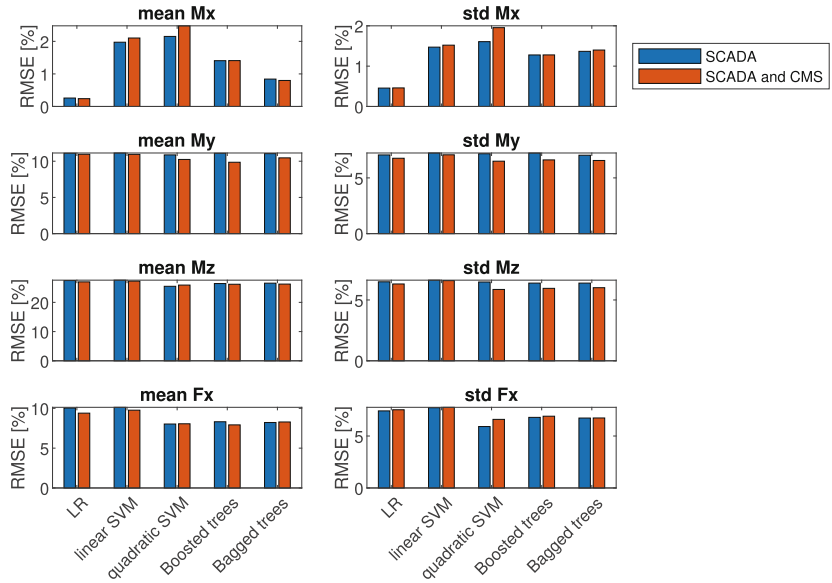
as the CMS vibrations at the HSS, the generator and the nacelle frame.

3.3 Hub load estimation

Several regression models, as described in Table 4, are used to map sensor measurements onto the aerodynamic hub loads. Two different scenarios of sensor input are considered: (1) only SCADA signals, (2) combined SCADA and CMS signals. This serves the purpose of assessing the added value of CMS vibration data and validating the novel approach of virtual sensing based on vibration measurements. The metric for model performance is the root mean square error (RMSE) between measured and predicted loads using 5-fold cross validation. Shown in Fig. 7 is the RMSE normalized to the maximum value of each hub load.

It is evident that the estimation of the mean and standard deviation of the rotor torque is accurate with minimum RMSE of 0.24% and 0.46% respectively. The best performance is observed is observed with a simple linear

regression model, due to the high linear correlation of the rotor torque with the measured generator torque.

Concerning the bending moments, it appears that estimating the mean value is much more challenging than estimating the standard deviation. A possible reason is that the mean bending moments unlike torque and thrust do not show a clear trend with respect to wind speed (Fig. 4). The inclusion of CMS vibration data slightly improves the prediction accuracy of bending moments in most cases. Nonlinear regression models are preferable, since the relationship of bending moments and dynamic drivetrain responses appear to be non-linear.

The mean thrust as well as the standard deviation is estimated with relatively low RMSE of 8.0% and 6.0%. It is clear that non-linear regression models are necessary to capture the non-linear behaviour such as the thrust-wind speed curve (Fig. 4). In this case CMS vibration data do not appear to increase performance.

Fig. 8 Normalized RMSE between measured and predicted bearing damage with different regression models and different SCADA/CMS input
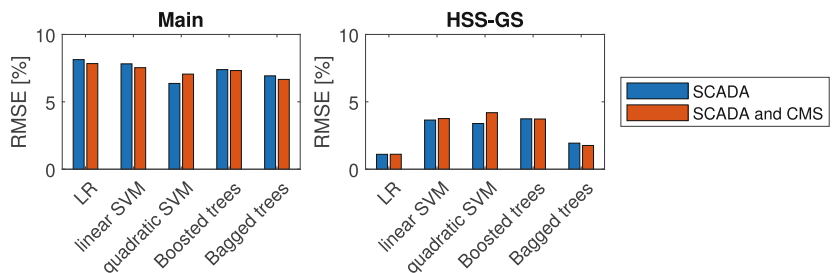
Fig. 9 Measured and predicted bearing RUL with the best performing regression model (quadratic SVM/LR)

legend:
- measured at 50 Hz
- predicted with 10 min avg loads
- predicted with 10 min avg loads and uncertainty factor (Eq. 17)
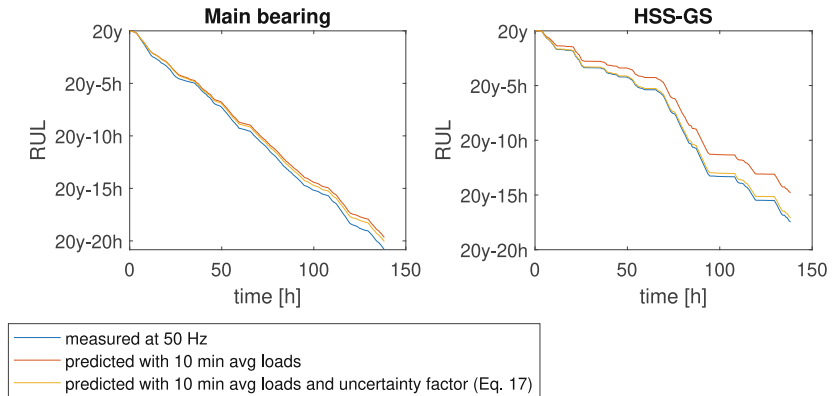
3.4 Fatigue damage and remaining useful life

The measured and estimated hub loads discussed in the previous section are converted into short-term (10 min) fatigue damage in the main bearing and the HSS-GS bearing using Eqs. 5–16. The RMSE of the fatigue damage normalized to its maximum value is presented in Fig. 8.

The damage in the main bearing is estimated with high accuracy (RMSE = 6.4%) despite high uncertainty in estimating the bending moments. These results suggest that the damage in the main bearing is governed by thrust, which can be estimated more accurately. The best performance is achieved by the quadratic SVM, which is able to capture the non-linear behaviour best. For monitoring the damage in the HSS-GS bearing a linear regression model suffices, which results in RMSE of 1.1%.

It appears that the inclusion of high-frequency CMS vibration measurements does not provide much value for monitoring bearing fatigue damage and that the considered 10 min average SCADA measurements are sufficient to estimate the damage within a 6.4% error margin.

Fig. 9 presents the measured and predicted RUL with the best performing regression model. During the recorded time frame of 138.3 h the measured RUL of the main and HSS-GS bearing is reduced only by 20.8 h and 17.5 h respectively. The discrepancy can be attributed to conservative design, for example in the selection of design load cases (DLC), which are more severe than the actual experienced environmental conditions. Furthermore, the sample size is relatively small and the time frame of the recordings of 31. Oct to 05. Dec is not representative for seasonality effects.

The RUL is overestimated significantly despite high accuracy in the predicted 10 min average loads. This is caused by high-frequency load dynamics for example from turbulence or internal drivetrain dynamics, which are not accounted for with 10 min average load estimates. The discrepancy is partially compensated with the damage uncer-

tainty model (Sect. 2.6). A good agreement with the measured RUL is observed at the HSS-GS bearing, while at the main bearing there remains a larger error possibly due to higher uncertainties in predicting bending moments and thrust.

3.5 Method limitations and further work

While the presented Digital Twin exhibits high accuracy in predicting aerodynamic loads and bearing damage, it is crucial to discuss the method assumptions and associated uncertainties, which limit the applicability of this method.

Field measurements: The data used in this study (Sect. 2.1) are representative for commercial SCADA and CMS measurements with the exception of the wind speed. The wind speed data were acquired with a MET mast about 150 m downwind of the turbine. Commercial wind turbine SCADA systems, however, mostly rely on nacelle mounted anemometers, which suffer from greater inaccuracies due to wake effects. The additional measurement uncertainty can be estimated with a coefficient of variation (COV) of $1-3\%$ according to Toft et al. [21].

Aeroelastic model: The presented regression model (Sect. 2.3) relies on a training data set of aerodynamic loads, in this case obtained by strain gauge measurements, which are not available in commercial wind turbines. Alternatively, it is possible to emulate field measurements with measurements from high-fidelity simulation models, similar to the approach of Azzam et al. [2]. Naturally, this shifts the challenge to the model construction and validation and introduces additional uncertainties due to modelling errors. Such uncertainties can be approximated with a COV of 5% according to Nejad et al. [13], however it is difficult to make generalized statements. In further studies it is planned to compare the data-driven regression models with an aeroelastic model of the DOE 1.5 turbine, which has

been developed and validated by other authors [5], in order to quantify modelling uncertainties.

Drivetrain model: State-of-the-art drivetrain models are highly complex multibody simulation (MBS) models [14, 22], and are not suitable as Digital Twin models, as discussed in [11]. First, the high number of degrees of freedom (DOF) make them numerically expensive and not capable of real-time simulation, which is necessary for online monitoring purposes. Secondly, wind turbine operators do not have the means of developing and validating complex models, since the drivetrain specifications are largely confidential to the OEMs. For this reason, a relatively simple drivetrain model is used in this article, which assumes a quasi-static transmission of torque and neglects all internal dynamics including effects of component flexibility, multi-body interaction and excitations from gear meshing or roller bearings (Sect. 2.4). The effects of internal dynamics on bearing fatigue damage are expected to be relatively small, as suggested by the results of a previous numerical case study [10], where RMSE of 5–15% in the bearing fatigue damage were observed. However, the scope of the numerical case study was limited to the high-speed gear stage bearings, normal power production at rated wind speed and one drivetrain configuration. Further numerical investigations are scheduled better quantify the modelling errors of such reduced order drivetain models.

4 Conclusion

This paper presents a Digital Twin for virtual sensing of wind turbine hub loads based on SCADA and CMS measurements, as well as monitoring the accumulated fatigue damage and remaining useful life in the main and HSS-GS bearing. The Digital Twin is constructed for the DOE 1.5 research turbine [18] and evaluated with field measurements. Several data-driven regression models including linear regression models, support vector machines and tree ensembles are trained on field measurements for the aerodynamic hub load estimation. For calculation of local bearing loads a low-fidelity physics-based model is constructed with the assumption of steady-state operation. The remaining useful life is calculated based on the consumed fatigue damage reserves according to ISO 281 [7].

While the estimation of rotor torque and thrust is accurate with RMSE of 0.24% and 6.0%, it proves to be much more challenging to estimate the yaw and pitch bending moments. The measured bending moments appear to be highly stochastic and do not show statistically significant correlation ($R < 0.5$) with any of the considered SCADA and CMS measurements.

Nonetheless, relatively low RMSE of 6.4% in the 10 min fatigue damage are observed at the main bearing despite the high uncertainty in the bending moment estimates. It appears that the damage in the main bearing is governed by thrust, which is estimated much more accurately than the bending moments. The damage at the HSS-GS bearings is assumed to only depend on the drivetrain torque and can thus be estimated with high accuracy (RMSE = 1.1%).

The main contribution of this article is the knowledge transfer of the virtual sensing concept from wind turbine structural elements to drivetrain components, and validation of the concept with field measurements. With regards to the quality and availability of physical sensor measurements the proposed virtual sensors are feasible. SCADA and CMS data contain sufficient information for accurate monitoring of bearing fatigue damage. Challenges are identified in the multi-body drivetrain dynamics, which are much more complex than the dynamics of the tower and blades. However, developing and validating models to capture complex drivetrain dynamics is difficult based on the information that is available to wind turbine operators. Low fidelity, quasi-static models, which largely neglect internal drivetrain dynamics, are shown to produce low errors of bearing fatigue damage, and are thus proposed for virtual sensing purposes. Further investigations are planned to quantify the uncertainties introduced by quasi-static drivetrain models.

References

1. Archeli RB, Keller J, Bankestrom O, Dunn M, Guo Y, Key A, Young E (2021) Up-tower investigation of main bearing cage slip and loads. Report NREL/TP-5000-81240. National Renewable Energy Laboratory

2. Azzam B, Schelenz R, Roscher B, Baseer A, Jacobs G (2021) Development of a wind turbine gearbox virtual load sensor using multibody simulation and artificial neural networks. Forsch Ingenieurwes 85(2):241–250. https://doi.org/10.1007/s10010-021-00460-3

3. van Binsbergen D et al (2022) A physics-, scada-based remaining useful life calculation approach for wind turbine drivetrains. J Phys: Conf Ser. https://doi.org/10.1088/1742-6596/2265/3/032079

4. Branlard E, Giardina D, Brown CSD (2020) Augmented kalman filter with a reduced mechanical model to estimate tower loads on a land-based wind turbine: a step towards digital-twin simulations. Wind Energy Sci 5(3):1155–1167. https://doi.org/10.5194/wes-5-1155-2020

5. Guo Y, Bankestrom O, Bergua R, Keller J, Dunn M (2021) Investigation of main bearing operating conditions in a three-point mount wind turbine drivetrain. Forsch Ingenieurwes 85(2):405–415. https://doi.org/10.1007/s10010-021-00477-8

6. Hastie T, Tibshirani R, Friedman J (2009) The elements of statistical learning: data mining, inference and prediction. Springer, New York https://doi.org/10.1007/b94608

7. ISO 281 (2007) Rolling bearings — dynamic load ratings and rating life

8. Kay SM (1998) Fundamentals of statistical signal processing. Detection theory vol 2. Prentice Hall, London

9. MATLAB (2022) Statistics and machine learning toolbox. https://se.mathworks.com/products/statistics.html. Accessed 02 Feb 2023

10. Mehlan FC, Nejad AR, Gao Z (2022) Digital twin based virtual sensor for online fatigue damage monitoring in offshore wind turbine drivetrains. J Offshore Mech Arct Eng. https://doi.org/10.1115/1.4055551

11. Mehlan FC, Pedersen E, Nejad AR (2022) Modelling of wind turbine gear stages for digital twin and real-time virtual sensing using bond graphs. J Phys Conf Ser. https://doi.org/10.1088/1742-6596/2265/3/032065

12. Moghadam FK, Rebouças GFS, Nejad AR (2021) Digital twin modeling for predictive maintenance of gearboxes in floating offshore wind turbine drivetrains. Forsch Ingenieurwes 85(2):273–286. https://doi.org/10.1007/s10010-021-00468-9

13. Nejad AR, Gao Z, Moan T (2014) On long-term fatigue damage and reliability analysis of gears under wind loads in offshore wind turbine drivetrains. Int J Fatigue 61:116–128. https://doi.org/10.1016/j.ijfatigue.2013.11.023

14. Nejad AR, Guo Y, Gao Z, Moan T (2016) Development of a 5 mw reference gearbox for offshore wind turbines. Wind Energy 19(6):1089–1106. https://doi.org/10.1002/we.1884

15. Perišić N, Kirkegaard PH, Pedersen BJ (2013) Cost-effective shaft torque observer for condition monitoring of wind turbines. Wind Energy. https://doi.org/10.1002/we.1678

16. Randall RB (2010) Vibration based condition monitoring: industrial, aerospace and automotive applications. Wiley & Sons, Chichester

17. Remigius WD, Natarajan A (2021) Identification of wind turbine main-shaft torsional loads from high-frequency scada (supervisory control and data acquisition) measurements using an inverse-problem approach. Wind Energy Sci 6(6):1401–1412. https://doi.org/10.5194/wes-6-1401-2021

18. Santos R, van Dam J (2015) Mechanical loads test report for the u.s. department of energy 1.5-megawatt wind turbine. Report. National Renewable Energy Laboratory

19. Stehly T, Beiter P (2020) 2018 cost of wind energy review. Report. National Renewable Energy Laboratory

20. Tarpø M, Amador S, Katsanos E, Skog M, Gjødvad J, Brincker R (2021) Data-driven virtual sensing and dynamic strain estimation for fatigue analysis of offshore wind turbine using principal component analysis. Wind Energy 25(3):505–516. https://doi.org/10.1002/we.2683

21. Toft HS, Svenningsen L, Sørensen JD, Moser W, Thøgersen ML (2016) Uncertainty in wind climate parameters and their influence on wind turbine fatigue loads. Renew Energy 90:352–361. https://doi.org/10.1016/j.renene.2016.01.010

22. Wang S, Nejad AR, Moan T (2020) On design, modelling, and analysis of a 10-mw medium-speed drivetrain for offshore wind turbines. Wind Energy 23(4):1099–1117. https://doi.org/10.1002/we.2476

23. Wilkinson M, Hendriks B, Spinato F, Gomez E, Bulacio H, Roca J, Tavner P, Feng Y, Long H (2010) Methodology and results of the reliawind reliability field study. In: European wind energy conference

24. Wind Europe (2020) Offshore wind in europe: Key trends and statistics 2019. https://windeurope.org/wp-content/uploads/files/about-wind/statistics/WindEurope-Annual-Offshore-Statistics-2019.pdf. Accessed 1 Nov 2022

A.5 Paper 5

Rotor imbalance detection and diagnosis in floating wind turbines by means of drivetrain condition monitoring

Felix C. Mehlan *, Amir R. Nejad

Norwegian University of Technology and Science (NTNU), Jonsvannsveien 82, Trondheim, 7030, Norway

ARTICLE INFO

ABSTRACT

This paper presents a novel approach for detection and diagnosis of the rotor imbalance types pitch misalignment, yaw misalignment and mass imbalance by monitoring the drivetrain vibration response. Traditionally, only SCADA signals including nacelle accelerations, rotor speed and electrical power are utilized for this purpose, while drivetrain condition monitoring signals are mainly used for fault detection in gears and bearings. A diagnostic method is proposed using statistical change detection methods for fault detection, phase angle estimation for localizing the faulty blade, and physics-based decision criteria for fault classification. The proposed method is tested in a numerical case study with aeroelastic and drivetrain multi-body models of the 10 MW DTU reference wind turbine. The results suggest that drivetrain condition monitoring signals are particularly beneficial for detecting and diagnosing pitch misalignment, since this fault type uniquely induces periodic out-of-plane bending moments that excite drivetrain bending modes. Drivetrain signals improved the detection rate of a 1° pitch error from 19% to near 100% and reduced the standard error in locating the faulty blade from 71.5° to 11.2°. In addition, by using drivetrain vibration amplitudes as a decision criterion, all considered pitch error cases are correctly distinguished from other fault types.

1. Introduction

Recent market trends show an increase in offshore wind turbine installations driven by higher energy yields and fewer land displacement and noise issues compared to onshore sites [1]. However, offshore wind turbines are faced with additional reliability challenges. Replacement and repair of components is expensive and time-consuming due to difficulties accessing the site and dependency on good weather conditions. Thus, unscheduled downtimes as a result of component failure can lead to high operational and maintenance expenditures (O&M). For offshore wind turbines the O&M expenditures can reach 34% of the levelised cost of energy (LCOE) [2]. A major contributor to O&M expenditures is the rotor system consisting of blades, hub, pitch actuators and bearings with frequent failures and long downtimes [3]. Imbalances in the rotor system are considerably harmful, as they not only reduce the electrical power output [4,5], but also increase fatigue loads on the blades and the tower [6].

The term imbalance refers in this article to physical disturbances of the rotor system and is not to be confused with class imbalance, which describes the uneven distribution of training data in data-driven fault diagnosis methods. Rotor imbalances are generally categorized as aerodynamic imbalances, which include pitch and yaw misalignment, and mass imbalances. Pitch misalignment refers to the incorrect angular

positioning of one or multiple blades and can be caused by manufacturing errors, installation errors or failures of pitch sensors and actuators. Certification guidelines (GL Standards, 2010, Sect. 4.3.4.1, pp. 4–20) require relatively small pitch misalignment of ±0.3° [7]. Nonetheless, a recent measurement campaign of 1100 turbines revealed that 38% of operating turbines do not meet these requirements [8]. Yaw misalignment, the misalignment of rotor axis and wind direction, occurs to a degree in most operating wind turbines, since yaw control systems activate only when the yaw angle exceeds a certain threshold in order to reduce duty cycles [9]. In addition to operational yaw misalignment, the inaccuracy of wind wanes due to wake turbulence, poor calibration or errors on the control side can cause static or dynamic misalignment. Residual mass imbalance can occur due to imperfect manufacturing and installation of the blades, which is generally alleviated before commissioning of the turbine, where the rotor is rebalanced by technicians according to ISO 21940-11:2016 [10] by adding compensating masses. During operation, however, accretion of dirt, moisture or ice can cause additional mass imbalance [11].

Research on wind turbine faults generally falls into to the areas of fault diagnosis, fault prognosis and resilient control. Fault diagnosis refers to the detection and classification of different failure modes, fault prognosis describes the prediction of the fault progression and

---

remaining useful life, and resilient control is a technique to minimize the effects of faulty components on the wind turbine operation [12]. This paper, like most publications on rotor imbalance, is exclusively concerned with fault diagnosis.

Effective techniques for rotor imbalance detection are frequency-domain methods, which monitor the once per revolution (1P) frequency peak. This is based on the knowledge that in the case of rotor imbalance faults the aerodynamic, gravitational or inertial forces are not in balance, such that the turbine is excited with additional periodic loads at the rotor frequency 1P. The SCADA signals rotor speed and side-side nacelle accelerations are the state-of-the-art for rotor imbalance detection according to Hyers et al. [13]. Studies have also demonstrated the possibility of rotor imbalance detection with electrical signatures of the generator [14,15] or by direct measurement of blade loads with strain gauges [9,11].

While rotor imbalance detection is straightforward, more research is required for diagnostics, which includes the classification of different rotor imbalance types and the estimation of the fault severity, e.g the pitch or yaw angle. Niebsch et al. [16] developed a method for simultaneous estimation of mass and aerodynamic imbalances, which entails physical modelling of rotor imbalances and wind turbine dynamics, and solving the inverse problem. Kusnick et al. [11] argue that pitch misalignment decreases the power output contrary to mass imbalance and advocate for the mean power as a simple diagnostic criterion. Investigations concerned exclusively on detection and diagnosis of pitch misalignment are found in [7,17,18]. Bertele et al. propose a method for pitch misalignment detection and correction that linearly correlates the error in pitch angle with the amplitude of nacelle accelerations at 1P [7]. Cacciola et al. as well as Cho et al. use neural networks to quantify pitch misalignment severity and identify the faulty blade [17, 19]. Kusiak et al. apply data mining algorithms and predictive machine learning models to diagnose pitch misalignment [18]. Many studies are devoted to indirectly estimating the yaw angle and thus circumventing the inaccuracy of wind vanes [9,20,21]. Botasso et al. estimate yaw misalignment and wind shear by observation of blade root bending moments [9]. Choi et al. apply machine learning methods to estimate yaw misalignment from SCADA data [20]. Jing et al. estimate yaw misalignment based on the reduction in electrical power output [21].

Diagnostic methods reported in literature can be broadly classified as physics-based [7,9,16], data-driven [15,17–21] and knowledge-based approaches [11], each with their own limitations. Physics-based methods require accurate aeroelastic models, which are challenging to construct and validate without full knowledge on turbine specifications and system parameters such as stiffness values. The added uncertainty from model assumptions and simplifications invariably increases the uncertainty in diagnosis. Data-driven methods on the other hand are shown to perform with high accuracy, but the challenge lies in obtaining sufficient training data of faulty conditions. Field measurements of naturally occurring faults are generally sparse and may require additional, expensive equipment such as LIDAR [20] to determine the ground truth. Knowledge-based methods rely on theoretical and practical expertise of fault causes and effects. The main difficulties lie in the acquisition and management of domain knowledge. This paper presents a knowledge-based approach to detection and diagnosis of rotor imbalance faults, summarized as follows:

1. Knowledge-based expert system
2. Classification of pitch misalignment, yaw misalignment and mass imbalances
3. Leveraging drivetrain CMS data
4. Stochastic approach that accounts for turbulence induced variance

A knowledge-based expert system is proposed, which is comprised of heuristic 'if-then' decision rules. The expert system is developed on the basis of domain knowledge acquired from literature review, first principles reasoning and analysis of aeroelastic simulation results.

Neither physical modelling nor training data of faulty conditions are required for the method implementation.

Secondly, the proposed diagnostic method aims at distinguishing the three types of rotor imbalances pitch misalignment, yaw misalignment and mass imbalance, while earlier works have mainly focused on one fault type or the distinction of pitch misalignment and mass imbalance.

Thirdly, the proposed method incorporates drivetrain condition monitoring system (CMS) signals, while the state-of-the-art are SCADA signals characterizing global turbine dynamics such as nacelle accelerations and rotor speed. Drivetrain CMS vibration signals can provide further insight into the dynamics of the closely coupled rotor and drivetrain systems and the impact of rotor imbalances in a holistic perspective. In addition, CMS sensors are cost-effective and available in most modern offshore wind turbines.

Lastly, the proposed method explicitly accounts for the volatility of environmental conditions and the measurement noise of sensors. Statistical methods of change detection are employed here, which are proven to be robust methods for fault detection under noise and unknown disturbances and have found application in the detection of main bearing faults in earlier works [22].

The remainder of this paper is organized as follows: Section 2 presents in detail the methodology of fault detection and diagnosis, as well as the high-fidelity simulation models to evaluate the proposed method. The following Section 3 discusses dynamic system responses to rotor imbalances both qualitatively and with simulation results; and assesses the detection and diagnostic performances against a benchmark machine learning classifier. Concluding remarks are provided in Section 4.

2. Methodology

The proposed method for rotor imbalance diagnosis based on drivetrain condition monitoring is formalized in the following sections. Simulations are conducted with high-fidelity models of the global wind turbine and the drivetrain for different rotor imbalance cases and varying environmental conditions (Section 2.1). Several simulated signals are selected to emulate SCADA and drivetrain CMS signals, and are postprocessed to extract frequency- and time-domain statistical features that are indicative of rotor imbalances (Section 2.2). Statistical methods of change detection are then applied to derive test statistics for fault detection (Section 2.3.1). Classification of the rotor imbalance type uses domain knowledge formalized as an expert system (Section 2.3.2). Identification of the faulty blade is based on maximum likelihood estimates of the phase angle (Section 2.3.3). The detection and diagnostic performance of the proposed method is evaluated on simulated sensor samples of different fault and environmental conditions against a benchmark machine learning classifier (Section 2.4).

2.1. Simulation

High-fidelity dynamic simulation models based on the DTU 10 MW reference wind turbine [23] mounted on the Nautilus semisubmersible floating platform [24] are used in this study. Selected specifications of the reference turbine are listed in Table 1. The decoupled analysis approach is employed with two separate models for simulation of the global wind turbine response and the drivetrain response, respectively. The global model is implemented in the aero-servo-elastic simulation tool OpenFAST [25]. Rotor imbalances of pitch misalignment, mass imbalance and yaw misalignment are introduced in the global model. The simulated rotor hub loads and nacelle motions in six degrees of freedom obtained from the global model are imposed as boundary conditions on the higher-fidelity drivetrain model. The drivetrain model is implemented in the multi-body simulation software SIMPACK [26], which allows for detailed analysis of internal drivetrain dynamics [27].

Table 1
DTU 10MW reference turbine specifications [23].

Wind turbine type	3 blade, upwind horizontal axis
Controller type	pitch regulated, variable speed
Drivetrain type	3 stage, medium speed
Cut-in wind speed [m/s]	4
Cut-out wind speed [m/s]	25
Rated wind speed [m/s]	11.4
Rated power [MW]	10
Rotor diameter [m]	178.3
Rotor mass [kg]	229 000
Blade mass [kg]	41 000
Hub Height [m]	119.0
Gearbox ratio [–]	1:50.039
Minimum rotor speed [rpm]	6.0
Maximum rotor speed [rpm]	9.8

Table 2
Fault cases (FC). Mass imbalances are expressed in the quality grade G of ISO 21940-11:2016 [10]. Faults are constant over the entire simulation period of 4000 s.

	h	m1	m2	m3	p1	p2	p3	y1	y2	y3
Mass [–]	0	G32	G48	G64	0	0	0	0	0	0
Pitch [deg]	0	0	0	0	1	2	3	0	0	0
Yaw [deg]	0	0	0	0	0	0	0	5	10	15

Table 3
Environmental conditions (EC) with wave height H_s, wave period T_p, wind speed U and turbulence intensity I.
Source: Adopted from Nejad et al. [28].

	EC1	EC2	EC3	EC4	EC5	EC6
H_s [m]	2.0	4.5	5.0	5.0	4.0	5.5
T_p [s]	8.0	12.0	14.0	12.0	10.0	14.0
U [m/s]	4.0	7.0	10.0	12.0	14.0	20.0
I [–]	0.26	0.19	0.16	0.15	0.14	0.12
# seeds	6	6	6	6	6	6

Several fault cases are simulated, as specified in Table 2. Three cases of pitch misalignment (p1, p2, p3), mass imbalances (m1, m2, m3) and yaw misalignment (y1, y2, y3), as well as one reference case of healthy conditions (h) are considered. The selection of realistic pitch misalignment values is based on the findings of Saathoff et al. [8], who report that pitch misalignment of 0.6°–2.0° occurred in 35.3% and higher cases of > 2° occurred only in 2.6% of investigated operating wind turbines. Only positive misalignment (towards feather) and only misalignment of a single blade is considered in this study. Pitch misalignment is implemented by increasing the structural twist of one blade in the aeroelastic model.

The mass imbalance cases are expressed in the imbalance quality scale G of standard ISO 21940-11:2016 [10] in accordance to Kusnick et al. [11]. The standard recommends permissible residual imbalance levels U_{per} for different applications, rotor speeds N and weight W, expressed by Eq. (1)

$$U_{per}[\text{g mm}] = 9549 \cdot G[-] \frac{W[\text{kg}]}{N[\text{rpm}]}. \tag{1}$$

Wind turbine rotors are generally rebalanced to a residual imbalance of G16 before commissioning [11]. Guided from this classification, the levels of G32, G48 and G64 are selected as low to severe mass imbalances in operating turbines caused for example by ice accretion. The mass imbalance faults are implemented in the global simulation model by increasing the mass density of one blade by 0.58%, 0.88% and 1.17% respectively. It should be noted that ice accretion in reality also affect the aerodynamic properties of the blades, which may cause aerodynamic imbalances and reduce the electrical power output. These effects are not considered in this numerical study; the faults are rather modelled as pure inertial imbalances. The yaw misalignment cases of 5°, 10° and 15° are selected based on comparable works on yaw misalignment simulation [9,29].

The ten fault cases are simulated under six different environmental conditions (EC) adopted from Nejad et al. [28], where EC1 to EC3 are below and EC4 to EC6 are above rated wind speed of 11.4 m/s (Table 3). Each combination of FC and EC is simulated for a time period of 4000 s for 6 seeds of turbulent wind fields complying with IEC 61400-3. The numerical step size is 0.025 s for the aeroelastic simulations and 0.005 s for the drivetrain simulations. The first 400 s of simulated time series are disregarded due to simulation start-up transients and the remaining 3600 s are partitioned into 60 s sections for further signal processing. This concludes to a total number of 360 data points for each FC and EC combination.

2.2. Signal and feature selection

Synthetic SCADA and drivetrain CMS signals are generated by simulation of the aeroelastic and the drivetrain model respectively. White Gaussian noise (WGN) is added to each simulated signal to represent measurement noise. The signal-to-noise-ratio ($SNR = \sigma^2_{signal}/\sigma^2_{WGN}$) is set to a relatively conservative value of 10 based on data sheets of commercial CMS vibration sensors and typical amplitudes under normal operation. The following SCADA signals, which are traditionally used for rotor imbalance detection, are included in the analysis: rotor speed ω_{rot}, side-side nacelle accelerations $a_{Nac,Y}$ and electrical power output P_{el}. Drivetrain CMS signals are selected based on ISO 10816-21 [30], which recommends the placement of piezo-resistive or capacitive accelerometers on the housing of the main bearings, the gearbox and the generator for condition monitoring. ISO 10816-21[30] furthermore recommends the use of velocity signals by integration of measured accelerations for monitoring faults with low characteristic frequencies in the range of 0.1 to 10 Hz. The MBS drivetrain model is capable of simulating gearbox housing velocities, but is limited with regard to main bearing and generator housing vibrations, since the respective housings are not specifically implemented but rather considered part of the bedplate. The subsequent analysis focuses on gearbox housing velocities, as these represent the most realistic CMS vibration signals. The velocities are extracted in all three coordinate directions (axial v_X side-side v_Y, vertical v_Z), since ISO 10816-21[30] recommends both axial and radial measurements.

Statistical features or health indicators (HI) are generally extracted for condition monitoring, which should ideally be sensitive to faults and increase monotonically with fault progression to facilitate fault diagnosis by trend analysis [31]. According to ISO 10816-21[30], the recommended feature for general drivetrain CMS is the root mean square, however other time-domain statistical variables including mean, kurtosis, skewness, peak value, crest factor are also applied [31]. In this specific case, however, the once per revolution (1P) vibration amplitude and phase are reported to be much more effective features to detect rotor imbalance faults, and show a linear correlation with the magnitude and the location of the fault under idealized conditions [7]. The 1P-amplitude and the 1P-phase of vibration signals describe the dynamic turbine response to the imbalance loads, which are typically sinusoidal with a frequency of 1P. Discrete Fourier transform (DFT) can be applied to calculate these features, however, the variability of the rotor speed must be taken into consideration, which leads to smearing of the 1P-peak in the frequency spectrum and may introduce errors in the amplitude estimates. For this reason, computed order tracking (COT) is applied, which is commonly used in rotating machinery to eliminate the influence of shaft speed variations when extracting characteristic bearing and gear fault frequencies [32]. COT is a resampling and interpolation technique that transforms a discrete signal from the time domain to the angular domain using shaft speed measurements. The signal x measured at constant time intervals given by the sampling frequency $f_s = 1/\Delta t$ is resampled in the angular domain with equidistant angular increments $\Delta\alpha$

$$x(i\Delta t) \mapsto x^*(n\Delta\alpha). \tag{2}$$
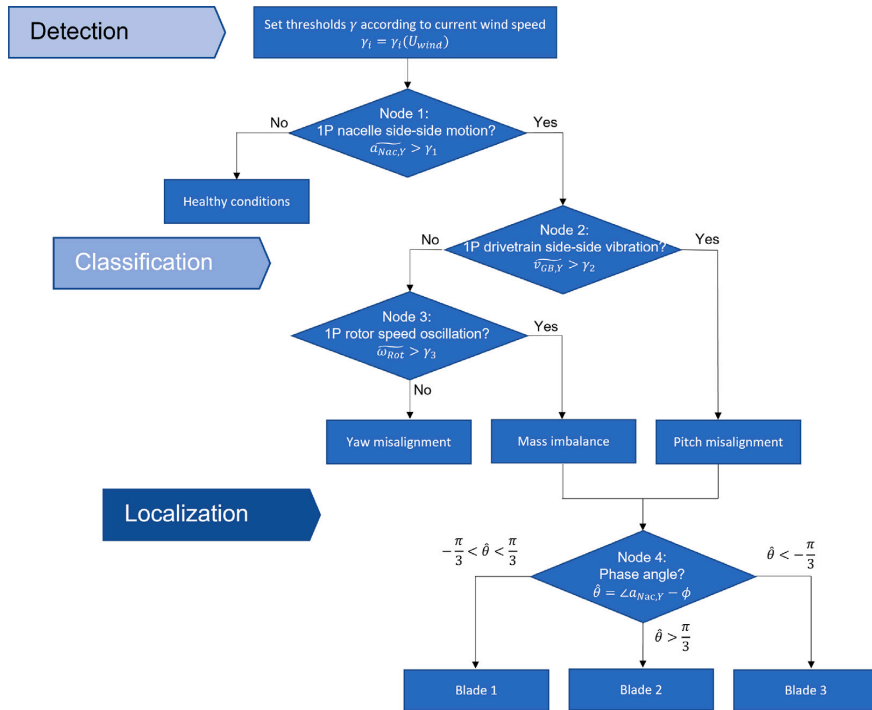
Fig. 1. Proposed knowledge-based expert system for diagnosis of rotor imbalance faults using SCADA and CMS measurements. $\widetilde{a_{Nac,Y}}$: Nacelle side-side acceleration amplitudes, $\widetilde{v_{GB,Y}}$: CMS vibration amplitudes at the gearbox housing, $\widetilde{\omega_{Rot}}$: Rotor speed amplitudes.

The 1P-amplitude $\tilde{x}$ and 1P-phase $\angle x$ are then calculated in the angular domain by DFT [33]

$$\tilde{x} = \sqrt{\hat{a}_1^2 + \hat{a}_2^2},$$
$$\angle x = \arctan\left(\frac{-\hat{a}_2}{\hat{a}_1}\right). \tag{3}$$

where

$$\hat{a}_1 = \frac{2}{N} \sum_{n=0}^{N} x^*(n\Delta\alpha) \cdot \cos(n\Delta\alpha),$$
$$\hat{a}_2 = \frac{2}{N} \sum_{n=0}^{N} x^*(n\Delta\alpha) \cdot \sin(n\Delta\alpha). \tag{4}$$

The 1P-amplitude and phase are selected as statistical feature for all SCADA and CMS vibration signals that indicate the wind turbine dynamic response. For the electrical power signals the mean value is chosen, as it is reported that both pitch and yaw misalignment decrease the power production [4,21].

2.3. Proposed fault diagnosis strategy

The proposed diagnostic method for rotor imbalances comprises the three steps detection, classification and localization, as depicted in Fig. 1. Fault detection is realized with methods of statistical change detection from normal behaviour (Section 2.3.1). Classification of the rotor imbalance type uses domain knowledge formalized as an expert system (Section 2.3.2). Identification of the faulty blade is based on maximum likelihood estimates of the phase angle (Section 2.3.3).

2.3.1. Fault detection by statistical change detection

Statistical change detection is a robust methodology for fault detection under noise and unknown disturbances [22]. It provides a

framework to identify statistically significant changes to the normal behaviour, which captures the naturally occurring variation of measurements from turbulence, wakes and other environmental influences. In statistical change detection the null-hypothesis H_0 and the alternative hypothesis H_1 are defined [33], representing in this case healthy and faulty behaviour. A sequence of independent random variables $x[n], n = 1, 2...N$ is sampled in order to test for each hypothesis. Under healthy conditions H_0 the samples $x[n]$ are assumed to be normally distributed with mean μ_0 and standard deviation σ_0. Under faulty conditions the dynamic response deviates from its normal behaviour, which entails a change in the distribution parameters of $x[n]$. The mean value μ_1 under H_1 is assumed to increase, while the standard deviation σ_1 is considered invariant. The assumptions of normal distributions and constant standard deviation is supported by the simulation results (Section 3.3). It is found that the signal variance is primarily a result of wind turbulence and insensitive to the fault case. The problem at hand is referred to as a binary hypothesis testing problem and expressed by Eq. (5)

$$H_0 : x[n] \sim N(\mu_0, \sigma_0),$$
$$H_1 : x[n] \sim N(\mu_1, \sigma_1), \ \mu_1 > \mu_0, \sigma_1 = \sigma_0. \tag{5}$$

It is feasible that the operator has acquired knowledge of the distribution parameters under H_0, known as the normal behaviour model, from historical measurements. However, the behaviour under any rotor fault given by μ_1, σ_1 is considered unknown. In this scenario the generalized likelihood ratio test (GLRT) provides the optimal decision criterion or *test statistic*. The GLRT decides for the hypothesis H_1, if the likelihood ratio $L(x)$, given by Eq. (6), exceeds a threshold γ [33]

$$L(x) = \frac{p(x; \hat{\mu}_1, \ \hat{\sigma}_1, H_1)}{p(x; H_0)} > \gamma. \tag{6}$$

The unknown mean μ_1 is replaced by its maximum likelihood estimate (MLE) $\hat{\mu}_1$ given by the sample mean $\bar{x}$ (Eq. (7)), while the unknown

variance σ_1^2 is assumed to be identical to the variance of healthy conditions σ_0^2

$$\hat{\mu}_1 = \bar{x} = \frac{1}{N} \sum_{n=0}^{N-1} x[n], \quad \hat{\sigma}_1 = \sigma_0. \tag{7}$$

By inserting the Gaussian probability density functions and substituting the MLE (Eq. (7)) in the likelihood ratio (Eq. (6)), the test statistic $T(x)$ can be derived as the scaled square of the sample mean, as shown in Eq. (8)

$$T(x) = \frac{N \bar{x}^2}{\sigma_0^2} > \gamma'. \tag{8}$$

Under the assumption of normally distributed variables $x[n]$ (Eq. (5)), the test statistic follows a Chi-squared distribution with degrees of freedom ν and non-centrality parameter λ. With this information, adequate thresholds γ' can be set such that a maximum probability of false alarm P_{FA} is met, as shown in Eq. (9), where F^{-1} expresses the inverse cumulative density function of the non-central Chi-squared distribution

$$\gamma' = F^{-1}(1 - P_{FA}; \nu = 1, \lambda = \frac{N \mu_0^2}{\sigma_0^2}). \tag{9}$$

The probability of false alarm serves as a parameter to balance false positive and false negative rates [33]. Frequent false positives are disruptive to the wind turbine operation and detrimental to the productivity, while the missed detection of a fault (false negative) is potentially harmful and may lead to critical failures. The reported value of P_{FA} in comparable publications on statistical fault detection in wind turbines ranges widely from 10^{-2} to 10^{-12} [34,35]. In this study P_{FA} is set to 10^{-4}.

2.3.2. Knowledge-based fault classification: Expert system

Wind turbine operators may not have sufficient training data to construct data-driven models or quantitative domain knowledge to formulate accurate aeroelastic models for model-based diagnosis, but instead have acquired heuristic expertise in the form of qualitative system behaviour, conditional statements or causal relations of faults and effects. Knowledge-based methods exhibit high flexibility in data representation and thus take full advantage of such heuristic domain knowledge. In this paper, a knowledge-based expert system is proposed, which is developed with qualitative knowledge of rotor imbalance effects. For comparison, a classical data-driven approach is presented in Section 2.4 using a Linear Discriminant Analysis (LDA) classifier, which is constructed by regression on training data of faulty conditions.

Expert systems are knowledge-based methods that can find application in drivetrain condition monitoring [36,37]. Kusnick et al. [11] also presented an expert system for pitch misalignment and mass imbalance diagnosis. Expert systems are predictive models that map observations to fault types by recursive application of decision rules and thus mimic and automate human reasoning in the process of problem solving [38]. The decision rules and hierarchical structure of expert systems are formulated with the knowledge-base, a collection of domain-knowledge maintained by experienced professionals. The main advantages of expert systems are the high transparency of the decision process, which positively affects the trust of stakeholders in the diagnosis, and low requirements of quantitative domain knowledge for implementation. Limitations of expert systems are the high uncertainties in the thresholds of decision rules, which are commonly addressed with fuzzy logic or probabilistic methods.

The proposed expert system, depicted in Fig. 1, distinguishes between the four classes Healthy, Mass imbalance, Yaw misalignment and Pitch misalignment with three binary decision rules. Statistical change detection methodology is adopted to formulate the decision rules. Each node is considered a binary hypothesis testing problem, specifically a mean-shifted Gauss problem (Eq. (5)). The decision rules are then given by the test statistic in Eq. (8) and respective thresholds, which

are a function of the normal behaviour model μ_0, σ_0 and the parameter P_{FA} (Eq. (9)). Since the normal behaviour is strongly influenced by environmental conditions, measurements of current wind speed U_{wind} are necessary to set appropriate thresholds. The first node represents fault detection by testing for increased side-side nacelle acceleration amplitudes $\widetilde{a_{Nac,Y}}$ caused by periodical shear forces. Both aeroelastic simulations in this study (Section 3.3) and literature suggest that $\widetilde{a_{Nac,Y}}$ is a universal indicator of any rotor imbalance type. In the second node pitch misalignment is isolated by testing for increased lateral gearbox housing vibrations at 1P ($\widetilde{v_{GB,Y}}$), which indicate periodic out-of-plane bending moments that are characteristic for pitch misalignment (Section 3.3). Lastly, mass imbalance is distinguished from yaw misalignment by its characteristic oscillation in rotor speed ($\widetilde{\omega_{Rot}}$) induced by gravitational imbalances (Section 3.3). The probability of false alarm is set to a relatively low value of $P_{FA} = 10^{-4}$ in all three nodes, which correspond to high detection thresholds γ_i.

2.3.3. Fault localization by phase angle estimation

In addition to the classification of the rotor imbalance type, it is necessary to localize the fault, i.e. identify the blade with deviating mass or pitch angle, in order to perform corrective measures. The fault location is defined as the angle θ in the rotor plane, where $\theta = 0$ refers to blade 1, $\theta = 2\pi/3$ to blade 2 and $\theta = -2\pi/3$ to blade 3. It can be derived analytically that the phase of the 1P harmonic of nacelle accelerations is directly related to the fault location in the rotor [7]. The fault location is obtained by correcting the 1P-phase estimate $\angle x$ (Eq. (3) with the current rotor azimuth angle ϕ. The rotor azimuth angle is commonly measured with encoders on the main shaft and logged in the SCADA system

$$\hat{\theta} = \angle x - \phi. \tag{10}$$

Lastly, the estimated fault location $\hat{\theta}$ is associated with the blade number using the boundaries $\pi/3$ and $-\pi/3$ (Fig. 1).

2.4. Reference fault diagnosis method: Linear discriminant analysis

A Linear Discriminant Analysis (LDA) classifier is selected as a benchmark to evaluate the proposed diagnostic method. LDA is a supervised machine learning method used for classification [39]. The prerequisites for LDA are similar to those of the statistical change detection method, in that (a) each class k follows multivariate Gaussian distributions and (b) shares a common covariance matrix $\vec{\Sigma}$, which are valid assumptions according to the simulation results (Section 3.3)

$$H_k : \vec{x} \sim N(\vec{\mu}_k, \vec{\Sigma}), \quad \vec{\Sigma}_k = \vec{\Sigma} \forall k. \tag{11}$$

LDA distinguishes between classes k, in this context fault types, by imposing a sample vector $\vec{x}$ of different predictors (here sensor signals) on linear discriminant functions δ_k. The class G is predicted, whose mean vector $\vec{\mu}_k$ is most closely aligned with the sample vector $\vec{x}$ and thus maximizes the respective linear discriminant function (Eq. (12))

$$
\begin{aligned}
G(\vec{x}) &= \text{argmax}_k(\delta_k) \\
&= \text{argmax}_k \left(\vec{x}^T \vec{\Sigma}^{-1} \vec{\mu}_k - \frac{1}{2} \vec{\mu}_k^T \vec{\Sigma}^{-1} \vec{\mu}_k + \ln \pi_k \right),
\end{aligned} \tag{12}
$$

where

$$
\begin{aligned}
\vec{\mu}_k &= \frac{1}{N_k} \sum_k^{N_k} \vec{x}_k, \\
\vec{\Sigma} &= \vec{\Sigma}_1 = \frac{1}{N_k - 1} \sum_k^{N_k} (\vec{x}_k - \vec{\mu}_1)(\vec{x}_k - \vec{\mu}_1)^T.
\end{aligned} \tag{13}
$$

The distribution parameters $\vec{\mu}_k$, $\vec{\Sigma}$ and class priors π_k are not known beforehand and must be estimated with labelled training data. The class priors of each class are identical, since an equal number of simulations are conducted for each FC, and can thus be omitted in Eq. (12). The mean vector and covariance matrix are determined by their maximum likelihood estimate (Eq. (13)).

Table 4
First principles analysis of rotor imbalances and induced drivetrain responses.

Fault type	Mass imbalance		Pitch misalignment		Yaw misalignment	
Imbalance forces	$F_G = const$ ⇓	$F_C = const$ ⇓	$\Delta F_N = const$ ⇓	$\Delta F_t = const$ ⇓	$\Delta F_N(\omega t)$ ⇓	$\Delta F_t(\omega t)$ ⇓
Rotating frame	$M_x(\omega t)$ ⇓	$F_z = const$ ⇓	$M_y = const$ ⇓	$F_y = const$ ⇓	N/A ⇓	
Fixed frame	$M_X(\omega t)$ ⇓	$F_{Y,Z}(\omega t)$ ⇓	$M_{Y,Z}(\omega t)$ ⇓	$F_{Y,Z}(\omega t)$ ⇓	$F_Y(\omega t)$ ⇓	
Structural response	–	$\ddot{Y}(t)$	–	$\ddot{Y}(t)$	$\ddot{Y}(t)$	
Drivetrain response	$\dot{\omega}(t)$	–	$\ddot{Y}(t)$	–	–	
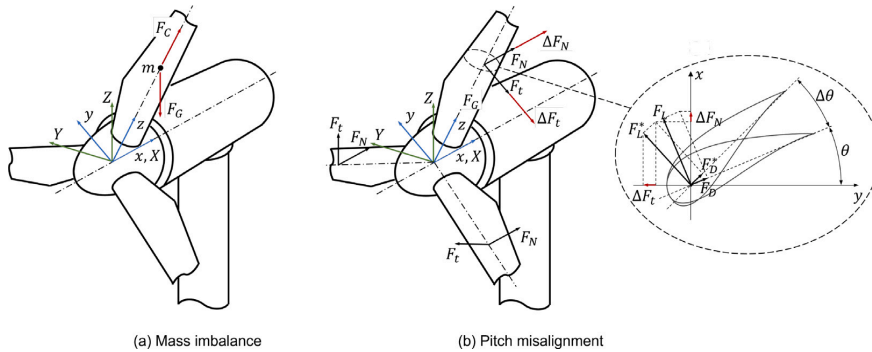
Fig. 2. Imbalance forces in rotating (x, y, z) and fixed coordinate frame (X, Y, Z) for different rotor imbalances.

3. Results and discussion

3.1. Analysis based on first principles

For the development of robust, physics-based diagnostic methods, it is crucial to understand the physical relationship of faults and dynamic system responses. In this section a short elaboration on the effect of rotor imbalance faults on main shaft loads in the rotating and fixed frame and their corresponding dynamic responses in the wind turbine structure and drivetrain is presented and summarized in Table 4. An idealized case without turbulence, wind shear, rotor axis tilt and tower shadow effects is considered to better isolate the primary effects of rotor imbalances.

Mass imbalance can be represented by a point mass m with distance r from the rotor axis that entails imbalance forces in the form of gravitational F_G and centrifugal forces F_C (Fig. 2). Centrifugal imbalance forces cause constant main shaft loads in the radial direction of the rotating frame (F_z), which translate to periodical shear forces in the fixed frame (F_Y, F_Z). Shear forces primarily excite transverse bending modes of the tower. Gravitational imbalance forces are constant in the fixed frame, but cause torque oscillations (M_x, M_X) due to periodical changes of lever length (ΔY), which excite torsional modes of the drivetrain.

A pitch misalignment of $\Delta\theta$ leads to discrepancies of lift forces F_L and drag forces F_D between faulty and healthy blades, which in turn can be represented as differences in thrust ΔF_N and tangential forces ΔF_t. Thrust imbalances translate to constant bending moments in the rotating frame (M_y) and periodical yaw and tilting moments in the fixed frame (M_Y, M_Z). Imbalances in tangential forces correspond to constant circumferential forces in the rotating frame (F_y) and periodical shear forces in the fixed frame (F_X, F_Y). The combination of shear forces and bending moments has an impact on both structural and drivetrain responses. Shear forces pass through the main bearings into the structure due to the high radial bearing stiffness and excite transverse tower bending modes, while out-of-plane bending moments

primarily excite bending modes of the main shaft, which further impact the dynamics of downwind gear stages.

In the case of yaw misalignment, the effective angle of attack varies periodically as a function of the blade azimuth angle; it is increased in the upper half of the rotor disk and decreased in the lower half compared to non-yawed conditions. As a result the thrust and tangential forces of each blade oscillate in the rotating frame ($F_t(\omega t)$, $F_N(\omega t)$). The load effects of yaw misalignment on the tower and the drivetrain are highly complex and can exhibit both upwards and downwards trends depending on the operational region and the yaw angle sign [29,40]. Dynamic responses to yaw misalignment are reportedly increased tower sway and platform roll motions due to shear force excitations [41].

3.2. Main shaft loads

The qualitative analysis of rotor imbalance dynamics in Section 3.1 is underlined with aeroelastic simulation results of the global wind turbine model. The analysis is limited to the amplitudes of the once per revolution (1P) oscillatory load component, where the effect imbalance faults is observable. Shown in Fig. 3 are the 1P-amplitudes of main shaft loads averaged over 6 realizations of one hour simulations for each FC–EC combination. The loads are extracted at the rotor hub in the fixed reference frame, where X is aligned with the rotor axis. First, a significant influence of environmental conditions can be observed. Shear forces (F_Y) and out-of-plane bending moments (M_Y, M_Z) show a positive trend with increasing wind speeds due to higher aerodynamic loads. Thrust (F_X) and torque (M_X) on the other hand level off or decrease above rated wind speed, which can be attributed to the pitch control system limiting the aerodynamic torque. Furthermore, there is a discernible peak in the thrust excitations at EC3 ($U = 10$ m/s), which is slightly below rated wind speed. Similar results are reported by Nejad et al. [42], where the highest axial damage equivalent loads (DEL) in floating offshore wind turbines are simulated at $U = 11$ m/s. Nejad et al. argue that the frequent activation and deactivation of the pitch control system in the region close to rated wind speed is the causes of increased axial DEL.
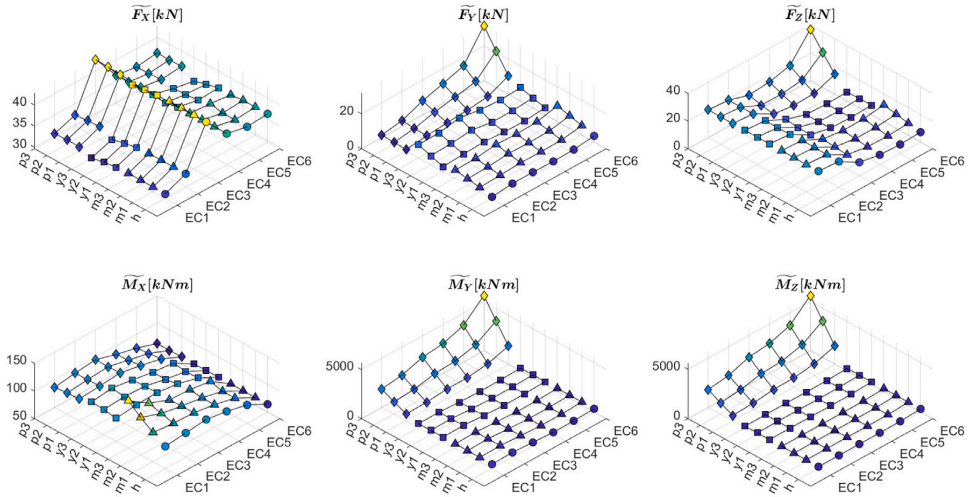
Fig. 3. 1P-amplitude $\tilde{x}$ (Eq. (3)) of main shaft loads averaged over 6 seeds of one hour simulations for different rotor imbalances and environmental conditions.
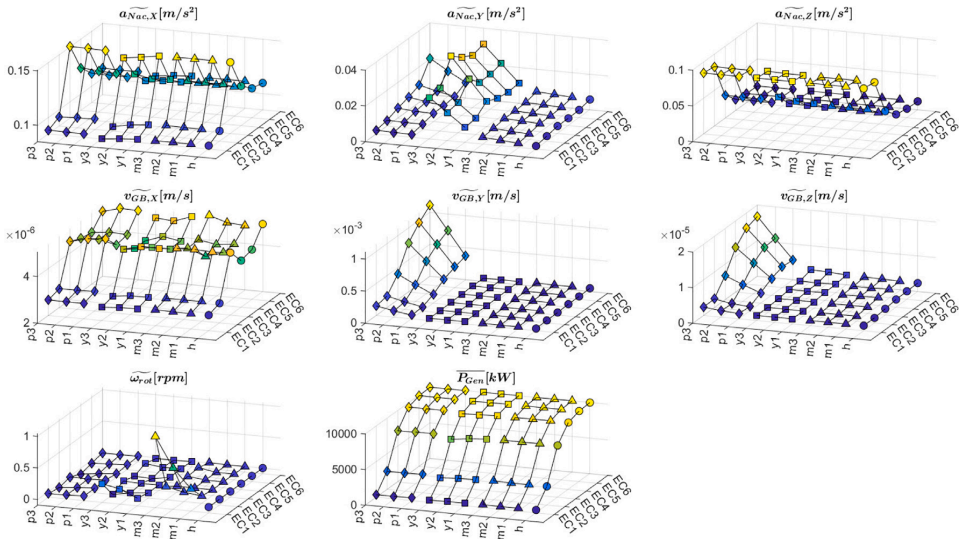
Fig. 4. 1P-amplitude (Eq. (3)) of global and drivetrain signals averaged over 6 seeds of one hour simulations of for different rotor imbalances and environmental conditions.

The effect of different rotor imbalances is indicated in Fig. 3 by the change relative to healthy conditions (h). It is apparent that mass imbalances (m1, m2, m3) cause significant excitations in shear (F_Y) and vertical forces (F_Z) due to centrifugal forces (F_C, Table 4), as well as torsional excitations (M_X) from gravitational forces (F_G, Table 4). Torsional excitations are only noticeable at lower wind speeds (EC1, EC2), where gravitational forces are more significant compared to aerodynamic forces. At EC1 the torque amplitudes due to mass imbalance reach 135 kN m, which amounts to 22% of the mean aerodynamic torque of 616 kN m. For reference, at EC6 the torque amplitudes of 55 kN m are insignificant compared to the rated aerodynamic torque of 10,000 kN m. Yaw misalignment (y1, y2, y3) appears to consistently increase amplitudes of shear forces (F_Y) for all EC, while the effect other load components is insignificant. Similar results are reported by Cardaun et al. [29]. Pitch misalignment (p1, p2, p3) results in high

excitations in shear (F_Y), vertical forces (F_Z) from circumferential force imbalances (ΔF_t, Table 4) and out-of-plane bending moments (M_Y, M_Z), which can directly be attributed to thrust imbalances (ΔF_N, Table 4). In this regard pitch misalignment is unique, as it is the only rotor imbalance fault that causes 1P excitation with bending moments.

3.3. Dynamic structural and drivetrain responses

Dynamic responses in the wind turbine structure and the drivetrain to the periodic imbalance forces discussed in Section 3.2 are characterized with a selection of simulated SCADA and drivetrain CMS signals, shown in Fig. 4. Indicative of structural dynamics are nacelle accelerations a_{Nac} in fore-aft (X), side-side (Y) and vertical (Z) direction. Gearbox housing velocities v_{GB}, as well as rotor speed ω_{Rot} and electrical power output P_{el} are shown to illustrate the lateral and

torsional drivetrain response. The vibration signals at the main bearings and the generator exhibit similar behaviour to the gearbox housing signals and are omitted for brevity. The respective statistical features 1P-amplitude or mean are calculated for each signal and averaged over 6 seeds of one hour simulations for each FC–EC combination. Central to this discussion is the signal sensitivity towards faults, which is required for robust fault detection. The signal sensitivity is formally quantified by the change in mean value relative to the signal variance ($S = \frac{\mu_1 - \mu_0}{\sigma_0}$) and is indicated in Fig. 4 by the slope with respect to increasing fault severity.

Mass imbalances appear to increase side-side nacelle motion as a result of periodic shear forces, as well as increase torsional vibration in the drivetrain due to torque imbalances. Increased torsional vibrations are unique to mass imbalance faults, however the signal sensitivity is relatively low except at cut-in wind speeds (EC1). This is likely a result of the high aerodynamic torque that overshadows any torque amplitudes from mass imbalances (Section 3.2). The effect of yaw misalignment can primarily be observed in an increase of nacelle side-side acceleration amplitudes, which show a high sensitivity. The drivetrain torsional dynamics are affected by yaw misalignment as well, however a consistent upwards or downwards trend cannot be observed. Furthermore, it is evident that yaw misalignment reduces the mean electrical power by reducing the effective inflow wind speed, as stated in many references, however the environmental influences seem to dominate over effects of yaw misalignment. Unique dynamic responses to pitch misalignment can be observed in the drivetrain vibration signals that show increased velocity amplitudes in side-side and vertical direction, which are likely a result of periodic out-of-plane bending moments. In addition, pitch misalignment increases nacelle side-side motion with shear force excitation similar to the other rotor imbalance faults. A minor reduction in power output is also observed due to reduced lift forces at the faulty blade.

In conclusion, the following characteristic traits of each rotor imbalance are identified, which are leveraged as heuristic domain knowledge for the proposed diagnostic method:

- Increased side-side nacelle acceleration amplitudes as a result of periodical shear forces may be used universally for detection of any type of rotor imbalance.
- Pitch misalignment may be isolated from other fault types by increased lateral drivetrain vibration amplitudes caused by out-of-plane bending moments.
- Mass imbalance may be identified at lower wind speeds by increased rotor speed oscillations due to torque excitations.

3.4. Fault detection by means of drivetrain CMS signals

Focus of this section is to assess the capabilities of drivetrain CMS signals relative to traditionally used SCADA signals for fault detection. According to statistical change detection theory [33], the probability of detection is primarily affected by three factors: the signal sensitivity ($S = \frac{\mu_1 - \mu_0}{\sigma_0}$), the sample size N and the probability of false alarm P_{FA}. The signal sensitivity towards faults is discussed for different signals in Section 3.3. Increased sample sizes N effectively reduce the variance of the test statistic and thus improve the confidence in fault detection. Two test scenarios with sample lengths of 10 and 60 min ($N = [10, 60]$) are considered here to analyse the influence of N and to give an indication of expected detection times. The parameter P_{FA} regulates the expected false positive rate by increasing or decreasing the detection threshold. In field operation P_{FA} must be set appropriately to balance costs of false positives and detection rates. In this study a relatively low value of $P_{FA} = 10^{-4}$ is assumed.

The test statistic $T(x)$ (Eq. (8)) is applied on samples of simulated drivetrain CMS and SCADA signals in order to quantitatively assess fault detection performances. The detection thresholds (Eq. (9)) are set for each signal and EC based on training data of healthy behaviour only.

The testing data set consists of 360 realizations of the statistical features mean and 1P-amplitude extracted from 1 min intervals for each FC–EC combination. The resulting true positive rates (TPR) aggregated for all environmental conditions are shown in Tables 5, 6 for sample lengths of 10 and 60 min respectively.

The electrical power signal $\overline{P_{el}}$, shows underwhelming performance with TPR of less than 10% for the severe pitch and yaw misalignment cases p3, y3. The signal sensitivity appears to be insufficient to reliably detect pitch and yaw misalignment based a one hour observation. Side-side nacelle acceleration amplitudes $\widetilde{a_{Nac,Y}}$ show a response for every rotor imbalance type. The highest TPR (> 0.95) are calculated for yaw misalignment, even for short time frames of 10 min. The signal is less sensitive to pitch misalignment and mass imbalance with maximum TPR of 0.64 and 0.61 for one hour observations. Hence, nacelle accelerations may be utilized as a universal detector for rotor imbalances, however larger sample sizes are necessary for robust detection of all fault types. Rotor speed amplitudes $\widetilde{\omega_{Rot}}$ can be used in principle for mass imbalance detection, however with a maximum TPR of 0.22 the detection performance is inferior to nacelle accelerations. Gearbox housing vibration signals show a significant response to pitch misalignment, predominantly in side-side direction $\widetilde{v_{GB,Y}}$, which results in TPR near 1 for a 10 min sample. Similar results are obtained for vibration signals at the main bearings and the generator housing, which are omitted for brevity.

It is concluded that drivetrain vibration signals are particularly beneficial for the detection of pitch errors, since they show much higher sensitivity than classical nacelle acceleration signals.

3.5. Classification performance

The proposed knowledge-based expert system and the reference LDA classifier are trained and tested on the simulated SCADA and CMS signals $\widetilde{a_{Nac,Y}}, \widetilde{v_{GB,Y}}, \widetilde{\omega_{Rot}}$ using 6-fold cross validation. The expert system is trained exclusively on data of healthy conditions to determine the normal behaviour model (μ_0, σ_0) and set the thresholds γ_i (Eq. (9)), while LDA classifier is trained on the entire dataset to estimate distribution parameters $\vec{\mu}_k, \Sigma_k$ (Eq. (13)) of each fault case. Each EC is trained and tested separately to factor out influences of wind speed, which would be available from measurements in field operation.

The results for the expert system are shown in Fig. 5 as confusion matrices. Confusion matrices relate the predicted values of a classifier with the actual values and are commonly used for performance assessment in machine learning. The diagonal elements denote the number of instances, where a class is correctly predicted, whereas the off-diagonal elements represent misclassifications between classes. The individual fault severity levels (eg. m1, m2, m3) are aggregated into a single class (m), since the method is unable to estimate these. First, it is observed that all healthy cases with one exception are correctly classified as a result of the relatively low value of $P_{FA} = 10^{-4}$ and corresponding high detection thresholds. In addition, all pitch misalignment cases are correctly identified regardless of the environmental conditions, which suggests that the gearbox housing vibration signal $\widetilde{v_{GB,Y}}$ is effective at isolating this fault type. Yaw misalignment is correctly predicted in the majority of cases using nacelle accelerations $\widetilde{a_{Nac,Y}}$ with the exception of three misclassifications as mass imbalance. Mass imbalance is identified in 10 out of 18 cases at cut-in wind speeds (EC1) using rotor speed amplitudes $\widetilde{\omega_{Rot}}$. At higher wind speeds, however, the signal sensitivity of $\widetilde{\omega_{Rot}}$ is insufficient such that mass imbalances are either not detected or misclassified as yaw misalignment. Reasons for the low sensitivity at higher wind speeds may be higher influences of the aerodynamic torque compared to the torque excitation from gravitational imbalance. It is also feasible that above rated wind speeds the pitch controller is actively damping the 1P torque fluctuations.

For comparison, the results for a traditional LDA classifier are presented in Fig. 6. The LDA classifier is able to predict both fault type and fault severity, as it is trained on a labelled dataset of faulty conditions.

Table 5
True positive rates for fault detection with a 10 min sample size ($N = 10$) with test statistic $T(x)$ (Eq. (8)).

		h	m1	m2	m3	p1	p2	p3	y1	y2	y3
Classical SCADA	$\overline{P_{el}}$	0.98	0.02	0.02	0.03	0.02	0.03	0.03	0.03	0.03	0.04
	$\overline{a_{Nac,Y}}$	1	0.01	0.06	0.23	0.05	0.25	0.42	0.95	1	1
	$\overline{\omega_{Rot}}$	0.98	0.03	0.04	0.07	0.02	0.02	0.02	0.02	0.02	0.02
Proposed drivetrain CMS	$\overline{v_{GB,X}}$	1	0	0	0	0	0.01	0,01	0	0	0
	$\overline{v_{GB,Y}}$	1	0	0	0	0.82	1	1	0	0	0
	$\overline{v_{GB,Z}}$	1	0	0	0	0.59	0.75	0.89	0	0	0.01

Table 6
True positive rates for fault detection with a 60 min sample size ($N = 60$) with test statistic $T(x)$ (Eq. (8)).

		h	m1	m2	m3	p1	p2	p3	y1	y2	y3
Classical SCADA	$\overline{P_{el}}$	1	0	0	0	0	0	0.03	0	0	0
	$\overline{a_{Nac,Y}}$	1	0.14	0.31	0.64	0.19	0.44	0.61	1	1	1
	$\overline{\omega_{Rot}}$	0.94	0.06	0.17	0.22	0.06	0.06	0.06	0.06	0.06	0.06
Proposed drivetrain CMS	$\overline{v_{GB,X}}$	1	0	0	0	0	0	0	0	0	0
	$\overline{v_{GB,Y}}$	1	0	0	0	1	1	1	0	0	0
	$\overline{v_{GB,Z}}$	1	0	0	0	0.67	0.81	1	0	0.03	0.14
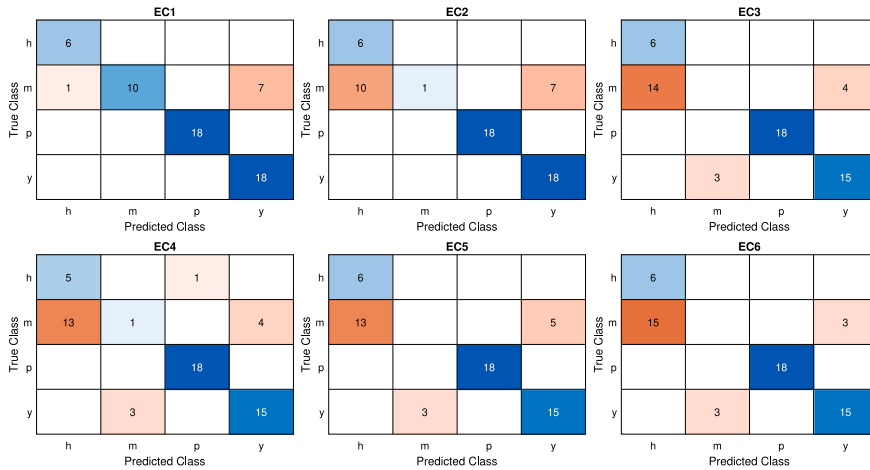
Fig. 5. Confusion matrix for knowledge-based expert system (Section 2.3.2) tested on one hour samples of simulated SCADA and CMS signals under healthy conditions (h) and rotor imbalance faults (m, p, y).

With regard to pitch misalignment and yaw misalignment classification the performance is comparable to the expert system with a TPR of close to 100%. The prediction of mass imbalance is significantly improved: Mass imbalance is longer misclassified as yaw misalignment, however it still suffers from low detection rates due to a generally weak dynamic system response and low signal sensitivities.

From these results it can be concluded that the SCADA signals $\overline{a_{Nac,Y}}$ and $\overline{\omega_{Rot}}$ in combination with the CMS signal $\overline{v_{GB,Y}}$ are suitable to detect and classify the three considered rotor imbalance types, at least at lower wind speeds. With the inclusion of training data of faulty conditions, the classification accuracy may be improved, however such information is rarely available in practice.

3.6. Fault localization accuracy

The accuracy of localizing the faulty blade is displayed in Fig. 7 for both classical SCADA signals and the proposed CMS drivetrain signals. The fault location is estimated with Eq. (10) based on one hour samples and shown here aggregated for all environmental conditions. In all simulated cases the fault is implemented at blade 1, which corresponds

to $\theta = 0$. The results show that an accurate localization of mass imbalances is possible with the phase of nacelle acceleration signals $\angle a_{Nac,Y}$. The expected error (mean ± standard deviation) ranges from $-0.1 \pm 27.4.5°$ (m1) to $2.0 \pm 16.4°$ (m3). The remaining signals show standard errors of higher than ±100° and are thus not suitable for localizing mass imbalance. The best performance for localizing pitch misalignment show side-side gearbox housing velocities $\angle v_{GB,Y}$ with errors between $0.6 \pm 11.2°$ (p1) to $0.1 \pm 13.2°$ (p3). This is a significant improvement compared to classical SCADA signals ($\angle a_{Nac,Y}$), which result in much higher standard errors of up to ±71.5° (p1)

Similar conclusions as in Section 3.4 can be drawn in that drivetrain CMS vibration signals outperform classical SCADA signals and facilitate the detection and localization of pitch errors with much higher accuracy. For mass imbalance and yaw misalignment, however, the classical approach with nacelle acceleration signals prevails.

3.7. Considerations for field implementation and sources of uncertainty

Implementation of the proposed knowledge-based diagnostic method requires only the normal behaviour model. In practice, this
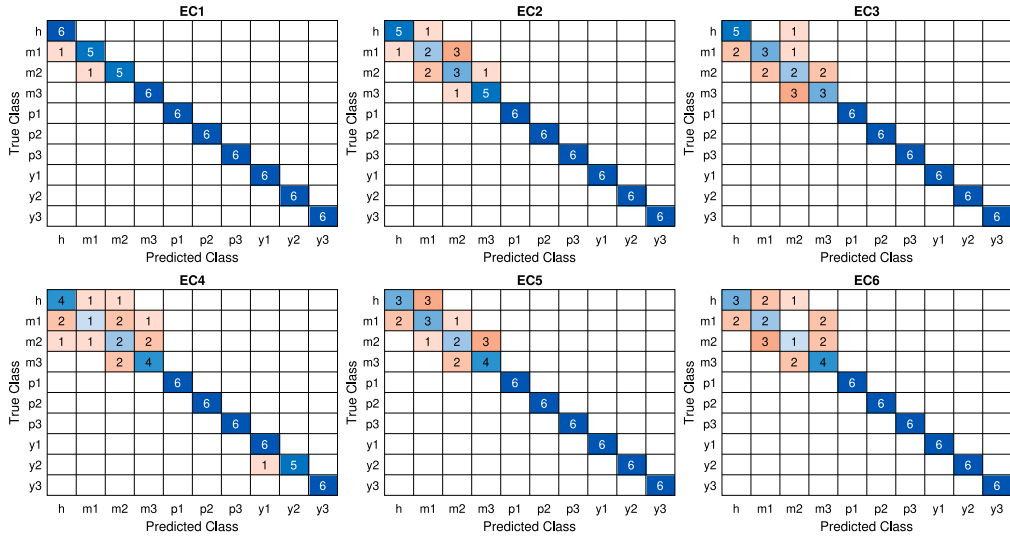
Fig. 6. Confusion matrix for data-driven LDA classifier (Section 2.4) trained and tested on one hour samples of simulated SCADA and CMS signals under healthy conditions (h) and rotor imbalance faults of varying severity (m, p, y).
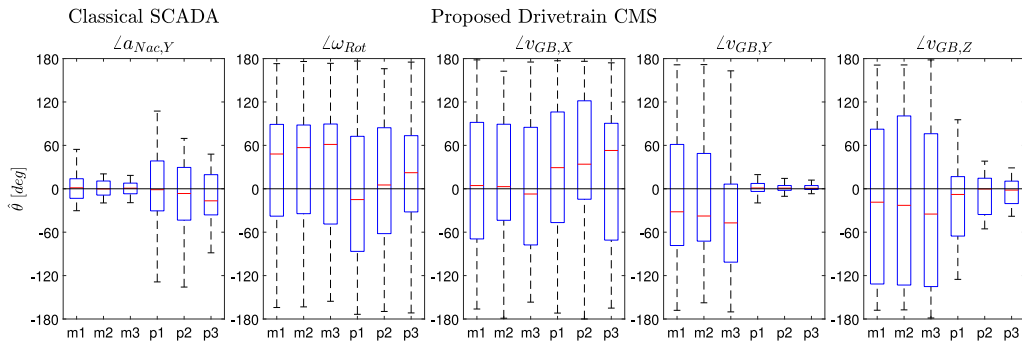
Fig. 7. Estimated fault location $\hat{\theta}$ (Eq. (10)) based on 60 min samples of simulated SCADA and CMS signals. Shown are median, 25 and 75 percentiles, and extreme values aggregated for all EC. The true fault location is $\theta = 0$ (blade 1).

would entail measuring long-term mean values and standard deviation of the signals nacelle side–side acceleration, gearbox housing side–side vibrations, and rotor speed for different wind speed bins.

It is feasible to integrate the proposed diagnostic method with resilient control techniques, which aim at minimizing fault consequences by compensating the faulty signal. Resilient control strategies for pitch misalignment are presented by Bertele et al. [7], who propose a rebalancing algorithm to iteratively correct for pitch imbalance. Other signals compensation methods such as Takagi–Sugeno fuzzy models may also be applicable in this case [43].

In addition, the detection thresholds must be set to appropriate values using the parameter P_{FA} (Eq. (9)). Unfortunately, standards or guidelines on setting detection thresholds for this specific application have not been developed yet, and the values of P_{FA} reported in scientific publications range widely from 10^{-2} to 10^{-12} [34,35]. Lower thresholds are desirable to maximize fault detection rates and to mitigate potentially harmful consequences of rotor imbalance faults such as increased fatigue loads, reduced lifetime and higher risks of failure of wind turbine components. On the other hand, low thresholds are conducive to false positives and lead to unnecessary activation of automatic rebalancing algorithms, which are disruptive to the wind

turbine operation. This represents an optimization problem with the objective of minimizing the combined costs associated with false negatives K_{FN} and false positives K_{FP} and can be expressed with a cost function K [44]

$$\min_{P_{FA}} K = K_{FP} + K_{FN} \tag{14}$$

Defining the cost functions of false positives K_{FP} and false negatives K_{FN} is challenging, as it requires extensive economical analysis and risk assessment on the effects of rotor imbalance faults. Wind farm operators may instead resort to empirical methods based on confidence intervals commonly employed for drivetrain condition monitoring. Typical threshold values are $\gamma = \mu_0 + 3\sigma_0$, which corresponds to a 99.7% confidence interval [45].

Lastly, several limitations of the presented methodology and other sources of uncertainty need to be carefully considered for implementation in the field.

- *Simulation model limitations*: Simulation-based studies with academic reference models are effective for demonstrating the proof of concept of novel methods. Simulation models enable the exploration of many different fault scenarios in a short time frame,

however due to model assumptions and complexity reduction they do not fully reflect the dynamics of real wind turbines. The 10 MW DTU reference drivetrain model is considered state-of-the-art for load calculations, but is limited with regard to vibration analysis. Flexible housing models for the main bearings, gearbox and the generator are not implemented and as a result the simulated drivetrain CMS signals may suffer from inaccuracies. It should also be noted that the analysis of this paper is limited to four point support, medium speed drivetrains and that the findings are not directly transferable to direct drive systems.

- *Considered fault cases*: The scope of this paper is limited to a small amount of fault cases to retain reasonable simulation times, in particular with the computationally expensive MBS drivetrain model. Only static pitch misalignment of a single blade towards feather is investigated. Combinations of aerodynamic and mass imbalances, which are likely to occur in practice, are not considered in this study. Shaft misalignment faults are not considered in this study, but may cause similar dynamic responses at 1P and thus be misclassified as a rotor imbalance by the diagnostic method. Other faults including main bearing and gear faults are out of the scope of this paper, since they typically have much higher characteristic frequencies and would be filtered out by the proposed method.

- *Fault severity*: The proposed method is not capable of estimating the rotor imbalance severity, as this would require additional model assumptions and/or training data. For instance, the power reduction with respect to the yaw misalignment angle can be modelled with the third power of the cosine function [20]. Velocity and acceleration amplitudes can be well described by linear functions of the rotor imbalance severity, as seen in Fig. 4, however additional training data would be required to determine the unknown slopes.

- *Operational conditions*: The proposed method is only robust at cut-in wind speeds, where mass imbalance cause significant torque excitations and induce an observable torsional response in the drivetrain. At higher wind speeds the method is unable to distinguish between yaw misalignment and mass imbalance. Furthermore the method was not tested under other IEC 61400-1 load cases such as start-up or emergency shutdown.

- *Measurement noise*: Sensors in the field are subject to measurement noise and other sources of uncertainty, which could affect the diagnostic performance. However, it can be argued that the measurement noise of commercial accelerometers has relatively low energy compared to the excitations of rotor imbalance faults. Typical values for measurement noise in the low frequency range of 1P are specified to 4 µg or $4 \cdot 10^{-5}$ m/s^2 (see PCB Model 622B01), whereas simulated acceleration amplitudes under faulty conditions were of the order 10^{-4} m/s^2 at the gearbox housing and 10^{-2} m/s^2 at the nacelle (Fig. 4). Furthermore, it is observed in this study that the employed statistical methods are effective at filtering out the energetic 1P component from a noisy background.

- *Signal resolution*: Sensor data quality is also limited by the signal resolution. The minimum required sample frequency to estimate 1P-amplitudes of nacelle and drivetrain signals is 0.2 Hz at a minimum rotor speed of 6 rpm. Classical SCADA data stored as 10 min averages do not suffice for this purpose, however, it is reported that wind farm operators are moving towards high-frequency (1 Hz) SCADA data [46].

4. Conclusions

This paper presented a novel approach for diagnosis of rotor imbalance faults, namely pitch misalignment, yaw misalignment and mass imbalance, by monitoring the drivetrain vibration response. Traditionally, only SCADA signals indicative of structural dynamics including

nacelle accelerations, rotor speed and electrical power are utilized for this purpose. Drivetrain CMS signals on the other hand are normally used for diagnosis of local drivetrain faults in gears and bearings. The proposed method comprises the three steps fault detection, classification and localization. Fault detection is realized with methods of statistical change detection from normal behaviour. Classification of the rotor imbalance type uses heuristic, physics-based decision criteria derived from simulations and literature review. Localization of the faulty blade is based on maximum likelihood estimates of the phase angle.

Simulations were conducted with both high-fidelity aeroelastic and drivetrain models of the floating 10 MW DTU reference turbine to synthesize SCADA and CMS signals and evaluate the proposed method. Six environmental conditions with wind speeds ranging from cut-in to cut-out and three fault severity levels were carefully selected based on literature review to emulate realistic conditions.

The proposed drivetrain CMS signal (gearbox housing side-side velocity) outperformed classical SCADA signals in detecting pitch misalignment and increased the detection rate of a 1° pitch error from 19% to near 100% based on one hour measurements. Furthermore, the standard error in localizing the blade with faulty pitch angle was reduced from 71.5° to 11.2°. For mass imbalance and yaw misalignment, however, the classical approach using nacelle accelerations remained more accurate.

The benefit of drivetrain CMS signals is also seen in the classification of the rotor imbalance type. Pitch misalignment uniquely causes once per revolution (1P) bending moments on the main shaft, which are observable throughout the drivetrain as increased lateral vibration amplitudes. Thus, the 1P-amplitudes of CMS signals are proposed as an indicator to distinguish pitch misalignment from other rotor imbalance types. Using CMS signals all simulated test cases of pitch misalignment ranging from 1° to 3° were correctly classified regardless of the environmental conditions.

A unique characteristic of mass imbalance are periodic 1P torque loads, which excite torsional modes of the drivetrain. For this reason the 1P-amplitude of the main shaft speed is proposed as an identifier for mass imbalances, however, in practice the signal sensitivity is relatively low due to environmental influences and controller effects. Only at cut-in wind speeds (EC1) this criterion was shown to be robust and able to identify 10 out of 18 of test cases. A benchmark linear discriminant analysis (LDA) classifier representative for a fully data-driven approach showed significantly higher classification performance for both mass imbalance and yaw misalignment. However, the success of this approach relies on the availability of training data of faulty conditions, which in practice is rarely the case.

From these results it can be concluded that the SCADA signals nacelle side-side acceleration ($\widetilde{a_{Nac,Y}}$) and rotor speed ($\widetilde{\omega_{Rot}}$) in combination with the CMS signal gearbox housing velocity ($\widetilde{v_{GB,Y}}$) are suitable to detect and classify the three considered rotor imbalance types, at least at lower wind speeds. For practical implementation in operating turbines it is recommended to apply the change detection framework presented in this paper, as it has very low requirements. Only the normal behaviour model of healthy conditions must be established from historical measurements. However, some method limitations have to be considered including lower accuracy than data-driven methods, the inability to estimate the fault severity, the required signal resolution of 1 Hz and the limited operational range near cut-in wind speeds.

CRediT authorship contribution statement

Declaration of competing interest

The authors declare that they have no known competing financial interests or personal relationships that could have appeared to influence the work reported in this paper.

Data availability

Data will be made available on request.

Acknowledgements

References

[1] Y. Kumar, J. Ringenberg, S.S. Depuru, V.K. Devabhaktuni, J.W. Lee, E. Nikolaidis, B. Andersen, A. Afjeh, Wind energy: Trends and enabling technologies, Renew. Sustain. Energy Rev. 53 (2016) 209–224, http://dx.doi.org/10.1016/j.rser.2015.07.200.

[2] T. Stehly, P. Beiter, 2018 Cost of Wind Energy Review, Report, National Renewable Energy Laboratory, 2020.

[3] M. Wilkinson, B. Hendriks, F. Spinato, E. Gomez, H. Bulacio, J. Roca, P. Tavner, Y. Feng, H. Long, Methodology and results of the reliawind reliability field study, in: European Wind Energy Conference, Warsaw, Poland, 2010.

[4] D. Astolfi, A study of the impact of pitch misalignment on wind turbine performance, Machines 7 (1) (2019) http://dx.doi.org/10.3390/machines7010010.

[5] U. Elosegui, I. Egana, A. Ulazia, G. Ibarra-Berastegi, Pitch angle misalignment correction based on benchmarking and laser scanner measurement in wind farms, Energies 11 (12) (2018) http://dx.doi.org/10.3390/en11123357.

[6] P. Frohboese, A. Anders, Effects of Icing on wind turbine fatigue loads, J. Phys. Conf. Ser. 75 (2007) http://dx.doi.org/10.1088/1742-6596/75/1/012061.

[7] M. Bertelè, C.L. Bottasso, S. Cacciola, Automatic detection and correction of pitch misalignment in wind turbine rotors, Wind Energy Sci. 3 (2) (2018) 791–803, http://dx.doi.org/10.5194/wes-3-791-2018.

[8] M. Saathoff, M. Rosemeier, T. Kleinselbeck, B. Rathmann, Effect of individual blade pitch angle misalignment on the remaining useful life of wind turbines, Wind Energy Sci. 6 (5) (2021) 1079–1087, http://dx.doi.org/10.5194/wes-6-1079-2021.

[9] C.L. Bottasso, C.E.D. Riboldi, Estimation of wind misalignment and vertical shear from blade loads, Renew. Energy 62 (2014) 293–302, http://dx.doi.org/10.1016/j.renene.2013.07.021.

[10] ISO 21940-11, Mechanical vibration — Rotor balancing — Part 11: Procedures and tolerances for rotors with rigid behaviour, 2016.

[11] J. Kusnick, D.E. Adams, D.T. Griffith, Wind turbine rotor imbalance detection using nacelle and blade measurements, Wind Energy 18 (2) (2015) 267–276, http://dx.doi.org/10.1002/we.1696.

[12] Z. Gao, X. Liu, An overview on fault diagnosis, prognosis and resilient control for wind turbine systems, Processes 9 (2) (2021) http://dx.doi.org/10.3390/pr9020300.

[13] R.W. Hyers, J.G. McGowan, K.L. Sullivan, J.F. Manwell, B.C. Syrett, Condition monitoring and prognosis of utility scale wind turbines, Energy Mater. 1 (3) (2013) 187–203, http://dx.doi.org/10.1179/174892406x163397.

[14] X. Gong, W. Giao, Simulation investigation of wind turbine imbalance faults, in: International Conference on Power System Technology, IEEE, 2010, http://dx.doi.org/10.1109/POWERCON.2010.5666455.

[15] G.R. Hübner, H. Pinheiro, C.E. de Souza, C.M. Franchi, L.D. da Rosa, J.P. Dias, Detection of mass imbalance in the rotor of wind turbines using support vector machine, Renew. Energy 170 (2021) 49–59, http://dx.doi.org/10.1016/j.renene.2021.01.080.

[16] J. Niebsch, R. Ronny, Simultaneous estimation of mass and aerodynamic rotor imbalances for wind turbines, J. Math. Ind. 4 (12) (2014) http://dx.doi.org/10.1186/2190-5983-4-12.

[17] S. Cacciola, I.M. Agud, C. Bottaso, Detection of rotor imbalance, including root cause, severity and location, J. Phys. Conf. Ser. 753 (2016) http://dx.doi.org/10.1088/1742-6596/753/7/072003.

[18] A. Kusiak, A. Verma, A data-driven approach for monitoring blade pitch faults in wind turbines, IEEE Trans. Sustain. Energy (2010) http://dx.doi.org/10.1109/tste.2010.2066585.

[19] S. Cho, M. Choi, Z. Gao, T. Moan, Fault detection and diagnosis of a blade pitch system in a floating wind turbine based on Kalman filters and artificial neural networks, Renew. Energy 169 (2021) 1–13, http://dx.doi.org/10.1016/j.renene.2020.12.116.

[20] D. Choi, W. Shin, K. Ko, W. Rhee, Static and dynamic Yaw misalignments of wind turbines and machine learning based correction methods using LiDAR data, IEEE Trans. Sustain. Energy 10 (2) (2019) http://dx.doi.org/10.1109/TSTE.2018.2856919.

[21] B. Jing, Z. Qian, Y. Pei, L. Zhang, T. Yang, Improving wind turbine efficiency through detection and calibration of Yaw misalignment, Renew. Energy 160 (2020) 1217–1227, http://dx.doi.org/10.1016/j.renene.2020.07.063.

[22] M. Ghane, A. Rasekhi Nejad, M. Blanke, Z. Gao, T. Moan, Condition monitoring of spar-type floating wind turbine drivetrain using statistical fault diagnosis, Wind Energy 21 (7) (2018) 575–589, http://dx.doi.org/10.1002/we.2179.

[23] C. Bak, F. Zahle, R. Bitsche, T. Kim, A. Yde, L.C. Henriksen, M.H. Hansen, J.P.A.A. Blasques, M. Gaunaa, A. Natarajan, The DTU 10-MW Reference Wind Turbine, Report, DTU Wind Energy, 2013.

[24] R.R. Arias, J. Galvan, NAUTILUS-DTU10 MW Floating Offshore Wind Turbine at Gulf of Maine, WindEurope, 2018.

[25] OpenFAST, https://github.com/OpenFAST.

[26] Dassault Systèmes, Simpack: Multibody simulation, 2021, https://www.3ds.com/fileadmin/PRODUCTS/SIMULIA/PDF/brochures/simulia-simpack-brochure.pdf.

[27] S. Wang, A.R. Nejad, T. Moan, On design, modelling, and analysis of a 10-MW medium-speed drivetrain for offshore wind turbines, Wind Energy 23 (4) (2020) 1099–1117, http://dx.doi.org/10.1002/we.2476.

[28] A.R. Nejad, E.E. Bachynski, M.I. Kvittem, C. Luan, Z. Gao, T. Moan, Stochastic dynamic load effect and fatigue damage analysis of drivetrains in land-based and TLP, spar and semi-submersible floating wind turbines, Mar. Struct. 42 (2015) 137–153, http://dx.doi.org/10.1016/j.marstruc.2015.03.006.

[29] M. Cardaun, B. Roscher, R. Schelenz, G. Jacobs, Analysis of wind-turbine main bearing loads due to constant yaw misalignments over a 20 years timespan, Energies 12 (9) (2019) http://dx.doi.org/10.3390/en12091768.

[30] ISO10816-21, Mechanical vibration — Evaluation of machine vibration by measurements on non-rotating parts — Part 21: Horizontal axis wind turbines with gearbox, 2015.

[31] R.B. Randall, Vibration Based Condition Monitoring: Industrial, Aerospace and Automotive Applications, Wiley I& Sons Ltd, 2010.

[32] K.S. Wang, P.S. Heyns, Application of computed order tracking, Vold–Kalman filtering and EMD in rotating machine vibration, Mech. Syst. Signal Process. 25 (1) (2011) 416–430, http://dx.doi.org/10.1016/j.ymssp.2010.09.003.

[33] S.M. Kay, Fundamentals of Statistical Signal Processing. Volume II. Detection Theory, Prentice Hall PTR, 1998.

[34] S. Nath, J. Wu, Y. Zhao, W. Qiao, Low latency bearing fault detection of direct-drive wind turbines using stator current, IEEE Access 8 (2020) 44163–44174, http://dx.doi.org/10.1109/access.2020.2977632.

[35] M. Ghane, A.R. Nejad, M. Blanke, Z. Gao, T. Moan, Statistical fault diagnosis of wind turbine drivetrain applied to a 5MW floating wind turbine, J. Phys. Conf. Ser. 753 (2016) http://dx.doi.org/10.1088/1742-6596/753/5/052017.

[36] W. Qiao, D. Lu, A survey on wind turbine condition monitoring and fault diagnosis—Part II: Signals and signal processing methods, IEEE Trans. Ind. Electron. 62 (10) (2015) 6546–6557, http://dx.doi.org/10.1109/tie.2015.2422394.

[37] M.C. Garcia, M.A. Sanz-Bobi, J. del Pico, SIMAP: Intelligent system for predictive maintenance, Comput. Ind. 57 (6) (2006) 552–568, http://dx.doi.org/10.1016/j.compind.2006.02.011.

[38] W. Li, H. Li, S. Gu, T. Chen, Process fault diagnosis with model- and knowledge-based approaches: Advances and opportunities, Control Eng. Pract. 105 (2020) http://dx.doi.org/10.1016/j.conengprac.2020.104637.

[39] T. Hastie, R. Tibshirani, J. Friedman, The Elements of Statistical Learning: Data Mining, Inference and Prediction, Springer, 2009, http://dx.doi.org/10.1007/b94608.

[40] R. Damiani, S. Dana, J. Annoni, P. Fleming, J. Roadman, J. van Dam, K. Dykes, Assessment of wind turbine component loads under Yaw-offset conditions, Wind Energy Sci. 3 (1) (2018) 173–189, http://dx.doi.org/10.5194/wes-3-173-2018.

[41] X. Li, C. Zhu, Z. Fan, X. Chen, J. Tan, Effects of the Yaw error and the wind-wave misalignment on the dynamic characteristics of the floating offshore wind turbine, Ocean Eng. 199 (2020) http://dx.doi.org/10.1016/j.oceaneng.2020.106960.

[42] A.R. Nejad, E.E. Bachynski, T. Moan, Effect of axial acceleration on drivetrain responses in a Spar-type floating wind turbine, J. Offshore Mech. Arct. Eng. 141 (3) (2019) http://dx.doi.org/10.1115/1.4041996.

[43] X. Liu, Z. Gao, M.Z.Q. Chen, Takagi–Sugeno fuzzy model based fault estimation and signal compensation with application to wind turbines, IEEE Trans. Ind. Electron. 64 (7) (2017) 5678–5689, http://dx.doi.org/10.1109/tie.2017.2677327.

[44] A. Youssef, C. Delpha, D. Diallo, An optimal fault detection threshold for early detection using Kullback–Leibler divergence for unknown distribution data, Signal Process. 120 (2016) 266–279, http://dx.doi.org/10.1016/j.sigpro.2015.09.008.

[45] A. Alkaya, I. Eker, Variance sensitive adaptive threshold-based PCA method for fault detection with experimental application, ISA Trans. 50 (2) (2011) 287–302, http://dx.doi.org/10.1016/j.isatra.2010.12.004, URL https://www.ncbi.nlm.nih.gov/pubmed/21251651.

[46] E. Gonzalez, B. Stephen, D. Infield, J.J. Melero, Using high-frequency SCADA data for wind turbine performance monitoring: A sensitivity study, Renew. Energy 131 (2019) 841–853, http://dx.doi.org/10.1016/j.renene.2018.07.068.

A.6   Paper 6

Highlights

On the uncertainty of digital twin models for load monitoring and fatigue assessment in wind turbine drivetrains

Felix C. Mehlan, Amir R. Nejad

- 10 min averaging of SCADA data results in a significant loss of information.

- The state estimation uncertainty is driven by estimating the unknown rotor torque.

- The uncertainty in the system parameters is highest at cut-in and rated wind speed.

- The model uncertainty originates from neglecting non-torsional dynamics

On the uncertainty of digital twin models for load monitoring and fatigue assessment in wind turbine drivetrains

Felix C. Mehlan[a], Amir R. Nejad[a]

[a]*Norwegian University of Science and Technology, Jonsvannsveien 82, Trondheim, 7050, , Norway*

Abstract

This article presents a systematic assessment of the uncertainty in digital twins for load and fatigue monitoring in wind turbine drivetrains. The uncertainty in the measurement input, the reduced order drivetrain models and the model updating methods are investigated. A statistical analysis is conducted on gear and bearing load measurements from numerical studies with 5 and 10 MW drivetrain models and from field measurements of a 1.5 MW research turbine. The uncertainty is quantified using lognormal distributions and limitations of digital twin are discussed such as the measurement uncertainty in 10 min averaged SCADA data, the uncertainty in estimating the unknown rotor torque, and the modelling errors in torsional reduced order drivetrain models. This study contributes to a deeper understanding of the origin and the effects of uncertainty in digital twins and delivers a foundation for further reliability and risk assessment studies.

Keywords: Digital twin, wind turbine drivetrain, uncertainty, fatigue assessment, reduced order model, virtual sensing

1. Introduction

Offshore wind turbine installations are projected to accelerate rapidly in the near future driven by better wind resources and higher social acceptance rates compared to onshore sites [1]. However, a major economic limitation of offshore wind turbines are high operational and maintenance expenditures (OPEX), which amount to about 34 % of the levelized cost of energy (LCOE)

[2]. These are caused by lower reliability due to harsher environmental conditions and time-consuming replacement or repair due to difficulties accessing the site and dependency on good weather conditions. A major contributor to the OPEX is the geared drivetrain with frequent failures and long downtimes and is thus the subject of current research [3].

Digital twin (DT) is an emerging technology with prospects of decreasing the OPEX and improving the market competitiveness of offshore wind farms. The wind turbine drivetrain DT proposed by the authors in [4] would enable monitoring drivetrain loads and fatigue damage at otherwise inaccessible locations such as bearing and gear contacts using "virtual sensors". A DT framework with the three components data, virtual model and decision support is envisioned for this objective (Fig. 1). The *Data* comprise continuous data streams provided by the supervisory control and data acquisition system (SCADA) and the condition monitoring system (CMS), the data history including the load history and the accumulated fatigue damage, asset information such as the drivetrain topology, and general domain knowledge on drivetrain physics. The *virtual model* refers to physics-based models to simulate internal drivetrain dynamics. Reduced order models (ROMs) are derived from high-fidelity multibody simulation (MBS) models for the purpose of real-time simulation. The virtual model and its physical counterpart are synchronized with real-time field measurements using model updating techniques. State estimators such as Kalman filters are applied to infer the dynamic states of the drivetrain at small time intervals, given by the sensor sample frequency of 200 Hz. System identification methods are used to estimate system parameters such as inertia, stiffness and damping parameters, as a means to validate values provided by gearbox manufacturers or to track long-term parameter variations due to faults, material degradation or other mechanisms. Therefore it is sufficient to update the model parameters at longer time intervals, here set to 10 min. The model updating, also referred to as data fusion or digital twinning, is essential as it facilitates the use of virtual sensors in the synchronized model. The virtual sensor measurements are converted to value-adding information for the turbine operator in the component called *decision support*. The focus lies on long-term fatigue damage and remaining useful life (RUL) assessment of drivetrain components, which is necessary to advance from corrective to predictive maintenance strategies. In previous numerical and field studies the proof of concept of the DT framework could be demonstrated [4][5], however, there remain research questions on the sources and the magnitude of the the virtual measurements' uncer-

2

tainty. Uncertainty is present in the DT's data input due to the stochastic nature of wind and wave loads, as well as in the load and fatigue calculations due to the limitations of the DT model.

The uncertainty in long-term fatigue damage calculation of wind turbine drivetrains is addressed in several studies on reliability-based design [6][7][8]. Nejad et al. presents a method for fatigue analysis for gear tooth root bending and differentiate between the uncertainty in the aeroelastic model, the drivetrain model and the fatigue damage model [6]. The uncertainty is characterized by lognormal distributions with standard deviation values ranging from 0.01 for the drivetrain model to 0.1 for the aeroelastic model. Li et al. present a study on reliability-based design optimization of gear profiles and consider the uncertainty of the wind conditions with a joint probability density function of the wind speed and turbulence intensity [7]. Dong et al. further consider model uncertainties in a wide range of drivetrain and fatigue model parameters [8].

The aforementioned studies are focused on the design of wind turbine drivetrains, where the aleatory uncertainty in the unknown environmental conditions is most influential. For DTs of operating wind turbines the challenge shifts from aleatory uncertainty towards epistemic uncertainty, since the environmental conditions and the dynamic system response are continuously estimated using real-time measurements and state estimation methods. The epistemic uncertainty of such methods has not yet been investigated systematically, as this approach is relatively novel in the field of wind energy. The presented study bridges this gap and contributes to a better knowledge of the origin, the magnitude and the distribution shape of the uncertainty in DTs for fatigue damage monitoring.

The remainder of this article is structured as follows: Sec. 2 presents the methodology of the DT framework for fatigue damage monitoring and defines the numerical and experimental case studies for uncertainty assessment. Sec. 3 discusses the uncertainty in different DT components and their impact on long-term fatigue damage. Concluding remarks are provided in Sec. 4.

2. Methodology

2.1. Definition of uncertainty

The proposed DT framework comprises several interacting models and data processing algorithms, each of which introduce characteristic uncertainties. These uncertainties are grouped into the categories of measurement,
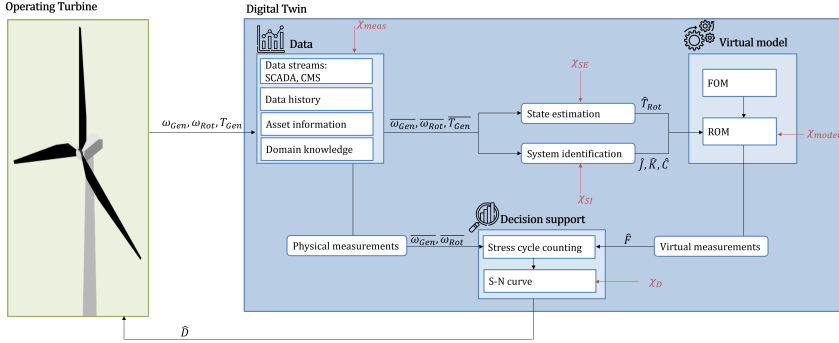
3

Figure 1: Digital twin framework for continuous remaining useful life estimation in wind turbine drivetrain components and sources of uncertainty. [4].

state estimation, system identification, model and fatigue damage uncertainty. The measurement uncertainty χ_{meas} originates from poor sensor data quality due to measurement noise, sensor failure or the low sampling frequency, which imposes a frequency limit on the observable drivetrain load spectrum. Only the latter is investigated in this study, since simulation measurements are used. The measurement uncertainty is defined here as the ratio of the true generator torque T_{Gen} to the measured generator torque $\bar{T}_{Gen}$. The true generator torque is sampled from simulation measurements at 200 Hz, which is sufficient to reflect all relevant drivetrain dynamics, while the measured generator torque is obtained by averaging the simulation measurements in 1 s or 10 min intervals, which is the typical resolution of SCADA data.

$$\chi_{meas} = \frac{T_{Gen}}{\bar{T}_{Gen}} \tag{1}$$

The state estimation uncertainty χ_{SE} refers to errors caused by the Kalman filter algorithm. The Kalman filter fuses uncertain information from measurements and model predictions and is the optimal state estimator in case of white Gaussian measurement and process noise. However, this assumption is not valid here since the unknown rotor torque modelled as process noise exhibits non-uniformity such as peaks at characteristic excitation frequencies (1P, 3P, ...). It is therefore expected that use of Kalman filter introduces an additional uncertainty in the drivetrain case. This uncertainty is defined as the ratio of the true dynamic states x to the states estimated by Kalman

4

filtering $\hat{x}$.

$$\chi_{SE} = \frac{x}{\hat{x}} \qquad (2)$$

The system identification uncertainty χ_{SI} reflects the error that is introduced by the inverse methods to estimate the system's inertia, stiffness and damping matrices $\hat{J}, \hat{K}, \hat{C}$ and is defined as the ratio of the true system parameters θ to the estimated parameter set $\hat{\theta}$.

$$\chi_{SI} = \frac{\theta}{\hat{\theta}} \qquad (3)$$

The model uncertainty χ_{model} refers to to the limitations of the DT model to simulate all relevant drivetrain dynamics. ROMs with a limited number of torsional DOFs are considered, which are unable to capture non-torsional drivetrain dynamics such as shaft bending modes or complex torsional dynamics such as gear meshing. The error caused by the model complexity reduction is described with the model uncertainty and defined as the ratio of the drivetrain loads $F, \hat{F}$ calculated with the FOM and the ROM, respectively

$$\chi_{model} = \frac{F}{\hat{F}} \qquad (4)$$

The uncertainty of the fatigue damage model, χ_D as shown in Fig. 1, including the stress cycle counting method and the S-N curves is related to the material and fatigue testing which is out the scope of this numerical case study.

2.2. Numerical case studies

Two numerical case studies with the National Renewable Energy Laboratory (NREL) 5 MW baseline turbine [9] and the DTU 10 MW reference turbine are conducted [10]. The best practice for dynamic drivetrain simulation is the decoupled analysis approach, where the "global", structural blade and tower dynamics and the "internal" drivetrain dynamics are simulated separately [6]. The global system response is simulated first with an aeroelastic model and the resultant main shaft loads and nacelle motions are then imposed as boundary conditions on the drivetrain model. This procedure is motivated by the fact that the global dynamics are governed by aerodynamic excitations and occur at low frequencies ($< 10Hz$), while much higher frequencies such as gear meshing frequencies at $> 100Hz$ need to be considered

for the drivetrain dynamics. The simulation cases are designed according to the IEC 61400-1 requirements for long-term fatigue analysis. Twelve wind speed cases ranging from cut-in wind speed of 3 m/s to cut-out wind speed of 25 m/s are considered. One case of turbulence intensity is considered and modelled with the IEC turbulence classes A. Only one case of wave height and wave period are considered, since the drivetrain bearing and gear loads are reportedly insensitive to the sea state. The primary effect of harsher sea states can be observed in increased axial loads induced by pitch motions, which are compensated by the main bearings in a four-point suspension and do not propagate further into the drivetrain [11]. Each environmental condition (EC) is simulated for one hour with six different random realizations (seeds) of turbulent wind fields.

Table 1: Environmental conditions for simulation with global and drivetrain models.

Wind speed [m/s]	3...25
Turbulence intensity [-]	IEC class A
Wave height [m]	5
Wave period [s]	12
Simulation length [s]	6×3600

2.3. Global models

The global wind turbine dynamics are simulated with open source aeroelastic models of the NREL 5 MW and DTU 10 MW reference turbines mounted on the OC4 and Nautilus semisubmersible platforms, respectively [12][13]. The models are implemented in the aeroelastic code OpenFAST that comprises of computational modules for calculation of the aerodynamics, hydrodynamics, structural dynamics and wind turbine control [14]. The aerodynamics are calculated with blade element momentum (BEM) theory, where the turbulent wind field is generated with the Kaimal turbulence model. The structural dynamics of the blades and the tower are based on Timoshenko elastic beam theory. The incident wave loads on the floater are modelled with a Jonswap spectrum. A variable-speed controller is implemented for the 5 MW and the 10 MW model.

2.4. Full order drivetrain models

Multibody simulation (MBS) models of the NREL 5 MW and DTU 10 MW reference turbine serve as benchmark in this study [15][16]. The MBS
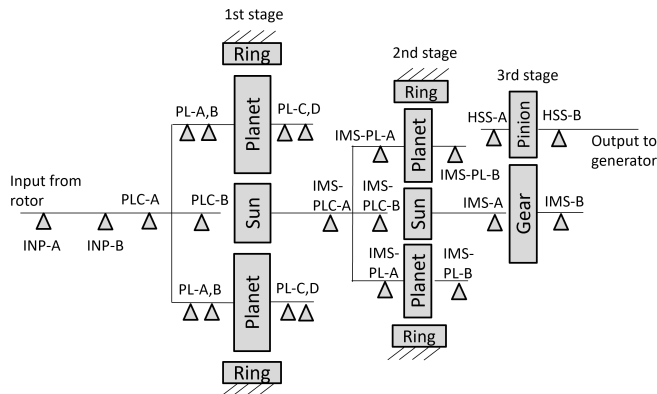
Figure 2: Topology and component nomenclature of the NREL 5MW and DTU 10MW drivetrain models.

models are developed according to best practices and current model fidelity guidelines [17] and are thus considered as full order models (FOMs). Both FOMs have similar topology and comprise a four-point suspension for the main shaft and a gearbox with two planetary gear stages and one parallel gear stage (Fig. 2). However, the 5 MW model represents a high-speed gearbox with a gear ratio of 1:96.354, while the 10 MW model represents a medium-speed gearbox with a gear ratio of 1:50.039. The FOMs allow shaft motion in all six degrees of freedom (DOF) and consider the flexibility in the main shaft and the planet carriers. The bearings and the torque arm bushings are modelled as linear spring-damper connections in six DOF with diagonal stiffness and damping matrices. The gear compliance is modelled with a time-invariant mesh stiffness function capable of emulating gear meshing excitations. The input loads simulated with aeroelastic models are imposed on the main shaft, while the generator shaft speed is controlled with a PI-controller.

2.5. Reduced order drivetrain models

Reduced order models (ROMs) are preferable as DT models due to the high computational costs in real-time monitoring applications [18]. The complexity of DT models is also limited by the observability requirement of the state estimator. The state estimator that is used to match the dynamics

7

of the DT model with the physical turbine requires that all dynamic states are observable with the available measurement input. The SCADA measurements of the main and generator shaft speeds allow the observation of torsional drivetrain modes. Bending and lateral drivetrain modes are observable with CMS accelerometers mounted on the gearbox housing, however the sensitivity is relatively low due to measurement noise and the observation function is complex due to the transfer path of the vibration through the housing [18]. For this reason, the ROMs are limited to torsional degrees of freedom (DOF) only. Lumped parameter models with one and two torsional DOFs are considered. The input torques at each gear stage $T_{in,k}$ are calculated with the torsional ROMs and then further used to determine local gear and bearing forces (Sec. 2.5.3).

2.5.1. Rigid one degree of freedom ROM

The first ROM represents a rigid, torsional model with one degree of freedom (DOF). The flexibility of shafts and gear contacts are neglected, which yields direct coupling of the angular shaft velocities ω_k and input torques at each gear stage $T_{in,k}$ via the gear ratios i_k

$$
\begin{aligned}
\omega_{Rot} &= \omega_{in,2}/i_1 = \omega_{in,3}/i_1/i_2 = \omega_{Gen}/i_1/i_2/i_3 \\
T_{in,1} &= i_1 T_{in,2} = i_1 i_2 T_{in,3} = i_1 i_2 i_3 T_{Gen}
\end{aligned}
\tag{5}
$$

The rigid ROM is advantageous, in that it does not require inertia, stiffness or damping parameters for model construction and validation, which minimizes the uncertainty associated with system identification techniques for parameter estimation (χ_{SI}). In addition, it is not necessary to apply state estimation methods, since the gear stage torques and thus all drivetrain loads are directly observable with the measured generator torque, which reduces state estimation uncertainties (χ_{SE}).

2.5.2. Flexible two degree of freedom ROM

The second ROM introduces one additional torsional DOF and is able to represent the first torsional mode. However, this model assumes knowledge of inertia, stiffness and damping parameters, which may be estimated via system identification techniques. The flexibility of all drivetrain components are lumped into a scalar drivetrain stiffness k_{DT}, while the torsional inertias are lumped into either the rotor inertia J_{Rot} or the generator inertia J_{Gen}.

The equations of motion are then given by

$$\mathbf{J}\ddot{\phi} + \mathbf{C}\dot{\phi} + \mathbf{K}\phi + \mathbf{f} = \mathbf{0} \qquad (6)$$

where $\mathbf{J}$ denotes the inertia matrix, $\mathbf{C}$ is the damping matrix, $\mathbf{K}$ is the stiffness matrix, $\mathbf{f}$ is the external force vector and ϕ are the independent dynamic states

$$\mathbf{J} = \begin{bmatrix} J_{Rot} & 0 \\ 0 & J_{Gen} \end{bmatrix}, \mathbf{C} = \begin{bmatrix} c_{DT} & -c_{DT}/i_{DT} \\ -c_{DT}/i_{DT} & c_{DT}/i_{DT}^2 \end{bmatrix}, \mathbf{K} = \begin{bmatrix} k_{DT} & -k_{DT}/i_{DT} \\ -k_{DT}/i_{DT} & k_{DT}/i_{DT}^2 \end{bmatrix}$$

$$\phi = \begin{bmatrix} \phi_{Rot} \\ \phi_{Gen} \end{bmatrix}, \mathbf{f} = \begin{bmatrix} -T_{Rot} \\ T_{Gen} \end{bmatrix},$$

$$(7)$$

The gear stage input torques are still coupled and only a function of the rotor and generator shaft angular positions ϕ

$$T_{in,1} = i_1 T_{in,2} = i_1 i_2 T_{in,3} = [c_{DT}, \ -c_{DT}/i_{DT}]\dot{\phi} + [k_{DT}, \ -k_{DT}/i_{DT}]\phi \quad (8)$$

2.5.3. Bearing and gear forces

The gear forces are determined with free body diagrams and moment balances as a function of the gear stage input torques. Dynamic effects of planet load sharing are not considered at the planetary gear stages, hence the gear stage torque is distributed equally among the number of planets N_{PL}. Furthermore, the gear forces at the ring-planet and the sun-planet contacts are assumed to be equal. The circumferential (z-direction) gear forces F_t are then obtained as follows

$$\begin{aligned} F_{t,1} &= T_{in,1} \cdot i_1/r_{b,S,1}/N_{PL,1} \\ F_{t,2} &= T_{in,2} \cdot i_2/r_{b,S,2}/N_{PL,2} \\ F_{t,3} &= T_{in,3}/r_{b,G,3} \end{aligned} \qquad (9)$$

where r_b are the base radii of the first and second stage sun and of the third stage gear wheel. The remaining gear force components in x- and y-direction, the axial and radial gear force components F_a, F_r, are determined with the tangential pressure angle α_t and helix angle β. The planetary gear stage is modelled with spur gears ($\beta = 0$), while the parallel gear stage is modelled with a helix angle of $\beta = 10°$

$$\begin{aligned} F_r &= F_t \tan(\alpha_t)/\cos(\beta) \\ F_a &= F_t \tan(\beta) \end{aligned} \qquad (10)$$

9

At the planetary gear stages the radial bearing forces F_{rad} are directly proportional to the circumferential gear forces with the assumption of negligible gravity forces.

$$F_{rad,PL-A} = 2 \cdot F_{t,1}$$
$$F_{rad,IMS-PL-A} = 2 \cdot F_{t,2} \tag{11}$$

At the helical gear stage the radial bearing forces are derived with moment balances

$$F_{rad} = \sqrt{F_y^2 + F_z^2} \tag{12}$$

where

$$F_{y,IMS-A} = -F_r \frac{d_{IMS-B} - d_W}{d_{IMS-B} - d_{IMS-A}} + F_a \frac{r_{p,W}}{d_{IMS-B} - d_{IMS-A}}$$

$$F_{y,IMS-B} = -F_r \frac{d_W - d_{IMS-A}}{d_{IMS-B} - d_{IMS-A}} - F_a \frac{r_{p,W}}{d_{IMS-B} - d_{IMS-A}}$$

$$F_{y,HSS-A} = F_r \frac{d_{HSS-B} - d_P}{d_{HSS-B} - d_{HSS-A}} + F_a \frac{r_{p,P}}{d_{HSS-B} - d_{HSS-A}} \tag{13}$$

$$F_{y,HSS-B} = F_r \frac{d_P - d_{HSS-A}}{d_{HSS-B} - d_{HSS-A}} - F_a \frac{r_{p,P}}{d_{HSS-B} - d_{HSS-A}}$$

$$F_{z,IMS-A} = -F_{t,3} \frac{d_{IMS-B} - d_W}{d_{IMS-B} - d_{IMS-A}}$$

$$F_{z,IMS-B} = -F_{t,3} \frac{d_W - d_{IMS-A}}{d_{IMS-B} - d_{IMS-A}}$$

$$F_{z,HSS-A} = F_{t,3} \frac{d_{HSS-B} - d_P}{d_{HSS-B} - d_{HSS-A}} \tag{14}$$

$$F_{z,HSS-B} = F_{t,3} \frac{d_P - d_{HSS-A}}{d_{HSS-B} - d_{HSS-A}}$$

The axial gear force component of the helical high-speed gear stage is supported by the HSS-B and IMS-B bearings.

$$F_{ax,IMS-B} = F_a$$
$$F_{ax,HSS-B} = -F_a \tag{15}$$

2.6. Experimental case study

The simulation measurements are partially validated with field measurements of the department of energy (DOE) 1.5 MW research turbine located

at the National Renewable Energy Laboratory (NREL) [19]. The DOE 1.5 MW turbine is equipped with a commercial Winergy PEAB 4410.4 high-speed gearbox with similar three stage topology as the above simulation models. The dataset, originally collected for the analysis of cage and roller slip in the HSS-A bearing [20], is repurposed for this study. The original sample frequency of 5 kHz necessary to observe slip dynamics restricted the measurement duration and as a result the total recorded data amounts to only about 30 min. Nonetheless, the full wind spectrum is covered, which allows for comparison with simulated data.

The loading of the HSS is fully determined with three shaft mounted strain gauge bridges, one for measuring torque and two 90-degree offset bridges for measuring bending moments. The forces at the HSS-A bearing are calculated with the torque T and bending moment measurements M_y, M_z [20]

$$
\begin{aligned}
F_{y,HSS-A} &= \frac{1}{d_B - d_{HSS-A}} \left[-M_z - T/r_b(d_B - d_P)\sin\beta \right] \\
F_{z,HSS-A} &= \frac{1}{d_B - d_{HSS-A}} \left[-M_y - T/r_b(d_B - d_P)\cos\beta \right]
\end{aligned}
\tag{16}
$$

These measurements are considered FOM bearing load measurements, since all relevant torsional and shaft bending dynamics are captured. The FOM loads are set in relation to the ROM loads calculated solely with torque measurements and the rigid ROM (eq. 14) to assess the model uncertainty.

2.7. State and input estimation

The DT model is synchronized with the operating wind turbine at regular time intervals Δt such that gear and bearing loads can be measured with "virtual sensors" in the synchronized model. The challenge lies in the incomplete and noisy measurements of both the dynamic states and the input forces, which poses a joint state and input estimation problem. The measurements of the dynamic states, the shaft angular velocities and positions, are corrupted with measurement noise, while the input forces at the main shaft are unknown; only the generator side torque is measured. The augmented Kalman filter is applied here as an joint state and input estimator, as it is the optimal estimator for dynamic systems governed by linear, stochastic equations subjected to white Gaussian process and measurement noise. For this purpose the equations of motion of the flexible ROMs are first brought
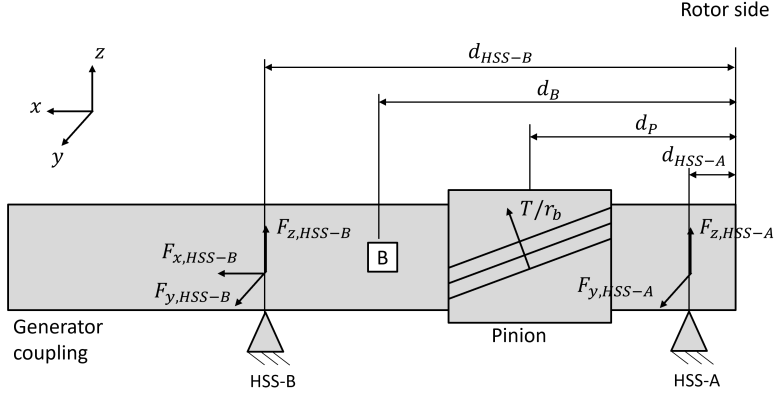
Figure 3: Forces at the HSS.

into discrete state-space representation

$$\mathbf{x_{n+1}} = \mathbf{F^d x_n} + \mathbf{G_k^d u_{k,n}} + \mathbf{G_u^d u_{u,n}} + \mathbf{w_n}, \qquad (17)$$

$$\mathbf{y_n} = \mathbf{H^d x_n} + \mathbf{v_n}, \qquad (18)$$

where the state vector $\mathbf{x}$ is obtained by stacking the shaft angular positions and velocities, the input forces $\mathbf{u}$ are split into the known generator torque $\mathbf{u_k}$ and the unknown rotor torque $\mathbf{u_u}$, the measurement vector $\mathbf{y}$ contains the rotor and generator shaft speeds, the unknown dynamic component of the rotor torque is considered white Gaussian process noise $\mathbf{w}$ with covariance $\mathbf{Q}$, and $\mathbf{v}$ is white Gaussian measurement noise with covariance $\mathbf{R}$

$$
\begin{aligned}
\mathbf{x} &:= [\phi \ \dot{\phi}]^\mathrm{T} \\
\mathbf{u_k} &:= T_{Gen} \\
\mathbf{u_u} &:= T_{Rot} \\
\mathbf{y} &:= [\dot{\phi}_{Rot}, \dot{\phi}_{Gen}]^\mathrm{T} \\
\mathbf{w} &\sim \mathcal{N}(\mathbf{0}, \mathbf{Q}) \\
\mathbf{v} &\sim \mathcal{N}(\mathbf{0}, \mathbf{R})
\end{aligned}
\qquad (19)
$$

12

The system matrix $\mathbf{F^d}$, the input matrix $\mathbf{G^d}$ and the observation matrix $\mathbf{H^d}$ of the discrete state-space model are calculated as follows

$$\mathbf{F^d} = \exp(\mathbf{F^c}\Delta t), \tag{20}$$

$$\mathbf{G^d} = \begin{bmatrix} \mathbf{G^d_k} \ \mathbf{G^d_u} \end{bmatrix} = (\mathbf{F^c})^{-1}(\mathbf{F^d} - \mathbf{I}^{2N \times 2N})\begin{bmatrix} \mathbf{G^c_k} \ \mathbf{G^c_u} \end{bmatrix} \tag{21}$$

$$\mathbf{H^d} = \begin{bmatrix} \mathbf{0}^{N \times N} & \mathbf{I}^{N \times N} \end{bmatrix} \tag{22}$$

where N denotes the model's DOF, $\mathbf{0}$ is the null matrix, $\mathbf{I}$ is the identity matrix, and $\mathbf{F^c}$, $\mathbf{G^c_k}$, $\mathbf{G^c_u}$ and $\mathbf{H^c}$ are the matrices of the continuous state space model

$$\begin{aligned}
\mathbf{F^c} &= \begin{bmatrix} \mathbf{0}^{N \times N} & \mathbf{I}^{N \times N} \\ -\mathbf{J}^{-1}\mathbf{K} & -\mathbf{J}^{-1}\mathbf{C} \end{bmatrix} \\
\mathbf{G^c_k} &= \begin{bmatrix} \mathbf{0}^{1 \times 2N-1} & 1/J_{Gen} \end{bmatrix}^{\mathrm{T}} \\
\mathbf{G^c_u} &= \begin{bmatrix} \mathbf{0}^{1 \times N} & -i_{DT}/J_{Rot} & \mathbf{0}^{1 \times N-1} \end{bmatrix}^{\mathrm{T}} \\
\mathbf{H^c} &= \mathbf{H^d}
\end{aligned} \tag{23}$$

For the purpose of simultaneous state and input estimation, the state vector $\mathbf{x}$ is expanded with the unknown input force $\mathbf{u_u}$, yielding the state-space representation with the augmented state vector $\mathbf{x^a} = \begin{bmatrix} \mathbf{x} \ \mathbf{u_u} \end{bmatrix}^{\mathrm{T}}$.

$$\mathbf{x^a_{n+1}} = \mathbf{F}\mathbf{x^a_n} + \mathbf{G_k}\mathbf{u_{k,n}} + \mathbf{w_n}, \tag{24}$$

$$\mathbf{y_n} = \mathbf{H}\mathbf{x^a_n} + \mathbf{v_n}, \tag{25}$$

where the system matrix $\mathbf{F}$, the input matrix $\mathbf{G}$ and the observation matrix $\mathbf{H}$ of the augmented state space model are calculated as follows

$$\mathbf{F} = \begin{bmatrix} \mathbf{F^d} & \mathbf{G^d_u} \\ \mathbf{0}^{1 \times N} & 1 \end{bmatrix} \tag{26}$$

$$\mathbf{G} = \begin{bmatrix} \mathbf{G^d_k} \\ 0 \end{bmatrix} \tag{27}$$

$$\mathbf{H} = \begin{bmatrix} \mathbf{H^d} & \mathbf{0}^{N \times 1} \end{bmatrix} \tag{28}$$

The Kalman filter produces the state estimates $\hat{\mathbf{x}}$ in a two-step algorithm, comprising of the prediction step and the measurement update step.

$$\hat{\mathbf{x}}^{\mathbf{a}}_{\mathbf{n}|\mathbf{n-1}} = \mathbf{F}\hat{\mathbf{x}}^{\mathbf{a}}_{\mathbf{n-1}|\mathbf{n-1}} + \mathbf{G}\mathbf{u_{n-1}}, \tag{29}$$

$$\hat{\mathbf{P}}_{\mathbf{n}|\mathbf{n-1}} = \mathbf{F}\hat{\mathbf{x}}^{\mathbf{a}}_{\mathbf{n-1}|\mathbf{n-1}}\mathbf{F^T} + \mathbf{Q}. \tag{30}$$

$$\mathbf{M_n} = \mathbf{\hat{P}_{n|n-1}} \mathbf{H^T} (\mathbf{H} \mathbf{\hat{P}_{n|n-1}} \mathbf{H^T} + \mathbf{R})^{-1}, \tag{31}$$

$$\mathbf{\hat{x}^a_{n|n}} = \mathbf{\hat{x}^a_{n|n-1}} + \mathbf{M_n}(\mathbf{y_n} - \mathbf{H}\mathbf{\hat{x}^a_{n|n-1}}), \tag{32}$$

$$\mathbf{\hat{P}_{n|n}} = (\mathbf{I} - \mathbf{M_n} \mathbf{H}) \mathbf{\hat{P}_{n|n-1}}. \tag{33}$$

2.8. System identification

System identification methods are applied to continuously update the model properties to ensure the convergence of the virtual model and the physical wind turbine's dynamic behaviour. The rotor inertia, generator inertia, drivetrain torsional stiffness and damping are considered time-variant parameters to reflect long-term changes of the physical wind turbine. The rotor inertia may increase due to the accretion of dirt, moisture and ice, or decrease as a result of leading edge erosion or similar damages. The drivetrain stiffness and damping values are affected by material fatigue and localized faults such as spalls or tooth root cracks. The second line of the equations of motion (Eq. 2.5.2) is used to estimate the parameter set $\theta = [J_{Gen}, c_{DT}, k_{DT}, \alpha_0]$, since the boundary conditions are fully determined here by measurements of the generator torque. The following least-squares optimization problem is then formulated

$$\hat{\theta} = \arg\min_{\theta} ||J_{Gen}\ddot{\phi}_{Gen} - c_{DT}/i_{DT}\dot{\alpha} - k_{DT}/i_{DT}(\alpha - \alpha_0) + T_{Gen}||_2^2 \tag{34}$$

The generator shaft acceleration $\ddot{\phi}_{Gen}$ is obtained by numerical differentiation of the measured SCADA generator shaft speed. The drivetrain torsion defined as $\alpha = \phi_{Rot} - \phi_{Gen}/i_{DT}$ is calculated by numerical integration of the shaft speeds. As a result of the numerical integration of noisy signals, a runaway trend or sensor drift is observed, which is removed via MATLAB's *detrend* function. Furthermore, the initial state α_0 of the integrated signal is unknown and therefore added to the parameter set of the optimization problem. The optimization problem is solved for 10 min time sections at each EC using a least-squares solver.

Unfortunately, the same procedure cannot be employed to obtain the remaining parameter, the rotor inertia J_{Rot}, since the rotor torque is typically not measured by SCADA systems, which leaves the rotor side equations of motion undefined (Eq. 2.5.2). Operational modal analysis (OMA) techniques are used instead. The first torsional natural frequency $\hat{f}_N$ is estimated using peak finding algorithms in the frequency spectrum of the drivetrain torsion signal α. Since the natural frequency is a function of the drivetrain inertia

and stiffness, one may solve for the unknown rotor inertia as follows

$$\hat{J}_{eq} = \frac{\hat{k}_{DT}}{(2\pi \hat{f}_N)^2}$$
$$\hat{J}_{Rot} = (1/\hat{J}_{eq} - 1/\hat{J}_{Gen}/i_{DT})^{-1}$$
(35)

2.9. Fatigue damage

The gear and bearing fatigue damage is based on the gear tooth root stress calculation of ISO 6336 [21] and the nominal bearing life calculation of ISO 281 [22]. The gear tooth root stress s is determined from the circumferential gear force F_t, the flank width b, the normal modul m_n and the modification factors Y and K [21]

$$s = \frac{F_t}{bm_n} Y_S Y_F Y_\beta Y_B Y_{DT} K_A K_V K_{F\beta} K_{F\alpha} K_\gamma$$
(36)

The pendant for bearings is the equivalent dynamic load P that is defined for for cylindrical roller bearings (CRB) and tapered roller bearings (TRB) as follows [22]:

$$\text{for CRB:} \quad P = F_{rad}$$
(37)

$$\text{for TRB:} \quad P = \begin{cases} F_{rad} + Y_1 F_{ax}, & \text{if } F_{ax}/F_{rad} \leq e \\ 0.67 F_{rad} + Y_2 F_{ax}, & \text{otherwise} \end{cases}$$
(38)

where Y_1, Y_2, e are bearing-specific parameters.

The load duration distribution (LDD) method is used as stress cycle counting method for components in rotating machinery that experience cyclic loading due to entering and exiting the load zone [6]. The LDD method counts one stress cycle per shaft revolution and distributed the cycles n_i into 64 bins of increasing stress range. The permissible stress cycles N_i for each stress range is modelled with S-N curves for gear tooth root fatigue

$$N_i = K_c \, s_i^{-m}$$
(39)

where $m = 6.225$ and $K_c = 10^{24.744}$ [6], and the nominal bearing life equation for bearing fatigue [22]

$$N_i = 10^6 \left(\frac{C}{P_i}\right)^m$$
(40)

15

where C is the basic dynamic load rating and $m = 10/3$ for roller bearings. The short-term fatigue damage is then calculated for 10 min time sections by summation of all stress range bins

$$D^{ST} = \sum_i n_i/N_i \tag{41}$$

The long-term fatigue damage D^{LT} for the nominal life time of 20 years is extrapolated from the short-term fatigue damage by weighting with the wind speed probability density function $f(u_k)$. A representative wind speed distribution measured at Anholt, Denmark is selected.

$$D^{LT} = \frac{20 \text{ year}}{10 \text{ min}} \sum_k f(u_k) D_k^{ST} \tag{42}$$

3. Results and discussions

3.1. Choice of uncertainty distribution

The first step in the statistical analysis of the uncertainty in DTs is the identification of the distribution types, which are of importance in reliability and risk assessment studies. A common assumption is to use lognormal distributions for representing model uncertainties [6][8]. The numerical results of the measurement, state estimation, system identification and model uncertainty are fitted with fourteen different statistical distributions and ranked according their goodness of fit given by the coefficient of determination R^2. Fig. 4 shows the R^2-values of the six best performing distributions aggregated for all EC of the 5 MW case study. The results are inconclusive as to which distribution is best suited, but it can be stated that the lognormal distribution yields a reasonable fit of $R^2 > 0.9$ for all types of uncertainty in DTs. The further statistical analysis is continued with lognormal distributions to maintain the comparability with other publications.

3.2. Measurement uncertainty

The first source of uncertainty in the proposed load and fatigue monitoring approach originates from the the low temporal resolution of the SCADA data input. Typical SCADA systems operate with sampling frequencies of 1 Hz, but store the data only as 10 min averages, which has already been identified as a limiting factor for monitoring approaches. The generator torque
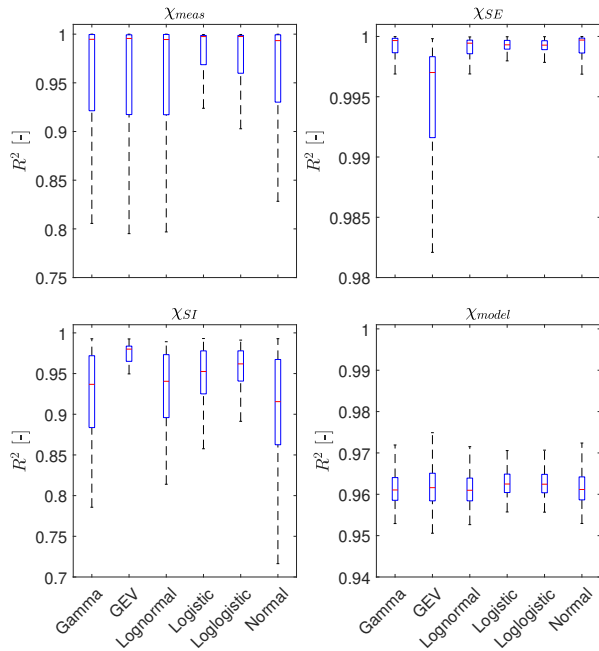
Figure 4: Goodness of fit of different distribution shapes for the measurement, state estimation, system identification and model uncertainty, aggregated for all ECs of the 5 MW case study.

reportedly has the fastest decaying autocorrelation out of all SCADA signals, which results in a large loss of information when using time averaged signals [23]. This motivated efforts in the industry to adopt high frequency (1 Hz) SCADA systems; however, even a sampling frequency 1 Hz is arguably insufficient to fully capture drivetrain dynamics, since the first torsional natural frequency and internal excitation frequencies such as gear meshing frequencies lie well above the Nyquist frequency of 0.5 Hz. The effects of this are illustrated in Fig. 5, which shows the standard deviation $\sigma_{\chi meas}$ of the fitted measurement uncertainty χ_{meas} resulting from either 1 s or 10 min averaging of the generator torque input. The measurement uncertainty of 10 min data is particularly high below rated wind speed and reaches values of up to 0.75 near cut-in wind speed. In wind turbines with variable-speed controllers
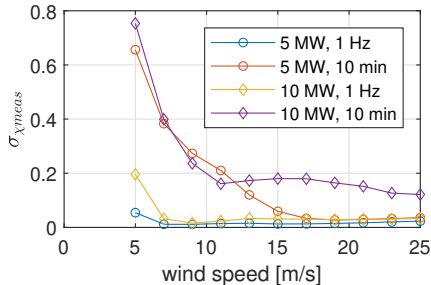
Figure 5: Standard deviation of fitted lognormal distributions for measurement uncertainty as a function of wind speed.

this operational regime is characterized by a high variance in the drivetrain torque, which is not reflected in 10 min averaged data. The uncertainty of 1 Hz data only amounts to only about 0.03 for most operational conditions with the exception of cut-in wind speeds, which suggests that this resolution is sufficient to observe low-frequency ($< 0.5\ Hz$) load variations due to the wind speed volatility. The remaining uncertainty is related to neglecting higher frequency dynamics such as torsional drivetrain modes. Based on these results it a measurement resolution of at least 1 Hz is recommended for load and fatigue damage monitoring in wind turbine drivetrains.

3.3. State estimation uncertainty

The second source of uncertainty is also related to the limitations of the SCADA measurements, in that the rotor torque is typically not measured and must be estimated indirectly using the augmented Kalman filter as joint input-state estimation method. The error in the estimated rotor torque is described by the state estimation uncertainty χ_{SE}. Fig. 6 shows the standard deviation of χ_{SE} from numerical case studies with the 5 MW and 10 MW model at different ECs. Particularly high uncertainty is observed around cut-in wind speeds, which can be attributed to start-up and shut-down effects. At normal power generation the uncertainty is limited to values of 0.07 and 0.04 for the 5 MW and 10 MW turbine, respectively. A slightly higher error is observed with the 5 MW model, which is also apparent in the frequency spectra and time series shown in Fig. 7. The rotor torque estimates for the 10 MW turbine show a good agreement in the low-frequency range and at the peaks of the first torsional natural frequency (2.08 Hz). For the 5 MW

18
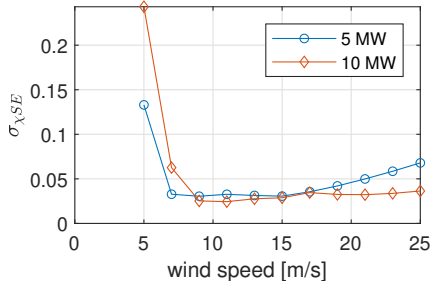
Figure 6: Standard deviation of fitted lognormal distributions for state estimation uncertainty as a function of wind speed.

turbine, on the other hand, the rotor torque is underestimated at the first torsional natural frequency (1.7 Hz) and at higher order modes.

3.4. System identification uncertainty

The third source of uncertainty originates from the aleatory uncertainty of the system properties, for instance, the rotor inertia may vary due to ice accretion or leading edge erosion and the drivetrain stiffness may decrease due to tooth root cracks or spalling. System identification methods are applied to detect these changes and update the model parameters accordingly, nonetheless, a small uncertainty of epistemic nature remains due to method limitations, referred to as the system identification uncertainty χ_{SI}. The system identification uncertainty in the parameters $J_{Rot}, J_{Gen}, k_{DT}, c_{DT}$ is investigated in numerical case studies with the 5 MW and 10 MW models. The numerical results are shown in Fig. 8 as the mean and the standard deviation of the fitted lognormal distributions across all ECs. The uncertainty in the inertia and stiffness parameter estimation shows similar behaviour. Local maxima in the bias and variance are observed near cut-in (5 m/s) and near rated wind speeds (11-13 m/s), while the minimum is located at cut-out wind speed (25 m/s). It appears that the quasi-stationary conditions in the torque controlled operational regime above rated wind speeds are conducive to accurate parameter estimation, while the transient dynamics at rated wind speeds due to activation and deactivation of the pitch controller introduce higher estimation errors.

Contrary to the inertia and stiffness estimates, the damping parameter estimates show significantly higher uncertainty reaching values of up to $\sigma > 0.55$.
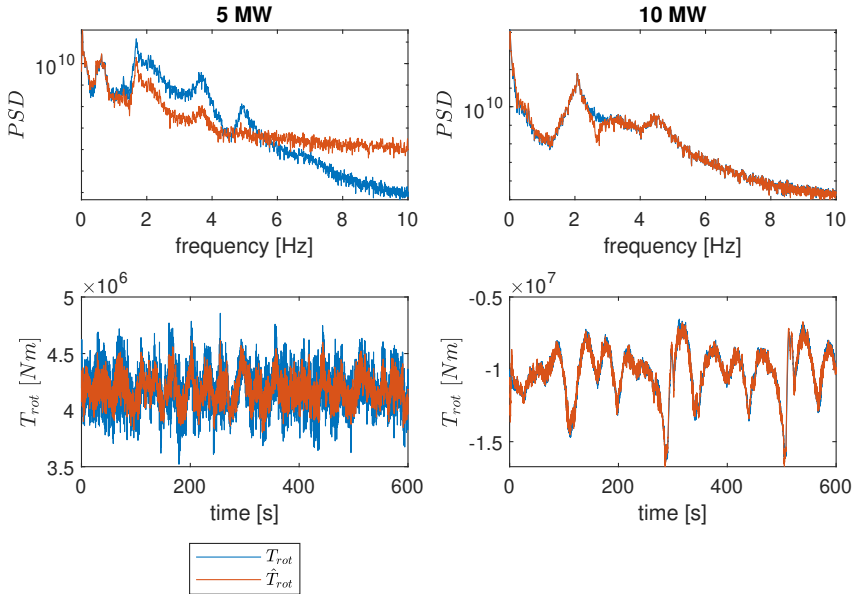
Figure 7: True and estimated rotor torque $T_{rot}, \hat{T}_{rot}$ using joint state-input estimation methods. Shown are the PSD frequency spectrum and the time series at EC8

This finding is in agreement with recent studies on drivetrain model validation, where it is reported that the estimation of damping values by OMA techniques is challenging due to the low parameter sensitivity [24]. The damping parameter has outside of the resonance area, at the considered operational conditions a small influence on the dynamic response.

3.5. Model uncertainty

Lastly, the model uncertainty χ_{model} is investigated, which characterizes the uncertainty in the calculated bearing and gear loads due to modelling errors and the complexity reduction of the ROMs. The discussion is divided into a frequency analysis (Sec. 3.5.1), the analysis of the model bias (Sec. 3.5.2) and the analysis of the dynamic model error (Sec. 3.5.3).
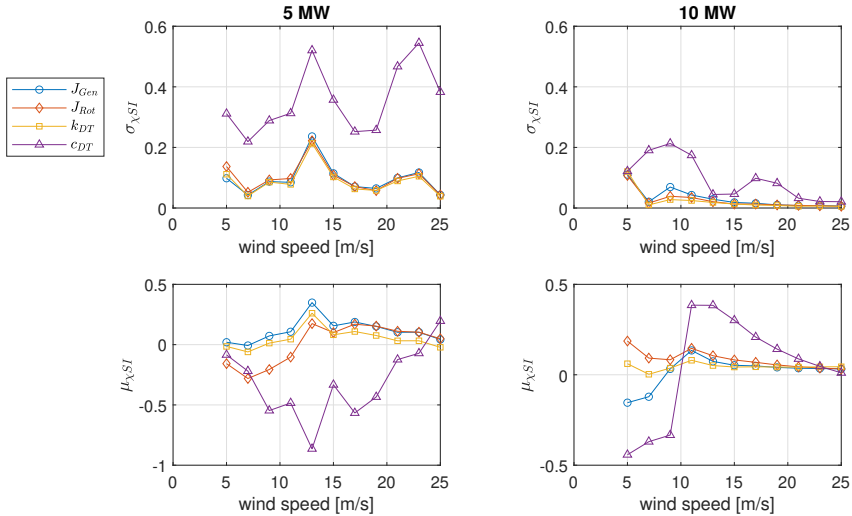
Figure 8: Mean and standard deviation of fitted lognormal distributions for system identification uncertainty as a function of wind speed.

3.5.1. Characterization of drivetrain dynamics

A frequency analysis of the simulated drivetrain loads is conducted to identify which aspects of the drivetrain dynamics the ROMs are able to represent well and which aspects are sources of uncertainty. The drivetrain dynamics can be generally characterized as dynamic responses to a variety of both internal and external excitations. These excitations can be further differentiated into torque and non-torque loads, i.e lateral forces and bending moments (Tab. 3.5.1).

External excitations are mainly the result of aerodynamics and are prevalent at low frequencies. Aerodynamic imbalance is present in healthy conditions due to turbulence, wind shear, the vertical wind profile and the rotor axis tilt, or caused by faulty yaw and pitch misalignment. This results in periodic load variations in the rotor torque, thrust and bending moments at the rotor frequency 1P [5]. The tower shadow is also known to induce similar torque and non-torque excitations at the blade passing frequency 3P.

The system boundaries of the drivetrain models cut through the rotor hub and the yaw bearing, hence, all structural dynamics of the blades and the

Table 2: Type of excitations and characteristic frequencies in wind turbine drivetrains

	Torque	Non-Torque
External	Aerodynamic imbalance (f_{1P})	Aerodynamic imbalance (f_{1P})
	Tower shadow (f_{3P})	Tower shadow (f_{3P})
	Blade edgewise modes (f_N)	-
	-	Blade flapwise modes (f_N)
	-	Tower bending modes (f_N)
Internal	Planet carriers (f_{plc})	Planet carriers (f_{plc})
	Gear meshing (f_{gm})	Gear meshing (f_{gm})
	-	Bearings (f_{bpf})

tower are considered as external excitations. These are simulated with the global aeroelastic models and the resulting main shaft loads and tower motions are applied as boundary conditions in the drivetrain models. The deformation of the blades with edgewise bending modes translates to torque excitations at the main shaft, while flapwise bending modes cause primarily non-torque excitations. Similarly, fore-aft and side-side tower bending introduces excitations in the thrust and bending moments.

Internal excitations are caused by periodic changes of component stiffnesses and occur generally at much higher frequencies. Gear mesh excitations are a result of the changing number of tooth contacts during one meshing cycle. Gear meshing primarily results in periodic variation of the transmitted torque, but may also have non-torque components in helical gear stages. Bearing excitations are caused by roller elements passing the load zone and result in non-torque excitations at the ball passing frequencies. Further internal excitations are observed at the planet carrier rotational frequencies. Shaft misalignment, mass imbalance or non-torque loading may result in bending of the flexible planet carrier and in skewing of the load distribution between planets, such that each planet bearing experiences periodic load changes during one planet carrier revolution.

The characteristic excitations are observable in the power spectral densities (PSD) of the bearing loads (Fig 9). Shown are the simulated bearing loads at each gear stage for EC8 (17 m/s) using the FOM and the rigid and flexible ROM. The rigid ROM exhibits a good agreement in the lowest frequency range ($< 1\ Hz$) governed by wind and wave load excitations, but generally underestimates higher frequency dynamics, as it is only considering rigid body modes. The flexible ROM achieves more accurate load estimates by inclusion of the first torsional drivetrain mode. It is able to match the

22
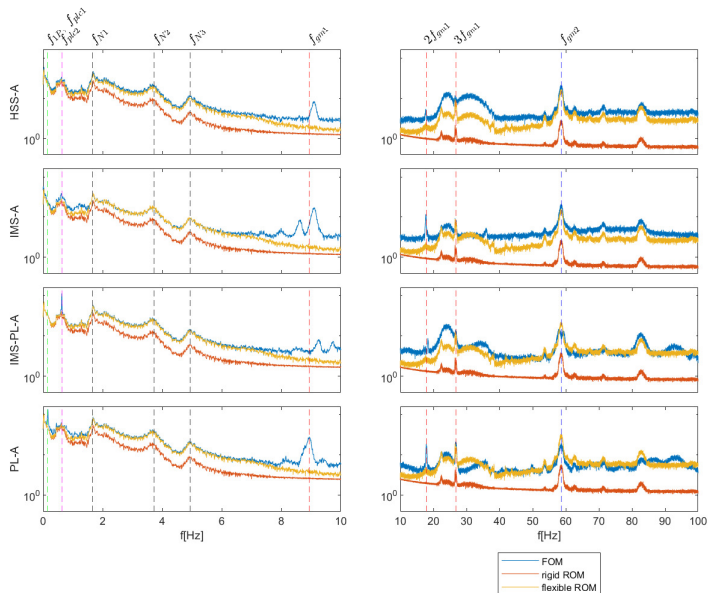
Figure 9: Power spectral densities of bearing radial loads simulated with the 5 MW FOM, rigid ROM and flexible ROM at EC8.

peaks of external excitations such as the first collective edgewise blade bending mode (f_{N1}) and higher order modes. The internal dynamics are captured reasonably well with a good agreement in the second stage gear meshing frequency (f_{gm2}). However, some discrepancies remain in the first stage gear meshing frequency peak (f_{gm1}) and in the planet carrier excitations (f_{plc1}, f_{plc2}) visible at the first and second stage planet bearings (PL-A, IMS-PL-A). These suggest the presence of non-torque loads at the planet carriers. The investigated 5 and 10 MW drivetrain models are designed with a four-point main bearing suspension, where it is generally assumed that all non-torque loads of the rotor are fully compensated by the main bearings, but it appears that this is not the case and that non-torque loads partially propagate further downwind into the drivetrain. The results showcase the limitations of torsional ROMS and suggest that a significant source of uncertainty originates from neglecting planetary carrier bending modes.

23

3.5.2. Model bias

The focus of the statistical analysis lies first on the model bias, which is quantified by the mean value of the fitted model uncertainty distribution. Values of greater than one represent consistent underestimation of drivetrain loads by the ROMs and vice versa for values smaller than one. Shown in Fig. 10 are the model biases of the rigid and flexible ROM in numerical and experimental case studies. The field measurements are only available for the HSS-A bearing. The highest biases are observed near cut-in wind speeds (5 m/s), which can be associated with start-up and shut-down effects. At higher wind speeds ($> 7m/s$) the environmental conditions have a marginal influence on the model bias. Significant biases of up to 0.46 are observed at the high-speed gear stage. The loads at the upwind HSS-A and IMS-A bearings are consistently underestimated, while the loads at the downwind HSS-B and IMS-B bearings are overestimated. One reason for these discrepancies could lie in the physical simplifications of the ROMs, which reduces the gear contact force to a singular vector along the line of action. The load distribution along the gear flank is not considered and thus the bending moments resulting from inhomogeneous load distributions are neglected. Other authors introduce a "twist stiffness" perpendicular to the circumferential gear meshing stiffness to account for the load distribution [25]. However, in this approach the solution requires knowledge of gear and bearing stiffness parameters, which are difficult to determine and validate in practice. Another factor could be the assumption of open-ended shafts that do not allow the transfer of non-torque loads. In the FOMs this is not the case, since the generator coupling at the HSS and the sun-planet gear contact at the IMS allow the transfer of shear forces. These could skew the HSS and IMS bearing loads and further contribute to the model bias. The persistence of model biases in such analytical ROMs is further supported with field measurements of the DOE 1.5 MW turbine. The measured model bias is independent of the EC and amounts to about 0.15, which is of similar magnitude as the values of the numerical case studies.

3.5.3. Dynamic error

The standard deviation of the of the fitted uncertainty distributions indicates how well the ROMs capture drivetrain dynamics compared the FOM. As depicted in Fig. 11, the standard deviation is positive for all considered cases, which suggests that the ROMs generally underestimate the load dy-
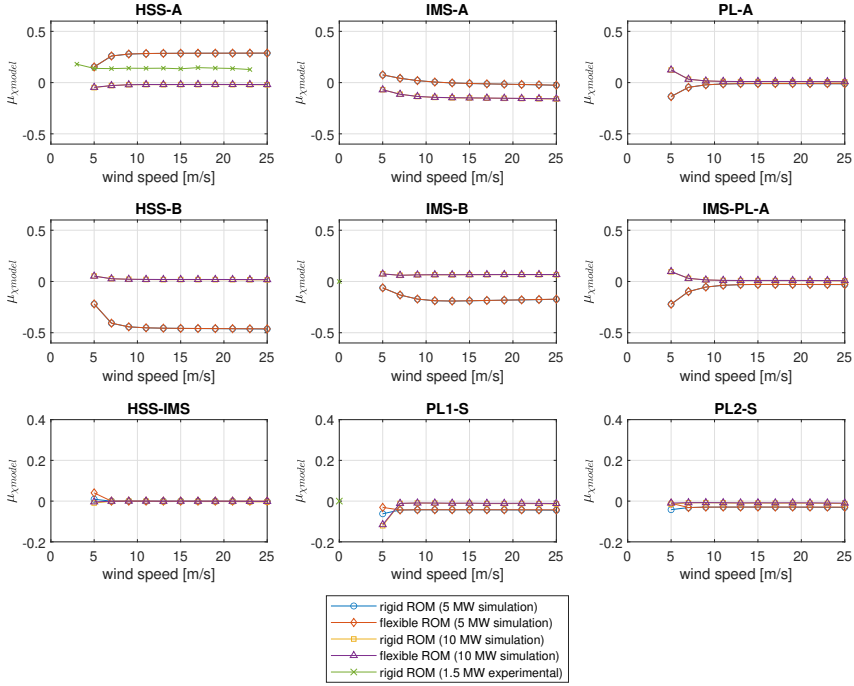
Figure 10: Mean values of fitted lognormal distributions for model uncertainty as a function of wind speed.

namics. The uncertainty distributions show similar trends across all bearing and gear types. The highest values are observed near cut-in wind speeds (5 m/s), followed by a steep decline to the global minimum at 9 m/s and a gradual progressive trend towards cut-out wind speeds (25 m/s). Similarly to the high model bias, the high uncertainty at cut-in wind speeds can be attributed to start-up and shut-down effects. The progressive trend can be attributed to aerodynamic non-torque loads transferred from the rotor into the drivetrain. While the torque is controlled to rated conditions above rated wind speed, the non-torque loads, in particular pitch and yaw bending moments, continue to increase with higher wind speeds [18]. These can excite non-torsional modes of the drivetrain, in particular planet carrier bending modes (see Sec. 3.5.1), which the purely torsional ROMs do not account for.

25
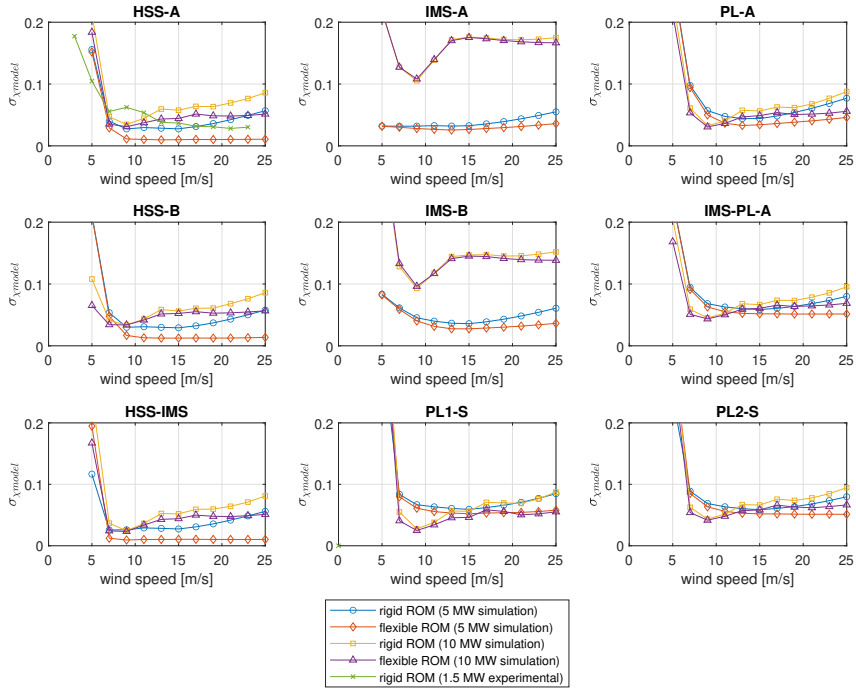
Figure 11: Standard deviation of fitted lognormal distributions for model uncertainty as a function of wind speed.

The flexible ROM appears to capture the drivetrain dynamics to a much higher degree than the rigid ROM resulting in lower uncertainty values across all bearing and gear locations. The largest differences are observed above rated wind speed, where the excitation of the first drivetrain torsional mode becomes increasingly more energetic. Below rated wind speed the relative improvement is much lower, since in this operational regime the drivetrain dyanamics are governed by rigid-body modes.

The uncertainty standard deviation based on field measurements shows a similar trend and order of magnitude and supports the previous findings of the numerical case studies.

3.6. Long-term fatigue damage error

The use case of long-term fatigue damage monitoring is considered to assess the impact of the uncertainties in the DT framework. Three scenarios are hereby considered with increasing resolution of SCADA measurements, ranging from 10 min, 1 Hz to 200 Hz. The resolution of 10 min and 1 Hz limits the DT model to the rigid torsional ROM, since the first torsional natural frequency lies above the Nyquist-frequency, while the case of 200 Hz measurements allows the application of the flexible ROM. The long-term fatigue damage is calculated by weighting the short-term fatigue damage of each EC with the wind speed distribution.

As shown in Fig. 12, the contribution of wind speeds near cut-in (3-7 m/s) to long-term fatigue does not exceed 2% due to the low probability of such wind speeds in addition to small aerodynamic loads. The small contribution suggests that the high uncertainty observed at cut-in wind speeds due to start-up and shut-down effects (Sec. 3.5.2) has a negligible impact. The highest contribution have wind speeds of 13 m/s, where model and measurement uncertainty are fortunately near their minima.

The relative error in long-term fatigue damage for each of the scenarios is shown in Fig. 13. The long-term fatigue damage is generally underestimated by the DTs due to underestimation of the load amplitudes. It should be noted that the error in the bearing and gear load estimates is amplified by exponentiation with the S-N curve exponent of 10/3 and 6.225, respectively. Hence, the gear fatigue damage error tends to be larger due to the larger exponent.

The first scenario with 10 min SCADA data results in relative errors of up to -44.4% in the gear fatigue damage and up to -15.9% in the bearing fatigue damage due to the high measurement uncertainty χ_{meas} (Sec. 3.2). The resolution is insufficient to capture neither the low-frequency aerodynamics nor the high-frequency internal drivetrain dynamics. The second scenario with 1 Hz data yields significantly smaller relative errors limited to -11.2% and -6.6% in the gear and bearing fatigue damage, respectively. In this case, the rigid ROM is able to represent low frequency load variations due to wind and wave excitations, but is limited with respect to higher frequency internal dynamics dynamics. The third scenario with 200 Hz measurements and the two DOF flexible ROM results in only marginally lower fatigue damage errors of -9.7% and -5.5%, which showcase the trade-off of increasing the model fidelity. While the addition of a torsional DOF in the flexible ROM significantly reduces the modelling errors and the model uncertainty χ_{model}

Figure 12: Contribution of each wind speed bin to long-term fatigue damage for the example of the 5 MW HSS-A bearing.

(Sec. 3.5.3), it introduces one unknown variable in the rotor torque and four unknown parameters in the rotor intertia, generator inertia, drivetrain stiffness and damping. The estimation of the rotor torque and the parameters by inverse methods cause additional uncertainty χ_{SE}, χ_{SI} (Sec. 3.3 and 3.4), which partially diminish the benefit of the lower model uncertainty.

4. Conclusion

This paper presents a systematic assessment of the uncertainty of DTs for load and fatigue damage monitoring in wind turbine drivetrains. Numerical studies with the NREL 5 MW and DTU 10 MW reference turbines and experimental studies with the DOE 1.5 MW research turbine were conducted to assess the uncertainty of different DT elements and their impact of long-term fatigue damage. The measurement uncertainty in the SCADA data input χ_{meas}, the uncertainty in the state estimation and system identification methods χ_{SE}, χ_{SI}, and the model uncertainty of the drivetrain ROMs χ_{model} were investigated and quantified using lognormal distributions (Tab. 4)
The investigation of the measurement uncertainty revealed a significant loss of information by using 10 min averaged SCADA data. The measurement resolution is insufficient to observe the low frequency drivetrain load dynamics due to the wind speed and rotor torque volatility, which resulted in

28
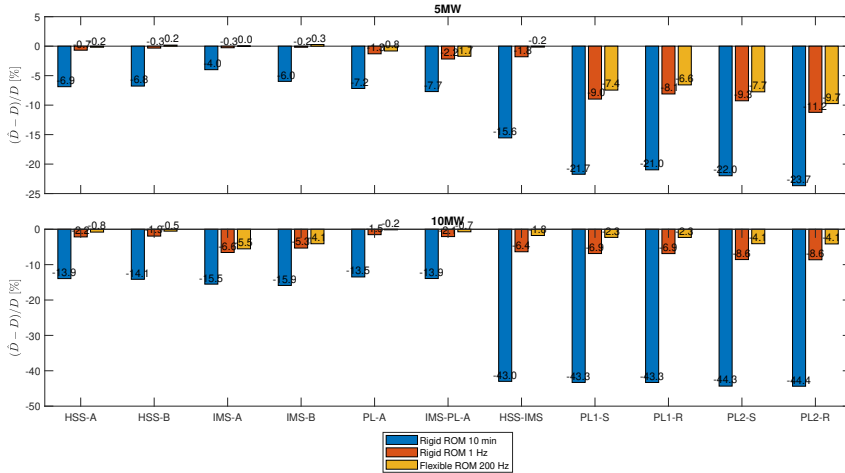
Figure 13: Relative error [%] in long-term bearing and gear fatigue damage

maximum uncertainty of $\sigma = 0.75$ and long-term fatigue damage errors of up to -44.4% in the gears and -15.9% in the bearings. The results strongly suggest the use of high-frequency SCADA data with a resolution of at least 1 Hz for fatigue monitoring purposes.

The second source of uncertainty is identified in the state estimation method, the augmented Kalman filter, that is applied to match the dynamic state of the DT model with the physical wind turbine based on real-time data streams. The challenge lies in estimating the rotor torque, which is not measured directly and must be estimated by the Kalman filter. The Kalman filter tends to underestimate the rotor torque at the first torsional natural frequency, which results in a uncertainty standard deviation ranging from 0.03 to 0.07 at normal operational conditions ($> 5m/s$).

The third source of uncertainty originates from the aleatory uncertainty of the system properties. Inertia, stiffness and damping values may vary over the turbine's life cycle as a result of faults, material degradation or part replacement. System identification methods are applied to detect these changes and update the model parameter accordingly. The uncertainty in the parameter estimates is particularly high at cut-in and near rated wind speeds ($\sigma < 0.22$) due to transient dynamics and the high variance in the drivetrain torque, while the lowest uncertainty is observed in the torque controlled

29

Table 3: Summary of the uncertainty quantification in DTs.

Uncertainty	distribution	mean μ	standard deviation σ
χ_{meas}	lognormal	0	0.02...0.75
χ_{SE}	lognormal	0	0.03...0.07
χ_{SI}	lognormal	$-0.86..0.38$	0.01...0.55
χ_{model}	lognormal	$-0.45...0.28$	0.01...0.17

regime above rated wind speed ($\sigma > 0.006$). Furthermore, it is observed that the estimation of the drivetrain torsional damping is significantly more inaccurate than inertia and stiffness parameters ($\sigma < 0.22$). This is likely due to the low sensitivity of the damping parameter with respect to the drivetrain torsional dynamics at normal power production.

Lastly, the epistemic model uncertainty due to the ROMs' limitations is investigated. ROMs with one or two torsional DOFs are used as DT models due to their lower computational loads in real-time monitoring applications, their lower validation costs, and the limited observability of non-torsional dynamic states with the available SCADA measurements. One DOF rigid ROMs are only able to match the dynamics in the lowest frequency range ($< 1\ Hz$) governed by wind and wave load excitations, while two DOF flexible ROMs better capture the dynamic drivetrain response to higher frequency internal excitations such as gear meshing. Remaining limitations are observed in capturing non-torsional dynamics, in particular the bending dynamics of the first and second stage planet carriers. The uncertainty in the load estimates of the flexible ROM is noticeably smaller, however only a small improvement with respect to the fatigue damage estimates is observed (-6.6% to -5.5%). While the addition of a torsional DOF in the flexible ROM significantly reduces the modelling errors, it introduces additional unknown variables and parameters with associated uncertainties that partially diminish the benefit of lower modelling uncertainty.

The presented study contributes to a deeper understanding of the uncertainty in DTs for load and fatigue monitoring. The reported uncertainty distributions may be used in reliability studies, in risk assessment and the derivation of safety factors, or assist in the decision processes on the model fidelity and the sensor measurement resolution.

Acknowledgments

CRediT author statement

Felix Mehlan: Methodology, Software, Investigation, Writing - Original Draft, **Amir R. Nejad**: Conceptualization, Writing - Review & Editing, Funding acquisition

References

[1] Wind Europe, Offshore wind in europe: Key trends and statistics 2019, https://windeurope.org/wp-content/uploads/files/about-wind/statistics/WindEurope-Annual-Offshore-Statistics-2019.pdf, last access: 01 Nov 2022 (2020).

[2] T. Stehly, P. Beiter, 2018 cost of wind energy review, Report, National Renewable Energy Laboratory (2020).

[3] M. Wilkinson, B. Hendriks, F. Spinato, E. Gomez, H. Bulacio, J. Roca, P. Tavner, Y. Feng, H. Long, Methodology and results of the reliawind reliability field study, in: European Wind Energy Conference.

[4] F. C. Mehlan, A. R. Nejad, Z. Gao, Digital twin based virtual sensor for online fatigue damage monitoring in offshore wind turbine drivetrains, Journal of Offshore Mechanics and Arctic Engineering 144 (6) (2022). `doi:10.1115/1.4055551`.

[5] F. C. Mehlan, J. Keller, A. R. Nejad, Virtual sensing of wind turbine hub loads and drivetrain fatigue damage, Forschung im Ingenieurwesen 87 (1) (2023) 207–218. `doi:10.1007/s10010-023-00627-0`.

[6] A. R. Nejad, Z. Gao, T. Moan, On long-term fatigue damage and reliability analysis of gears under wind loads in offshore wind turbine drivetrains, International Journal of Fatigue 61 (2014) 116–128. `doi:10.1016/j.ijfatigue.2013.11.023`.

[7] H. Li, H. Cho, H. Sugiyama, K. K. Choi, N. J. Gaul, Reliability-based design optimization of wind turbine drivetrain with integrated multibody gear dynamics simulation considering wind load uncertainty, Structural and Multidisciplinary Optimization 56 (1) (2017) 183–201. `doi:10.1007/s00158-017-1693-5`.

[8] W. Dong, A. R. Nejad, T. Moan, Z. Gao, Structural reliability analysis of contact fatigue design of gears in wind turbine drivetrains, Journal of Loss Prevention in the Process Industries 65 (2020). `doi:10.1016/j.jlp.2020.104115`.

[9] J. Jonkman, S. Butterfield, W. Musial, G. Scott, Definition of a 5-mw reference wind turbine for offshore system development, Report, National Renewable Energy Laboratory (NREL) (2009).

[10] C. Bak, F. Zahle, R. Bitsche, T. Kim, A. Yde, L. C. Henriksen, M. H. Hansen, J. P. Blasques, A. Amaral, M. Gaunaa, A. Natarajan, The DTU 10-MW reference wind turbine (23.03.21 2013).

[11] A. R. Nejad, E. E. Bachynski, M. I. Kvittem, C. Luan, Z. Gao, T. Moan, Stochastic dynamic load effect and fatigue damage analysis of drivetrains in land-based and tlp, spar and semi-submersible floating wind turbines, Marine Structures 42 (2015) 137–153. `doi:10.1016/j.marstruc.2015.03.006`.

[12] A. Robertson, J. Jonkman, M. Masciola, S. H., A. Goupee, A. Coulling, C. Luan, Definition of the semisubmersible floating system for phase ii of oc4, Report, National Renewable Energy Laboratory (2012).

[13] R. R. Arias, J. Galvan, NAUTILUS-DTU10 MW floating offshore wind turbine at gulf of maine, WindEurope (2018).

[14] OpenFAST, https://github.com/OpenFAST (2022).

[15] A. R. Nejad, Y. Guo, Z. Gao, T. Moan, Development of a 5 mw reference gearbox for offshore wind turbines, Wind Energy 19 (6) (2016) 1089–1106. `doi:10.1002/we.1884`.

[16] S. Wang, A. R. Nejad, T. Moan, On design, modelling, and analysis of a 10-mw medium-speed drivetrain for offshore wind turbines, Wind Energy 23 (4) (2020) 1099–1117. `doi:10.1002/we.2476`.

[17] Y. Guo, J. Keller, W. La Cava, J. Austin, A. R. Nejad, C. Halse, L. Bastard, J. Helsen, Recommendations on model fidelity for wind turbine gearbox simulations (2015).

[18] F. C. Mehlan, E. Pedersen, A. R. Nejad, Modelling of wind turbine gear stages for digital twin and real-time virtual sensing using bond graphs, Journal of Physics: Conference Series 2265 (032065) (2022). `doi:10.1088/1742-6596/2265/3/032065`.

[19] R. Santos, J. van Dam, Mechanical loads test report for the u.s. department of energy 1.5-megawatt wind turbine, Report, National Renewable Energy Laboratory (2015).

[20] Y. Guo, J. Keller, Validation of combined analytical methods to predict slip in cylindrical roller bearings, Tribology International 148 (2020). `doi:10.1016/j.triboint.2020.106347`.

[21]

[22] ISO 281, Rolling bearings — dynamic load ratings and rating life (2007).

[23] E. Gonzalez, B. Stephen, D. Infield, J. J. Melero, Using high-frequency scada data for wind turbine performance monitoring: A sensitivity study, Renewable Energy 131 (2019) 841–853. `doi:10.1016/j.renene.2018.07.068`.

[24] F. Vanhollebeke, P. Peeters, J. Helsen, E. Di Lorenzo, S. Manzato, J. Peeters, D. Vandepitte, W. Desmet, Large scale validation of a flexible multibody wind turbine gearbox model, Journal of Computational and Nonlinear Dynamics 10 (4) (2015). `doi:10.1115/1.4028600`.

[25] T. Eritenel, R. G. Parker, Three-dimensional nonlinear vibration of gear pairs, Journal of Sound and Vibration 331 (15) (2012) 3628–3648. `doi:10.1016/j.jsv.2012.03.019`.

Appendix B

List of previous PhD theses at Dept. of Marine Tech.

Previous PhD theses published at the Department of Marine Technology
(earlier: Faculty of Marine Technology)
NORWEGIAN UNIVERSITY OF SCIENCE AND TECHNOLOGY

Report No.	Author	Title
	Kavlie, Dag	Optimization of Plane Elastic Grillages, 1967
	Hansen, Hans R.	Man-Machine Communication and Data-Storage Methods in Ship Structural Design, 1971
	Gisvold, Kaare M.	A Method for non-linear mixed-integer programming and its Application to Design Problems, 1971
	Lund, Sverre	Tanker Frame Optimalization by means of SUMT-Transformation and Behaviour Models, 1971
	Vinje, Tor	On Vibration of Spherical Shells Interacting with Fluid, 1972
	Lorentz, Jan D.	Tank Arrangement for Crude Oil Carriers in Accordance with the new Anti-Pollution Regulations, 1975
	Carlsen, Carl A.	Computer-Aided Design of Tanker Structures, 1975
	Larsen, Carl M.	Static and Dynamic Analysis of Offshore Pipelines during Installation, 1976
UR-79-01	Brigt Hatlestad, MK	The finite element method used in a fatigue evaluation of fixed offshore platforms. (Dr.Ing. Thesis)
UR-79-02	Erik Pettersen, MK	Analysis and design of cellular structures. (Dr.Ing. Thesis)
UR-79-03	Sverre Valsgård, MK	Finite difference and finite element methods applied to nonlinear analysis of plated structures. (Dr.Ing. Thesis)
UR-79-04	Nils T. Nordsve, MK	Finite element collapse analysis of structural members considering imperfections and stresses due to fabrication. (Dr.Ing. Thesis)
UR-79-05	Ivar J. Fylling, MK	Analysis of towline forces in ocean towing systems. (Dr.Ing. Thesis)
UR-80-06	Nils Sandsmark, MM	Analysis of Stationary and Transient Heat Conduction by the Use of the Finite Element Method. (Dr.Ing. Thesis)
UR-80-09	Sverre Haver, MK	Analysis of uncertainties related to the stochastic modeling of ocean waves. (Dr.Ing. Thesis)
UR-81-15	Odland, Jonas	On the Strength of welded Ring stiffened cylindrical Shells primarily subjected to axial Compression

Report No.	Author	Title
UR-82-17	Engesvik, Knut	Analysis of Uncertainties in the fatigue Capacity of Welded Joints
UR-82-18	Rye, Henrik	Ocean wave groups
UR-83-30	Eide, Oddvar Inge	On Cumulative Fatigue Damage in Steel Welded Joints
UR-83-33	Mo, Olav	Stochastic Time Domain Analysis of Slender Offshore Structures
UR-83-34	Amdahl, Jørgen	Energy absorption in Ship-platform impacts
UR-84-37	Mørch, Morten	Motions and mooring forces of semi submersibles as determined by full-scale measurements and theoretical analysis
UR-84-38	Soares, C. Guedes	Probabilistic models for load effects in ship structures
UR-84-39	Aarsnes, Jan V.	Current forces on ships
UR-84-40	Czujko, Jerzy	Collapse Analysis of Plates subjected to Biaxial Compression and Lateral Load
UR-85-46	Alf G. Engseth, MK	Finite element collapse analysis of tubular steel offshore structures. (Dr.Ing. Thesis)
UR-86-47	Dengody Sheshappa, MP	A Computer Design Model for Optimizing Fishing Vessel Designs Based on Techno-Economic Analysis. (Dr.Ing. Thesis)
UR-86-48	Vidar Aanesland, MH	A Theoretical and Numerical Study of Ship Wave Resistance. (Dr.Ing. Thesis)
UR-86-49	Heinz-Joachim Wessel, MK	Fracture Mechanics Analysis of Crack Growth in Plate Girders. (Dr.Ing. Thesis)
UR-86-50	Jon Taby, MK	Ultimate and Post-ultimate Strength of Dented Tubular Members. (Dr.Ing. Thesis)
UR-86-51	Walter Lian, MH	A Numerical Study of Two-Dimensional Separated Flow Past Bluff Bodies at Moderate KC-Numbers. (Dr.Ing. Thesis)
UR-86-52	Bjørn Sortland, MH	Force Measurements in Oscillating Flow on Ship Sections and Circular Cylinders in a U-Tube Water Tank. (Dr.Ing. Thesis)
UR-86-53	Kurt Strand, MM	A System Dynamic Approach to One-dimensional Fluid Flow. (Dr.Ing. Thesis)
UR-86-54	Arne Edvin Løken, MH	Three Dimensional Second Order Hydrodynamic Effects on Ocean Structures in Waves. (Dr.Ing. Thesis)
UR-86-55	Sigurd Falch, MH	A Numerical Study of Slamming of Two-Dimensional Bodies. (Dr.Ing. Thesis)
UR-87-56	Arne Braathen, MH	Application of a Vortex Tracking Method to the Prediction of Roll Damping of a Two-Dimension Floating Body. (Dr.Ing. Thesis)
UR-87-57	Bernt Leira, MK	Gaussian Vector Processes for Reliability Analysis involving Wave-Induced Load Effects. (Dr.Ing. Thesis)

Report No.	Author	Title
UR-87-58	Magnus Småvik, MM	Thermal Load and Process Characteristics in a Two-Stroke Diesel Engine with Thermal Barriers (in Norwegian). (Dr.Ing. Thesis)
MTA-88-59	Bernt Arild Bremdal, MP	An Investigation of Marine Installation Processes – A Knowledge-Based Planning Approach. (Dr.Ing. Thesis)
MTA-88-60	Xu Jun, MK	Non-linear Dynamic Analysis of Space-framed Offshore Structures. (Dr.Ing. Thesis)
MTA-89-61	Gang Miao, MH	Hydrodynamic Forces and Dynamic Responses of Circular Cylinders in Wave Zones. (Dr.Ing. Thesis)
MTA-89-62	Martin Greenhow, MH	Linear and Non-Linear Studies of Waves and Floating Bodies. Part I and Part II. (Dr.Techn. Thesis)
MTA-89-63	Chang Li, MH	Force Coefficients of Spheres and Cubes in Oscillatory Flow with and without Current. (Dr.Ing. Thesis
MTA-89-64	Hu Ying, MP	A Study of Marketing and Design in Development of Marine Transport Systems. (Dr.Ing. Thesis)
MTA-89-65	Arild Jæger, MH	Seakeeping, Dynamic Stability and Performance of a Wedge Shaped Planing Hull. (Dr.Ing. Thesis)
MTA-89-66	Chan Siu Hung, MM	The dynamic characteristics of tilting-pad bearings
MTA-89-67	Kim Wikstrøm, MP	Analysis av projekteringen for ett offshore projekt. (Licenciat-avhandling)
MTA-89-68	Jiao Guoyang, MK	Reliability Analysis of Crack Growth under Random Loading, considering Model Updating. (Dr.Ing. Thesis)
MTA-89-69	Arnt Olufsen, MK	Uncertainty and Reliability Analysis of Fixed Offshore Structures. (Dr.Ing. Thesis)
MTA-89-70	Wu Yu-Lin, MR	System Reliability Analyses of Offshore Structures using improved Truss and Beam Models. (Dr.Ing. Thesis)
MTA-90-71	Jan Roger Hoff, MH	Three-dimensional Green function of a vessel with forward speed in waves. (Dr.Ing. Thesis)
MTA-90-72	Rong Zhao, MH	Slow-Drift Motions of a Moored Two-Dimensional Body in Irregular Waves. (Dr.Ing. Thesis)
MTA-90-73	Atle Minsaas, MP	Economical Risk Analysis. (Dr.Ing. Thesis)
MTA-90-74	Knut-Ariel Farnes, MK	Long-term Statistics of Response in Non-linear Marine Structures. (Dr.Ing. Thesis)
MTA-90-75	Torbjørn Sotberg, MK	Application of Reliability Methods for Safety Assessment of Submarine Pipelines. (Dr.Ing. Thesis)

Report No.	Author	Title
MTA-90-76	Zeuthen, Steffen, MP	SEAMAID. A computational model of the design process in a constraint-based logic programming environment. An example from the offshore domain. (Dr.Ing. Thesis)
MTA-91-77	Haagensen, Sven, MM	Fuel Dependant Cyclic Variability in a Spark Ignition Engine – An Optical Approach. (Dr.Ing. Thesis)
MTA-91-78	Løland, Geir, MH	Current forces on and flow through fish farms. (Dr.Ing. Thesis)
MTA-91-79	Hoen, Christopher, MK	System Identification of Structures Excited by Stochastic Load Processes. (Dr.Ing. Thesis)
MTA-91-80	Haugen, Stein, MK	Probabilistic Evaluation of Frequency of Collision between Ships and Offshore Platforms. (Dr.Ing. Thesis)
MTA-91-81	Sødahl, Nils, MK	Methods for Design and Analysis of Flexible Risers. (Dr.Ing. Thesis)
MTA-91-82	Ormberg, Harald, MK	Non-linear Response Analysis of Floating Fish Farm Systems. (Dr.Ing. Thesis)
MTA-91-83	Marley, Mark J., MK	Time Variant Reliability under Fatigue Degradation. (Dr.Ing. Thesis)
MTA-91-84	Krokstad, Jørgen R., MH	Second-order Loads in Multidirectional Seas. (Dr.Ing. Thesis)
MTA-91-85	Molteberg, Gunnar A., MM	The Application of System Identification Techniques to Performance Monitoring of Four Stroke Turbocharged Diesel Engines. (Dr.Ing. Thesis)
MTA-92-86	Mørch, Hans Jørgen Bjelke, MH	Aspects of Hydrofoil Design: with Emphasis on Hydrofoil Interaction in Calm Water. (Dr.Ing. Thesis)
MTA-92-87	Chan Siu Hung, MM	Nonlinear Analysis of Rotordynamic Instabilities in Highspeed Turbomachinery. (Dr.Ing. Thesis)
MTA-92-88	Bessason, Bjarni, MK	Assessment of Earthquake Loading and Response of Seismically Isolated Bridges. (Dr.Ing. Thesis)
MTA-92-89	Langli, Geir, MP	Improving Operational Safety through exploitation of Design Knowledge – an investigation of offshore platform safety. (Dr.Ing. Thesis)
MTA-92-90	Sævik, Svein, MK	On Stresses and Fatigue in Flexible Pipes. (Dr.Ing. Thesis)
MTA-92-91	Ask, Tor Ø., MM	Ignition and Flame Growth in Lean Gas-Air Mixtures. An Experimental Study with a Schlieren System. (Dr.Ing. Thesis)
MTA-86-92	Hessen, Gunnar, MK	Fracture Mechanics Analysis of Stiffened Tubular Members. (Dr.Ing. Thesis)
MTA-93-93	Steinebach, Christian, MM	Knowledge Based Systems for Diagnosis of Rotating Machinery. (Dr.Ing. Thesis)
MTA-93-94	Dalane, Jan Inge, MK	System Reliability in Design and Maintenance of Fixed Offshore Structures. (Dr.Ing. Thesis)

Report No.	Author	Title
MTA-93-95	Steen, Sverre, MH	Cobblestone Effect on SES. (Dr.Ing. Thesis)
MTA-93-96	Karunakaran, Daniel, MK	Nonlinear Dynamic Response and Reliability Analysis of Drag-dominated Offshore Platforms. (Dr.Ing. Thesis)
MTA-93-97	Hagen, Arnulf, MP	The Framework of a Design Process Language. (Dr.Ing. Thesis)
MTA-93-98	Nordrik, Rune, MM	Investigation of Spark Ignition and Autoignition in Methane and Air Using Computational Fluid Dynamics and Chemical Reaction Kinetics. A Numerical Study of Ignition Processes in Internal Combustion Engines. (Dr.Ing. Thesis)
MTA-94-99	Passano, Elizabeth, MK	Efficient Analysis of Nonlinear Slender Marine Structures. (Dr.Ing. Thesis)
MTA-94-100	Kvålsvold, Jan, MH	Hydroelastic Modelling of Wetdeck Slamming on Multihull Vessels. (Dr.Ing. Thesis)
MTA-94-102	Bech, Sidsel M., MK	Experimental and Numerical Determination of Stiffness and Strength of GRP/PVC Sandwich Structures. (Dr.Ing. Thesis)
MTA-95-103	Paulsen, Hallvard, MM	A Study of Transient Jet and Spray using a Schlieren Method and Digital Image Processing. (Dr.Ing. Thesis)
MTA-95-104	Hovde, Geir Olav, MK	Fatigue and Overload Reliability of Offshore Structural Systems, Considering the Effect of Inspection and Repair. (Dr.Ing. Thesis)
MTA-95-105	Wang, Xiaozhi, MK	Reliability Analysis of Production Ships with Emphasis on Load Combination and Ultimate Strength. (Dr.Ing. Thesis)
MTA-95-106	Ulstein, Tore, MH	Nonlinear Effects of a Flexible Stern Seal Bag on Cobblestone Oscillations of an SES. (Dr.Ing. Thesis)
MTA-95-107	Solaas, Frøydis, MH	Analytical and Numerical Studies of Sloshing in Tanks. (Dr.Ing. Thesis)
MTA-95-108	Hellan, Øyvind, MK	Nonlinear Pushover and Cyclic Analyses in Ultimate Limit State Design and Reassessment of Tubular Steel Offshore Structures. (Dr.Ing. Thesis)
MTA-95-109	Hermundstad, Ole A., MK	Theoretical and Experimental Hydroelastic Analysis of High Speed Vessels. (Dr.Ing. Thesis)
MTA-96-110	Bratland, Anne K., MH	Wave-Current Interaction Effects on Large-Volume Bodies in Water of Finite Depth. (Dr.Ing. Thesis)
MTA-96-111	Herfjord, Kjell, MH	A Study of Two-dimensional Separated Flow by a Combination of the Finite Element Method and Navier-Stokes Equations. (Dr.Ing. Thesis)
MTA-96-112	AEsøy, Vilmar, MM	Hot Surface Assisted Compression Ignition in a Direct Injection Natural Gas Engine. (Dr.Ing. Thesis)

Report No.	Author	Title
MTA-96-113	Eknes, Monika L., MK	Escalation Scenarios Initiated by Gas Explosions on Offshore Installations. (Dr.Ing. Thesis)
MTA-96-114	Erikstad, Stein O., MP	A Decision Support Model for Preliminary Ship Design. (Dr.Ing. Thesis)
MTA-96-115	Pedersen, Egil, MH	A Nautical Study of Towed Marine Seismic Streamer Cable Configurations. (Dr.Ing. Thesis)
MTA-97-116	Moksnes, Paul O., MM	Modelling Two-Phase Thermo-Fluid Systems Using Bond Graphs. (Dr.Ing. Thesis)
MTA-97-117	Halse, Karl H., MK	On Vortex Shedding and Prediction of Vortex-Induced Vibrations of Circular Cylinders. (Dr.Ing. Thesis)
MTA-97-118	Igland, Ragnar T., MK	Reliability Analysis of Pipelines during Laying, considering Ultimate Strength under Combined Loads. (Dr.Ing. Thesis)
MTA-97-119	Pedersen, Hans-P., MP	Levendefiskteknologi for fiskefartøy. (Dr.Ing. Thesis)
MTA-98-120	Vikestad, Kyrre, MK	Multi-Frequency Response of a Cylinder Subjected to Vortex Shedding and Support Motions. (Dr.Ing. Thesis)
MTA-98-121	Azadi, Mohammad R. E., MK	Analysis of Static and Dynamic Pile-Soil-Jacket Behaviour. (Dr.Ing. Thesis)
MTA-98-122	Ulltang, Terje, MP	A Communication Model for Product Information. (Dr.Ing. Thesis)
MTA-98-123	Torbergsen, Erik, MM	Impeller/Diffuser Interaction Forces in Centrifugal Pumps. (Dr.Ing. Thesis)
MTA-98-124	Hansen, Edmond, MH	A Discrete Element Model to Study Marginal Ice Zone Dynamics and the Behaviour of Vessels Moored in Broken Ice. (Dr.Ing. Thesis)
MTA-98-125	Videiro, Paulo M., MK	Reliability Based Design of Marine Structures. (Dr.Ing. Thesis)
MTA-99-126	Mainçon, Philippe, MK	Fatigue Reliability of Long Welds Application to Titanium Risers. (Dr.Ing. Thesis)
MTA-99-127	Haugen, Elin M., MH	Hydroelastic Analysis of Slamming on Stiffened Plates with Application to Catamaran Wetdecks. (Dr.Ing. Thesis)
MTA-99-128	Langhelle, Nina K., MK	Experimental Validation and Calibration of Nonlinear Finite Element Models for Use in Design of Aluminium Structures Exposed to Fire. (Dr.Ing. Thesis)
MTA-99-129	Berstad, Are J., MK	Calculation of Fatigue Damage in Ship Structures. (Dr.Ing. Thesis)
MTA-99-130	Andersen, Trond M., MM	Short Term Maintenance Planning. (Dr.Ing. Thesis)
MTA-99-131	Tveiten, Bård Wathne, MK	Fatigue Assessment of Welded Aluminium Ship Details. (Dr.Ing. Thesis)

Report No.	Author	Title
MTA-99-132	Søreide, Fredrik, MP	Applications of underwater technology in deep water archaeology. Principles and practice. (Dr.Ing. Thesis)
MTA-99-133	Tønnessen, Rune, MH	A Finite Element Method Applied to Unsteady Viscous Flow Around 2D Blunt Bodies With Sharp Corners. (Dr.Ing. Thesis)
MTA-99-134	Elvekrok, Dag R., MP	Engineering Integration in Field Development Projects in the Norwegian Oil and Gas Industry. The Supplier Management of Norne. (Dr.Ing. Thesis)
MTA-99-135	Fagerholt, Kjetil, MP	Optimeringsbaserte Metoder for Ruteplanlegging innen skipsfart. (Dr.Ing. Thesis)
MTA-99-136	Bysveen, Marie, MM	Visualization in Two Directions on a Dynamic Combustion Rig for Studies of Fuel Quality. (Dr.Ing. Thesis)
MTA-2000-137	Storteig, Eskild, MM	Dynamic characteristics and leakage performance of liquid annular seals in centrifugal pumps. (Dr.Ing. Thesis)
MTA-2000-138	Sagli, Gro, MK	Model uncertainty and simplified estimates of long term extremes of hull girder loads in ships. (Dr.Ing. Thesis)
MTA-2000-139	Tronstad, Harald, MK	Nonlinear analysis and design of cable net structures like fishing gear based on the finite element method. (Dr.Ing. Thesis)
MTA-2000-140	Kroneberg, André, MP	Innovation in shipping by using scenarios. (Dr.Ing. Thesis)
MTA-2000-141	Haslum, Herbjørn Alf, MH	Simplified methods applied to nonlinear motion of spar platforms. (Dr.Ing. Thesis)
MTA-2001-142	Samdal, Ole Johan, MM	Modelling of Degradation Mechanisms and Stressor Interaction on Static Mechanical Equipment Residual Lifetime. (Dr.Ing. Thesis)
MTA-2001-143	Baarholm, Rolf Jarle, MH	Theoretical and experimental studies of wave impact underneath decks of offshore platforms. (Dr.Ing. Thesis)
MTA-2001-144	Wang, Lihua, MK	Probabilistic Analysis of Nonlinear Wave-induced Loads on Ships. (Dr.Ing. Thesis)
MTA-2001-145	Kristensen, Odd H. Holt, MK	Ultimate Capacity of Aluminium Plates under Multiple Loads, Considering HAZ Properties. (Dr.Ing. Thesis)
MTA-2001-146	Greco, Marilena, MH	A Two-Dimensional Study of Green-Water Loading. (Dr.Ing. Thesis)
MTA-2001-147	Heggelund, Svein E., MK	Calculation of Global Design Loads and Load Effects in Large High Speed Catamarans. (Dr.Ing. Thesis)
MTA-2001-148	Babalola, Olusegun T., MK	Fatigue Strength of Titanium Risers – Defect Sensitivity. (Dr.Ing. Thesis)

Report No.	Author	Title
MTA-2001-149	Mohammed, Abuu K., MK	Nonlinear Shell Finite Elements for Ultimate Strength and Collapse Analysis of Ship Structures. (Dr.Ing. Thesis)
MTA-2002-150	Holmedal, Lars E., MH	Wave-current interactions in the vicinity of the sea bed. (Dr.Ing. Thesis)
MTA-2002-151	Rognebakke, Olav F., MH	Sloshing in rectangular tanks and interaction with ship motions. (Dr.Ing. Thesis)
MTA-2002-152	Lader, Pål Furset, MH	Geometry and Kinematics of Breaking Waves. (Dr.Ing. Thesis)
MTA-2002-153	Yang, Qinzheng, MH	Wash and wave resistance of ships in finite water depth. (Dr.Ing. Thesis)
MTA-2002-154	Melhus, Øyvin, MM	Utilization of VOC in Diesel Engines. Ignition and combustion of VOC released by crude oil tankers. (Dr.Ing. Thesis)
MTA-2002-155	Ronæss, Marit, MH	Wave Induced Motions of Two Ships Advancing on Parallel Course. (Dr.Ing. Thesis)
MTA-2002-156	Økland, Ole D., MK	Numerical and experimental investigation of whipping in twin hull vessels exposed to severe wet deck slamming. (Dr.Ing. Thesis)
MTA-2002-157	Ge, Chunhua, MK	Global Hydroelastic Response of Catamarans due to Wet Deck Slamming. (Dr.Ing. Thesis)
MTA-2002-158	Byklum, Eirik, MK	Nonlinear Shell Finite Elements for Ultimate Strength and Collapse Analysis of Ship Structures. (Dr.Ing. Thesis)
IMT-2003-1	Chen, Haibo, MK	Probabilistic Evaluation of FPSO-Tanker Collision in Tandem Offloading Operation. (Dr.Ing. Thesis)
IMT-2003-2	Skaugset, Kjetil Bjørn, MK	On the Suppression of Vortex Induced Vibrations of Circular Cylinders by Radial Water Jets. (Dr.Ing. Thesis)
IMT-2003-3	Chezhian, Muthu	Three-Dimensional Analysis of Slamming. (Dr.Ing. Thesis)
IMT-2003-4	Buhaug, Øyvind	Deposit Formation on Cylinder Liner Surfaces in Medium Speed Engines. (Dr.Ing. Thesis)
IMT-2003-5	Tregde, Vidar	Aspects of Ship Design: Optimization of Aft Hull with Inverse Geometry Design. (Dr.Ing. Thesis)
IMT-2003-6	Wist, Hanne Therese	Statistical Properties of Successive Ocean Wave Parameters. (Dr.Ing. Thesis)
IMT-2004-7	Ransau, Samuel	Numerical Methods for Flows with Evolving Interfaces. (Dr.Ing. Thesis)
IMT-2004-8	Soma, Torkel	Blue-Chip or Sub-Standard. A data interrogation approach of identity safety characteristics of shipping organization. (Dr.Ing. Thesis)
IMT-2004-9	Ersdal, Svein	An experimental study of hydrodynamic forces on cylinders and cables in near axial flow. (Dr.Ing. Thesis)
IMT-2005-10	Brodtkorb, Per Andreas	The Probability of Occurrence of Dangerous Wave Situations at Sea. (Dr.Ing. Thesis)

Report No.	Author	Title
IMT-2005-11	Yttervik, Rune	Ocean current variability in relation to offshore engineering. (Dr.Ing. Thesis)
IMT-2005-12	Fredheim, Arne	Current Forces on Net-Structures. (Dr.Ing. Thesis)
IMT-2005-13	Heggernes, Kjetil	Flow around marine structures. (Dr.Ing. Thesis
IMT-2005-14	Fouques, Sebastien	Lagrangian Modelling of Ocean Surface Waves and Synthetic Aperture Radar Wave Measurements. (Dr.Ing. Thesis)
IMT-2006-15	Holm, Håvard	Numerical calculation of viscous free surface flow around marine structures. (Dr.Ing. Thesis)
IMT-2006-16	Bjørheim, Lars G.	Failure Assessment of Long Through Thickness Fatigue Cracks in Ship Hulls. (Dr.Ing. Thesis)
IMT-2006-17	Hansson, Lisbeth	Safety Management for Prevention of Occupational Accidents. (Dr.Ing. Thesis)
IMT-2006-18	Zhu, Xinying	Application of the CIP Method to Strongly Nonlinear Wave-Body Interaction Problems. (Dr.Ing. Thesis)
IMT-2006-19	Reite, Karl Johan	Modelling and Control of Trawl Systems. (Dr.Ing. Thesis)
IMT-2006-20	Smogeli, Øyvind Notland	Control of Marine Propellers. From Normal to Extreme Conditions. (Dr.Ing. Thesis)
IMT-2007-21	Storhaug, Gaute	Experimental Investigation of Wave Induced Vibrations and Their Effect on the Fatigue Loading of Ships. (Dr.Ing. Thesis)
IMT-2007-22	Sun, Hui	A Boundary Element Method Applied to Strongly Nonlinear Wave-Body Interaction Problems. (PhD Thesis, CeSOS)
IMT-2007-23	Rustad, Anne Marthine	Modelling and Control of Top Tensioned Risers. (PhD Thesis, CeSOS)
IMT-2007-24	Johansen, Vegar	Modelling flexible slender system for real-time simulations and control applications
IMT-2007-25	Wroldsen, Anders Sunde	Modelling and control of tensegrity structures. (PhD Thesis, CeSOS)
IMT-2007-26	Aronsen, Kristoffer Høye	An experimental investigation of in-line and combined inline and cross flow vortex induced vibrations. (Dr. avhandling, IMT)
IMT-2007-27	Gao, Zhen	Stochastic Response Analysis of Mooring Systems with Emphasis on Frequency-domain Analysis of Fatigue due to Wide-band Response Processes (PhD Thesis, CeSOS)
IMT-2007-28	Thorstensen, Tom Anders	Lifetime Profit Modelling of Ageing Systems Utilizing Information about Technical Condition. (Dr.ing. thesis, IMT)
IMT-2008-29	Berntsen, Per Ivar B.	Structural Reliability Based Position Mooring. (PhD-Thesis, IMT)
IMT-2008-30	Ye, Naiquan	Fatigue Assessment of Aluminium Welded Box-stiffener Joints in Ships (Dr.ing. thesis, IMT)

Report No.	Author	Title
IMT-2008-31	Radan, Damir	Integrated Control of Marine Electrical Power Systems. (PhD-Thesis, IMT)
IMT-2008-32	Thomassen, Paul	Methods for Dynamic Response Analysis and Fatigue Life Estimation of Floating Fish Cages. (Dr.ing. thesis, IMT)
IMT-2008-33	Pákozdi, Csaba	A Smoothed Particle Hydrodynamics Study of Two-dimensional Nonlinear Sloshing in Rectangular Tanks. (Dr.ing.thesis, IMT/ CeSOS)
IMT-2008-34	Grytøyr, Guttorm	A Higher-Order Boundary Element Method and Applications to Marine Hydrodynamics. (Dr.ing.thesis, IMT)
IMT-2008-35	Drummen, Ingo	Experimental and Numerical Investigation of Nonlinear Wave-Induced Load Effects in Containerships considering Hydroelasticity. (PhD thesis, CeSOS)
IMT-2008-36	Skejic, Renato	Maneuvering and Seakeeping of a Singel Ship and of Two Ships in Interaction. (PhD-Thesis, CeSOS)
IMT-2008-37	Harlem, Alf	An Age-Based Replacement Model for Repairable Systems with Attention to High-Speed Marine Diesel Engines. (PhD-Thesis, IMT)
IMT-2008-38	Alsos, Hagbart S.	Ship Grounding. Analysis of Ductile Fracture, Bottom Damage and Hull Girder Response. (PhD-thesis, IMT)
IMT-2008-39	Graczyk, Mateusz	Experimental Investigation of Sloshing Loading and Load Effects in Membrane LNG Tanks Subjected to Random Excitation. (PhD-thesis, CeSOS)
IMT-2008-40	Taghipour, Reza	Efficient Prediction of Dynamic Response for Flexible amd Multi-body Marine Structures. (PhD-thesis, CeSOS)
IMT-2008-41	Ruth, Eivind	Propulsion control and thrust allocation on marine vessels. (PhD thesis, CeSOS)
IMT-2008-42	Nystad, Bent Helge	Technical Condition Indexes and Remaining Useful Life of Aggregated Systems. PhD thesis, IMT
IMT-2008-43	Soni, Prashant Kumar	Hydrodynamic Coefficients for Vortex Induced Vibrations of Flexible Beams. PhD thesis, CeSOS
IMT-2009-43	Amlashi, Hadi K.K.	Ultimate Strength and Reliability-based Design of Ship Hulls with Emphasis on Combined Global and Local Loads. PhD Thesis, IMT
IMT-2009-44	Pedersen, Tom Arne	Bond Graph Modelling of Marine Power Systems. PhD Thesis, IMT
IMT-2009-45	Kristiansen, Trygve	Two-Dimensional Numerical and Experimental Studies of Piston-Mode Resonance. PhD thesis, CeSOS

Report No.	Author	Title
IMT-2009-46	Ong, Muk Chen	Applications of a Standard High Reynolds Number Model and a Stochastic Scour Prediction Model for Marine Structures. PhD-thesis, IMT
IMT-2009-47	Hong, Lin	Simplified Analysis and Design of Ships subjected to Collision and Grounding. PhD-thesis, IMT
IMT-2009-48	Koushan, Kamran	Vortex Induced Vibrations of Free Span Pipelines, PhD thesis, IMT
IMT-2009-49	Korsvik, Jarl Eirik	Heuristic Methods for Ship Routing and Scheduling. PhD-thesis, IMT
IMT-2009-50	Lee, Jihoon	Experimental Investigation and Numerical in Analyzing the Ocean Current Displacement of Longlines. Ph.d.-Thesis, IMT.
IMT-2009-51	Vestbøstad, Tone Gran	A Numerical Study of Wave-in-Deck Impact usin a Two-Dimensional Constrained Interpolation Profile Method, Ph.d.thesis, CeSOS.
IMT-2009-52	Bruun, Kristine	Bond Graph Modelling of Fuel Cells for Marine Power Plants. Ph.d.-thesis, IMT
IMT-2009-53	Holstad, Anders	Numerical Investigation of Turbulence in a Sekwed Three-Dimensional Channel Flow, Ph.d.-thesis, IMT.
IMT-2009-54	Ayala-Uraga, Efren	Reliability-Based Assessment of Deteriorating Ship-shaped Offshore Structures, Ph.d.-thesis, IMT
IMT-2009-55	Kong, Xiangjun	A Numerical Study of a Damaged Ship in Beam Sea Waves. Ph.d.-thesis, IMT/CeSOS.
IMT-2010-56	Kristiansen, David	Wave Induced Effects on Floaters of Aquaculture Plants, Ph.d.-thesis, CeSOS.
IMT-2010-57	Ludvigsen, Martin	An ROV-Toolbox for Optical and Acoustic Scientific Seabed Investigation. Ph.d.-thesis IMT.
IMT-2010-58	Hals, Jørgen	Modelling and Phase Control of Wave-Energy Converters. Ph.d.thesis, CeSOS.
IMT-2010-59	Shu, Zhi	Uncertainty Assessment of Wave Loads and Ultimate Strength of Tankers and Bulk Carriers in a Reliability Framework. Ph.d. Thesis, IMT/ CeSOS
IMT-2010-60	Shao, Yanlin	Numerical Potential-Flow Studies on Weakly-Nonlinear Wave-Body Interactions with/without Small Forward Speed, Ph.d.thesis, CeSOS.
IMT-2010-61	Califano, Andrea	Dynamic Loads on Marine Propellers due to Intermittent Ventilation. Ph.d.thesis, IMT.
IMT-2010-62	El Khoury, George	Numerical Simulations of Massively Separated Turbulent Flows, Ph.d.-thesis, IMT
IMT-2010-63	Seim, Knut Sponheim	Mixing Process in Dense Overflows with Emphasis on the Faroe Bank Channel Overflow. Ph.d.thesis, IMT

Report No.	Author	Title
IMT-2010-64	Jia, Huirong	Structural Analysis of Intect and Damaged Ships in a Collission Risk Analysis Perspective. Ph.d.thesis CeSoS.
IMT-2010-65	Jiao, Linlin	Wave-Induced Effects on a Pontoon-type Very Large Floating Structures (VLFS). Ph.D.-thesis, CeSOS.
IMT-2010-66	Abrahamsen, Bjørn Christian	Sloshing Induced Tank Roof with Entrapped Air Pocket. Ph.d.thesis, CeSOS.
IMT-2011-67	Karimirad, Madjid	Stochastic Dynamic Response Analysis of Spar-Type Wind Turbines with Catenary or Taut Mooring Systems. Ph.d.-thesis, CeSOS.
IMT-2011-68	Erlend Meland	Condition Monitoring of Safety Critical Valves. Ph.d.-thesis, IMT.
IMT-2011-69	Yang, Limin	Stochastic Dynamic System Analysis of Wave Energy Converter with Hydraulic Power Take-Off, with Particular Reference to Wear Damage Analysis, Ph.d. Thesis, CeSOS.
IMT-2011-70	Visscher, Jan	Application of Particla Image Velocimetry on Turbulent Marine Flows, Ph.d.Thesis, IMT.
IMT-2011-71	Su, Biao	Numerical Predictions of Global and Local Ice Loads on Ships. Ph.d.Thesis, CeSOS.
IMT-2011-72	Liu, Zhenhui	Analytical and Numerical Analysis of Iceberg Collision with Ship Structures. Ph.d.Thesis, IMT.
IMT-2011-73	Aarsæther, Karl Gunnar	Modeling and Analysis of Ship Traffic by Observation and Numerical Simulation. Ph.d.Thesis, IMT.
IMT-2011-74	Wu, Jie	Hydrodynamic Force Identification from Stochastic Vortex Induced Vibration Experiments with Slender Beams. Ph.d.Thesis, IMT.
IMT-2011-75	Amini, Hamid	Azimuth Propulsors in Off-design Conditions. Ph.d.Thesis, IMT.
IMT-2011-76	Nguyen, Tan-Hoi	Toward a System of Real-Time Prediction and Monitoring of Bottom Damage Conditions During Ship Grounding. Ph.d.thesis, IMT.
IMT-2011-77	Tavakoli, Mohammad T.	Assessment of Oil Spill in Ship Collision and Grounding, Ph.d.thesis, IMT.
IMT-2011-78	Guo, Bingjie	Numerical and Experimental Investigation of Added Resistance in Waves. Ph.d.Thesis, IMT.
IMT-2011-79	Chen, Qiaofeng	Ultimate Strength of Aluminium Panels, considering HAZ Effects, IMT
IMT-2012-80	Kota, Ravikiran S.	Wave Loads on Decks of Offshore Structures in Random Seas, CeSOS.
IMT-2012-81	Sten, Ronny	Dynamic Simulation of Deep Water Drilling Risers with Heave Compensating System, IMT.
IMT-2012-82	Berle, Øyvind	Risk and resilience in global maritime supply chains, IMT.
IMT-2012-83	Fang, Shaoji	Fault Tolerant Position Mooring Control Based on Structural Reliability, CeSOS.

Report No.	Author	Title
IMT-2012-84	You, Jikun	Numerical studies on wave forces and moored ship motions in intermediate and shallow water, CeSOS.
IMT-2012-85	Xiang, Xu	Maneuvering of two interacting ships in waves, CeSOS
IMT-2012-86	Dong, Wenbin	Time-domain fatigue response and reliability analysis of offshore wind turbines with emphasis on welded tubular joints and gear components, CeSOS
IMT-2012-87	Zhu, Suji	Investigation of Wave-Induced Nonlinear Load Effects in Open Ships considering Hull Girder Vibrations in Bending and Torsion, CeSOS
IMT-2012-88	Zhou, Li	Numerical and Experimental Investigation of Station-keeping in Level Ice, CeSOS
IMT-2012-90	Ushakov, Sergey	Particulate matter emission characteristics from diesel enignes operating on conventional and alternative marine fuels, IMT
IMT-2013-1	Yin, Decao	Experimental and Numerical Analysis of Combined In-line and Cross-flow Vortex Induced Vibrations, CeSOS
IMT-2013-2	Kurniawan, Adi	Modelling and geometry optimisation of wave energy converters, CeSOS
IMT-2013-3	Al Ryati, Nabil	Technical condition indexes doe auxiliary marine diesel engines, IMT
IMT-2013-4	Firoozkoohi, Reza	Experimental, numerical and analytical investigation of the effect of screens on sloshing, CeSOS
IMT-2013-5	Ommani, Babak	Potential-Flow Predictions of a Semi-Displacement Vessel Including Applications to Calm Water Broaching, CeSOS
IMT-2013-6	Xing, Yihan	Modelling and analysis of the gearbox in a floating spar-type wind turbine, CeSOS
IMT-7-2013	Balland, Océane	Optimization models for reducing air emissions from ships, IMT
IMT-8-2013	Yang, Dan	Transitional wake flow behind an inclined flat plate – Computation and analysis, IMT
IMT-9-2013	Abdillah, Suyuthi	Prediction of Extreme Loads and Fatigue Damage for a Ship Hull due to Ice Action, IMT
IMT-10-2013	Ramìrez, Pedro Agustìn Pèrez	Ageing management and life extension of technical systems. Concepts and methods applied to oil and gas facilities, IMT
IMT-11-2013	Chuang, Zhenju	Experimental and Numerical Investigation of Speed Loss due to Seakeeping and Maneuvering. IMT
IMT-12-2013	Etemaddar, Mahmoud	Load and Response Analysis of Wind Turbines under Atmospheric Icing and Controller System Faults with Emphasis on Spar Type Floating Wind Turbines, IMT

Report No.	Author	Title
IMT-13-2013	Lindstad, Haakon	Strategies and measures for reducing maritime CO2 emissons, IMT
IMT-14-2013	Haris, Sabril	Damage interaction analysis of ship collisions, IMT
IMT-15-2013	Shainee, Mohamed	Conceptual Design, Numerical and Experimental Investigation of a SPM Cage Concept for Offshore Mariculture, IMT
IMT-16-2013	Gansel, Lars	Flow past porous cylinders and effects of biofouling and fish behavior on the flow in and around Atlantic salmon net cages, IMT
IMT-17-2013	Gaspar, Henrique	Handling Aspects of Complexity in Conceptual Ship Design, IMT
IMT-18-2013	Thys, Maxime	Theoretical and Experimental Investigation of a Free Running Fishing Vessel at Small Frequency of Encounter, CeSOS
IMT-19-2013	Aglen, Ida	VIV in Free Spanning Pipelines, CeSOS
IMT-1-2014	Song, An	Theoretical and experimental studies of wave diffraction and radiation loads on a horizontally submerged perforated plate, CeSOS
IMT-2-2014	Rogne, Øyvind Ygre	Numerical and Experimental Investigation of a Hinged 5-body Wave Energy Converter, CeSOS
IMT-3-2014	Dai, Lijuan	Safe and efficient operation and maintenance of offshore wind farms, IMT
IMT-4-2014	Bachynski, Erin Elizabeth	Design and Dynamic Analysis of Tension Leg Platform Wind Turbines, CeSOS
IMT-5-2014	Wang, Jingbo	Water Entry of Freefall Wedged – Wedge motions and Cavity Dynamics, CeSOS
IMT-6-2014	Kim, Ekaterina	Experimental and numerical studies related to the coupled behavior of ice mass and steel structures during accidental collisions, IMT
IMT-7-2014	Tan, Xiang	Numerical investigation of ship's continuous-mode icebreaking in leverl ice, CeSOS
IMT-8-2014	Muliawan, Made Jaya	Design and Analysis of Combined Floating Wave and Wind Power Facilities, with Emphasis on Extreme Load Effects of the Mooring System, CeSOS
IMT-9-2014	Jiang, Zhiyu	Long-term response analysis of wind turbines with an emphasis on fault and shutdown conditions, IMT
IMT-10-2014	Dukan, Fredrik	ROV Motion Control Systems, IMT
IMT-11-2014	Grimsmo, Nils I.	Dynamic simulations of hydraulic cylinder for heave compensation of deep water drilling risers, IMT
IMT-12-2014	Kvittem, Marit I.	Modelling and response analysis for fatigue design of a semisubmersible wind turbine, CeSOS
IMT-13-2014	Akhtar, Juned	The Effects of Human Fatigue on Risk at Sea, IMT

Report No.	Author	Title
IMT-14-2014	Syahroni, Nur	Fatigue Assessment of Welded Joints Taking into Account Effects of Residual Stress, IMT
IMT-1-2015	Bøckmann, Eirik	Wave Propulsion of ships, IMT
IMT-2-2015	Wang, Kai	Modelling and dynamic analysis of a semi-submersible floating vertical axis wind turbine, CeSOS
IMT-3-2015	Fredriksen, Arnt Gunvald	A numerical and experimental study of a two-dimensional body with moonpool in waves and current, CeSOS
IMT-4-2015	Jose Patricio Gallardo Canabes	Numerical studies of viscous flow around bluff bodies, IMT
IMT-5-2015	Vegard Longva	Formulation and application of finite element techniques for slender marine structures subjected to contact interactions, IMT
IMT-6-2015	Jacobus De Vaal	Aerodynamic modelling of floating wind turbines, CeSOS
IMT-7-2015	Fachri Nasution	Fatigue Performance of Copper Power Conductors, IMT
IMT-8-2015	Oleh Karpa	Development of bivariate extreme value distributions for applications in marine technology, CeSOS
IMT-9-2015	Daniel de Almeida Fernandes	An output feedback motion control system for ROVs, CeSOS/AMOS
IMT-10-2015	Bo Zhao	Particle Filter for Fault Diagnosis: Application to Dynamic Positioning Vessel and Underwater Robotics, CeSOS
IMT-11-2015	Wenting Zhu	Impact of emission allocation in maritime transportation, IMT
IMT-12-2015	Amir Rasekhi Nejad	Dynamic Analysis and Design of Gearboxes in Offshore Wind Turbines in a Structural Reliability Perspective, CeSOS
IMT-13-2015	Arturo Jesùs Ortega Malca	Dynamic Response of Flexibles Risers due to Unsteady Slug Flow, CeSOS
IMT-14-2015	Dagfinn Husjord	Guidance and decision-support system for safe navigation of ships operating in close proximity, IMT
IMT-15-2015	Anirban Bhattacharyya	Ducted Propellers: Behaviour in Waves and Scale Effects, IMT
IMT-16-2015	Qin Zhang	Image Processing for Ice Parameter Identification in Ice Management, IMT
IMT-1-2016	Vincentius Rumawas	Human Factors in Ship Design and Operation: An Experiential Learning, IMT
IMT-2-2016	Martin Storheim	Structural response in ship-platform and ship-ice collisions, IMT
IMT-3-2016	Mia Abrahamsen Prsic	Numerical Simulations of the Flow around single and Tandem Circular Cylinders Close to a Plane Wall, IMT

Report No.	Author	Title
IMT-4-2016	Tufan Arslan	Large-eddy simulations of cross-flow around ship sections, IMT
IMT-5-2016	Pierre Yves-Henry	Parametrisation of aquatic vegetation in hydraulic and coastal research,IMT
IMT-6-2016	Lin Li	Dynamic Analysis of the Instalation of Monopiles for Offshore Wind Turbines, CeSOS
IMT-7-2016	Øivind Kåre Kjerstad	Dynamic Positioning of Marine Vessels in Ice, IMT
IMT-8-2016	Xiaopeng Wu	Numerical Analysis of Anchor Handling and Fish Trawling Operations in a Safety Perspective, CeSOS
IMT-9-2016	Zhengshun Cheng	Integrated Dynamic Analysis of Floating Vertical Axis Wind Turbines, CeSOS
IMT-10-2016	Ling Wan	Experimental and Numerical Study of a Combined Offshore Wind and Wave Energy Converter Concept
IMT-11-2016	Wei Chai	Stochastic dynamic analysis and reliability evaluation of the roll motion for ships in random seas, CeSOS
IMT-12-2016	Øyvind Selnes Patricksson	Decision support for conceptual ship design with focus on a changing life cycle and future uncertainty, IMT
IMT-13-2016	Mats Jørgen Thorsen	Time domain analysis of vortex-induced vibrations, IMT
IMT-14-2016	Edgar McGuinness	Safety in the Norwegian Fishing Fleet – Analysis and measures for improvement, IMT
IMT-15-2016	Sepideh Jafarzadeh	Energy effiency and emission abatement in the fishing fleet, IMT
IMT-16-2016	Wilson Ivan Guachamin Acero	Assessment of marine operations for offshore wind turbine installation with emphasis on response-based operational limits, IMT
IMT-17-2016	Mauro Candeloro	Tools and Methods for Autonomous Operations on Seabed and Water Coumn using Underwater Vehicles, IMT
IMT-18-2016	Valentin Chabaud	Real-Time Hybrid Model Testing of Floating Wind Tubines, IMT
IMT-1-2017	Mohammad Saud Afzal	Three-dimensional streaming in a sea bed boundary layer
IMT-2-2017	Peng Li	A Theoretical and Experimental Study of Wave-induced Hydroelastic Response of a Circular Floating Collar
IMT-3-2017	Martin Bergström	A simulation-based design method for arctic maritime transport systems
IMT-4-2017	Bhushan Taskar	The effect of waves on marine propellers and propulsion
IMT-5-2017	Mohsen Bardestani	A two-dimensional numerical and experimental study of a floater with net and sinker tube in waves and current

Report No.	Author	Title
IMT-6-2017	Fatemeh Hoseini Dadmarzi	Direct Numerical Simualtion of turbulent wakes behind different plate configurations
IMT-7-2017	Michel R. Miyazaki	Modeling and control of hybrid marine power plants
IMT-8-2017	Giri Rajasekhar Gunnu	Safety and effiency enhancement of anchor handling operations with particular emphasis on the stability of anchor handling vessels
IMT-9-2017	Kevin Koosup Yum	Transient Performance and Emissions of a Turbocharged Diesel Engine for Marine Power Plants
IMT-10-2017	Zhaolong Yu	Hydrodynamic and structural aspects of ship collisions
IMT-11-2017	Martin Hassel	Risk Analysis and Modelling of Allisions between Passing Vessels and Offshore Installations
IMT-12-2017	Astrid H. Brodtkorb	Hybrid Control of Marine Vessels – Dynamic Positioning in Varying Conditions
IMT-13-2017	Kjersti Bruserud	Simultaneous stochastic model of waves and current for prediction of structural design loads
IMT-14-2017	Finn-Idar Grøtta Giske	Long-Term Extreme Response Analysis of Marine Structures Using Inverse Reliability Methods
IMT-15-2017	Stian Skjong	Modeling and Simulation of Maritime Systems and Operations for Virtual Prototyping using co-Simulations
IMT-1-2018	Yingguang Chu	Virtual Prototyping for Marine Crane Design and Operations
IMT-2-2018	Sergey Gavrilin	Validation of ship manoeuvring simulation models
IMT-3-2018	Jeevith Hegde	Tools and methods to manage risk in autonomous subsea inspection,maintenance and repair operations
IMT-4-2018	Ida M. Strand	Sea Loads on Closed Flexible Fish Cages
IMT-5-2018	Erlend Kvinge Jørgensen	Navigation and Control of Underwater Robotic Vehicles
IMT-6-2018	Bård Stovner	Aided Intertial Navigation of Underwater Vehicles
IMT-7-2018	Erlend Liavåg Grotle	Thermodynamic Response Enhanced by Sloshing in Marine LNG Fuel Tanks
IMT-8-2018	Børge Rokseth	Safety and Verification of Advanced Maritime Vessels
IMT-9-2018	Jan Vidar Ulveseter	Advances in Semi-Empirical Time Domain Modelling of Vortex-Induced Vibrations
IMT-10-2018	Chenyu Luan	Design and analysis for a steel braceless semi-submersible hull for supporting a 5-MW horizontal axis wind turbine
IMT-11-2018	Carl Fredrik Rehn	Ship Design under Uncertainty
IMT-12-2018	Øyvind Ødegård	Towards Autonomous Operations and Systems in Marine Archaeology

Report No.	Author	Title
IMT-13- 2018	Stein Melvær Nornes	Guidance and Control of Marine Robotics for Ocean Mapping and Monitoring
IMT-14-2018	Petter Norgren	Autonomous Underwater Vehicles in Arctic Marine Operations: Arctic marine research and ice monitoring
IMT-15-2018	Minjoo Choi	Modular Adaptable Ship Design for Handling Uncertainty in the Future Operating Context
MT-16-2018	Ole Alexander Eidsvik	Dynamics of Remotely Operated Underwater Vehicle Systems
IMT-17-2018	Mahdi Ghane	Fault Diagnosis of Floating Wind Turbine Drivetrain- Methodologies and Applications
IMT-18-2018	Christoph Alexander Thieme	Risk Analysis and Modelling of Autonomous Marine Systems
IMT-19-2018	Yugao Shen	Operational limits for floating-collar fish farms in waves and current, without and with well-boat presence
IMT-20-2018	Tianjiao Dai	Investigations of Shear Interaction and Stresses in Flexible Pipes and Umbilicals
IMT-21-2018	Sigurd Solheim Pettersen	Resilience by Latent Capabilities in Marine Systems
IMT-22-2018	Thomas Sauder	Fidelity of Cyber-physical Empirical Methods. Application to the Active Truncation of Slender Marine Structures
IMT-23-2018	Jan-Tore Horn	Statistical and Modelling Uncertainties in the Design of Offshore Wind Turbines
IMT-24-2018	Anna Swider	Data Mining Methods for the Analysis of Power Systems of Vessels
IMT-1-2019	Zhao He	Hydrodynamic study of a moored fish farming cage with fish influence
IMT-2-2019	Isar Ghamari	Numerical and Experimental Study on the Ship Parametric Roll Resonance and the Effect of Anti-Roll Tank
IMT-3-2019	Håkon Strandenes	Turbulent Flow Simulations at Higher Reynolds Numbers
IMT-4-2019	Siri Mariane Holen	Safety in Norwegian Fish Farming – Concepts and Methods for Improvement
IMT-5-2019	Ping Fu	Reliability Analysis of Wake-Induced Riser Collision
IMT-6-2019	Vladimir Krivopolianskii	Experimental Investigation of Injection and Combustion Processes in Marine Gas Engines using Constant Volume Rig
IMT-7-2019	Anna Maria Kozlowska	Hydrodynamic Loads on Marine Propellers Subject to Ventilation and out of Water Condition.
IMT-8-2019	Hans-Martin Heyn	Motion Sensing on Vessels Operating in Sea Ice: A Local Ice Monitoring System for Transit and Stationkeeping Operations under the Influence of Sea Ice

Report No.	Author	Title
IMT-9-2019	Stefan Vilsen	Method for Real-Time Hybrid Model Testing of Ocean Structures – Case on Slender Marine Systems
IMT-10-2019	Finn-Christian W. Hanssen	Non-Linear Wave-Body Interaction in Severe Waves
IMT-11-2019	Trygve Olav Fossum	Adaptive Sampling for Marine Robotics
IMT-12-2019	Jørgen Bremnes Nielsen	Modeling and Simulation for Design Evaluation
IMT-13-2019	Yuna Zhao	Numerical modelling and dyncamic analysis of offshore wind turbine blade installation
IMT-14-2019	Daniela Myland	Experimental and Theoretical Investigations on the Ship Resistance in Level Ice
IMT-15-2019	Zhengru Ren	Advanced control algorithms to support automated offshore wind turbine installation
IMT-16-2019	Drazen Polic	Ice-propeller impact analysis using an inverse propulsion machinery simulation approach
IMT-17-2019	Endre Sandvik	Sea passage scenario simulation for ship system performance evaluation
IMT-18-2019	Loup Suja-Thauvin	Response of Monopile Wind Turbines to Higher Order Wave Loads
IMT-19-2019	Emil Smilden	Structural control of offshore wind turbines – Increasing the role of control design in offshore wind farm development
IMT-20-2019	Aleksandar-Sasa Milakovic	On equivalent ice thickness and machine learning in ship ice transit simulations
IMT-1-2020	Amrit Shankar Verma	Modelling, Analysis and Response-based Operability Assessment of Offshore Wind Turbine Blade Installation with Emphasis on Impact Damages
IMT-2-2020	Bent Oddvar Arnesen Haugaløkken	Autonomous Technology for Inspection, Maintenance and Repair Operations in the Norwegian Aquaculture
IMT-3-2020	Seongpil Cho	Model-based fault detection and diagnosis of a blade pitch system in floating wind turbines
IMT-4-2020	Jose Jorge Garcia Agis	Effectiveness in Decision-Making in Ship Design under Uncertainty
IMT-5-2020	Thomas H. Viuff	Uncertainty Assessment of Wave-and Current-induced Global Response of Floating Bridges
IMT-6-2020	Fredrik Mentzoni	Hydrodynamic Loads on Complex Structures in the Wave Zone
IMT-7-2020	Senthuran Ravinthrakumar	Numerical and Experimental Studies of Resonant Flow in Moonpools in Operational Conditions
IMT-8-2020	Stian Skaalvik Sandøy	Acoustic-based Probabilistic Localization and Mapping using Unmanned Underwater Vehicles for Aquaculture Operations

Report No.	Author	Title
IMT-9-2020	Kun Xu	Design and Analysis of Mooring System for Semi-submersible Floating Wind Turbine in Shallow Water
IMT-10-2020	Jianxun Zhu	Cavity Flows and Wake Behind an Elliptic Cylinder Translating Above the Wall
IMT-11-2020	Sandra Hogenboom	Decision-making within Dynamic Positioning Operations in the Offshore Industry – A Human Factors based Approach
IMT-12-2020	Woongshik Nam	Structural Resistance of Ship and Offshore Structures Exposed to the Risk of Brittle Failure
IMT-13-2020	Svenn Are Tutturen Værnø	Transient Performance in Dynamic Positioning of Ships: Investigation of Residual Load Models and Control Methods for Effective Compensation
IMT-14-2020	Mohd Atif Siddiqui	Experimental and Numerical Hydrodynamic Analysis of a Damaged Ship in Waves
IMT-15-2020	John Marius Hegseth	Efficient Modelling and Design Optimization of Large Floating Wind Turbines
IMT-16-2020	Asle Natskår	Reliability-based Assessment of Marine Operations with Emphasis on Sea Transport on Barges
IMT-17-2020	Shi Deng	Experimental and Numerical Study of Hydrodynamic Responses of a Twin-Tube Submerged Floating Tunnel Considering Vortex-Induced Vibration
IMT-18-2020	Jone Torsvik	Dynamic Analysis in Design and Operation of Large Floating Offshore Wind Turbine Drivetrains
IMT-1-2021	Ali Ebrahimi	Handling Complexity to Improve Ship Design Competitiveness
IMT-2-2021	Davide Proserpio	Isogeometric Phase-Field Methods for Modeling Fracture in Shell Structures
IMT-3-2021	Cai Tian	Numerical Studies of Viscous Flow Around Step Cylinders
IMT-4-2021	Farid Khazaeli Moghadam	Vibration-based Condition Monitoring of Large Offshore Wind Turbines in a Digital Twin Perspective
IMT-5-2021	Shuaishuai Wang	Design and Dynamic Analysis of a 10-MW Medium-Speed Drivetrain in Offshore Wind Turbines
IMT-6-2021	Sadi Tavakoli	Ship Propulsion Dynamics and Emissions
IMT-7-2021	Haoran Li	Nonlinear wave loads, and resulting global response statistics of a semi-submersible wind turbine platform with heave plates
IMT-8-2021	Einar Skiftestad Ueland	Load Control for Real-Time Hybrid Model Testing using Cable-Driven Parallel Robots

Report No.	Author	Title
IMT-9-2021	Mengning Wu	Uncertainty of machine learning-based methods for wave forecast and its effect on installation of offshore wind turbines
IMT-10-2021	Xu Han	Onboard Tuning and Uncertainty Estimation of Vessel Seakeeping Model Parameters
IMT-01-2022	Ingunn Marie Holmen	Safety in Exposed Aquacultrue Operations
IMT-02-2022	Prateek Gupta	Ship Performance Monitoring using In-service Measurements and Big Data Analysis Methods
IMT-03-2022	Sangwoo Kim	Non-linear time domain analysis of deepwater riser vortex-induced vibrations
IMT-04-2022	Jarle Vinje Kramer	Hydrodynamic Aspects of Sail-Assisted Merchant Vessels
IMT-05-2022	Øyvind Rabliås	Numerical and Experimental Studies of Maneuvering in Regular and Irregular Waves
IMT-06-2022	Pramod Ghimire	Simulation-Based Ship Hybrid Power System Conspet Studies and Performance Analyses
IMT-07-2022	Carlos Eduardo Silva de Souza	Structural modelling, coupled dynamics, and design of large floating wind turbines
IMT-08-2022	Lorenzo Balestra	Design of hybrid fuel cell & battery systems for maritime vessels
IMT-09-2022	Sharmin Sultana	Process safety and risk management using system perspectives – A contribution to the chemical process and petroleum industry
IMT-10-2022	Øystein Sture	Autonomous Exploration for Marine Minerals
IMT-11-2022	Tiantian Zhu	Information and Decision-making for Major Accident Prevention – A concept of information-based strategies for accident prevention
IMT-12-2022	Siamak Karimi	Shore-to-Ship Charging Systems for Battery-Electric Ships
IMT-01-2023	Huili Xu	Fish-inspired Propulsion Study: Numerical Hydrodynamics of Rigid/Flexible/Morphing Foils and Observations on Real Fish
IMT-02-2023	Chana Sinsabvarodom	Probabilistic Modelling of Ice-drift and Ice Loading on Fixed and Floating Offshore Structures
IMT-03-2023	Martin Skaldebø	Intelligent low-cost solutions for underwater intervention using computer vision and machine learning
IMT-04-2023	Hans Tobias Slette	Vessel operations in exposed aquaculture – Achieving safe and efficient operation of vessel fleets in fish farm systems experiencing challenging metocean conditions
IMT-05-2023	Ruochen Yang	Methods and models for analyzing and controlling the safety in operations of autonomous marine systems
IMT-06-2023	Tobias Rye Torben	Formal Approaches to Design and Verification of Safe Control Systems for Autonomous Vessels

Report No.	Author	Title
IMT-07-2023	YoungRong Kim	Modeling Operational Performance for the Global Fleet & Application of an Energy Saving Measure
IMT-08-2023	Henrik Schmidt-Didlaukies	Modeling and Hybrid Feedback Control of Underwater Vehicles
IMT-09-2023	Ehsan Esmailian	Optimal Ship Design for Operating in Real Sea States
IMT-10-2023	Astrid Vamråk Solheim	Exploring the performance of conceptual offshore production systems for deep-sea mining
IMT-11-2023	Benjamin Lagemann	Conceptual design of low-emission ships
IMT-12-2023	Erling Neerland Lone	Fatigue reliability of offshore Mooring chains under influence of mean load and corrosion
IMT-13-2023	Kamyar Malek-ibagherabadi	Simulator Approach to Concept Analysis and Optimization of Marine Power Plants
IMT-14-2023	Håvard Snefjellås Løvås	Optical Techniques for Hyperspectral Imaging of the Seafloor
IMT-15-2023	Stian Høegh Sørum	Uncertainties in the Design of Monopile Offshore Wind Turbines
IMT-16-2023	Nathalie Ramos	Mechanical and thermal simulations of 3D printed structures and the 3D printing process
IMT-17-2023	Daeseong Park	Model-Based Design of Marine Hybrid Power Systems
IMT-18-2023	Chuanqi Guo	Analysis and modeling of risk of an autonomous ferry for safer design and operation
IMT-01-2024	Dennis David Langer	Hyperspectral Push-broom Systems: Operations,Software Development, and Spatial Resolution
IMT-02-2024	Jens Einar Bremnes	Safe Autonomy in Marine Robotics
IMT-03-2024	George Katsikogiannis	Estimation of Long-Term Fatigue and Extreme Responses of Large-Diameter Monopiles for Offshore Wind Turbines
IMT-04-2024	Alexandre Cardaillac	Towards autonomous underwater navigation and perception for end-to-end ship hull inspection
IMT-05-2024	Tale Egeberg Aasland	Numerical studies of viscous flow around straight and curved tandem cylinders
IMT-06-2024	Felix Mehlan	Digital Twins for Fault Prognosis in Offshore Wind Turbine Drivetrains